SILICON FOR THE CHEMICAL AND SOLAR INDUSTRY XV

Trondheim, NORWAY

June 15-18, 2020



Editors: Birger Andresen, Harry Rong, Merete Tangstad, Halvard Tveit, Ingrid Gamst Page

The Norwegian University of Science and Technology
N-7491 Trondheim, Norway

Front page: Silox plant – Published with permission from Elkem Silicones

ISBN 978-82-997357-9-7

SILICON FOR THE CHEMICAL AND SOLAR INDUSTRY XV

Trondheim, NORWAY

June 15-18, 2020

Editors: Birger Andresen, Wacker Chemie

Harry Rong Elkem ASA,

Merete Tangstad, NTNU

Halvard Tveit, Elkem/NTNU

Ingrid Gamst Page

The Norwegian University of Science and Technology

N-7491 Trondheim, Norway

Welcome to this year's digital conference!

2020 will be remembered as the year Covid-19 changed the world as we know it. This tragedy has changed our daily patterns of behaviour, both professionally and privately. For most of us this has resulted in home officing that will no doubt extend beyond the time period of the Corona pandemic, as well as less travel and less consumption. For the Silicon for Chemical and Solar Industry conference, it has resulted in an integrated webinar with proceedings and online talks. Unfortunately this also means we will not be able to interact with future clients and partners in person, as well as not being able to have the time to get a complete overview over new technology regarding a number of topics within silicon. In two years time, in 2022, we hope that we can again meet face-to-face in Trondheim at enjoying the next Silicon for Chemical and Solar Industry conference. At that time we will also see how the pandemic has affected the business scenarios for the Silicon industry.

While people are currently putting their lives on hold, the urgency of restoring the climate is not waiting. More important than ever, this has led to an increasing amount of papers within this topic. We have thus chosen to give the environmental topics a considerable amount of time in the live streaming part of the conference. Silicon will be an integrated part in finding the technical solutions to reduce CO_2 emissions, through for example solar cells and wind mills, lighter cars using Al-alloys and the use of silicones. The need for silicon will thus increase.

There is a large, global effort to improve technical solutions within the production and use of silicon. The organizing committee appreciate the willingness to publish these solutions at the conference. It will enable all of us to be at the forefront of technology.

Merete Tangstad

Head of organizing committee,

Table of contents

Louise Daintith, Andy Jones, Peter Goossen and Sean Gaal
Sustainable production of chlorosilane in Dow 1

Geir Ausland, Harry M. Rong
Silicon production with high energy efficiency and low CO_2 footprint 13

Andrea Broggi, Eli Ringdalen and Merete Tangstad
Empirical analysis of clogging of SiC charges: effect of condensation of SiO and CO 23

Halvard Tveit, Eli Ringdalen and Hanne Edfeldt
Important parameters that control the crater pressure in a Silicon Furnace 37

André Meißner, Tim Sieber and Jörg Acker
Lattice strain and phase transformations in silicon introduced by the precipitation of Cu_3Si 47

Jorn de Linde
Silicon in the 2020s 57

Haley Hoover, Tommy A. Pedersen, Guðrún Sævarsdóttir and Merete Tangstad,
Bulk Resistivity of SiC and Carbon Materials in the Silicon Furnace 65

Ida Kero, Svend Grådahl and Gabriella Tranell
Particulate matter and related airborne emissions from silicon and ferrosilicon production 75

Robert Becker, Stefan Bauer
Carbon fibers – alternative to graphite core in composite technology? 89

Eli Ringdalen, Sarina Bao and Halvard Tveit
Effect of melting properties of quartz on industrial Si and FeSi production 101

Marit Buhaug Folstad, Michal Ksiazek and Merete Tangstad
Slag in the tapping area in a Si furnace 119

Gabriella Tranell, Jafar Safarian and Maria Wallin
SisAl – A New Process for Production of Silicon 129

Bjørn Sandberg, Ragnar Tronstad
New Philosophy for Metal Production in a Green Environment 141

Anja Rietig, Thomas Langner, and Jörg Acker
Advanced insights into the stoichiometry and kinetics of the reaction of silicon in HF/HNO_3 and $HF/HNO_3/H_2SiF_6$ mixtures 145

Jan Otto Hoel, Harry Morten Rong
Activation of silicon in the hydrochlorination process 161

Ingeborg-Helene Svenum, Sylvain Gouttebroze and Francesca L. Bleken
Reactivity of HCl at the Si(100)-c(4x2) reconstructed surface: a DFT study. 177

Matthias A. Colomb, Esteban J. Romano and Srinivas Palanki
Effects of Shortening a Pilot-Scale Hydrochlorination Reactor with Catalytic Considerations and Comparison to Mathematical Model Predictions 193

Eugénie Blaser, Cécile Rosier, Michel Huet, Christophe Geantet and Stéphane Loridant
Characterization of carbonaceous compounds formed in the methylchlorosilanes synthesis 205

Eugénie Blaser, Cécile Rosier, Michel Huet, Christophe Geantet and Stéphane Loridant
Catalytic cracking and thermal cracking of CH_3Cl occurring in the methylchlorosilanes synthesis 219

Guro Marie Wyller, Thomas J. Preston, Marte O. Skare, Hallgeir Klette and Anjitha S.K. Geetha
Experimental investigations of monosilane pyrolysis: The importance of cyclic silanes 233

Tomohiro Mizutani, Wataru Fukada and Kazuki Morita
Thermodynamics of B in Si–Cu based alloys for optimizing B removal from SOG-Si 247

Arman Hoseinpur, Gabriella Tranell and Jafar Safarian
Phosphorus and Boron removal from Si by vacuum and gas refining processes 261

Mengyi Zhu, Kai Tang and Jafar Safarian
The effect of Ti and Y addition on the microstructure and leaching purification of Ca-alloyed metallurgical silicon 273

Alejandro Datas
Silicon and ferrosilicon latent heat thermal batteries 285

Benedicte Eikeland Nilssen, Bjørn Rune Henriksen and Rolf Arne Kleiv
Effect of operation parameters and formulation on the submicron and nano size silicon powder properties produced by mechanical grinding 295

Songsheng Zheng, Zhaolin Wang, Jin Chen, Xiaohui Hu and Zhibin Lin
The PV market situation in China 2019 and the future 309

Jan-Philipp Mai, Qian Yu
Recycling Silicon Kerf: Challenges, Solutions and Applications 319

Silicon for the Chemical and Solar Industry XV
Trondheim, Norway, June 15 – 18, 2020

Sustainable production of chlorosilane in Dow

Louise Daintith[1], Andy Jones[1], Peter Goossen[2], Mike Squire[1] and Sean Gaal[3]
[1] *Dow Silicones, Cardiff Road, Barry, CF63 2YL, United Kingdom*
[2] *Dow Benelux B.V, Herbet H Dowweg 5, Hoek (Terneuzen), 4542 NM, Netherlands*
[3] *Dow Silicones, 2651 Salzburg Rd, Midland, MI, 48640, USA*

Abstract

Dow's commitment to safety and world-leading operations performance is key to the Company's success, its history and "license to operate" in communities around the world. In 1995, Dow launched the 2005 Environment, Health and Safety (EH&S) Goals, with a $1 billion investment to seek energy efficiency, water reduction/reuse and waste reduction. The Company saved $5 billion and fostered a culture of safety and sustainability. In the next stage, Dow set the 2015 goals, delivering similar results and is now working towards the 2025 Sustainability Goals, which commit to maintaining world-leading operations performance in natural resource efficiency, environment, health and safety. Dow are pursuing efficient operations that drive environmental benefits for communities and helping lead the transition to a sustainable planet and society.

The World Leading Operations Performance goals include a reduction in waste intensity and water intake by 20%, improving raw material efficiency by 10% relative to the 2015 baseline and maintaining absolute greenhouse gas emissions below the 2006 baseline, with a focus to source power from renewable sources. This paper will discuss how the production of chlorosilanes within Dow is aligned and will contribute to these goals.

Introduction

Focusing on sustainability is key to meeting our present needs without compromising future generations. The world is rapidly changing with climate change and population growth discussed every day in the media. The global population is expected to reach 8.3 billion by 2030, putting significant pressure on our planet's resources, especially additional food, production of energy and potable water resources. Global temperatures are increasing and the frequency of extreme weather events is escalating. In response, consumer demands for sustainable products is high, with a focus on purchasing responsible products whenever possible.

At Dow, sustainability is a key pillar to the Company's business strategy. Dow is an innovative Company founded in 1897, with 113 manufacturing sites in 31 countries. In over 120 years of innovation, Dow has been looking to save energy, cut waste and advance product stewardship. It aims to become the most innovative, customer-centric, inclusive and sustainable Materials Science Company in the world [1].

In 1995 Dow made a commitment to sustainability, launching the *2005 Environment, Health and Safety (EH&S) Goals*, with a $1 billion investment to seek energy efficiency, water reduction/reuse and waste reduction. This resulted in $5 billion savings, 1.6 billion pounds of solid waste reduction, 183 billion pounds water usage reduction, 900 trillion BTU's energy saved and 84% reduced personal safety and health incidents. It demonstrated the power of setting advanced stretch goals and consistently working towards them for a whole decade [2].

In the next stage, Dow set the 2015 goals [3], delivering similar results and setting expectations for future programs. Today the Company is working towards the *2025 Sustainability Goals*, developing the blueprint which commits the Company to maintaining world-leading operational performance in natural resource efficiency, environmental stewardship, health and safety [4, 5].

Dow's 2025 sustainability goals are the third set of sustainability goals, building on the commitment made in the previous two decades. They include a reduction in waste intensity and water intake by 20%, improving raw material efficiency by 10% relative to the 2015 baseline and maintaining absolute greenhouse gas emissions below the 2006 baseline, with a focus to source power from renewable sources [4].

From the outset, Dow has brought together science, business and marketing experts to develop the business' long-term approach to sustainability, inspiring and encouraging employees to collaborate and achieve these goals. Dow's 2025 sustainability goals are focused on the whole supply chain, from raw material sourcing through manufacturing to the end of product life [4].

In 2012 Denkstatt and Dekra published a report, commissioned by the Global Silicones Council on the Carbon Balance of Si-chemistry [6] investigating both the carbon emissions resulting from the production of silicone products and the reduction in carbon emissions from the usage of these products instead of less durable materials, clearly demonstrating that the reduction in the use of less durable products outweighs the emissions from silicones production multiple times. Dow is actively innovating and investing to bring silicones' unique performance properties to society [4, 6-9].

Dow has an integrated supply chain, producing and sourcing silicon throughout the world, producing chlorosilane on three continents, enabling supply of materials direct to the customer and minimising the transport of materials across geographies.

Dow's commitment to safety and world-leading operations performance is key to the Company's success, its history and "license to operate" in communities around the world. Pursuing efficient operations that drive environmental benefits for Dow's communities and help all of us transition to a sustainable planet and society.

2025 Sustainability Goals

Dow's ambition is to be the most innovative, customer-centric, inclusive and sustainable Materials Science Company in the world. Sustainability is more than an important ambition for Dow. It is key to how the Company applies science to drive growth, improve Dow's operations and help solve some of the world's most complex challenges. Over the last 25 years, Dow has been guided by three decade-long, sustainability goals. The current set of goals build on the two previous decades of goals. Aligned to the United Nations Sustainable

Development Goals, the ambitious Dow 2025 Sustainability Goals [1, 4] aim to expand the Company's positive impact by driving unprecedented collaborations and harnessing Dow's innovation strengths, global reach and dedicated team of employees.

Dow's emphasis on integrating sustainability metrics into the everyday plans of the Company has been key to its economic, environmental and social metric successes over the past two decades. Dow Consumer Solutions is certainly one of the business' at Dow that is in most direct dialog with final product specifiers around the world. Every day, the Company is witnessing sustainability driving the innovation pipeline and becoming the main discussion topic with consumer brands, architects, building owners, vehicle OEMs and their tier-1 suppliers.

Sustainability Framework

To achieve Dow's ambition, the Company is focused on three areas where it has the most impact and the most opportunity to create shared value for Dow and society, shown in Figure 1.



Figure 1 – Dow's 2025 Sustainability Goals

Circular Economy: Dow is collaborating with customers and the Global Silicones Council [10] to identify opportunities to close resource loops.

Dow received a 2020 BIG innovation award for DOWSIL™ TC-3015 Reworkable Thermal Gel, the world's first thermal conductive silicone gel designed for smartphone re-workability. The technology allows for easy device disassembly to limit discarding of flawed units during manufacturing, to facilitate device repair and to enable better end-of-life separation of components for recycling, thereby improving the sustainability profile of consumer and communications electronics while addressing the critical thermal management needs of these devices.

Dow successfully launched AMPLIFY™ SI 1000 in 2019, a technology enabled by silicone additives that allows a higher proportion of recycled plastic and a higher filler content in wood plastic composites [11]. This is another example of Dow bringing and promoting new post-use solutions and markets for recycled plastics, enabled through silicones.

Climate Protection: The Company is seeking to accelerate climate action within Dow's operations and across the wider value chains that Dow supports. Dow's approach to reducing carbon is deeply rooted in the Company's ambitions and values and demonstrated by the use of renewable energy, investment in new technologies and the benefit of Dow's products to the Company's customers.

Dow's silicone sealants and coatings also help lengthen the operational lifetime of buildings envelope and facades — one of the most important architectural components pertaining to sustainability. Over their lifetime, it is estimated that silicone sealants for buildings reduce emissions by around 200 kg CO_2e per kg of sealant, which is an essential and irreplaceable contribution to the energy efficiency of modern buildings. This is an important contribution to reducing society's greenhouse gas emissions as buildings account for nearly 40% of global energy consumption and the world's population living in urban areas is expected to increase from 55% to 68% by 2050.

Dow recently established a Renewable Power Agreement (RPA) with Kentucky Utilities (KU) to increase the use of solar energy at Dow's silicone site in Carrollton, Kentucky [12], supporting the development of a new solar facility. This brings Dow closer to achieving its 2025 Sustainability Goal to obtain 750 MW of the Company's power demand from renewable sources by 2025, of which 698 MW of clean energy has already secured.

Dow's global portfolio of silicones sites powered by renewable sources, includes Seneffe, Belgium where Dow inaugurated a second 2.3 MW wind turbine in 2019, enabling lower carbon intensity products that meet customer needs and society's expectations [13].

Dow is engaging with a broad range of external stakeholders to advance solutions to a lower carbon society and mitigate the effects of climate change. For example, Dow serves as a member of the Task Force on Climate-Related Financial Disclosures whose aim it is to develop voluntary, consistent climate-related financial risk disclosures for use by companies in providing information to investors, lenders, insurers and other stakeholders.

More Sustainable and Safer Materials: Dow is seeking to innovate more sustainable materials; advance open and transparent chemistry with the Company's value chain partners, customers and the public; collaborate with diverse stakeholders across the globe and share product safety information.

Dow is committed to continually reviewing its products and their compositions to ensure they meet evolving customers' needs. Dow is actively investing and innovating to make sure silicone materials continue to bring their unique performance and sustainability benefits to society.

Through outreach and collaboration, Dow is working to advance product safety practices around the globe. The Company's Product Stewardship Academy provides hands-on training as well as support and mentoring to customers and distributors to increase product safety knowledge and safe material handling practices to support responsible market growth in developing regions. Product Stewardship Academies have been held in Ghana, Nigeria, Kenya, Ethiopia, Egypt and the United Arab Emirates. This industry-leading initiative was awarded an American Chemistry Council Responsible Care Award in 2018.

Dow has been an active member of the Green Chemistry and Commerce Council (GC3) which is a premier forum for engaging with a broad range of stakeholders to share sustainability needs and drivers and to identify areas for collaboration to help jointly shape a sustainable future. In 2019 Dow was awarded the Sustainability Champion Award from GC3 for its leadership in value chain outreach, leading discussions on product safety and transparency and overall efforts to advance the development of sustainable materials.

World-leading operations performance underpins all that the Company does and success lies within the capable hands of Dow's employees, who are engaging for impact and advancing work in circular economy, climate protection and safer materials.

Regulations

In Europe new Industrial Emission Directive (IED) limits are being implemented to tighten emissions to water and air, driven by the desire to improve environmental protection. Most of Dow's facilities already comply with the tighter IED limits but the Company stays actively engaged and eager to put in place better abatement techniques where further improvements can be made and to ensure that Dow meets or exceeds future emission limits ahead of them being prescribed.

Under IED, BREF [14] documents have been written to address various industrial sectors. These define Best Available Techniques (BAT) that should be used to minimise emissions, including abatement equipment as well as operational techniques. The BREF documents contain BAT conclusions where associated emission limits are set which should be achievable if BAT techniques are implemented. Upon publication of BAT conclusions (BATc) in the Official Journal of The European Union, operators have a legal requirement to meet the emission limits within 4 years (unless the timing is driven by another BREF deemed to be the main activity). For silicone manufacture the main BREF's that apply to Dow's operations are:

- Common Waste Water and Waste Gas Treatment/Management Systems in the Chemical Sector (CWW BREF) [14]
- Common Waste Gas Treatment in the Chemical Sector (WGC BREF) [14]
- Large Combustion Plants (LCP BREF) [14]
- Production of Speciality Inorganic Chemicals (SIC BREF) [7]

The SIC BREF [7] was the main BREF but this will no longer be updated. Instead, silicones main activity regulations will be driven by the WGC BREF, with other BREF's implemented when WGC BAT conclusions are published.

The WGC BREF will drive reductions in volatile siloxanes, chloromethane and hydrocarbons emissions to air. Whilst LCP BREF will reduce NOx emissions from supporting combustion processes, the CWW BREF contains tighter emissions to water. Best Available Technique Processes built by Dow many years ago mean that compliance is mainly in place but Dow welcomes the support of the EU regulatory regime to ensure the Company upgrades facilities in Europe to close any gaps and help reduce emissions (which will also support meeting 2025 sustainability goals). Improvement plans in this region will be leveraged to other geographies, for example via the Global Silicones Council (GSC) to support a reduction in the global footprint of silicones and any impact on the environment from their manufacture.

Methylchlorosilane Production

The “Direct Process” or “Müller-Rochow synthesis” is the copper catalysed reaction of silicon with organic chlorides to form organochlorosilanes, primarily used for the production of methylchlorosilanes, the monomeric intermediates used to prepare silicone products [15]. Production of methylchlorosilanes is energy intensive; the primary raw materials, silicon and methanol, along with energy for distillation, are the largest contributors to the total greenhouse gas emissions. The reaction of silicon with methylchloride in the “Direct Process” also results in some waste products, primarily disilanes, which are reported to be about 1% of the total production [8, 15].

There is also a solid residue containing the catalysts required for the process, as well as the impurities in the silicon and a small amount of un-reacted silicon. Most of this is returned to smelters to recover the catalysts, minimising waste production and sustainably recovering valuable resources [16-18].

The methylchlorosilanes are hydrolysed with water, producing hydrogen chloride, either anhydrous or aqueous, which is then reacted with methanol to produce the required methylchloride. Although chlorine is required to produce silicones, most of it is recycled back to the process, minimising waste and ensuring high raw material utilisation.

The Global Silicone Council, of which Dow is a member, has studied the life cycle analysis of silicone products from raw materials to manufacturing and product use, estimating the emissions related to silicone manufacture and use [6, 8].

Sustainable Methylchlorosilane Production

Methylchlorosilanes are the building blocks for most silicone materials, which are more durable and have a higher performance than most alternatives, but there are ways to further enhance their impact on society through constant process improvements. To meet the Company’s 2025 goals, some current actions include:

Advancing a circular economy:

- A focus on fence line plants, by partnering with other industries it is possible to reduce the transportation of intermediate products, enhancing sustainable production. A recent example is the installation of a new facility to produce fumed silica [19], converting chlorosilane to fumed silica and returning the hydrogen chloride for re-use [20].
- Constant focus on improved raw material efficiency, to better utilise the valuable resources used to make chlorosilanes.

Protecting the climate:

- Renewable energy sources, such as the installation of solar energy [12] for the production of chlorosilanes and wind turbines [13] for the production of silicones.
- Integrated silicones sites enable efficient use of resources, for example, production of methylchlorosilane is exothermic [15], the energy produced is recovered for other uses internally.

World Leading Operations:

- Constant focus on waste reduction through waste avoidance and reduction, Conversion and re-arrangement of by-products to valuable monomers [21]

- "Waste Reduction Always Pays" (WRAP) program – rewarding sustainable production [9]
-

Waste

Dow's EH&S policy and standards encourage waste minimization, which includes current efforts to reduce waste generation in our manufacturing units and elimination of waste in product R&D and process design. Dow's strategy is guided by a waste minimization hierarchy. The "waste hierarchy", shown in Figure 2 is used to rank and map all waste management options according to what is best for the environment. It gives top priority to preventing waste in the first place. When waste is created, it gives priority to preparing it for re-use, then recycling, then recovery, and last of all disposal (e.g. landfill).

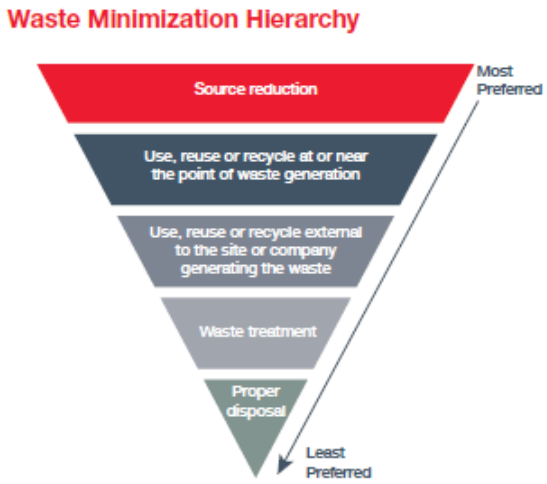


Figure 2 - Waste Minimisation Hierarchy [22]

The most preferred option is always source reduction combined with the most effective use of valuable raw materials and resources. Once this has been exhausted, the use, reuse or recycle at or near the point of waste generation is fully explored before external recycling or disposal options are evaluated. In some cases, due to the hazardous nature of the material it may require on site treatment to allow it to be shipped externally for reuse, recycle or disposal.

Focus is always on moving up the waste hierarchy combined with waste valorisation. Waste valorisation is the process of taking waste and changing it into constituent parts that can be utilized and have value beyond the cost of the energy or materials needed to effect the transformation.

Industrial symbiosis engages separate industries in a collective approach to competitive advantage involving physical exchange of materials, energy, water, and/or by-products. The keys to industrial symbiosis are collaboration and the synergistic possibilities offered by geographic proximity, which has also been achieved by Dow through fence line operations. These collaborative partnerships can make circularity more accessible, through sharing and reuse of resources to create shared value.

In 1986, Dow established the Waste Reduction Always Pays (WRAP) program [9]. WRAP unified the Company's waste reduction programs, leading to greater success decreasing or

eliminating waste and saving the Company money at the same time. Nominating and awarding internal WRAP awards on a yearly basis ensured a clear drive towards waste minimization. For example: in 2017 alone, 123 WRAP projects were chosen from approximately 300 nominations, representing the work of more than 900 Dow employees globally. This program is a focus within Dow, contributing and recognizing waste minimization globally across the Company.

Achieving the goals

In support of 2025 sustainability goals and challenges Dow has set up a regional ***Project Management Office (PMO) for Business and Sustainability*** based on **three work streams**, as follows:

1. Energy & Circularity
2. Waste & Circularity
3. Sustainable Finance

Key objectives of these work streams will be to consolidate existing efforts, conduct timely in-depth analysis and provide specific recommendations to the businesses for project prioritization. Furthermore, they will also help determine and mobilize the resources and trade association activity necessary to manage specific issues related to policy priorities. A PMO Coordination Team will help bring together and facilitate these activities and serve as the liaison to the Sustainability Leadership Team.

A key focus of the PMO team will also be on the very ambitious new ***European Commission Green Deal*** agenda, which sets out at least 47 new legislative or policy proposals that the Company can expect within the next 1-2 years. The vast majority of these are of direct relevance to the silicone industry.

Aside from focusing on policies and regulations Dow also runs a ***Sustainability Academy***, which is committed to the development of employees by building talent, employee attraction and retention, employee engagement and building business sustainability integration. The development program provides participants with the tools needed to bring sustainable business insights into their jobs, as well as hands on experience with a sustainability related project. The program also aims to:

- boost employee engagement
- develop global talent
- permeate sustainability into the companies' business functions by providing a unique opportunity to selected employees to work on a specific project where they will be exposed to other functions and leaders.

Dow is partnering with the University of Cambridge Institute for Sustainability Leadership to provide participants with an externally validated certification upon program completion. Each team works on a 6-month long project which is sponsored and coordinated by a sustainability coach. Projects are proposed then screened and selected by the Academy, which is run in all global geographies. Cohort 1 in Europe involved 10 teams who finished their assignment in February 2020, after which they presented their projects and recommendations to a broad global internal audience, including senior business and sustainability leaders. These thought-

provoking studies have focused on a diverse range of topics where sustainability and business opportunities exist in synergy. Innovative projects stemming from the Academy have the potential to make significant societal and business benefits – all of which link to one or more of the Dow 2025 sustainability goals. Graduates of the academy can go on to be sustainability leaders of the future to further cascade their knowledge and desire to other employees, whilst additional cohorts are run to maintain sustainability principles at the core of the business.

Future Outlook

After all that has been done so far, what will be the next steps?

Relentlessly searching for further minimization of energy usage and waste production will continue to be an integral part of Dow's efforts to achieve its goals: it directly contributes to the Company's bottom line. Dow is investing in renewable energy to reduce the use of fossil fuels, such as the installation of a wind turbines and the use of solar energy [23].

But more can be done.

Dow is aiming to close the loop and create a circular economy, developing processes where waste becomes a raw material for a new product.

Looking at a high level to silicone products and thinking in terms of circularity it is easy to see that one potential improvement could be to further explore and develop the recycling and re-use of silicone products. This could be through direct reuse, or in the recycling of products back to its building blocks in order to make new and high-quality products again without the usage of virgin raw materials.

From an energy point of view this makes good sense: the energy used to produce building blocks and subsequent products from recycled silicones is a fraction of the energy needed to make virgin materials. A project like that fits into Dow's Sustainability goals with which the Company leads the way into the future.

Looking towards silicone production from a very high level it is clear that truly sustainable products are indeed possible: producing silicon with biobased carbon and renewable energy and producing silicones with renewable energy and biobased methanol. It will not be an easy goal to achieve, but that shouldn't stop anyone from trying.

Conclusion

Consumer demand for sustainable products continues to grow and the population is looking to purchase responsible products.

The world is focusing on becoming a sustainable society and here at Dow it is no different. Dow is working towards its world leading operation 2025 goals, which build on work completed in the previous two decades. These stretch goals challenge all Dow employees to work on creative and innovative real solutions that will make a positive impact on the world. The 2025 goals are put in place for 10 years and do not change, enabling Dow's focus to remain on delivering these goals.

Life cycle analysis of silicones from raw material to finished goods has been evaluated with the production of methylchlorosilanes shown to be energy intensive. Through Dow's PMO for Business and Sustainability, its sustainability academy and WRAP awards it is developing processes which reduce energy intensity, minimise waste production, recover valuable resources and create a circular economy, closing the loop on waste. Dow is actively engaged with regulators to improve processes to meet or exceed future limits.

At Dow, sustainability is not just a program, it is part of who we are. All Dow employees are committed to sustainability and want to tackle the challenges by developing creative solutions and progressing innovative projects [24].

References

1. 2018 Sustainability Report. The Dow Chemical Company. 2018. Available from: https://corporate.dow.com/en-us/science-and-sustainability/reporting.html.
2. The Dow Chemical Company 2005 GRI Report. Sustainability Disclosure Database. 2005. Available from: https://database.globalreporting.org/reports/28956/.
3. Sustainability from the Start: Dow's Rich History of Environmental Stewardship. 2020. Available from: https://corporate.dow.com/en-us/about/company/history/environmental-stewardship.html.
4. Dow's 2025 goals:. The Dow Chemical Company. 2020. Available from: https://corporate.dow.com/en-us/science-and-sustainability/2025-goals.html.
5. 2015 Sustainability Report. The Dow Chemical Company. 2015. Available from: https://corporate.dow.com/en-us/science-and-sustainability/reporting.html.
6. Silicon- Chemistry Carbon Balance - An Assessment of Greenhouse Gas Emissions and Reductions. 2020. Available from: https://www.silicones.eu/wp-content/uploads/2019/05/SIL_exec-summary_en.pdf.
7. Integrated Pollution Prevention and Control Reference Document on Best Available Techniques for the Production of Speciality inorganic chemicals. August 2007. Available from: https://eippcb.jrc.ec.europa.eu/sites/default/files/2019-11/sic_bref_0907.pdf.
8. DCS sustainability talking points. 2020. Available from: gartois@dow.com
9. History of WRAP - Waste Reduction Always Pays. The Dow Chemical Company. 2020. Available from: https://corporate.dow.com/en-us/science-and-sustainability/2025-goals.html.
10. Global Silicone Council. 2020. Available from: https://globalsilicones.org/about-gsc, https://siliconesbenefits.com/silicones.
11. Yang C. AMPLIFY™ Si PE 1000 Polymer System from Dow enables stronger, more sustainable wood-plastic composites. 2019. Available from: https://www.dow.com/en-us/news/amplify-si-pe-1000-polymer-system-from-dow-enables-stronger-more.html.
12. Utilities propose Kentucky's largest solar power array, mostly for Toyota and Dow. 2020. Available from: https://www.kentucky.com/news/local/counties/fayette-county/article239573578.html.
13. A Luminus wind turbine at the Dow Silicones site in Seneffe. 2020. Available from: https://press.luminus.be/a-luminus-wind-turbine-at-the-dow-silicones-site-in-seneffe.
14. European IPPC Bureau - BREF Documents. August 2007. Available from: https://eippcb.jrc.ec.europa.eu/reference.
15. Kalchauer W, Pachaly B. Müller–Rochow Synthesis: The Direct Process to Methylchlorosilanes. Handbook of Heterogeneous Catalysis. . 2008:2635-47. Available from: https://onlinelibrary.wiley.com/doi/abs/10.1002/9783527610044.hetcat0134.

16. Zhang Y, Li J, Liu H, Ji Y, Zhong Z, Su F. Recent Advances in Rochow-Müller Process Research: Driving to Molecular Catalysis and to A More Sustainable Silicone Industry. ChemCatChem. 2019;11(12):2757-79. Available from: https://onlinelibrary.wiley.com/doi/abs/10.1002/cctc.201900385.
17. Li X, Zhang P, Chen G, Wang W, Li J. Waste minimization and efficient disposal of particles in optimized organic silicon production. Journal of Cleaner Production. 2020;242:118445. Available from: http://www.sciencedirect.com/science/article/pii/S0959652619333153.
18. Liu H, Ji Y, Zhu Y, Wang G, Wang X, Zhong Z, et al. Converting industrial waste contact masses into effective multicomponent copper-based catalysts for the Rochow process. Particuology. 2018;37:1-8. Available from: http://www.sciencedirect.com/science/article/pii/S1674200117301359.
19. Cabot Dow Groundbreaking Manufacturing Plant. 2017. Available from: https://corporate.dow.com/en-us/news/press-releases/cabot-dow-groundbreaking-manufacturing-plant.html.
20. McCoy M. Fumed silica links Cabot, Dow Corning, Neighboring Kentucky facilities will swap raw materials. Chemical Engineering News. 2017. Available from: https://cen-acs-org.ez117.infotrieve.com/articles/95/i23/Fumed-silica-links-Cabot-Dow-Corning.html.
21. Chadwick KM, Dhaul AK, Halm RL, Johnson RG, inventors; Dow Silicones Corp, assignee. Conversion of direct process high-boiling component to silane monomers in the presence of hydrogen gas. US5326896A. 1993.
22. 2017 Sustainability Report. The Dow Chemical Company. 2017. Available from: https://corporate.dow.com/en-us/science-and-sustainability/reporting.html.
23. Silicone sealants produced using CO2 emission saving energy technologies. 2020. Available from: https://www.feica.eu/information-center/good-practices/renewable-energy.
24. Dow CEO Jim Fitterling on leadership in a changing world. The Dow Chemical Company. 2020. Available from: https://www.greenbiz.com/video/dow-ceo-jim-fitterling-leadership-changing-world.

Silicon production with high energy efficiency and low CO_2 footprint

Geir Ausland[1)] and Harry Morten Rong[2)]
1) Elkem ASA, Silicon Materials, Fiskaaveien 100, 4621 Kristiansand
2) Elkem ASA, Silicon Materials, Fossegrenda 13, 7038 Trondheim

Abstract

The practical consequence of the Paris agreement is that the world must reduce the emission of greenhouse gases significantly from current level. This can only be obtained by accelerating and intensifying the actions and investments needed for a sustainable low-carbon future. Use of silicon materials will be an important part of the different global solution to reach these climate targets. Capability to deliver silicon produced with a minimum carbon footprint will therefore be important for both producers, customers and the coming generations.

Elkem is already on the way to reach our ambitious emission long term targets by:

- continuous developing and demonstrating basic silicon knowledge achieved over decades, which has made it possible to operate the silicon furnaces with silicon yield of significantly higher than 90%.
- renewable energy from hydro power used in the production and electric energy recovery of around 28-30% of the electrical energy.
- high targets for development of sustainable sources of biogenic carbon sources as replacement for fossil carbon. 40-100% biogenic carbon is tested in full industrial scale.
- modifying the furnace design making it possible to reduce the NOx emission from the silicon furnaces with more than 40 % and implemented it on new furnaces every year.
- already started feasibility studies on carbon capture for the combination of silicon production and energy recovery from the process
- ongoing studies on fundamentally new silicon processes together with SINTEF and NTNU.
- aiming to offer our customers certified LCA, including documentation of both our own process and incoming raw material footprint

Introduction

The Paris Agreement entered into force, 4th of November 2016. The central aim of the agreement is to strengthen the global response to the threat of climate change by keeping a global temperature rise this century well below 2 degrees Celsius above pre-industrial levels and to pursue efforts to limit the temperature increase even further to 1.5 degrees Celsius. The practical consequence is that the world must reduce the emission of greenhouse gases (GHG) from current level. This can only be obtained by accelerating and intensifying the actions and investments needed for a sustainable low-carbon future [4].

To reach the targets of the Paris agreement, many different solutions will be needed globally within energy production and use, transportation and industrial production processes among other areas. Many of these solutions will include use of silicon materials. In other words; a huge amount of silicon will be needed over the next years within areas like solar energy, batteries, lightweight materials, electronics or windmills. On the other hand, this increases the focus on being able to produce silicon with a low carbon footprint from now and into the future.

Silicon is produced by carbothermic reduction of silicon dioxide in open or semi-closed electric arc furnace. Silicon is not stable in the presence of carbon and therefore the silicon furnace is designed to separate the production of silicon carbide from the production of silicon. The added carbon reacts in the upper part of the silicon furnace to produce silicon carbide and carbon monoxide according to equation 1. The produced silicon carbide reacts with quartz in the lower part of the furnace to produce silicon, silicon monoxide and carbon monoxide according to equation 2. If too low amount of carbon is added to the furnace, excess quartz will react with the produced silicon to form SiO according to equation 3, and if too much carbon is added to the furnace SiC (equation 2) will start to accumulate in the bottom of the furnace. The main environmental challenges for the silicon production are the huge amount of energy used and the high CO_2 emissions [1].

$$SiO(g) + 2C(s) = SiC(s) + CO(g) \quad (1)$$

$$SiO_2(s,l) + SiC(s) = Si + SiO(g) + CO(g) \quad (2)$$

$$SiO_2(l) + Si(l) = SiO\ (g) \quad (3)$$

Combining equation 1 and 2 gives the overall reaction according to equation 4. If all SiO gas generated in the bottom of the furnace is reacted in the upper part of the furnace, the process consumes 2 mole of carbon per mole of silicon. Unfortunately,

some of the SiO gas will escape at the top of the furnace and oxidize with air to produce silica fume (SiO_2). One mole of SiO needs one mole of carbon and therefore formation of silica fume will increase the carbon consumption of the furnace. To take into consideration the loss of SiO equation 4 must be rewritten according to equation 5.

$$SiO_2(s) + 2C(s) = Si + 2CO(g) \quad (4)$$

$$(1+x)SiO_2(s) + (2+x)C(s) = Si + xSiO + (2+x)CO(g) \quad (5)$$

The production of silicon is highly endothermic and requires a temperature above 1800˚C [1]. Therefore, electric energy is added to the process through carbon electrodes. The electricity forms an arc at the tip of the electrode where the temperature is high enough for the process to occur. Almås et al [2] reported an electricity consumption of 11,8 MWh/ton of tapped silicon from the furnace. This includes auxiliary power used to operate pumps, fans, light, etc in the plant.

The CO and any SiO not captured in the furnace will react with air on top of the furnace to produce $CO_2(g)$ and $SiO_2(s)$. The coal typically contains about 30-60% of hydrocarbons that will burn on top of the furnace. Any humidity from the raw materials will also end up in the off gas as hydrogen. Traditionally, the silicon furnaces are rather open and a lot of air will be sucked into the furnace. This gives lower gas temperature on the equipment above the furnace, but it will also dilute the CO_2 in the off gas. The energy loss from the silicon furnace is in the form of high temperature process gas and liquid silicon at high temperature. Part of the energy in the liquid silicon is used in the refining process where some silicon by-products are recycled.

For energy recovery from the off gas it is beneficial to have high temperature in the off gas. Almås et al [2] reported a recovery of 2,4 MWt/ton silicon as electrical energy or about 22% of the electric energy added to the furnace. To obtain highest possible temperature in the off gas, the furnace was semi-closed to reduce the amount of air mixed with the off gas. In principle it is possible to close the furnace completely, but no one has reported success with such technology. Typically, an open furnace will have a CO_2 concentration in the off gas of about 2%, while a semi-closed furnace will have a CO_2 concentration of about 5% [3].

The focus on reduced emissions of GHG has increased strongly and in particular the last year. Many companies have started to map their emission of GHG, and we are seeing an increasing number of companies requesting Life Cycle Assessment (LCA) for production of silicon.

The coal used in the silicon production is typically washed and of a narrow particle size fraction. The fractions not suitable for the silicon production is normally used in coal fired power plants. Many countries have announced closure of the coal fired power plants to combat the climate change. With the poor prospects of the coal mining industry they are starting to get problem with financing since no one want to invest in this industry. Availability of coal might become a big threat for the silicon production.

Silicon and silica fume (Microsilica) are used in many areas that is reducing the GHG emission. Microsilica is for instance giving stronger concrete that allows constructions to be designed with less concrete. The lifetime of the concrete is also increased due to less salt erosion when silica is used. Silicon is used as an alloying element in aluminum to make stronger alloys. This will make it possible to make stronger and lighter aluminum parts saving GHG emission. Silicon is used to make solar cells. The solar cells are producing energy and today the GHG emissions is payed back after less than 2 years of operation. With a lifetime of the solar cells of more than 25 years the production of silicon for solar cells are highly environmentally friendly. However, there are potentials in reducing the GHG emission by choosing the cells produced with the lowest emission. Silicon used to produce electronic components is the fundamental backbone for our society. Without electronic silicon we would probably not be able to organize WEB conferences that we are forced to do due to the Covid 19 virus that struck the world in the beginning of 2020. Silicone is another important material with many applications increasing the lifetime and efficiency of products. Using silicones, siloxanes and silane products generates greenhouse-gas emission reductions that outweigh the impacts of production and end-of-life disposal by a factor of 9. This is mainly due to energy savings provided by silicones and silane in construction (insulation), in automotive (engine runs at higher temperature), or solar industry [5].
A new potential area currently in development is the use of silicon in rechargeable batteries. Silicon based anodes can in the future increase the capacity of batteries and make them less influenced by temperature conditions. New improved batteries will replace the use of equipment using fossil fuel and make it possible to recharge with renewable energy.

Elkem's approach for sustainable production

Fundamental understanding of the silicon process

To obtain the best possible environmental standards for the silicon process it is important to have a comprehensive understanding of the basic silicon process. Elkem has been supporting and participating in research programs for more than 30 years. This research has been managed by the Norwegian Ferroalloy Producers Association (FFF).

The research has been financed by the Norwegian Research Council and FFF. Most of the work have been carried out by SINTEF and NTNU in close cooperation with Elkem engineers. The work is partly done as PhD education. The R&D work has been carried out both as laboratory work, pilot scale experiments and short- and long-term measurements at different silicon furnaces. Increasingly the use of tools such as mathematical modelling has been taking into use.

Reducing NOx emissions from silicon production

Nitrogen oxides (NO and NO_2) are often referred to as NOx. They contribute to acid rain, eutrophication, photochemical air-pollution, and depletion of the ozone layer and have detrimental effects on health. Measurements showed that the Norwegian silicon alloy smelters occupy 6 out of top 10 positions on the list of Norwegian land-based industrial single NOx sources. From industrial measurement campaigns on the Norwegian silicon alloy plants it was found that most of the NOx in the silicon process is formed in the area between the charge burden and smoke hood. In this area SiO and CO together with moisture and volatiles from the raw materials are mixed with air and burned before it leaves in the off gas system. [6, 7]. Elkem has applied the obtained results and modified the furnace design making it possible to reduce the NOx emission from the silicon furnaces with more than 40 %. The new design has focused on improved combustion of the SiO, CO and volatiles above to avoid high temperatures. Elkem has implemented the new technology in all silicon furnaces in Norway by the end of 2020. The last furnace to be upgraded to the new technology is furnace 1 at Elkem Salten that will be closed for rebuilding in June - August 2020.

Improved Silicon yield in the silicon process

The amount of quartz that is converted to silicon is defined as the silicon yield. Lower silicon yield is caused by formation of silica fume. Higher silicon yield will give more silicon that can share the GHG emissions used in the production process. The new technology developed for reduced NOx emission was also positive for the silicon yield and with the new technology the silicon furnaces in Elkem can produce with a silicon yield significantly above 90% reducing the CO_2 footprint in silicon produced by Elkem.

Energy recovery from the silicon process

Fortunately, the Norwegian silicon plants are mainly using electrical power from renewable sources ((Norwegian power mix). However, as shown in Figure 1, the off gas from the silicon process has a lot of energy that can be recovered.

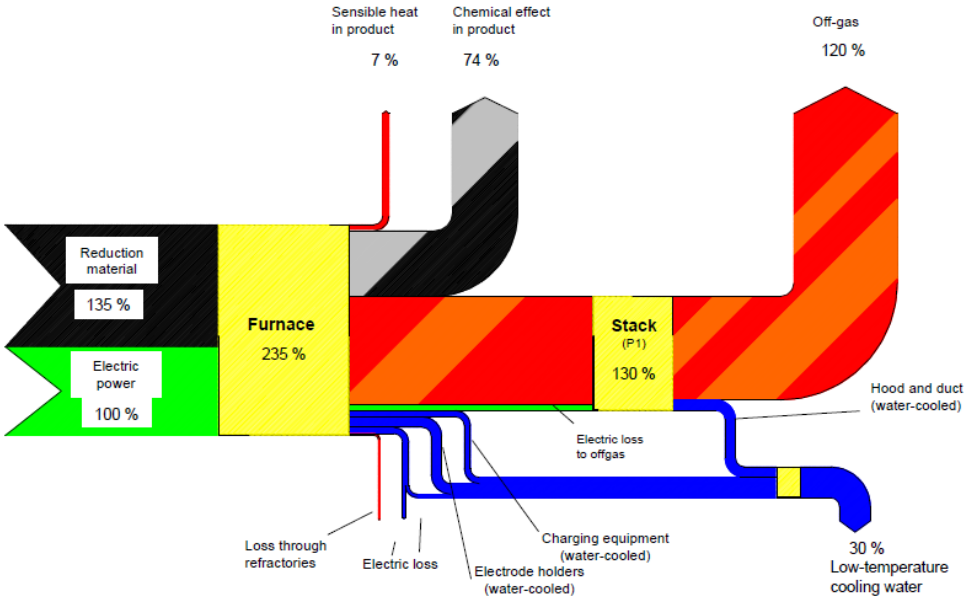


Figure 1: Energy flow in the conventional silicon production

The most effective form of energy recovery is to produce steam/hot water that is used in district heating or heating for other industrial activity close to the silicon plant. With such a system it is possible to recover as much as about 42% of the total energy (both reduction materials and electric power) put into the furnace. However, most of the silicon plants are found in minor communities with considerable distances to potential users of steam or hot water. In these plants the only effective way of energy recovery is to produce electrical power [2].

In 2002 Almås et al [2] gave an overview of the current status on energy recovery in the silicon and ferrosilicon industry. The main change from 2002 until today is that in 2012 Finnfjord Smelteverk installed an energy recovery plant with a steam turbine producing electrical energy and the Lilleby Metall plant was closed by the end of 2002.
Elkem have continued to improve the technology for energy recovery and today about 30% of the electrical energy added to the furnace will be recovered compared to 22% reported in the 2002. Elkem and Kvitebjørn Energi (Salten Energigjenvinning AS) are currently building a new energy recovery plant at the Elkem Salten plant in Norway. The start-up of the plant is scheduled for second half of 2020. The plan is to recover 28% of the electrical energy put into the furnace and the investment cost for the project is estimated to about 1 billion NOK.

Replacing coal with biomaterials

Biomaterials (wood chips, charcoal, wood briquettes, recycled wood, etc) can be used in the silicon furnace as a carbon source. Since the carbon in biogenic materials already are in circulation it is not included when calculating the GHG emissions. However, it is often requested that the amount of CO_2 emission from biogenic materials must be reported. Wood chips are typically used in the silicon production, but the purpose is mainly to give a porous charge needed to capture the SiO gas. Sustainable charcoal from plantations or regenerating forest are used extensive in the silicon production in for instance Brazil. Haug et al [8] presented in 2016 a new concept for integrating the charcoal production with the silicon production. Elkem's goal is to increase the use of biogenic carbon in the silicon process to 40% within 2030. Elkem's ferrosilicon plant in Paraguay is currently operating with 100% biocarbon.

Recycling of waste

Silicon waste can be recycled to the silicon furnace or in the silicon refining ladle. The energy required to melt silicon is much lower than the energy needed to reduce quartz. For instance, the sawing dust from the solar industry has changed properties the last years due to the replacement of sawing technology based on SiC powder to diamond wire sawing. This has increased the silicon content in the sawing dust and made it a potential candidate for recycling. Waste products should in principle have no allocation of GHG emission and therefore any recycle of waste products should reduce the GHG emission in the silicon production. Elkem has a collaboration with REC Solar that currently is building an agglomeration plant for sawing dust making it possible to recycle the agglomerates in the silicon process.

Closed and semi-closed furnaces

The furnaces operated in Elkem have reduced possibility for air to enter compared to a completely open furnace. However, the CO_2 concentration in the off gas is still rather low with about 5%. Elkem is currently working with technology to reduce the amount of air even further. The purpose with this project is to increase the concentration of CO_2 and to increase the energy recovery by increasing the temperature in the off gas. Higher CO_2 concentration will make possible with carbon capture. The silicon furnace can in principle be completely closed. The gases leaving the furnace is then CO, SiO, hydrogen and hydrocarbons. The off gases can be incinerated in a controlled process to give high CO_2 concentration in the off gas. The technology for operating closed furnaces is still not available.

Sulfur dioxide reduction

The raw materials contain some sulfur that is oxidized in the furnace to SO_2. Sulfur is present in raw materials and the plants in Norway have a maximum limit of how much

SO_2 the plant emits to the air. All Norwegian plant are paying a tax for the sulfur emitted to air. Elkem is currently evaluating technology for a sulfur dioxide cleaning plant at Elkem Bjølvefossen.

Carbon capture and use of CO_2

All analyzed pathways limiting global warming to 1.5°C with no or limited overshoot use carbon capture and removal to some extent to neutralize emissions from sources for which no mitigation measures have been identified [9].

Carbon capture and storage (CCS) has been studied on behalf of Norwegian authorities to develop full-scale CCS in Norway. The concept includes capturing CO_2 from various onshore industries, transporting it by ships and injecting and permanently storing it meters below the seabed.

Elkem is now starting a feasibility study to gain knowledge about what technical solutions for carbon capture that are most suitable for silicon furnaces in combination with energy recovery. Carbon capture could be used for CCS in combination with concepts where clean CO_2 is used in other processes (CCU). Examples of this is e-fuel, where reuse of CO_2 based of biogenic sources are replacing fossil CO_2 emissions in transport sector.

For the future silicon production, a combination of biogenic carbon in raw materials and CCS/CCU will in fact be a carbon negative solution. Many of the pathways described in the ICCP reports [9] include also some amount of these solutions. Producing silicon, an important part of the solution, and at the same time drain the atmosphere for CO_2 could be a unique part of the future low carbon society.

Recycling of biproducts and raw material loss

Operation of a silicon furnace can result in some secondary products such as fines grades from pre handling of raw materials, cyclone dust, slags and skulls. These products can either be upgraded to valuable biproducts or they need to be handled in a sustainable way to prevent unwanted waste generation from silicon production. Briquetting of these type of materials have been a part of Elkem's strategy and new projects in industrial scale is now being prepared. This will have a dual mission, both securing a zero-waste operation and it will also improve carbon footprint since both carbon and silicon is taken back into the process.

Life Cycle Assessment (LCA)

To reach climate targets, a well-functioning certified system for LCA calculations need to be in place for silicon production. In more and more markets, like solar and construction, these types of certifications have been established. The last years silicon customers have showed an increasing demand for LCA analysis on the silicon products, and a system for LCA and Environmental Product Declaration (EPD) is being defined.

Elkem is targeting to have LCA calculated for our product and has started that process. In the life cycle analysis, not only direct emissions and emissions related to the consumed energy becomes important, but also emissions related to transport and raw materials before they are used in the furnace. Monsen [10] calculated the CO_2 emission from the silicon process, but did not include emissions from production and transport of raw materials or the emission due to electricity (Norwegian electricity mix).

Conclusion

Use of silicon materials will continue to be an important part of the different global solution to reach the climate targets in the Paris agreement. Capability to deliver silicon produced with a minimum carbon footprint will therefore be important for both producers, customers and the coming generations.

Elkem is already on the way to reach our ambitious emission long term targets by:

- continuous developing and demonstrating basic silicon knowledge achieved over decades, which has made it possible to operate the silicon furnaces with silicon yield of significantly higher than 90%.
- renewable energy from hydro power used in the production and electric energy recovery of around 28-30%.
- high targets for development of sustainable sources of biogenic carbon sources as replacement for fossil carbon. Tested 40-100% biogenic carbon in full industrial scale.
- modifying the furnace design making it possible to reduce the NOx emission from the silicon furnaces with more than 40 % and implemented it on new furnaces every year.
- already started feasibility studies on carbon capture for the combination of silicon production and energy recovery from the process.
- ongoing studies on fundamentally new silicon processes together with SINTEF and NTNU.
- Elkem aim to offer our customers certified LCA including documentation of both our own process and incoming raw material footprint (cradle to gate).

References

1. H. Tveit and L. Kolbeinsen, *The (love & hate) role of entropy in process metallurgy*, Matériaux & Techniques **107**, 506 (2019)
2. K. Almås, H. Delbeck, T. Halland, H. M. Rong and H. Tveit, *Improved Environmental and Energy Recovery Performance with New Furnace Hood Design at Elkem Thamshavn*, Silicon for the Chemical Industry VI, Loen, Norway, June 17-21, 2002, Ed.: H.A. Øye, H.M. Rong, L. Nygaard, G. Schüssler, J.Kr. Tuset, Trondheim, Norway, 2002
3. Internal ongoing work in Elkem ASA, 2020.
4. The United Nations Climate Change Paris agreement, https://unfccc.int/process-and-meetings/the-paris-agreement/the-paris-agreement/.
5. B. Brandt, E. Kletzer, H. Pilz, D. Hadzhiyska, P. Seizov, Silicon-Chemistry Carbon Balance An assessment of Greenhouse Gas Emissions and Reductions, https://www.silicones.eu/wp-content/uploads/2019/05/SIL_exec-summary_en.pdf, 2012.
6. E. H. Myrhaug, H. Tveit, N. E. Kamfjord, G. J. Andersen and Å. Grøvlen, NOx Emissions from Silicon Production, Silicon for the Chemical and Solar Industry XI, Bergen - Ulvik, Norway, June 25 - 29, 2012
7. N.E. Kamfjord, Mass and Energy Balances of the Silicon Process – Improved Emission Standards, PhD-thesis, Norwegian University of Science and Technology, Trondheim, Norway, 2012.
8. A.T. Haug, E. Dahl, T. Videm Buø, H. Moe, P. Carlsson, T. Andresen, J. Sandquist and P. E. Wahl, Carbon neutral metal production a new environmental friendly method for production of silicon, Silicon for the Chemical and Solar Industry XIII, Kristiansand, Norway, June 13 - 16, 2016
9. ICCP report SR15, 2018
10. B. Monsen, Omregningsfaktorer for CO2-utslipp fra metallurgisk industri og sementproduksjon. Delprosjekt 2. Produksjon av ferrosilisium og silisium metall i Norge, STF24 A98537, 1998

Silicon for the Chemical and Solar Industry XV
Trondheim, Norway, June 15 – 18, 2020

Empirical analysis of clogging of SiC charges: effect of condensation of SiO and CO

Andrea Broggi[1)], Eli Ringdalen[2)], Merete Tangstad[3)]

1) Norwegian University of Science and Technology (NTNU), Department of Materials Science and Engineering, Alfred Getz vei 2, 7034 Trondheim, Norway.

2) Norwegian University of Science and Technology (NTNU), Department of Materials Science and Engineering, Alfred Getz vei 2, 7034 Trondheim, Norway

3) SINTEF Materials and Technology (NTNU), Department of Materials Science and Engineering, Alfred Getz vei 2, 7034 Trondheim, Norway

Abstract

Condensation of silicon monoxide is a serious issue for industrial silicon production. The condensation reactions develop at the surface of the charge particles. Charge particles are glued by white or brown condensates layers. . The particle size and the gas composition can affect condensation. The advantage of this reaction is a reduced SiO loss out of the furnace. The downside is first, that it prevents the material flow, and second, that the permeability in the charge decreases. Both can be remedied by stoking the furnace.

This work measures the positions and the temperatures at which clogging occurs, in laboratory-scale furnaces. SiC charges are chosen, to avoid effect of clogging from smelting of quartz. The parameters changed in the experiments are the gas temperature, the partial pressure of SiO(g), the injected inert gas flow and the particle size distribution of the SiC charge. Experiments are performed in two setups at different scale.

It was seen that clogging starts at 1670-1800°C, and it ends between 1400-1500°C. A broader charge size distribution makes condensation end at lower temperatures. Higher partial pressures of SiO(g) and longer holding times lead to higher amounts of condensates and stronger clogging.

Introduction

SiO(g) and CO(g) are two important gaseous compounds involved in silicon production. This gas mixture contains high amounts of both energy and silicon. The gases should concentrate at the high temperature zone of the furnace, to assure the highest yield for the silicon production reaction [1]. However, SiO(g) and CO(g) will flow upwards to colder temperatures, and trigger the condensation reactions 1-2 [2]:

$$2\ SiO(g) = SiO_2\ (s,l) + Si(s,l) \quad (1)$$

$$3\ SiO(g) + CO(g) = 2\ SiO_2(s,l) + SiC \quad (2)$$

An enhanced condensation prevents silicon losses and decreases the energy consumption, but the system will be strongly obstructed by the products of Reactions 1-2. Condensation makes the charge particles stick to each other into a crust. The charge will struggle in finding its way to the silicon production zone. If the crust blocks the descending charge, silicon will not be produced. In addition, the gas might constrain itself into a cavity, with a roof made of SiC, charge and condensates. The gas pierces the cavity roof by creating channels, leading to hot gas blows through the outer charge zone. On the other hand, a crust that is not mechanically stable will make the cavity collapse. When this happens, the trapped gas will come out from the charge as flames and hot gas blows, which are dangerous for the safety of the operators.

The channelling phenomenon is affected by the gas permeability in the charge. Permeability defines how much free space there is between the charge lumps. One can optimize the particle size distribution to tune permeability. Fines in the quartz charge should be avoided, as they both reduce the void fraction and glue the particles to each other when melting. Larger particles and woodchips will increase permeability and prevent clogging, without altering the fix-C content significantly [1,3].

Nowadays stoking is the technology that can face the problems caused by condensation, together with an optimal particle size of the input raw materials. By stoking, an operator can influence charge segregation, gas composition, chemical reactions in the process and durability of the oven. Stoking is typically performed every 30-75 minutes [3]. Stoking is performed at the crust layer present at the top of the furnace. This area contains SiO(g) and CO(g) condensation products, unreacted charge and SiC, regardless of the alloy produced [4]. Excavations in different furnaces led to the discovery of crusts with white condensates in the low temperature zone. The white condensate is believed to be SiO_2+SiC [5]. A crust with brown condensate is usually located behind the SiC-rich crater crust. This is believed to be SiO_2+Si.

The two condensation reactions produce two materials which differ in colour, composition and mechanical properties. The brown condensate comes from Reaction 1. This crust is mechanically stronger and located closer to the furnace core [6–9]. Its stronger mechanical properties [10] give a higher stability compared to the white scale,

produced by Reaction 2. The brown condensate generates above the white condensate on each particle [10–12]. When brown condensate covers the surface of the particles, this Si-SiO_2 mixture becomes hard to remove, and causes the previously discussed clogging problems in silicon industrial furnaces.

In this work, condensation of SiO(g) and CO(g) is carried out on SiC charges. The parameter chosen for the study are the particle size, the holding time at a target temperature, the inlet gas flow added and the gas composition. Two different setups will be used to analyze the phenomenon. The small-scale setup will focus on the effect of inlet gas flow. The larger one will be used to analyse the effect of the SiC charge size distribution and the holding time.

Experimental

The experimental part describes the two setups used. The first one is a small-scale setup (Figure 1a,1b), whereas the second one could generate 10 times the amount of gas in a volume which is 60 times larger (Figure 1c).

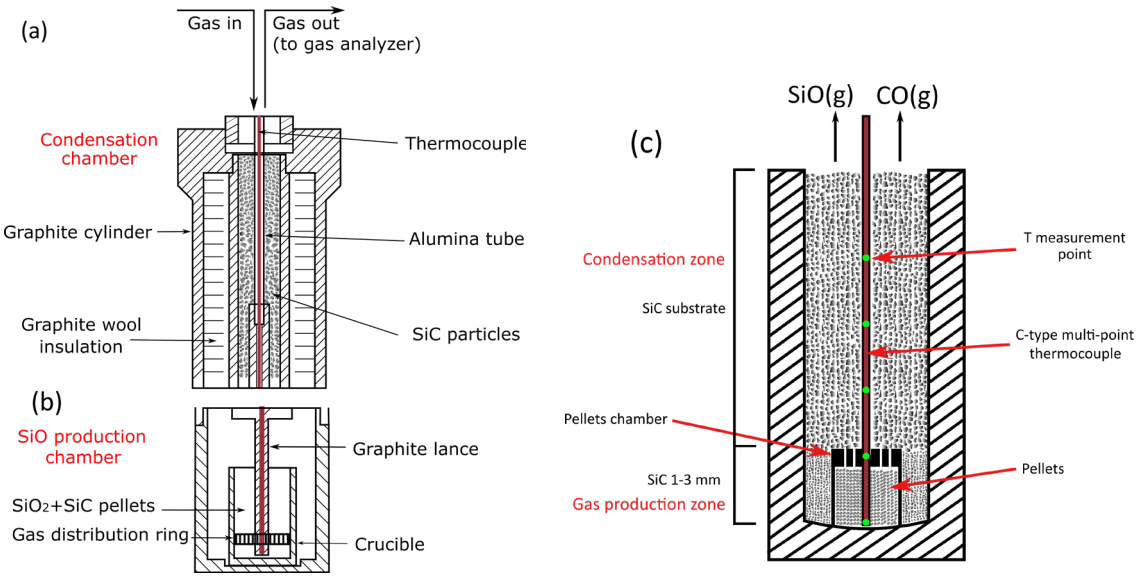


Figure 1: Condensation chamber (a) and SiO production chamber (b) in small scale setup; c) Large scale setup.

Small scale setup

The cylinder consists of two parts: a SiO(g) production chamber at the bottom, and a condensation crucible mounted at the top. The condensation crucible has an inner diameter of 25 mm and a height of 150 mm. SiC particles fill the condensation chamber up to 130 mm from the bottom of the condensation chamber. The dimensions of the cylindrical SiO(g) production chamber are 150 mm diameter and 65 mm height. A

smaller crucible of 40 mm diameter and 60 mm height hold 20 g of pellets. The pellets consist of a SiO_2-SiC mixture in a 2:1 molar ratio.
SiO(g) and CO(g) develop when the pellets are heated. Before the experiments has started, the chamber is purged with Ar(g) for 15 minutes. Then the gas is evacuated down to a pressure of 180 mbar. Afterwards, the chosen input gas (mixture of Ar, He and CO) is injected in the system. He(g) or Ar(g) acted also as protective gases around the whole setup. The inert gas pushed SiO(g) and CO(g) towards the upper condensation crucible.
The holding temperature in the SiO production chamber was set at 2000°C, according to the pyrometer. The average heating and cooling rates were fixed at 50°C/min and 35°C/min respectively. The setup variables are inert gas flow, holding time, and substrate size. The SiC particle size cumulative fractions are reported in Figure 2. Each experiment is marked with a number from 1 to 12, corresponding to the setups in Table 1, and by a letter from *a* to *e*, defining each experiment repetition. The experiments have been grouped into three main categories (R1, R2 and R3) to focus on the effect of the inert gas flow. A temperature gradient is generated inside the condensation chamber. The temperature was measured during the experiments, at three positions in the condensation chamber.

Table 1: Overview of experimental conditions.

Experiment group	Setup	Time (h)	Gas flow (l/min)	SiC size (mm)
Ar 0.02 (Group R1)	1 (a)	0.5	Ar 0.02	3-6
	2 (a-e)	1	Ar 0.02	3-6
	3 (a)	4	Ar 0.02	3-6
He 0.10 (Group R2)	4 (a)	0.5	He 0.1	1-3
	5 (a)	0.5	He 0.1	3-6
	6 (a,b)	1	He 0.1	3-6
	7 (a)	1	He 0.1	5-8
	8 (a)	4	He 0.1	1-3
	9 (a)	4	He 0.1	3-6
	10 (a)	4	He 0.1	5-8
He 0.40(Group R3)	11 (a-e)	1	0.4 Ar for a; He for b-e	3-6

Open graphite tube, larger scale

The crucible of the open graphite tube induction furnace is 380 mm high and 110 mm wide. As for the small-scale setup, the crucible is divided into a gas production zone and a condensation zone.

The gas production zone is located at the bottom of the crucible. The pellets were placed into another graphite cylinder, positioned at the bottom of the tube. This part is referred to as pellets chamber. The pellets chamber has a circular base of 100 mm diameter and is 70 mm high. The top part was drilled with numerous holes of 3 mm diameter, to let the gas escape from the chamber. A larger hole (25 mm diameter) was drilled at the centre. This tube contains a 5-point thermocouple, measuring the temperature every 70 mm from the bottom. The space around the pellets chamber was filled with SiC particles, with size between 1-3 mm. Such particles filled the graphite crucible up to 70 mm.

The condensation zone is the remaining space above the gas production zone. This volume is 310 mm high. SiC particles at different size fill the crucible up to the top. The particle sizes chosen were 5-8 mm, 3-10 mm, 12-20 mm and 8-14 mm. The cumulative fractions of the particle size distributions are represented in Figure 2.

The parameters varied were the pellets composition, the holding time and the SiC substrate particle size distribution. The pellets are either the SiO_2-SiC mixture used in the previous setup, or a Si-SiO_2 mixture. These pellets contain Si and SiO_2 in a 1:1 molar ratio. The holding time was fixed at 10 min, 30 min or 2 hours, when the target temperature was reached. The size cumulative fractions are represented in Figure 2. Table 2 gives an overview of the setup conditions, and the amount of leftover pellets at the end of the experiment, i.e. the pellets that have not transformed themselves into SiO(g) (and eventually CO(g) for SiO_2-SiC pellets). As before, the numbers identify a setup conditions, whereas the letters label repetitions of each experimental setup.

The parameters which were kept constant in the experiment were the amount of pellets (200 g), and the target temperature of the gas (1890±10°C). The thermal history of each experiment was controlled at the boundary between the gas production and the condensation zones. It was assumed that the gas came out of the gas production zone at the temperature measured at the top of the pellets chamber, i.e. at 70 mm from the bottom of the graphite crucible. The heating rate was fixed at 40°C/min. A position coordinate Y is measured starting from the bottom of the crucible.

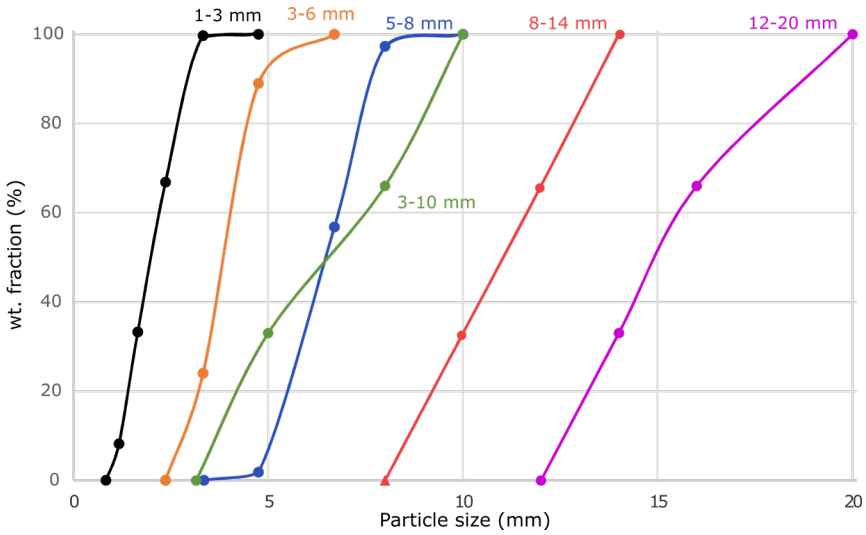


Figure 2: Particle size distribution of SiC substrates

Table 2: Overview of experimental conditions: pellets composition, amount of leftovers in pellets chamber, amount of condensates, condensation substrate size and holding time at 1890±10ºC.

Setup name	**Pellets used**	**Leftovers (g)**	**SiC substrate size**	**Holding time (h)**
IF 1 (a,b)	SiO_2-SiC	0	3-10	2 hours
IF 2 (a,b)	SiO_2-SiC	0	5-8	2 hours
IF 3 (a,b)	SiO_2-SiC	0	12-20	2 hours
IF 4 (a)	SiO_2-SiC	12	8-14	2 hours
IF 5 (a,b)	Si-SiO_2	0 (a); 3 (b)	3-10	2 hours
IF 6 (a,b)	Si-SiO_2	0	5-8	2 hours
IF 7 (a,b)	Si-SiO_2	0	12-20	2 hours
IF 8 (a)	Si-SiO_2	15	8-14	2 hours
IF 9 (a)	SiO_2-SiC	83	3-10	30 min
IF 10 (a)	Si-SiO_2	65	3-10	30 min
IF 11 (a)	SiO_2-SiC	125	3-10	10 min
IF 12 (a)	Si-SiO_2	114	3-10	10 min

Once the experiments were finished, the SiC charge is studied by excavating the crucible. The material is extracted with the help of a spoon. When the system is clogged, a steel pin is used to poke the charge.

Results and discussion

Pictures of crusts were collected only from the large-scale setup. Figure 3 shows the crust appearance before and after poking. Clogging is present from a certain position, where the material in the crucible does not flow if the crucible was flipped upside down. That position is called stoking point. This point corresponds to a temperature, called stoking temperature. The term “stoking point” intentionally recalls the industrial procedure. At the stoking point, the SiC the particles are well stuck to each other, as it happens for crusts in silicon furnaces [1,3].

The majority of the SiC particles are covered in white SiO_2-SiC condensates [2]. At higher temperatures (i.e. closer to the crucible bottom), brown Si-SiO_2 condensate will also show up and tie the particles together. It is enough to poke the charge to separate the particles tied by these compounds. However, it is more difficult to detach the brown condensate from the particle surface. Figure 4 shows the brown and white condensates in two different experiments, gluing even large SiC particles.



Figure 3: Surface of the crucible at Y=18 cm, T=1485°C. SiC charge before (left) and after poking (right), IF75-2a.



Figure 4: Left: Stoking point Y = 21 cm, T=1420°C, Exp IF75-7a**.** Right: Brown condensates at Y = 18 cm, T =1580°C for EXP IF75-7a.

The thickness of the condensate layers on the particles was measured at SEM. The thickness of white condensate ranges between 100 and 200 µm, whereas the brown can extend up to 1 mm in thickness. After analyzing the cross section of a SiC particle, it was seen that the white condensate sticks well on the substrate. Brown condensate stick well on white layers as well. Similar findings occurred in industrial excavations [4,5,8] and laboratory scale experiments [2,9–13]. Figure 5 was taken from two particles from experiments 7a and 11b. The brown condensate is thicker than the white condensate, and its thickness varies between different particles. The white condensate is lying between the brown and the SiC substrate, with a thickness of about 150 µm.

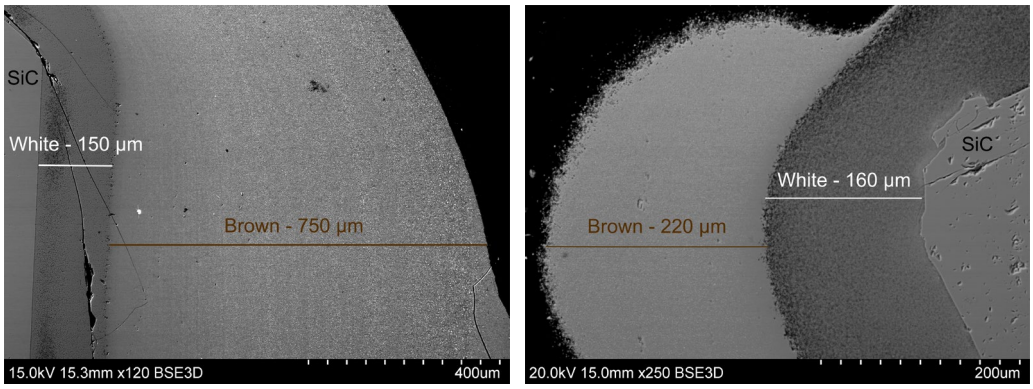


Figure 5: Phases layered on a SiC particle from experiment 7a, Y=3.5 cm, T=1450±50ºC (left) and 11b, Y= 3.0 cm, T=1500±50ºC (right).

Clogging at the stoking point is always characterized by high amounts of white SiO_2-SiC condensate placed between the substrates. The Si-SiO_2 condensate can also glue the particles to each other, and the clogging interval always includes the clogging caused by the brown Si-SiO_2 condensate. When this compound is present, the SiC particles are

held together so strongly that it is sometimes necessary to break the whole condensation chamber in order to free the material out. The glassy appearance of the brown condensate, together with the temperature of generation, are a clear hint that the compound generated when SiO_2 was close to the softened state [10–13]. The glassy compound would embed the substrate and solidify in a strong layer. This often happened in the small-scale setup experiments, especially for those at 4 hours holding time. In this case, the condensation chamber must be destroyed to extract the charge.

Figures 6 shows the clogging intervals and the stoking points for different experiments, sorted by increasing particle size and gas flow. The reported p_{SiO} in the picture defines the concentration of SiO in the gas coming from the gas production zone. The width of the interval is in ºC, and it is placed inside the corresponding coloured bar. The number on the left of the coloured bar is the temperature at which clogging ends, i.e. the stoking point. The interval corresponds to the thickness of the stoking crust generated in each experiment. Experiments with the same particle size distribution were coloured in the same colour.

The experiments of group R1, R2 and R3 are coloured in different shades, according to the amount of gas added during the experiment. The results from the experiments at small scale have been collected into groups. In these cases, the temperature intervals were not differing much, when it came to analyse the effect of SiC size or time. The largest effect was given by the input gas flow. Clogging a small-scale system is easier, since there is a smaller volume to be filled by the condensates. The void fraction could be the same in a close packed structure. For smaller particles, each void will be smaller, but there will be more voids. The size of each void changes, and the condensation area will be influenced.

Increasing the amount of injected inert gas will shift condensation up to lower temperatures. In fact, partial pressures vary between 0.74, 0.71 and 0.62, respectively for group R1, R2 and R3 [12]. A higher injection of gas should lead to a lower partial pressure of SiO(g), which should lead to lower amount of condensates produced, and a smaller clogging interval. However, this is not the case, since SiO(g) and CO(g) are pulled up in the system by the gas flow. In this way, condensation occurs also at very low temperatures, even down to 900ºC as it occurred in Broggi et al. [2].

Experiments with the largest particles (purple) have smaller clogging interval, compared to the others. By increasing the average diameter, the system is clogged for a smaller temperature interval. Larger particles leave larger voids in the system, and the crust becomes less stable. This will also be the case if the condensation rate is being affected by the substrate area. Hence, using large particles will lead to less condensation. The experiments which show the largest clogging interval are the ones having the broadest particle size distribution (3-10 mm, dark green).

By increasing the width of the particle size distribution, the voids are filled easier by the smallest particles, and the condensate layers will glue the charge. Clogging is affected

by the time spent by the raw materials in the low temperature zone. Materials with low density (e.g. charcoal) or packing factor (e.g. woodchips) descend faster and cause less clogging. The porosity of charcoal and woodchips affects the permeability of the gas, which is strictly related to the void size between charge particles.

Figure 7 shows the effect of time on the crust thickness and position. Experiment at shorter holding times give smaller crusts thicknesses and higher stoking temperatures. It was seen that the pellets were not completely consumed after 30 minutes (cf. Table 2). This means that the more gas is produced, the thicker the crust will be.

This result corresponds to a common issue in silicon furnaces: a SiO-rich gas will be an advantage in the high temperature zone, but it will create strong clogging in the low temperature zone. When this happens, one should add a charge to the furnace with narrow size distribution and large average size, to increase the charge permeability. This will temporarily decrease clogging, but the silicon losses will be higher from the gas phase. Clogging usually happens at low temperatures in nowadays practice, as one uses relatively small carbon particles, and as the quartz also disintegrates rapidly [14].

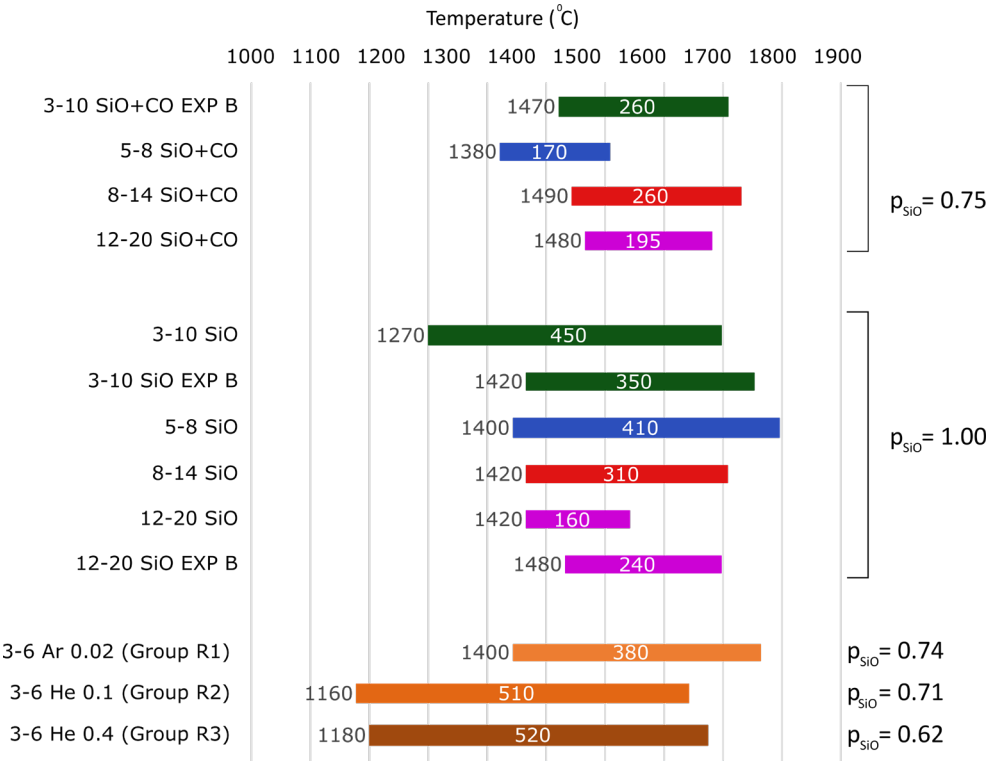


Figure 6: Overview of stoking points and clogging intervals by increasing particle size distribution and added gas. p_{SiO} before condensation is also reported.

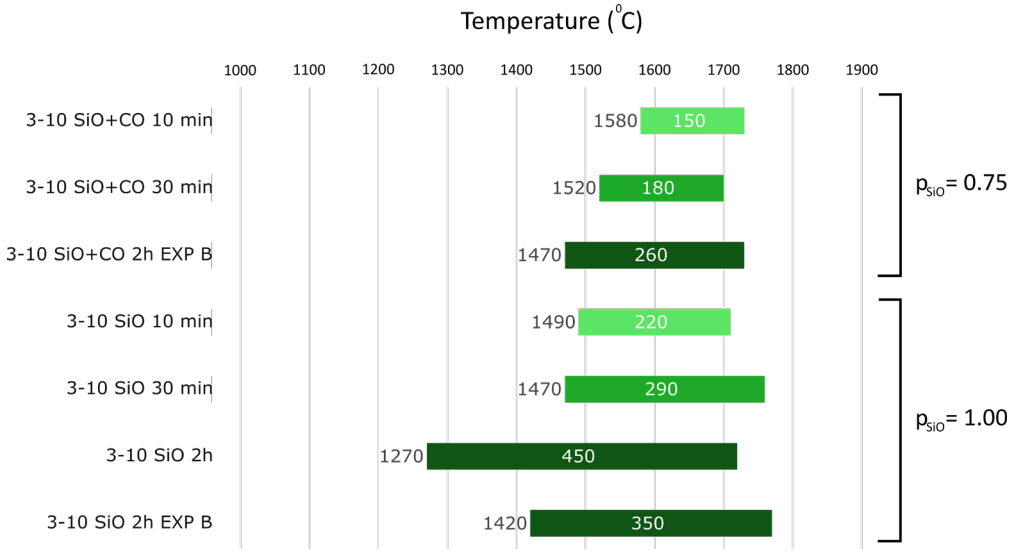


Figure 7: Clogging overview by increasing holding time and partial pressure

From Figure 6 and 7, one could notice that crusts are thicker in experiments with higher p_{SiO}. Figure 8 shows the effect of the partial pressure on clogging, in the large-scale setups. The experiments coloured in brown are those which had SiO(g) only in their starting gas composition (p_{SiO} = 1), whereas the grey ones are those containing both SiO(g) and CO(g) in the starting gas composition (p_{SiO} = 0.75). The experiments at 3-10 mm are also sorted by increasing holding time. Experiments with higher SiO(g) partial pressures favour the formation of brown Si-SiO_2 condensate. This compound has stronger mechanical properties, compared to the white [10], but the temperature of formation interval is narrower by decreasing the partial pressure [12].

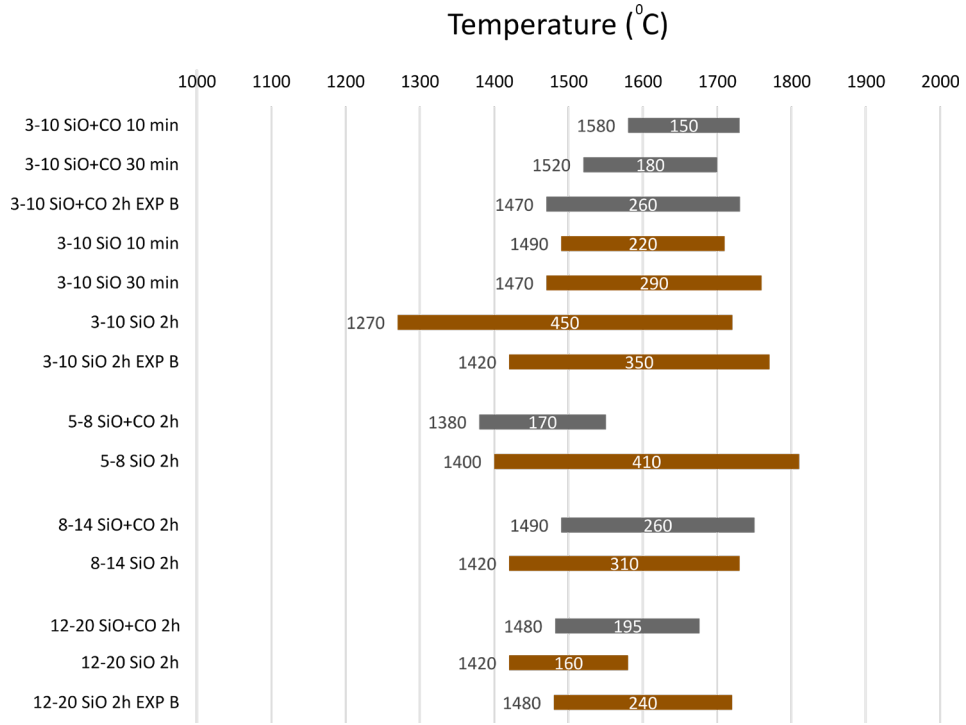


Figure 8: Clogging intervals and stoking point sorted by SiO(g) partial pressure. Experiments from the IF75 large-scale setup.

Conclusions

Clogging of SiC charges was analyzed in graphite tube furnaces at two different scales. The parameters analyzed in the experiments were the injected He flow, the gas composition, the SiC particles size distribution. Condensation occurred on the surfaces of the SiC particles, causing them to glue to each other in a compact crust. The crust could be broken with the help of a nail and a hammer.

It was seen that systems with smaller void size get clogged easier. This is valid for both setups at smaller scale and for setups with a wider particle size distribution. A longer exposure time at high temperature produces higher quantities of SiO(g) from the charge. A larger holding time corresponds to a higher amount of condensates, and therefore a thicker and stronger crust. When an inert gas is injected, the gas is moved towards lower temperatures, and condensates in a wider temperature range, down to lower temperatures. Finally, a gas richer in SiO(g) produces brown condensates at earlier times, thus giving higher mechanical stability to the crust.

Acknowledgments

The present study was supported by Elkem AS and the EnergiX program of the Research Council of Norway through project 269431 – SiNoCO2.

References

[1] M. Tangstad, Metal Production in Norway, 1st ed., Akademika Forlag, Trondheim, Norway, 2013.

[2] A. Broggi, M. Tangstad, E. Ringdalen, in: Silicon for the Chemical and Solar Industry XIV, Svolvær, Norway, 2018, pp. 139–152.

[3] A. Schei, J. Tuset, H. Tveit, Production of High Silicon Alloys, 1st ed., Tapir, Trondheim, Norway, 1998.

[4] M. Ksiazek, E. Ringdalen, in: Kristiansand, Norway, 2016, pp. 33–42.

[5] G. Tranell, in: Sustainable Future, Helsinki, Finland, 2010, pp. 709–716.

[6] A. Schei, Tidsskr Kjemi Bergvesen Met 27 (1967) 252–258.

[7] A. Schei, O. Sandberg, Selected Topics in High Temperature Chemistry, 1st ed., Universitetsforlaget, Oslo, Norway, 1966.

[8] Y. Otani, M. Saito, K. Usui, N. Chino, in: 6th International Congress of Electroheat, Brighton, 1968, pp. 1–7.

[9] W. Poch, A. Dietzel, Trans. Nat. Res. Inst. Metals 14 (1962) 22–51.

[10] J. Vangskåsen, Metal-Producing Reactions in the Carbothermic Silicon Process, Master thesis, NTNU, Department of Materials Science and Engineering, 2012.

[11] H. Mølnås, Investigation of SiO-Condensate Formation in the Silicon Process, NTNU, Trondheim, Norway, 2010.

[12] A. Broggi, M. Tangstad, E. Ringdalen, Metallurgical and Materials Transactions B 50 (2019) 2667–2680.

[13] E. Myrhaug, Non Fossil Reduction Materials in the Silicon Process - Properties and Behaviour, Doctoral thesis, NTNU, Department of Materials Science and Engineering, 2003.

[14] K.F. Jusnes, M. Tangstad, E. Ringdalen, in: INFACON XV, International Ferro-Alloy Congress, Cape Town, South Africa, 2018.

Important parameters that control the crater pressure in a Silicon Furnace

Halvard Tveit *1*, Eli Ringdalen *2*, Hanne Edfelt *3*
1. Corporate Specialist, Elkem, Norway and Adjunct Professor, NTNU
2. Senior Research Scientist, SINTEF, Trondheim, Norway
3. MSc Hanne Edfelt, Norway
Corresponding author: halvard.tveit@elkem.no

Abstract

The Silicon Process has a well known EHS challenge due to SiO_2-dust formation during the tapping process. The root cause for this is that the process gas contains SiO-gas that reacts to solid and very fine sized SiO_2-particles when exposed to air.

The main process reaction is $SiO_2 + 2C = Si + 2CO(g)$. The reactants are in a condensed phase – but the products are liquid silicon and CO-gas. For a large silicon furnace in the order of one litre per second of reactants converts to several cubic meters of gas. This creates a pressure inside the crater zone and SiO-containing gas may create tap-hole gassing.

In this project a pressure test for silicon charge material has been carried out. The results have been modelled in a Comsol model. The results have been transferred to the condition in a silicon furnace. The effect of some important parameters that control the pressure is studied. The most important parameter is the gas flow, the particle size and distribution, the charge void fraction and the charge height above the reaction zone.

Earlier industrial measurements indicate that there are 2 main sources that control the crater pressure! The resistance due to the flow through the bed is in the order of 40 mbar. In addition, there is a short-term variation with a time constant of about ½-1 hour that is supposed to be clogging due to condensation of SiO-gas. A total crater pressure of 140 mbar has been measured. These variations are important to the EHS-standard as well as the silicon process performance.

Background – the reason for crate pressure variation in silicon production

For the participants at the Silicon for Silicones conference the importance of the silicon based products in the global household is well known. And that the silicon is mainly produced in submerged electrical reduction furnace with a electrical load in the order of 10 to 45 MW. The raw material is proper quality quartz and carbon reductant material such as coal, coke and wood-based materials.

The overall reaction is:

$SiO_2 + 2C = Si + 2\ CO(g)$ (1)

The silicon process cannot be produced direct according to equation (1). Heating up quartz and carbon will mainly give SiC, CO-gas and probably some slag. The reaction (1) has to be carried out in 2 steps:

$SiO(g) + 2C = SiC + CO(g)$ (2)
$SiO_2 + SiC = Si + SiO(g) + CO(g)$ (3)

The reaction (2) will take place in the upper part of the reaction zone. The reaction is exotherm (heat producing). But the amount of gas molecules is the same for the reactants and the products - namely one. There is not a substantial volume increase for the reaction (2).

The reaction (3) takes place in the lower reaction zone – also called the crater zone. This is supposed to happen near the electrode tip where the huge amount of electrical energy is converted to thermal energy. The reaction (3) is strongly endothermic (energy consuming). The reactants in equation (3) is in condensed state. The quartz is melted and the SiC is in solid state. The products in equation (3) consist of 2 gas molecules – SiO and CO-gas. This give a huge volume increase for the reaction. For a theoretical silicon process in a 20 MW furnace the reactants are in the order of 0.8 litre per second – and the products in will be around 1.3 Nm3 per second. There will be an additional volume increase of the products due to the very high temperature of the gases. The temperature in the lower reaction zone is higher than 1800 C.

Simplified this can be stated that 1 litre reactant is converted to several cubic meters of gases every second. This conversion will create a pressure that balances the gas flow out from the charge and the charge resistance.

Industrial measurements and model calculations:

Industrial measurements have been carried out to measure the pressure in the crater. This was done by adding hydraulic pipes from the top of the electrode continuously till the end of the pipe reaches the electrode tip. This operation takes in the order of 14 days before the measurement can commence. The tube is indicated in figure 1. Some results from these measurements are presented in figure 2.

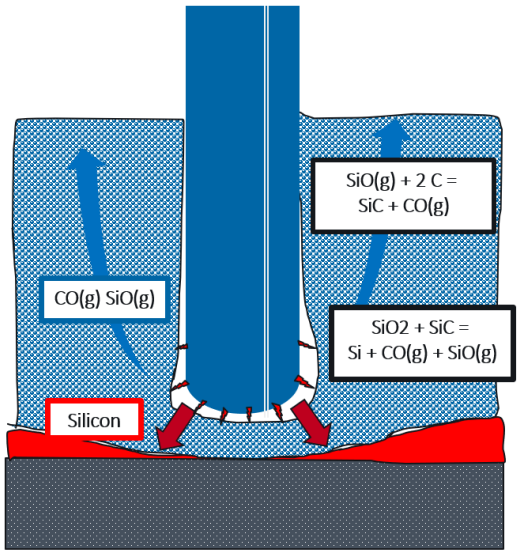


Figure 1 shows the main reaction in the silicon process. In the crater huge amount of CO-gas and SiO-gas are produced. The white "tube" in the electrode indicates the position of the tube for measurement of the crater pressure.

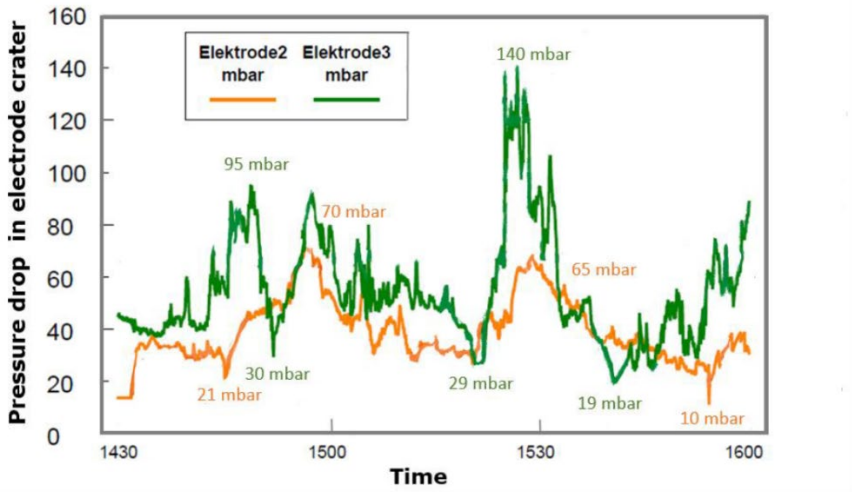


Figure 2 shows the pressure under two electrodes at a 40 MW ferrosilicon furnace. The pressure shows variation from approximately 30 to 140 mbar /1/.

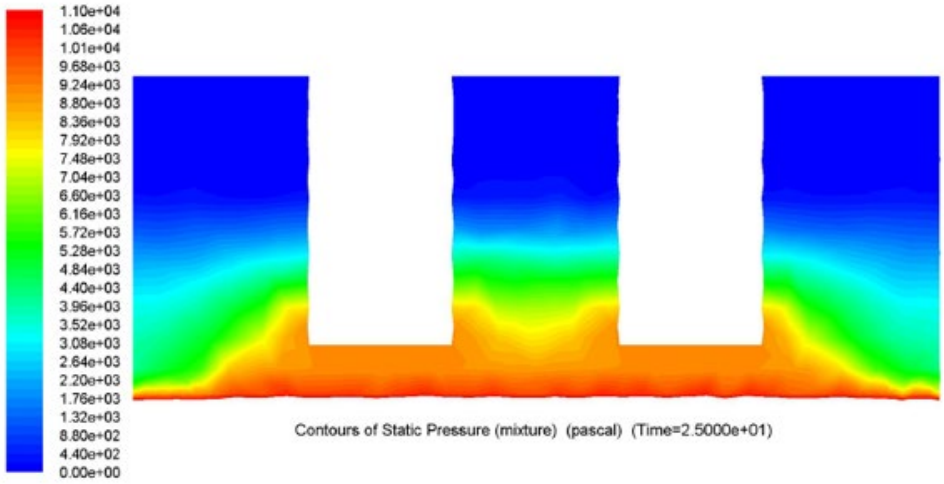


Figure 3 shows 2D contours of pressure in a vertical plane including two electrodes in a silicon producing furnace. /2/

The gas volume in a 30 MW silicon furnace will be the inner shaft volume minus electrode volume and raw material volume. The volume of the empty shaft is in the order of 200 m^3 and the free volume for gas is estimated less than 50% - i.e. less than 100 m3. The process gas production was calculated to approximately 10 m^3/sec which indicates that the available gas volume will be filled in about 10 seconds Even if this numbers are inaccurate they show clearly that the gas production is dominant and a there has to be a continuous gas outlet from the silicon charge.

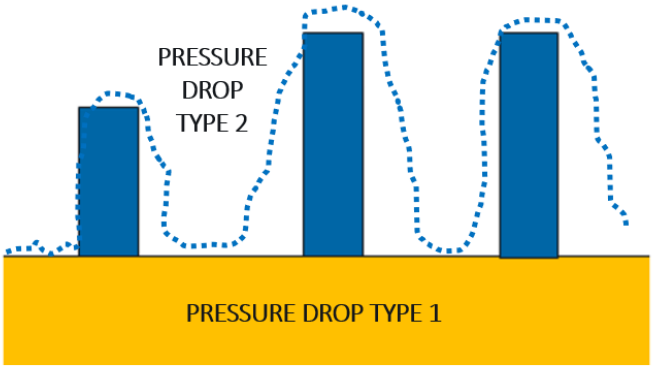


Figure 4 shows a simplified presentation of the pressure drop. The yellow box represents the constant pressure drop created by gas flow in the charge mixture (Charge pressure drop type 1) – and the blue boxes represents the dynamic pressure drop probably caused by the condensation of SiO-gas. (Charge pressure drop type 2)

There are normally only 2 outlets for the process gas. The main outlet is the top of the charge where SiO-gas, CO-gas and volatiles burns inside the furnace hood. The other outlet is the taphole that sometimes experiences the nasty taphole gas. Measurements shows that the taphole gas is far lower than the 10 m3/sec. But the problem with the taphole gas is a strong heat and the formation of fine condensed silica fume that both are an EHS problem.

Both the figure 2 and figure 3 show that the pressure in the silicon furnace has large variations. Pressure from 10 to 140 mbar has been measured. The variation has a frequency in order of the stoking period.

In order to study the furnace some hypothesis were made for the pressure in the furnace:

Hypothesis	Comments
There is a process gas production in the crater zone according to the theory for the process	According to accepted theory for the silicon production
The gas production is continuous when the furnace is operating	Measured both as off-gas temperature and dust emission from the furnace
The main gas outlet is the top of the charge – even when strong taphole gas	The other outlet – taphole – is measured to be maximum 10% of the off-gas energy
There is a lower limit for the crater pressure controlled by the gas resistance through the raw material	Results shown in this work
There is an upper limit for the crater pressure controlled by the weight of the charge. If exceed large channels and SiO-gas "blow-out" may occur.	The weight of the charge burden can be calculated – the maximum measured pressure approaches this limit
There is a "mechanism" that creates flow resistance in excess of the resistance open flow around the charge materials	Measurements of the off-gas energy indicates a build up – and sudden release – of entrapped process gas. This may result in flames out from furnace openings and increased off-gas temperature

Pilot measurement and calculation to validate the resistance to gas flow in an open charge (Charge resistance type 1)

In this work a charge bed of quartz, coal and wood chips was made to simulate the gas flow in the charge of a silicon process. Some typical charge materials are shown in figure 5. /3/



Figure 5 shows some raw materials used in the experiment. The picture shows quartz particles in the size of fraction 5-10 mm, coal and wood chips.

The pressure test equipment is shown in figure 6. Several tests were performed to check important parameters for the pressure drop in the charge. The column is 1meter height and has a 185 mm inner diameter. There are 3 pressure sensors and equipment for sampling of the test results.

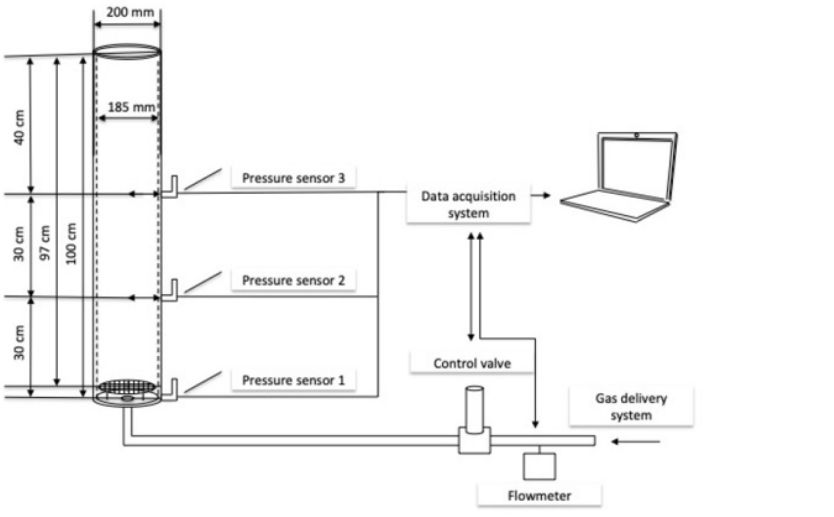


Figure 6 shows a schematic set-up of the pressure drop experimental system.

The test results were used to make model for the gas flow through the charge base on the Comsol program and Ergun's equation. One test example is shown in figure 7. /3/

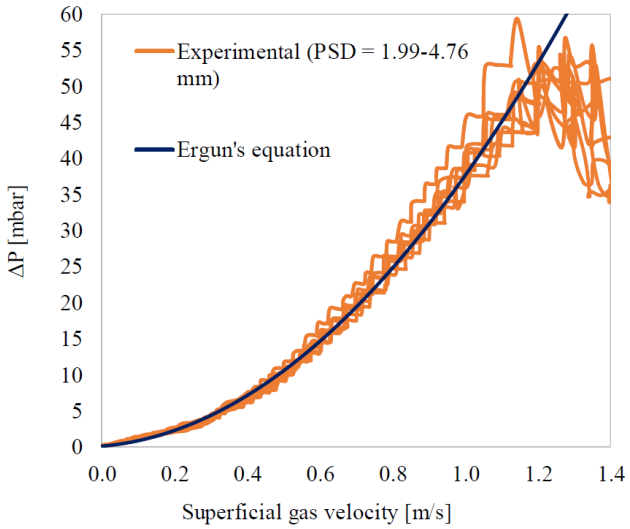


Figure 7 shows an example of the results from the test of the pressure drop in raw materials. The results fit very good with the Ergun's equation and the results was then used to calculate the pressure drop in an industrial size furnace.

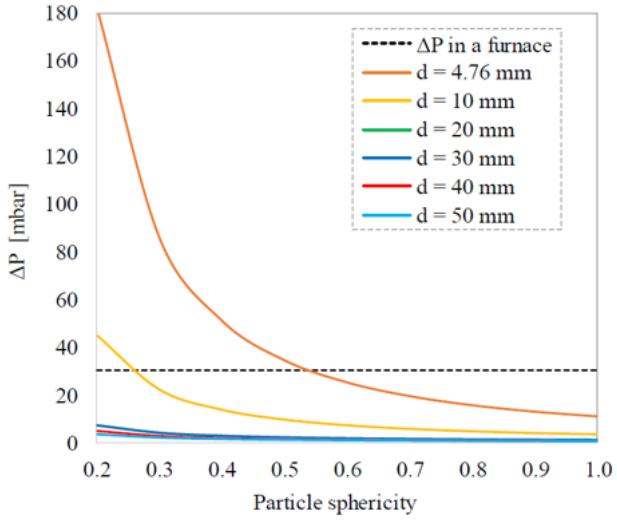


Figure 8 shows the simulated pressure drop in a 40 MW silicon furnace cause by gas flow. The results show the pressure drop with particle size and particle sphericity.

The results were converted to the dimensional and process parameters for å 40 MW silicon furnace. There are of course several parameters that is not known in a real size

furnace – but the modelling enables a qualitative parameter study of the industrial furnace.

Important parameters for the pressure drop in process gas flow was found to be:

Parameter	Comments
1. Furnace load	Controls the gas production in the crater
2. Charge particle size	Smaller particles give a higher pressure drop in the charge
3. Charge bed void fraction	Lower void fraction gives a higher pressure drop
4. Charge particle sphericity	Lower particle sphericity gives a higher pressure drop
5. Charge height	Higher charge height gives a higher pressure drop
6. SiO condensation or other phenomena that constrain the gas flow	The industrial measurements show a huge variation in the crater pressure timely linked to the stoking process

Conclusion

The pilot scale measurement and the modelling of the gas flow simulating the silicon process combines with earlier measurement of the crater process seems to support the following:

There are two main causes for the resistance to gas flow from the gas producing crater to the top of the charge:

1. Gas flow through the charge materials according that can be described by Ergun's formula. (Charge pressure drop type 1). This gas flow resistance is short time constant – and parameters that controls this resistance are presented in this study.
2. There are short term variation in the resistance of the gas flow (Charge pressure drop type 2). The resistance is timely linked to the stoking process and to furnace flaming. This variation is believed to be due to SiO-condensation.

Simulated pressure drop correlates well with experimentally measured pressure drop in an industrial furnace. This study confirms the continuous pressure drop caused by the charge mixture.

The macroscopic bed parameters were varied to study their influence on the pressure drop. A possible particle sphericity and bed void fraction for the furnace charge mixture

are 0.47 and 0.4 respectively. A decrease in void fraction, particle size and particle sphericity caused an increase in simulated pressure drop. A decrease in furnace load and charge height caused a decrease in simulated pressure drop.

The modified Ergun equation is in good agreement with the experimental pressure drop data for packed bed with quartz particles with size distribution 1.99-4.76 mm and 4.76-10.0 mm. The particle sphericity was estimated to be approximately 0.7 using a simple 2D projection of the quartz particles.

Acknowledgement:

This work has been funded by Elkem ASA, The Norwegian Ferroallys Research Association (FFF) and the Research Council of Norway through the RCN projects 256788 High-temp Quartz and 267621 Controlled Tapping. They are all acknowledged

References

1. Stein Tore Johansen & al, *Environmental aspects of Ferro-Silicon furnace operations – an investigation of waste gas dynamics, Infacon 8, Beijing China, June 1998*
2. Mehdi Kadkhodabeigi, *Modelling of Tapping Processes in Submerged Arc Furnaces*, PhD Thesis, Norwegian University of Science and Technology, Department of Materials Science and Engineering, Trondheim May 2011 ISBN 978-82-471-2841-1 (5)
3. Hanne Edfelt, *Pressure drop in charge mixture in silicon production,* Master Thesis, Norwegian University of Science and Technology, Department of Materials Science and Engineering, Trondheim January 2020

Silicon for the Chemical and Solar Industry XV
Trondheim, Norway, June 15 – 18, 2020

Lattice strain and phase transformations in silicon introduced by the precipitation of Cu_3Si

André Meißner, Tim Sieber and Jörg Acker
Brandenburg University of Technology Cottbus-Senftenberg, Department of Physical Chemistry, Universitätsplatz 1, D-01968 Senftenberg, Germany

Abstract

The reaction of Si with CuCl was studied by a combination of Raman microscopy, confocal microscopy and SEM-EDX. Two reaction pathways were observed to proceed at the same time. The first one is a solid state reaction between Si and Cu or CuCl that leads to a massive nucleation of Cu_3Si exactly at the interfacial contacts between CuCl and Si. This study shows how the presence of the Cu_3Si phase can be clearly identified and distinguished from areas simply covered with copper by means of Raman microscopic measurements. The second reaction pathway identified proceeds via a short-range gas phase transport of CuCl at low temperatures. The immediate reaction of the transported CuCl to the Si surface causes the massive spread of Cu in the close neighborhood around the CuCl source particles, however, without a nucleation of Cu_3Si. The nucleation of Cu_3Si precipitates and the short-range transport of CuCl have a tremendous impact on the underlying Si matrix. Tensile- and compressive-strained Si are generated in the immediate vicinity of the precipitates and at their interface to the surrounding silicon. Indications of high-pressure modifications of Si were found. Those areas of the Si surface which are affected by the short-range transport of CuCl and covered with low concentrations of copper exhibit a significant tensile strain. As recently shown, tensile and compressive strain in Si have a significant impact on the reactivity of Si. It might be assumed that Cu_3Si-induced lattice strain in Si affects the reactivity of Si in the Direct Reactions in a similar matter.

Introduction

Copper is the preferred catalytic element in the Direct Reaction of silicon because it causes a high selectivity of the formation of dimethyldichlorosilane in the Müller-Rochow synthesis and the preferred formation of trichlorosilane in hydrochlorination. Only copper, among all the metals investigated, is able to trigger this kinetic effect, since dimethyldichlorosilane and trichlorosilane are among the thermodynamically least

stable compounds in their reaction systems Si-H-Cl-C and Si-H-Cl, respectively [1]. It is unquestioned that the copper catalyst reacts to Cu_3Si and CuCl under the conditions of the Direct Reactions. However, in spite of the large number of experimental studies over the past few decades, the catalytic effect of copper in all its facets is still not fully understood. This includes particularly the aspect of whether the reaction of silicon with copper or copper compounds causes lattice strain, which might have an influence on the reactivity of silicon.

Lattice strain affects the chemical reaction behavior of silicon and silicon compounds (SiO_2, SiC, Si_3N_4) [2]. There are numerous examples related to the Direct Reactions of Si showing that mechanochemical treatments are used to optimize the synthesis of dimethylchlorosilane and trichlorosilane. Schrader et al. [3-5] reported that mechanical activation of the contact mass of the Direct Reaction of methylchlorosilanes shortened the induction period, increased the utilization rate of Si and improved the selectivity for dimethyldichlorosilane. Bade et al. [6,7] showed that a combination of vibration milling of Si during hydrochlorination significantly affects the length of the induction period, selectivity and Si utilization. Recent studies by Muzafarov et al. deal with mechanochemical methods and equipment for the direct synthesis of alkoxysilanes by mechanically activated silicon followed by a reaction with an alcohol [8,9]. In addition, a number of patents are known in which mechanically treated (strongly lattice disordered) copper is used as an effective catalyst in direct synthesis [10-12].

Initiated by an unusual reaction behaviour during etching of diamond wire-sawn silicon wafers with $HF/HNO_3/H_2SiF_6$ acid mixtures [13, 14] and the failure of classical explanations, the influence of lattice stresses transferred to the silicon by the sawing process was investigated in detail. For the first time, the type and extent of lattice strain was quantitatively related to the reactivity of the silicon expressed as the local etch rate at the respective lattice strained regions [15]. The highest etch rates were found for tensile-strained Si, followed by compressive strained Si, both of which exceed the etch rate of undisturbed Si by many times [15].

The present article is devoted to a question that has not been discussed in the context of Direct Reactions so far: Can the reaction between silicon and CuCl lead to strain in the silicon lattice, influencing the reaction behavior in the Direct Reactions? This study presents a first step towards answering this question.

Experimental

The surface topography during the reaction was analyzed by confocal microscopy using a 3D profiler, Sensofar PLμ neox (Sensofar), equipped with a 50× objective having a numerical aperture of 0.95. The wafer surfaces were mapped using a confocal Raman microscope (DXR SmartRaman, Thermo Fisher Scientific) in the backscattering configuration. The microscope was equipped with a 532 nm excitation laser (penetration depth in Si ~ 0.7 μm [16]) and a 900 grooves/mm grating, which enabled the acquisition

of Raman spectra in the wave number range of 150−1250 cm^{-1}. SEM-EDX measurements were performed using a ZEISS EVO M 15 equipped with EDAX TEAM™ EDS and a JEOL JSM 6400 equipped with a NORAN EDX system.

The reactions between CuCl and Si were performed on a high-gloss polished Czochralsky grown Si(111) wafer (p-doped, 400 µm thickness) purchased from Silchem GmbH Freiberg, Germany. CuCl was synthesized according to Stathis [17]. Cu_3Si was prepared from the pure elements by repeated arc furnace melting using a miniaturized lab apparatus described by Henneberg [18]. Furthermore, rapidly quenched Cu-Si alloys of different compositions from study [19] were investigated in this study.

Results

Raman spectroscopic identification of Cu_3Si

Various copper silicide samples were analyzed to determine the characteristic Raman bands of Cu_3Si. Both rapidly quenched silicide films [19] with the compositions $Cu_{76}Si_{24}$ and $Cu_{77}Si_{23}$ and Cu_3Si samples prepared from the elements by multiple arc melting [18] were examined. The reflexes occurring in the diffractograms of all of these samples can be fully indexed as Cu_3Si according to the ICCD X-ray database PDF-2 [PDF 01-076-7859].

Nevertheless, the Raman spectra in Figure 1a show differences in the signal shapes but not in the position of the signals. The deconvolution of the signals in Figure 1b results in a total of four characteristic bands, all of Lorentzian peak type. The parameters of the normalized peaks are: 91 cm^{-1} (FWHM: 15 cm^{-1}), 108 cm^{-1} (FWHM: 26 cm^{-1}), 148 cm^{-1} (FWHM: 8 cm^{-1}) and 217 cm^{-1} (FWHM: 27 cm^{-1}). The signal at 217 cm^{-1} always emerged as the most clearly recognizable feature of the Cu_3Si phase in all of the samples studied, which is, therefore, considered as the essential feature for its identification.

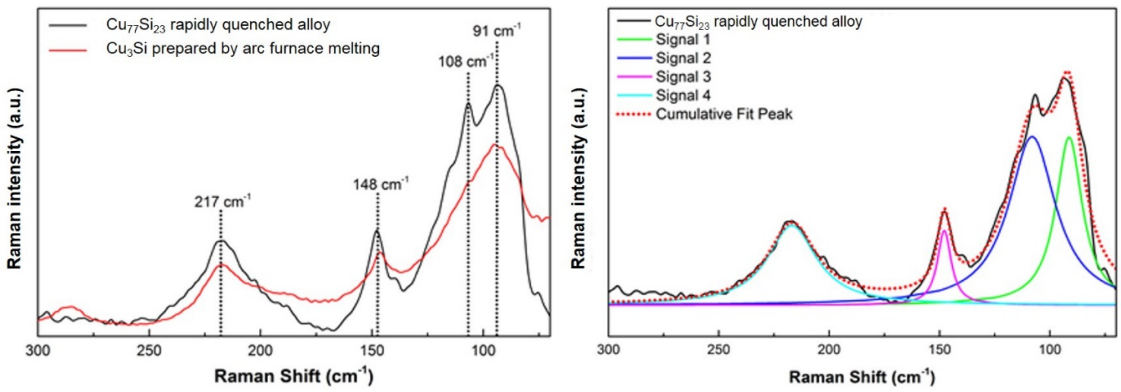


Figure 1: a) Comparison of the Raman spectra of rapidly quenched $Cu_{77}Si_{23}$ and Cu_3Si from arc furnace synthesis; b) deconvolution of the Raman spectrum of $Cu_{77}Si_{23}$.

The reaction between CuCl and Si

CuCl crystallites were finely distributed on the surface of a high-gloss polished Si(111) wafer to examine the formation of Cu_3Si. Figure 2a shows a typical SEM image of CuCl crystallites produced by reduction of $CuSO_4$ using ascorbic acid. The trigonal pyramids are very clearly visible and can be more or less merged together. Figure 2b shows a confocal microscopic image of the CuCl crystallites on the Si(111) surface. The trigonal-pyramidal patterns, a few micrometers in height, are recognizable if the crystallites are isolated from each other.

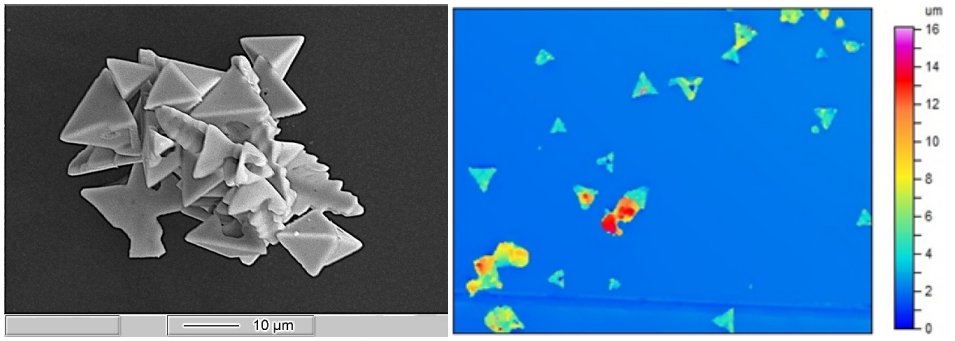
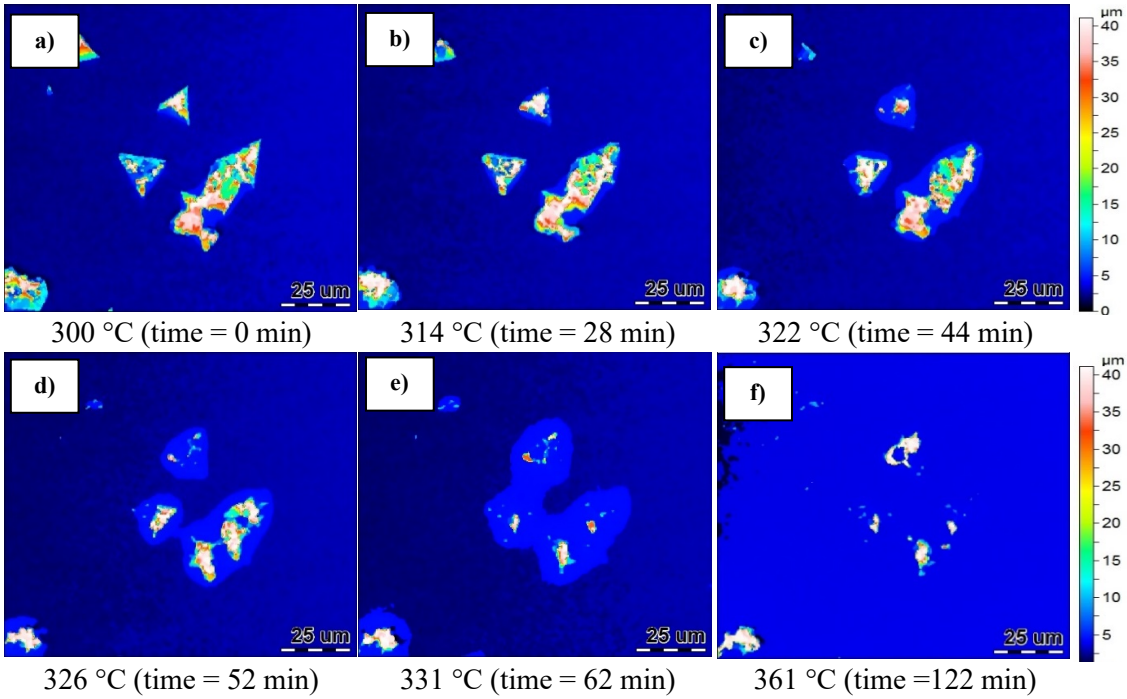


Figure 2: a) SEM micrograph of CuCl crystallites; b) Confocal microscopy images of CuCl crystals placed on the surface of a polished Si(111) wafer at room temperature.



300 °C (time = 0 min) 314 °C (time = 28 min) 322 °C (time = 44 min)

326 °C (time = 52 min) 331 °C (time = 62 min) 361 °C (time =122 min)

Figure 3: Confocal images of the reaction of CuCl on a Si(111) surface.

Undergoing continuous purging with argon, the samples were then first heated at 10 °C/min to 300 °C, then at 0.5 °C/min to 375 °C and kept at this temperature for 120 minutes while being continuously observed with the confocal microscope (Fig. 3).

The trigonal pyramids of CuCl remain unchanged up to a temperature of about 300 °C. With increasing temperature, beginning with Figure 3b, clear changes in the shape of the crystallites and their height can be seen. When the reaction is complete, the trigonal structures are no longer recognizable, the surface is comparatively flat and irregularly shaped structures are found instead.

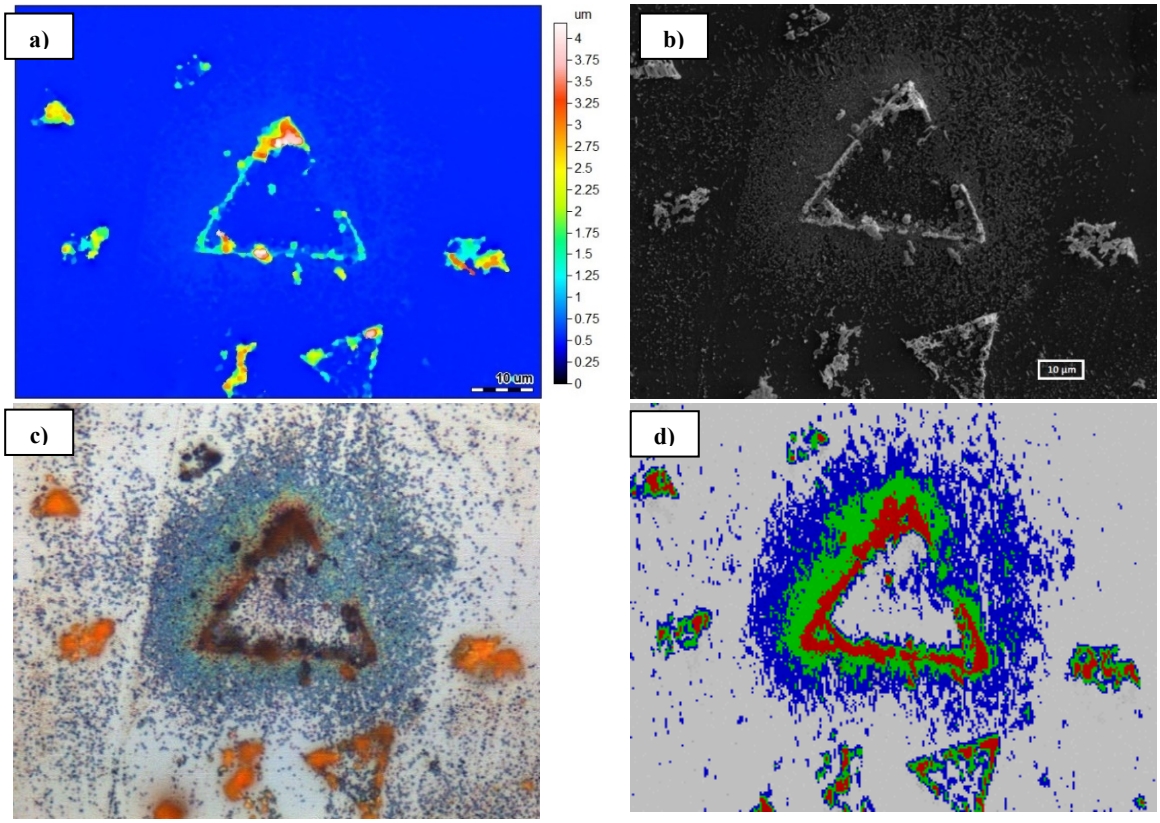


Figure 4: Pattern formed in the reaction of CuCl on a Si(111) surface after annealing at 375 °C under argon. a) Confocal image with height color scale, b) SEM image, c) optical microscope image and d) color map of phase composition determined by EDX.

After the reaction, the silicon surface was examined with confocal microscopy and SEM-EDX. The Figures 4a and 4b show a triangular contour with a height of more than 1 µm above the flat Si surface in their center. This contour is identical with the contact area between an individual (trigonal) CuCl crystallite and the silicon surface. The optical microscope image in Figure 4c shows that the triangular structure exhibits a copper-like coloration. As a second interesting feature, the scanning electron microscope image in Figure 4b and, moreover, the optical image in Figure 4c indicate a circled area around the trigonal contour. According to Figure 4a, this circular pattern does not cause any significant change in height. It is also interesting that the interior of the trigonal structure has apparently not experienced any significant change. The EDX mapping in Figure 4d provides information about the composition of the structures

created. As the EDX analyses in Table 1 show, the color-coded areas in Figure 4d differ significantly in their copper content. The composition marked in red in Figure 4d shows the presence of a phase with a high copper content, which is concentrated in those areas where the CuCl crystallite was in direct contact with the silicon surface. It is assumed that these structures were formed by a solid state reaction between CuCl and Si under the formation of $SiCl_4$. Starting from there, a slightly wider range of a medium copper content follows (marked green), which has preferably developed on the outer sides of the original CuCl crystallite. Finally, it follows the blue marked circular surrounding described above, which is characterized by a very low copper content. These patterns strongly suggest that, despite the comparatively low reaction temperature, a short-range gas phase transport of CuCl and a subsequent reaction with the Si surface under the formation of elemental Cu occurred.

Table 1: Phase composition of the areas marked in Figure 4b determined by EDX.

		phase 1		phase 2		phase 3	
area fraction (%)		19.05	%	8.29	%	3.90	%
element	line	composition					
O	K_α	4.18	at %	10.54	at %	18.34	at %
Cu	L_α	9.34	at %	24.10	at %	44.94	at %
Si	K_α	86.12	at %	64.64	at %	35.53	at %
Cl	K_α	0.35	at %	0.72	at %	1.19	at %

It is now possible to identify Cu_3Si using Raman microscopy. The intensity distribution of the Raman band at 217 cm^{-1} in Figure 5a clearly shows the positions where Cu_3Si had been formed. As expected, these are the areas where CuCl and Si were in direct contact with each other and where a solid state reaction could occur. This corresponds to all elevated areas shown in Figure 4a. By contrast, no silicide formation can be detected in the areas where CuCl was deposited via the gas phase and which are marked green and blue in the EDX mapping in Figure 4d. At present, it cannot be determined whether silicide formation did not occur or whether the amount of Cu_3Si formed is too small for Raman spectroscopic detection.

Strain and phase transitions in Si

The local formation of Cu_3Si and the transport of CuCl and its subsequent reaction at the silicon surface have an enormous effect on the surrounding silicon. Figure 5b shows a mapping of Raman intensities at the wave number of 517 cm^{-1}, which is characteristic for tensile-strained silicon [20-22]. Figure 5b shows that high tensile strain is present in

the vicinity of the trigonal Cu_3Si structure and particularly in areas of the CuCl transport that has taken place, which is a remarkable and unexpected result.

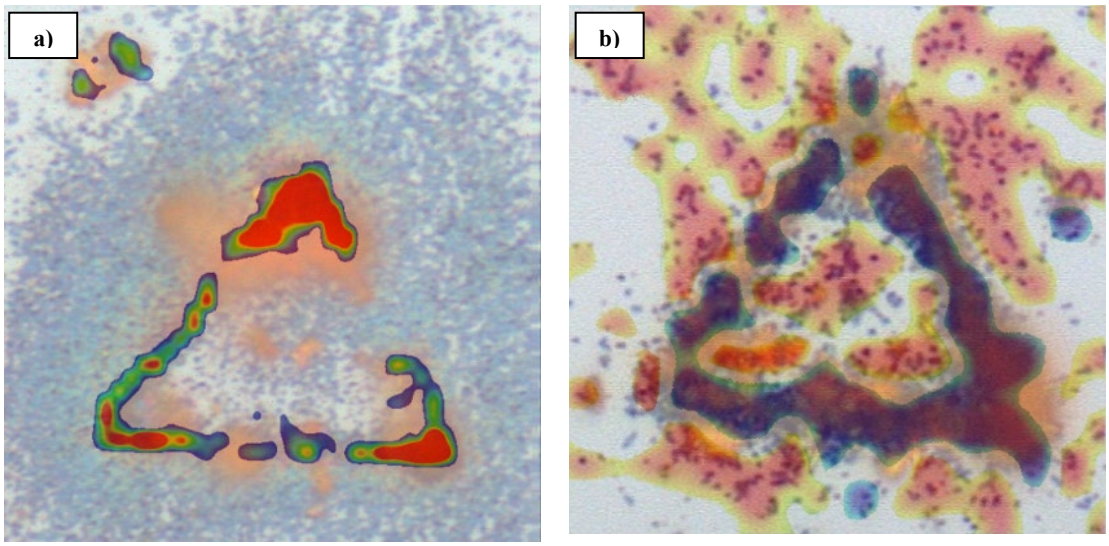


Figure 5: Raman analysis of the reacted surface of Si(111). Superpositions of the optical microscopic image from Figure 4c) with a) the normalized Raman intensities at 217 cm^{-1} and b) the normalized Raman intensities at 517 cm^{-1}. Color scale: red = high intensity, blue = low intensity.

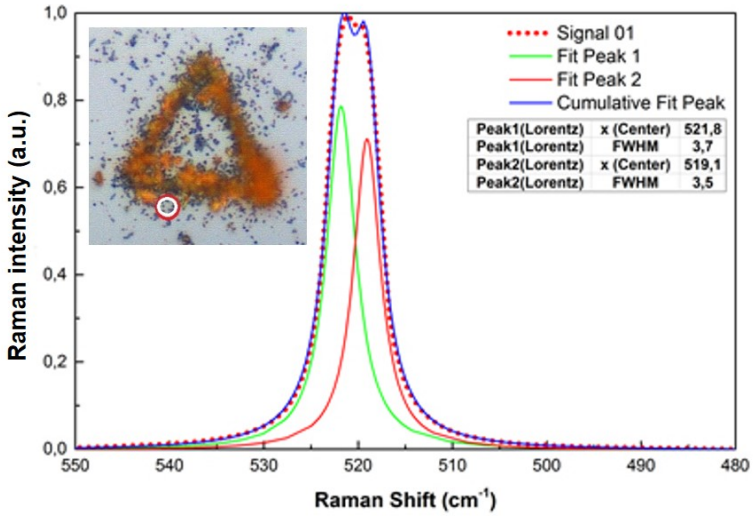


Figure 6: Raman spectrum measured at the measuring point marked in the image and located within the range of a high Raman intensity at 517 cm^{-1} in Figure 5b.

Figure 6 shows a typical Raman spectrum of a measurement point located in the high intensity band at 517 cm^{-1}. The unfolded signal at 521.8 cm^{-1} is assigned to the undisturbed crystalline Si and the one at 519.1 cm^{-1} indicates a more tensile-strained silicon. The Raman intensity recorded at 517 cm^{-1}, therefore, arises from the peak edge.

Figure 7 shows patterns from another spot of the same sample. Most of the triangular structures are fully converted into Cu_3Si according to the distribution of the 217 cm^{-1} Raman band intensities in Figure 7a. The mapping of the Raman band at 517 cm^{-1} as a feature for tensile-strained Si in Figure 7c exhibits sufficiently high intensities at only a few positions. It is not clear whether the presence of elemental copper has any impact on the Raman signal intensity, as has already been observed by Steegen et al. [23]. However, the most interesting feature is shown in Figure 7c, in which the presence of compressive-strained Si is indicated by a map of the Raman intensities at 524 cm^{-1}. Further analysis of the precipitates give strong indications of the presence of the high-pressure modifications Si-III and Si-IV [24].

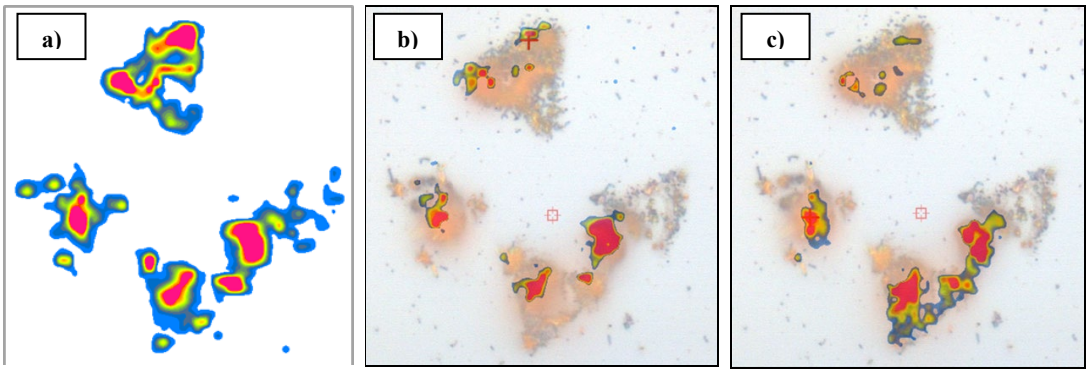


Figure 7: Pattern formed in the reaction of CuCl on a Si (111) surface after annealing at 375 °C under argon. Mapping of the normalized Raman intensities at 217 cm^{-1}, superposition of the optical microscopic image b) with the normalized Raman intensities at 517 cm^{-1} and c) with the normalized Raman intensities at 524 cm^{-1}. Color scale: red = high intensity, blue = low intensity.

Discussion

Raman spectroscopic characterization of different Cu_3Si samples has identified characteristic Raman bands that can be assigned to this compound. The most prominent band is located at 217 cm^{-1}, which was used for the first time to identify Cu_3Si as a result of the reaction of CuCl with Si. The classical EDX analysis is able to provide the typical information on the lateral distribution of the elements on the silicon surface, but the presence of Cu_3Si is difficult to quantify, since EDX cannot distinguish whether the Cu detected is elemental or has already been converted to a copper silicide phase. With the help of Raman microscopy, the detection of Cu_3Si can now be carried out with a lateral resolution of about 2 µm.

The results in Figure 4 indicate two different ways of reaction between CuCl and Si. One way is the solid state reaction between Si and Cu or CuCl described already that leads to a massive nucleation of Cu_3Si exactly at the contact position of the Si/CuCl or Si/Cu solid-solid interfaces [25]. The trigonal-pyramidal shape of the CuCl crystallites is found as a raised, triangular structure on the silicon surface. In addition to the highest

copper contents, these structures also exhibit the highest Raman intensity of the Raman band of 217 cm^{-1}, which is characteristic of the Cu_3Si phase.

The second reaction pathway identified proceeds via a gas phase transport of CuCl at temperatures below 300 °C. This gas phase transport causes the massive spread of Cu (after reaction with Si) in the close neighborhood around CuCl particles. This contradicts the assumption formulated previously that a gas phase transport does not occur at such temperatures because of the very low CuCl partial pressure of less than 0.1 mbar [25]. However, Souha et al. [26] assumed a significant gas phase transport already at 160 °C. Under the conditions of a flowing gas atmosphere, i.e. by purging with Ar, a long range transport of CuCl is observed (not shown in this paper) that leads to a nucleation of isolated microscopic Cu_3Si precipitates on the bare Si surface away from the source CuCl particles. Both the nucleation of Cu_3Si and the gas phase transport have enormous effects on the silicon. Areas of tensile and compressive stress in the silicon can be clearly detected in the close vicinity of the Cu_3Si precipitates. The transport of CuCl has an even more massive effect on the underlying silicon. Although the transport spreads only over a few micrometers around the CuCl crystallites and does not lead to any detectable silicide formation, large areas with a significant tensile stress are formed.

As has recently been shown, tensile and compressive strain in Si have a significant impact on the reactivity of Si, since they lead to a dramatic increase in reaction rate [15]. It might be assumed that the lattice strain introduced by the nucleation of Cu_3Si and particularly induced by the transport of CuCl and its reaction at the Si surface affect the reactivity of Si in the Direct Reactions in a similar, yet not fully understood matter. Lieske et al. [27,28], for example, supposed the existence of two-dimensional Cu-Si phases undetectable by XRD as catalytic active species in the Direct Synthesis. However, further research needs to be done to clarify all open questions.

References

1. J. Acker, K. Bohmhammel, J. Organomet. Chem., **693**, 2008, p2483
2. G. Heinicke, Tribochemistry, Akademieverlag, 1984
3. R. Schrader, K. Dreier, K.-H. Werner, Chem. Techn., **20**, 1968, p475
4. R. Schrader, K.-H. Werner, Chem. Techn., **26**, 1974, p302
5. R. Schrader, K.-H. Werner, Chem. Techn., **27**, 1975, p156
6. S. Bade, U. Hoffmann, K. Schönert, Int. J. Miner. Process, **44-45**, 1996, p167
7. S. Bade, U. Hoffmann, K. Schönert, Chem. Eng. Comm., **143**, 1996, p169
8. M.N. Temnikov, A.A. Anisimov, V. Zhemchugov, D.N. Kholodkov, A.S. Goloveshkin, A.V. Naumkin, S.M. Chistovalov, D. Katsoulis, A.M. Muzafarov, Green Chem., **20**, 2018, p1962

9. S.M. Chistovalov, V.M. Kotov, A.A. Anisimov, M.N. Temnikov, P.V. Zhemchugov, A.M. Muzafarov, Chem. Petrol. Eng., **54**, 2019, p703
10. M. Aramata, M. Furuya, Y. Shirota, A. Muraida, S. Ueno, T. Shinohara, US Patent 6,686,312, 2004
11. M. Aramata, H. Ozeki, A. Muraida, S. Ueno, T. Shinohara, T. Inukai, US Patent 6,984,748, 2006
12. T. Inukai, H. Ishizaka, M. Aramata, Y. Satou, US Patent 7,279,590, 2007
13. J. Acker, T. Langner, B. Meinel, T. Sieber, Mat. Sci. Semicond. Proc., **74**, 2018, p238
14. J. Acker, T. Sieber, T. Langner, S. Herold in: Silicon for the Chemical and Solar Industry XIV, Eds.:B. Andresen, L. Nygaard, H. Rong, M. Tangstad, H. Tveit, I.G. Page, The Norwegian University of Science and Technology, Trondheim, Norway, 2018, p11
15. T. Langner, T. Sieber, J. Acker, ACS Appl. Nano Mater., **1**, 2018, p4153.
16. I. De Wolf, Semicond. Sci. Technol., **11**, 1996, p139
17. E.K. Stathis, Chem. Ind., **21**, 1958, p633
18. E. Henneberg, Ph.D. Thesis, TU Bergakademie Freiberg, Germany, 2003
19. N. Mattern, R. Seyrich, L. Wilde, C. Baehtz, M. Knapp, J. Acker, J. Alloys Comp. **429**, 2007, p211
20. Y. Gogotsi, C. Baek, F. Kirscht, Silicon. Semicond. Sci. Technol., **14**, 1999, p936
21. Y. Gogotsi, G. Zhou, S.S. Ku, S. Cetinkunt, Semicond. Sci. Technol., **16**, 2001, p345
22. V. Domnich, Y. Gogotsi, Rev. Adv. Mater. Sci., **3**, 2002, p1
23. A. Steegen, K. Maex, Mat. Sci. Engineering R, **38**, 2002, p1
24. A. Meißner, Master Thesis, BTU Cottbus-Senftenberg, Germany, 2018
25. J. Acker, S. Köther, K.M. Lewis, K. Bohmhammel, Silicon Chem., **2**, 2003, p195
26. H. Souha, F. Bernard, E. Gaffet, B. Gillot, Thermochim. Acta., **351**, 2000, p71
27. H. Lieske, H. Fichtner, U. Kretzschmar, R. Zimmermann, Appl. Organomet. Chem., **9**, 1995, p657
28. H. Ehrich, D. Born, K. Richter, J. Richter-Mendau, H. Lieske, Appl. Organomet. Chem., **11**, 1997, p237

Silicon for the Chemical and Solar Industry XV
Trondheim, Norway, June 15 – 18, 2020

Silicon in the 2020s

Jorn P. de Linde
CRU

Abstract

The outlook for silicon demand, supply and prices during the 2020s is assessed. The discussion focuses on the major forces that will shape the global silicon market and industry over the coming decade, including the key drivers of future silicon consumption, the economics of investment in new production capacity, the growing importance of carbon taxation, and the changing position of China.

Introduction

The silicon market is now about four times larger than it was when the first *Silicon for the Chemical Industry* conference was held back in 1992. This growth has been facilitated by a dramatic expansion of silicon production and, increasingly, consumption in China. The chemical sector has been the main driver of these gains, fuelled in part by a rapid escalation of solar-related silicon consumption over the past decade.

As we enter the 2020s, short-term volatility apart, can this strong growth performance be sustained? What are the main opportunities and challenges facing the silicon industry over the next ten years?

Silicon demand

Global silicon demand reached an all-time high of close to 3.0 Mt in 2018 but has fallen sharply since that time. In 2019, sputtering economic growth and heightened uncertainties, caused in large part by trade conflicts, resulted in a nearly 5% drop in total silicon demand, reversing all the gains achieved in 2018. As of end-March 2020, the full impact of the novel coronavirus (Covid-19) on global silicon demand is still unfolding, but it is conceivable

that the y/y contraction of global silicon demand in 2020 will approach or even exceed the drop experienced in 2019.

What is clear is that the fortunes of the silicon industry will be closely intertwined with those of the auto and silicone industries. Production of cars and light trucks is the major driver of silicon demand from aluminium smelters and we have already seen significant closures of auto plants. Moreover, a significant share of silicone demand is linked to auto production. Activity within the construction sector, another major end-use of silicones, is also grinding to a halt in numerous locations. The solar industry will likely face a significant slowdown this year, as well, as plans for new installations are disrupted by the spreading virus.

Not only is it difficult at this juncture to accurately predict the severity and duration of the impending downturn, but the trajectory of the subsequent recovery is also subject to considerable speculation. However, growth, when it eventually resumes, will come from a base of consumption that is much lower than it was at the peak in 2018.

As it has been for a very long time, the chemical sector will remain the main engine of consumption gains going forward, supported in part by environmental protection and product life-cycle considerations. The silicone-intensity of many emerging economies is still comparatively low, keeping the medium- to longer-term growth in siloxane-related silicon consumption well above that of world GDP.

Cost reductions throughout the value chain have made solar energy more competitive and progressively less dependent on government support. The decline in manufacturing costs can in large part be attributed to efficiency improvements, including a steady drop in the amount of polysilicon needed per watt of installed capacity. Without significant future growth in solar-related silicon consumption, the advance in global silicon demand will be much lower than the GAGR of almost 5.2% achieved between 2008 and 2018.

Supported by a massive expansion of production capacity, China has accounted for virtually the entire net increase in chemical-related silicon demand over the past two decades. Much of this gain has been fuelled by a rapidly growing local economy as China has expanded at a rate that is more than double that of the world average. However, the country's trade position in silicones has also changed dramatically, with China going from being a major net importer to a substantial exporter.

China experienced a rapid build-up of siloxane capacity between 2007 and 2011, followed by a period of consolidation as more than half a dozen local plants shut down or were absorbed by other producers. The industry is now in the early stages of a second wave of investment that could double the country's siloxane capacity over the next five years. This capacity will be located in Xinjiang, Yunnan and Inner Mongolia.

These provinces, together with Sichuan, are also host to a number of large-scale polysilicon plants in various stages of development, construction and production. The new plants are transforming the competitive landscape, not just in China but worldwide. Recent casualties include the solar-related polysilicon operations of OCI Co. Ltd. and Hanwa in South Korea.

In contrast to its the trade position for silicones, China remains a large net polysilicon importer. However, domestic polysilicon producers are capturing a rising share of the Chinese solar market. China itself is no longer the main outlet for local manufacturers, and continued growth in this sector principally depends on the future level of solar installations outside China.

Aluminium-related silicon demand will benefit from a post-Covid-19 rebound in total auto production. However, future gains in aluminium-related silicon demand are likely to diminish because of increased recycling of silicon-intensive alloys and a gradual shift towards Electric Vehicles and increased use of aluminium alloys that contain smaller amounts of silicon. Moreover, lifestyle changes, such as ridesharing, will potentially lower the total demand for autos.

As the advance in demand from existing end-use sectors slows, significant consumption gains in new applications will be needed for the growth in global silicon demand to remain close to historical rates. Illustrating the power of compounding, if the CAGR in silicon demand between 2018 and 2030 were to drop from 4.0% to 3.0%, total demand would be nearly 520,000 t lower by the end of the decade.

As the economic shock of Covid-19 is absorbed, there will be longer-term repercussions for the silicon market as companies re-evaluate sourcing options and supply chains and take a closer look at optimal inventory levels. The implications for the future distribution of silicon demand and production is not yet clear, but the one-two punch of growing trade conflicts and Covid-19 could very well mark the end to a period of rapid globalisation.

Silicon supply

The distribution of silicon supply worldwide, as well as in individual markets, depends on available production capacity, cost competitiveness and barriers to trade, but total supply is fundamentally driven by the aggregate level of silicon demand. In response to the rapid growth in demand, global silicon production rose by more than 800,000 t over the past ten years. China accounted for nearly all the net gain.

Due to a protracted drop in demand, global silicon production is expected to fall further in 2020 on the back of a 7.3% decline in 2019. As of the end of 2020 Q1, more than 400,000 t of silicon capacity outside China that had been in production in mid-2018 was closed or redeployed to the manufacture of other alloys.

Short-term movements in Chinese silicon production are an order of magnitude larger than they are in other countries due to the impact of seasonal changes in the availability and cost of hydroelectric power in Southwest China. These seasonal variations make it more difficult to gauge changes in Chinese supply, but it is evident that a substantial amount of capacity has also been shut down in China over the past several years in response to sluggish demand and low prices and intensified competition from new large-scale, low-cost plants in Xinjiang that operate throughout the year.

Increased demand, reflecting a combination of rising underlying consumption and gradual restocking will spark a turnaround in global silicon production, likely from 2021 onwards, and support higher annual average capacity utilisation rates going forward. Still, the market will have to absorb a large overhang of idled capacity on top of a significant amount of supply associated with new furnaces commissioned in 2019.

However, it is far from certain that all of the furnaces that have been shut down since mid-2018 will return to production even after the impact of Covid-19 subsides. Whether closures become permanent or not will depend in large part on the future availability and cost of electric power. Commercial considerations, such as access to a stable base of consumers and market share limitations, will also play an important role in future operating decisions, as will trade restrictions.

Trade restrictions have had a major impact on trade flows and silicon prices in individual markets over the past two decades. Prohibitive penalty duties on Chinese silicon will remain in effect in the USA through to 2023. The anti-dumping duty on silicon of Chinese origin in the EU, the other major protected market, could expire sooner, potentially before end-2021.

In the current geo-political environment, we believe the probability that the current penalty duties will be lifted before the late-2020s is small. While expanded supply into the EU and, especially, the US market would lower local silicon prices, those in many other regions could rise, as trade flows are adjusted. The disruptive impact would also depend on the level of production costs in China at the time.

Most of the massive expansion of Chinese silicon production capacity has been in the form of greenfield investment. Outside of China, other options have played a bigger role in expanding the supply base but at a slowing rate, as many of the more cost-effective investments have already been made. Both inside and outside China, the location of greenfield silicon capacity is in large part determined by the cost and availability of electricity. This limits the number of suitable sites, but other significant hurdles exist, as well, notably the high capital costs and resulting financial burden that are associated with greenfield silicon projects, especially outside China. Recent history suggests that access to

process know-how and operating experience also are key to the successful performance of new plants.

Carbon taxation and more stringent environmental rules and regulations will also have a growing influence on location decisions and relative cost positions for silicon smelters worldwide over the coming decade. The impact depends on the policies adopted by governments, including the introduction of carbon border taxes and other measures to limit carbon-leakage, but also on the actions taken by investors and consumers. Higher production costs would push up silicon prices and would over time also shift output towards smelters in locations with a low-carbon footprint.

One unique feature of silicon supply is the prevalence of captive supply. Captive silicon supply is much less prevalent within the aluminium sector, but chemical-grade silicon consumers currently control more than 40% of Western nameplate production capacity. Much of the associated supply is consumed internally, although a significant share of the output from some plants is supplied to third parties. Nevertheless, it is evident that production from captive plants has been much more stable than non-captive production. This has important implications for how suppliers adjust to shifts in demand, as discussed in the next section.

During the 2020s, China will continue to account for a majority of global silicon output, underpinned by a rapidly expanding local market. The country will also remain the leading exporter and will retain a key role in balancing the global silicon market. However, as the growth in net capacity additions in China slows in response to structural reforms and a gradual restructuring of the local industry, we expect that other countries will meet a progressively higher proportion of global silicon demand, supported by a steady expansion of production capacity outside China.

The net amount of additional capacity that will be required by 2030 depends principally on the future level of demand. Without significant and persistent growth in chemical-related silicon consumption, the advance in global silicon demand will be much lower, delaying the need for capacity additions and keeping silicon prices from reaching a level supportive of greenfield investment. Still, the expansion of silicon supply on a longer-term basis will by all accounts require a sustained rise in prices compared with the levels that prevailed prior to 2007.

Market balances and silicon prices

Adjusted for inflation, silicon prices on average were substantially higher in all of the major markets over the past ten years than they were between 2000 and 2009. The reasons differ somewhat by market but are largely cost-driven and structural in nature.

As a result of this lift, silicon prices have risen to levels needed to support investment in greenfield capacity, but not on a consistent basis, as extended periods of oversupply have weighed on the market as the industry has struggled to make sufficient curtailments to production in the face of substantial declines in demand.

Despite overall strong growth in underlying consumption, silicon prices have become increasingly volatile since 2008, especially in the USA and the EU, the two main markets outside of Asia. The large fluctuations in silicon prices can principally be attributed to shifts in demand, starting with the sharp downturn triggered by the 2008 global financial crisis. Looking at the years in which prices have declined, global silicon demand tumbled by nearly 23% in 2009, far in excess of the 7.5% y/y drop recorded in 2012 and the 4.9% y/y decline experienced in 2019.

The swings in global silicon demand over the past decade reflect to a considerable extent the growing importance of the solar sector, which has provided a significant boost to silicon demand. However, the solar sector has also led to increased volatility due to large fluctuations in the production of polysilicon in response to substantial variations in the growth of new installations.

Nearly 44% of the total production capacity outside China is controlled by consumers and the output from these operations tends to be stable through the cycle. Because the utilisation rate of captive capacity remains fairly constant during market downturns, this puts a greater onus on non-captive producers to make required supply adjustments. At the same time, the silicon cost curve is flat, with a small cushion of high-cost capacity, which encourages silicon producers to delay closure decisions in the hope that someone else will cut supply sooner.

Chemical companies in China already possess significant amounts of silicon capacity and the prevalence of captive supply will increase further over the next several years as value-added manufacturing in Xinjiang and other provinces continues to grow. However, the dynamics in the Chinese market are different. Overall, changes in Chinese silicon prices have been smaller than those observed in the US and EU markets.

A unique feature of the Chinese market has been the influence of government policies on supply and production costs. Moreover, seasonal variations add a speculative component to prices. Still, within a given timeframe and a specific level of production costs, prices in the Chinese market tend to fluctuate within a relatively narrow range as moderate price changes tend to trigger significant shifts in supply.

The path of silicon prices over the next ten years will be influenced considerably, not only by that of the overall economy, but also by specific developments in the major end-use sectors. While the trend in production costs outside of China is influenced heavily by exchange rate movements, changes to Chinese costs are also being shaped by a steady

relocation of production towards lower-cost locations, principally Xinjiang, and this shift has moderated the increase in average production costs in China. The effect will diminish over time as Xinjiang accounts for a steadily larger share of the supply base. However, a combination of government measures and market forces will lead to the gradual consolidation of Chinese silicon production among a comparatively small number of companies. This concentration implies a likely departure from the traditional pattern of aggressive competition among suppliers that has tended to drive down prices in China towards the operating cost of the marginal supplier.

Regardless of what transpires, the long-term trend in international silicon prices will, to a considerable degree, still be determined by what happens to Chinese demand, supply and production costs. Under most scenarios, the country will not only account for a majority of the projected growth in total demand through to 2030, but China will also contribute a large share of incremental global silicon supply over this period.

Bulk Resistivity of SiC and Carbon Materials in the Silicon Furnace

H. Hoover[1)], T.A. Pedersen[1)], G. Sævarsdottir[2)], and M. Tangstad[1)]
1) NTNU, Department of Material Science and Engineering
2) Reykjavik University, Department of Engineering

Abstract

The amount of current that will pass through the charge material in the silicon furnace depends on the resistivity of the charge mix because the path will favor least resistance. Thus, this work seeks to examine the conductivity of various materials found in the silicon furnace, namely SiC and various carbon materials and isolate three main factors: carbon source, particle size, and type of SiC material. Charcoal is the least conductive carbon material, followed by char, then coal, and finally coke. The SiC material made from coal and char follows the same trend as the corresponding carbon materials, with the exception of deviations around 1200°C, likely due to volatiles. Compared to the carbon material from which it is made, the SiC material appears to be only slightly more conductive at high temperatures. SiC materials from different carbon sources, in this case from coal and char, appear to have conductive properties of the same magnitude, but the difference in resistivity between the two decreases with increasing temperature and their compositions are similar in range. Particle size does appear to affect the bulk resistivity of the SiC materials, although how it is affected is still disputable, as the results show conflict with previous findings.

Introduction

Silicon metal is produced by carbothermic reduction of quartz (SiO_2) in an electric arc furnace (EAF). The basic reaction is shown in Equation 1. However, this reaction is an overview and silicon dioxide is not reduced by solid carbon directly.

$$SiO_2(s) + C(s) = Si(l) + CO_2(g) \quad (1)$$

The process takes place in the EAF with three consumable carbon electrodes which supply electrical energy to the system.

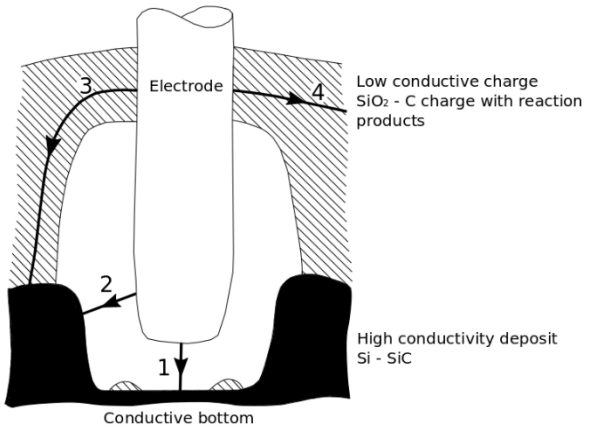


Figure 1: Diagram of possible current paths through an EAF, from (Schei, Tuset, & Tveit, 1998)

Based on the structure of the furnace, shown in Figure 1, there are four presumptive and logical paths the applied electric current may follow (Schei, Tuset, & Tveit, 1998). In the first path (1), the current travels via an electric arc from the electrode to the metal bottom that contains a liquid silicon and SiC-slurry, and slag. This path is believed to carry the majority of the current, given that all present components are conductive in nature. In the second path (2) the arc strikes the side wall, which is primarily made up of silicon carbide (SiC) (Tranell, Andersson, Ringdalen, Ostrovski, & Steinmo, 2010), with pores of liquid silicon, both of which will be good conductors. It is worth noting that the arcs in the furnace are small, they are unsustainable at lengths longer than about 10cm (Sævarsdottir & Bakken, 2010). However, typical electrode movement shows that the distance between the electrode tip and the liquid metal pool is greater than 10cm at many points in the process. Therefore, it stands to reason that there must be arcs striking the cavity walls in addition to the liquid metal pool, and thus there may be a significant portion of the current passing through the SiC crust in the second path. In the third path (3), the current is passing through the charge material, which will change both physically and chemically, depending on the position. However, as a general rule, SiO_2 is an insulator, but carbon and SiC materials are capable of conducting. The last path (4) is the electrode to electrode current via the charge material, which is believed to be very small, with some asymmetrical distribution of current between the electrodes (Gerritsen, Tracy, & Saber, 2015).

Some of the current will pass through the charge material (path 3), but how much depends on the resistivity of the charge mix because the path favors least resistance. Since there are several materials capable of conducting it is difficult to predict how they will behave mixed together and what path the current may take. Through measuring the bulk resistivity, or resistivity over an entire bed of particles, some inferences about the conductivity of the material can be drawn. Thus, this work seeks to examine the conductivity of SiC and various carbon materials. These materials have a lot of variability in the furnace and are more conductive compared to SiO_2, for example, so they are assumed to have to greatest effect on the conductivity of the bulk. There are many factors that affect the resistivity in the furnace; however, this work seeks to isolate three main factors: carbon source, particle size, and type of SiC material.

In 2014, Krokstad examined the resistivity of different materials found in the silicon furnace. As seen in Figure 2, the resistivity of silicon has the greatest sensitivity to temperature over the range of 0 to 1600°C, which is logical given its semi conductive nature. Meanwhile the conducting carbon materials and the SiC will also see changes in the resistivity, but they will be less dependent on temperature. Additionally, the impure SiC sample is at a lower resistivity than the intrinsic SiC, which confirms that the composition, such as the presence of impurities will change the resistivity (Krokstad, 2014).

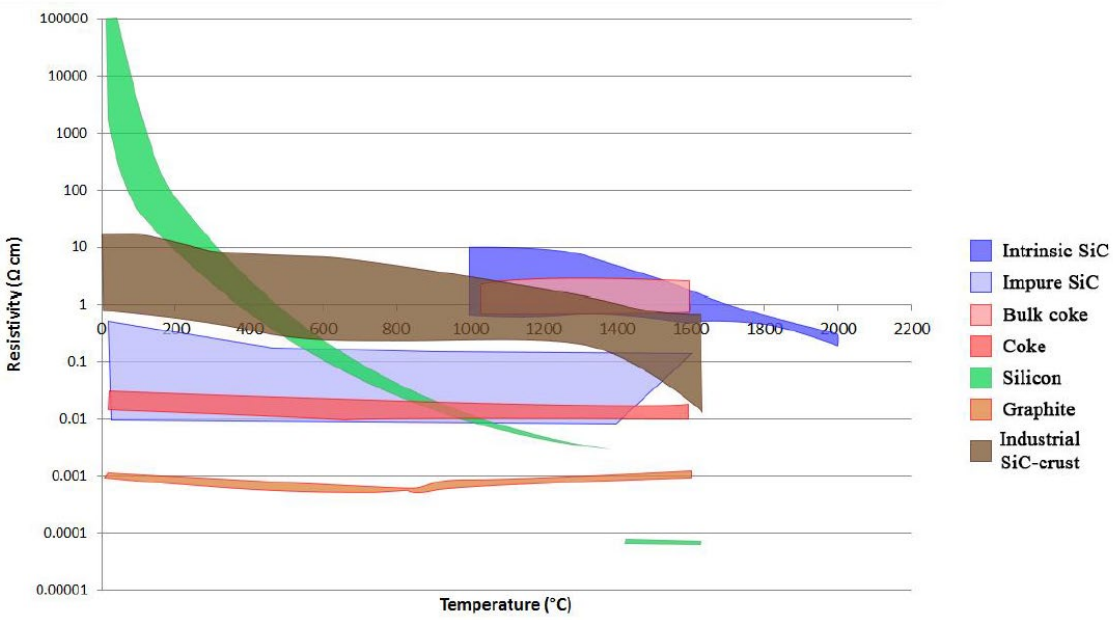


Figure 2: Resistivity variation with temperature of materials in the silicon furnace from (Krokstad, 2014)

While Krokstad's work provides a valuable baseline for the resistivity of the materials used in the silicon process, it is based on industrial α-SiC samples from excavations, accumulated in the Si furnace. The SiC material used in this work is β-SiC produced from various carbon materials produced in the lab. This will standardize experimental procedures while allowing for the freedom to manipulate variables such as the raw materials and the temperature.

Experimental Methodology

The experimental setup for bulk resistivity measurements is shown in Figure 3. Contained within the graphite crucible is an alumina crucible which acts to insulate and guide the current through the system. Molybdenum (Mo) wires are placed through the alumina crucible 10cm apart and the sample is loaded to cover both wires to measure the resistivity of the bulk. The main thermocouple, which controls when the voltage drop is measured, is placed through the top electrode and embedded in the center of the sample. An additional thermocouple is placed between the alumina crucible and the inside of the graphite crucible. This thermocouple controls the heating rate of the furnace to ensure the stability of the equipment. The weight, made from stainless steel, is insulated from the graphite top electrode, with the bottom of the graphite crucible acting as the bottom electrode. This can be seen in Figure 3.

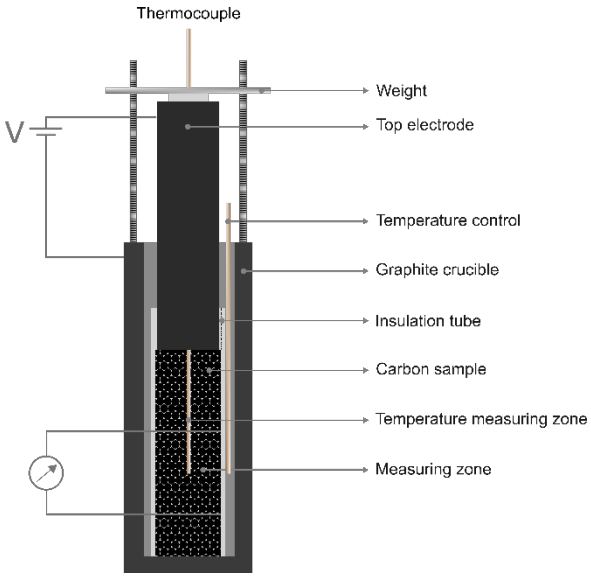


Figure 3: Drawing of experimental setup for bulk resistivity measurements

For the measurements of the carbon materials, coal and char were heat treated to 1200°C. From there, coal and char have been partly transformed to SiC. The chemical compositions of the various materials measured is shown in Table 1.

Table 1: Chemical composition and particle size of raw materials via XRD analysis

Experiment No.	Material	Particle Size (mm)	%C	%SiC
1	Charcoal A	4.5-9.5	77.0	-
2	Char A	4.5-9.5	83.2	-
3	HT Coal A	4.5-9.5	95.3	-
4	Russian Coke	4.5-9.5	87.7	-
5	SiC from Coal	4.5-10	78.9	13.7
6	SiC from Char	4.5-9.5	77.3	18.3

In order to run the experiment, current is applied in pulses every 25°C so the voltage drop between the two wires can be measured. Figure 4 shows an example of a typical pulse train at any given temperature with respect to time. Also shown on the graph by the dotted line is the 1 Volt threshold, under which the data is filtered out for calculations, because this is idle time where the current is negligible.

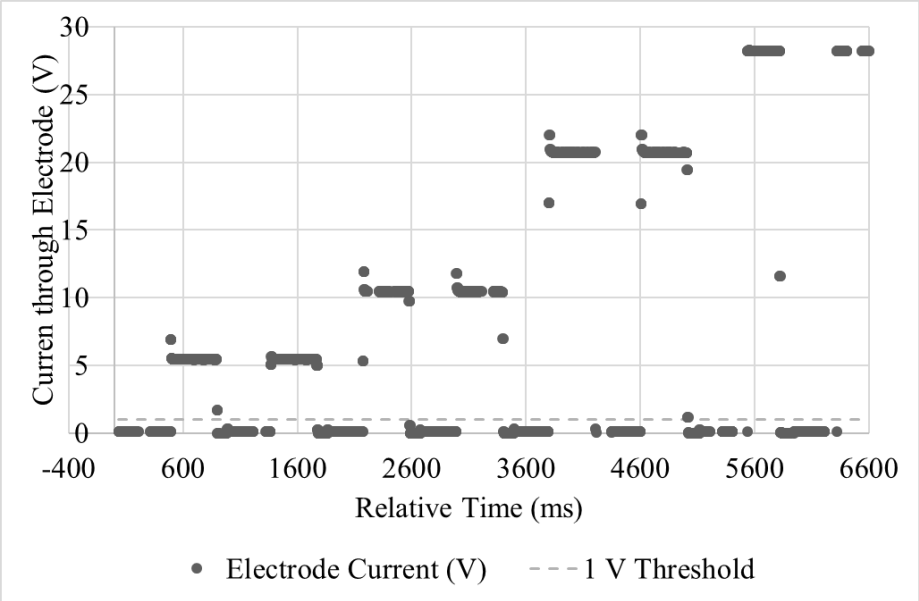


Figure 4: Typical pulse train showing the voltage over time and the 1V threshold for calculations

In simplest terms the method used for calculation of the bulk resistivity of the sample is the four-point method, as explained well by Eidem (2008). As current, I, is applied at each temperature (every 25°C), the voltage drop, V, is measured over the distance between the molybdenum wires, also known as the height of the bulk (h). From there the specific resistance, R, can be calculated via Ohm's law, which in turn allows for the calculation of bulk resistivity, ρ_{bulk}, over the given area via Equation 4. This progression is shown in Equations 2-4.

$$V = I \times R \tag{2}$$

$$R = \int \frac{\rho_{bulk}(h)}{A(h)} dh \tag{3}$$

$$\rho_{bulk} = \frac{V_{drop} \times A}{h \times I} \tag{4}$$

Results and Discussions

Bulk resistivity of carbon materials

The production of silicon relies heavily on the choice of carbon materials used in the furnace. The most commonly used carbon materials in industrial metal production are coal, charcoal, metallurgical coke, and petroleum coke. Within the (ferro)silicon industry, cokes are not widely used due to their low SiO reactivity (Tangstad, Beukes, Steenkamp, & Ringdalen, 2019). However, many studies have been conducted on various cokes (Eidem, 2008) and it is believed that the trends are analogous to what would occur in other carbon materials, therefore metallurgical coke is included in this work. Coal and charcoal are included because they are more typically used and because both show a normal to high SiO reactivity based on the SINTEF test (Myrhaug et al. 2004).

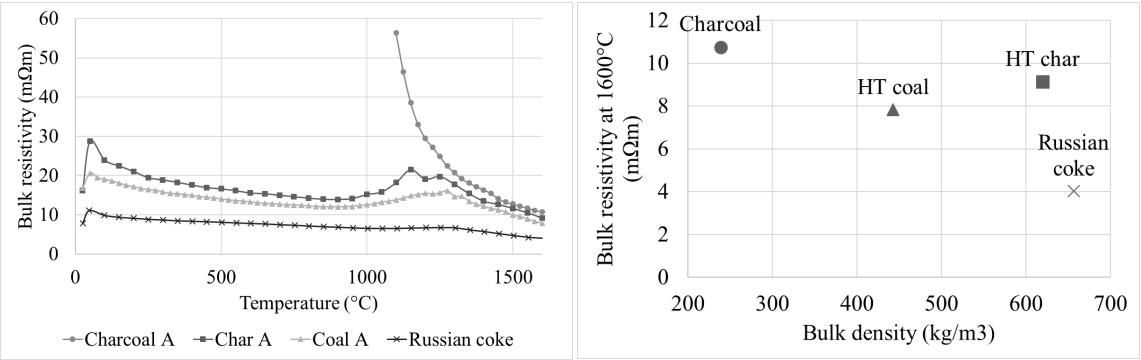


Figure 6: Bulk resistivity of carbon materials with increasing temperature (left) and bulk resistivity of carbon materials at 1600°C with increasing density (right)

Figure 6 shows the bulk resistivity of coal, char, charcoal, and Russian coke with respect to temperature. Immediately, it is noticeable that the charcoal behaves differently from all the other materials. It's resistivity below 1100°C is too high for the measurement software. However, it falls steeply in line with the others past this point. Since the charcoal is not heated treated beforehand like the coal and char, any lingering volatiles being driven off could be the cause of the deviation. Additionally, charcoal typically has 60-90% fixed-C on a dry weight basis compared to coal's 50-80% (Myrvågnes, 2008), so it might be surprising to see that is has a higher resistivity than coal. However, with this heat treatment the coal and char increase their carbon content.

Another factor affecting the resistivity may be the strength of the material. Fines are a significant problem in the use of charcoal for industrial processes, because fines decrease permeability and will block the flow of SiO gas (Myrvågnes, 2008). With regards to conductivity, the creation of fines will change the volume of the bulk as they will fill space between the unevenly sized particles and create additional points of contact. Materials with a lower strength will also have a better connection between the particles, and hence the contact resistance will decrease. Hence, neither of these arguments supports the charcoals higher resistivity.

Overall, the measurements show that charcoal is the least conductive, followed by char, then coal, and finally coke. This agrees with previous literature findings such as Eidem (2008). This is believed to be due to the various density of the materials. With a higher density the resistivity should decrease. The final bulk density and the bulk resistivity of all four carbon materials at 1600°C is shown in Figure 6 and it is seen that overall this seems to explain the resistivity of the charcoal and coke, while the char and coal show some deviation within the overall trend.

The relationship between SiC material and its carbon source

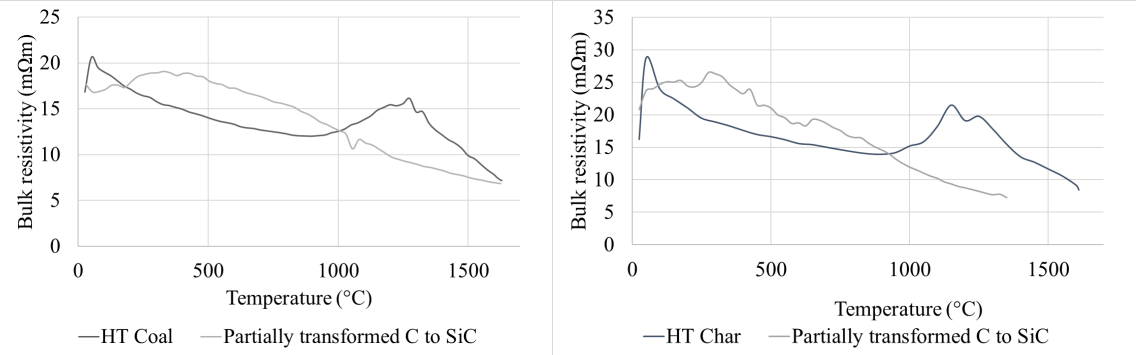


Figure 7: Bulk resistivity with respect to temperature of partially transformed coal and coal (left) and partially transformed char and char (right)

The bulk resistivity of the partially transformed coal material and the heat-treated coal is shown in Figure 7. According to the figure, the relationship between SiC and its carbon source shows a unique trend. Only after 1000°C does the SiC material become more conductive than the coal sample. Additionally, at the far end of the measurement range (1600°C) the samples are the same. As shown in Table 1, the SiC content in the sample is only 13.7%, with 78.9% carbon remaining. Therefore, it is not surprising that the bulk resistivity of the SiC sample is relatively close in range to the heat-treated coal. Furthermore, if we assume that the spike in resistivity of coal after 1200°C is due to volatiles, then it's possible the differences between the sample could be even smaller. This is supported by the apparent convergent of the samples after 1600°C.

The bulk resistivity of SiC made from char compared to the char itself is shown in Figure 7. Similar to the relationship between the SiC (from coal) and coal, the SiC is less conductive until around 950°C, where the resistivity of the materials converges. After that, the SiC material is more conductive for the remainder of the temperature range. Additionally, as can be seen in Table 1, the carbon content of the char and the SiC (from char) are even closer than with the coal-based run. The SiC has a carbon content of 77.3% and the char is 83.2%. Once again, volatiles may be responsible for the gap between the values, even though this begins to occur before 1200°C, not after, so this is unconfirmed. However, in the experimental run of the SiC, there was a thermocouple failure after 1350°C, so the measurements are not able to be compared past this temperature.

The low temperature zone of the industrial Si furnace is normally run in this temperature range. In this zone of the furnace, both the SiC material and the carbon material in the charge are of the same order of magnitude in terms of conductivity. Therefore, it appears that carbon materials with a high amount of volatiles will be less conductive. However, as the volatiles is released, the resistivity of the partly transformed carbon materials will not change with transformation, only with temperature.

The relationship between different types of SiC material

The bulk resistivity of SiC material made from coal and char are compared in Figure 8. Both sets of data confirm what is already expected, that the resistivity of the SiC material decreases with increasing temperature regardless of carbon raw material. However, there does appear to be some difference between the absolute values at "low" temperatures. At higher temperatures (around 1000°C and above) the differences in resistivity between the two samples become small. Additionally, the similarity in the results could be the result of the SiC content in each sample being close in value. The SiC material made from coal has 13.7% SiC and 78.9% carbon. Similarly, the SiC material from char has 18.3% SiC and 77.3% carbon. Given the similar end compositions, the starting carbon material may be of little relevance. Conversely, the SiC materials may not have enough SiC content to make a definitive conclusion, as the pattern agrees with the results of the carbon materials in Figure 6. The char has a higher resistivity than coal. However, this does not account for the change after 1100°C.

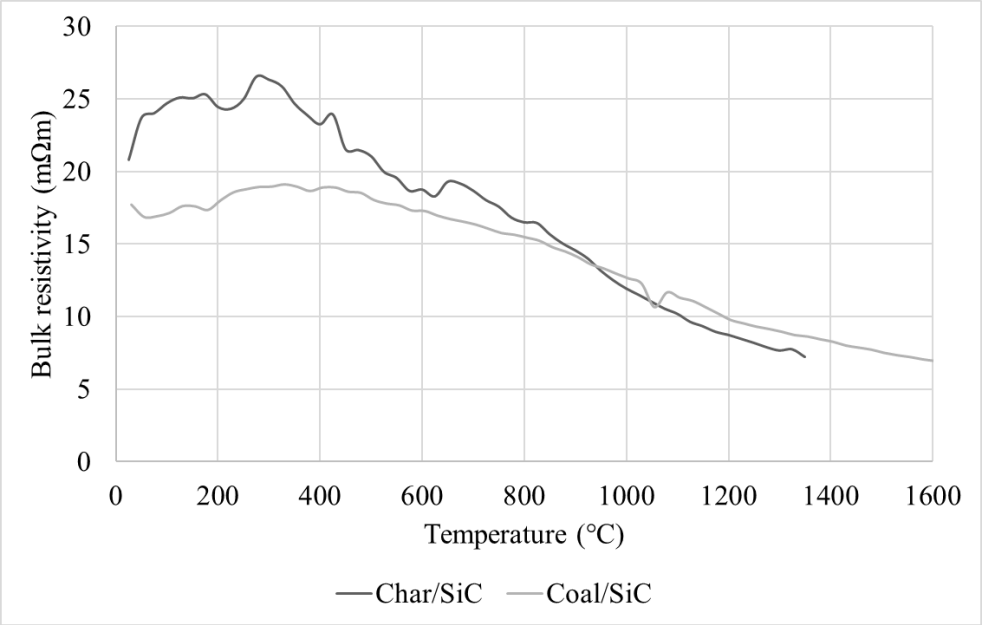


Figure 8: Bulk resistivity with respect to temperature of partially transformed SiC materials from coal and char

Particle size may affect the resistivity of the bulk in two ways: contact resistance and SiC-content (Eidem, 2008). When the size ranges are large, the particles are not able to be packed as tightly, leading to less areas of contact, which in turn would lower the overall effect of contact resistance on the bulk and presumably lower the resistivity. Figure 9 shows the comparison of SiC material made from coal at two different particle sizes. The smaller particle size of 4.5-10mm has a lower resistivity than the larger size of 10-16mm over the entire temperature range. The difference also appears to be getting larger at high temperatures. This conflicts with the expected results, as the larger size should have the lower resistivity according to Eidem (2008).

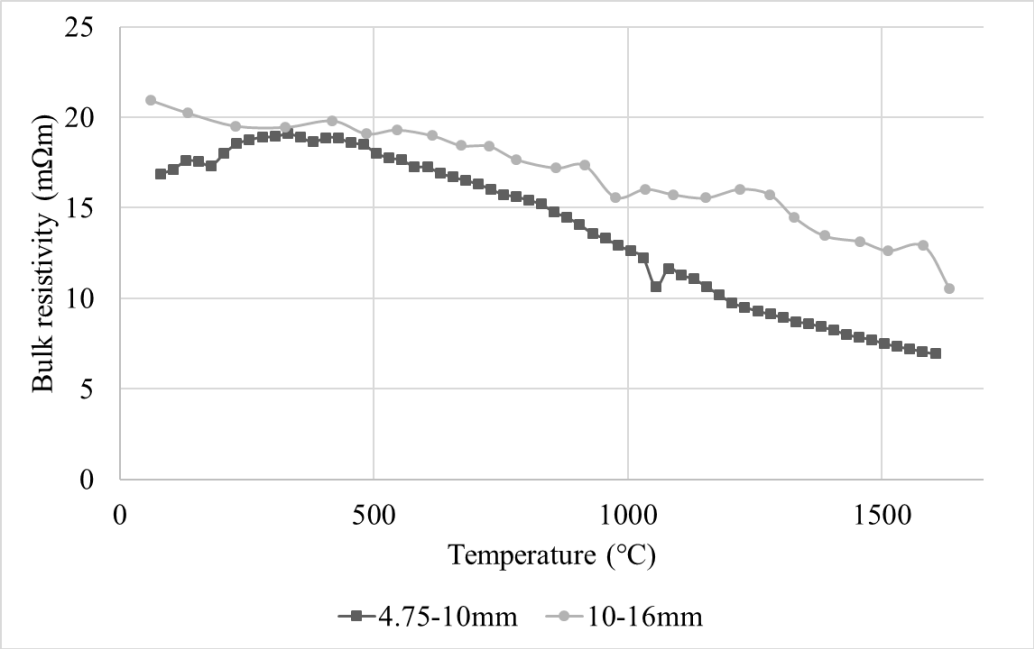


Figure 9: Bulk resistivity with respect to temperature for SiC material from coal with two different particle sizes

This depends on whether material resistivity or contact resistance is dominating the behavior of the bulk at any given temperature. One could argue that the fewer areas of resistance raise the resistivity as there are just simply less paths the current may travel due to less mechanical contact points. However, this idea is unproven, but will be confirmed or discarded after additional experimentation. It can also be argued that Eidem (2008) found that the smaller particles had different properties like composition and strength, than the larger particles. This could also be the case here, however this will be investigated.

Conclusions

The results show that charcoal is the least conductive carbon material, followed by char, then coal, and finally coke. The SiC material made from coal and char follows the same trend as the corresponding carbon materials with electrical resistivity decreasing with increasing temperature, except for deviations around 1200°C, likely due to volatiles.

Compared to the carbon material from which it is made, the SiC material appears to be only slightly more conductive at high temperatures, but both materials appear to reach the same resistivity as they approach temperatures above 1600°C. SiC materials from different carbon sources, in this case from coal and char, appear to have conductive properties of the same magnitude, but the difference in resistivity between the two decreases with increasing temperature and their compositions are similar in range. Particle size does appear to affect the bulk resistivity of the SiC materials, although how it is affected is still disputable, as the results shown conflict with previous findings.

Acknowledgements

This publication has been partly funded by the SFI Metal Production, (Centre for Research-based Innovation, 237738). The authors gratefully acknowledge the financial support from the Research Council of Norway and the partners of the SFI Metal Production.

References

Eidem, P. A. (2008). *Electrical Resisitivity of Coke Beds.* Faculty of Natural Sciences and Technology , Department of Material Science and Engineering. Trondheim: NTNU.

Gerritsen, T., Tracy, P., & Saber, F. (2015). Electrode Voltage Measurement in Electric Furnaces: Analysis of Error in Measurement and Calculation. *INFACON Energy efficiency and environmental friendliness are the future of the global Ferroalloy industry*, 338-348.

Krokstad, M. A. (2014). *Electric Resistivity in Industrial SiC-slag.* Institute of Material Technology, Department of Natural Sciences. Trondheim: NTNU.

Myrhaug, .., Tuset, J., & Tveit, H. (2004). Reaction Mechanisms of Charcoal and Coke inthe Silicon Process. *Tenth International Ferroalloys Congress*, (pp. 108-121). Cape Town.

Myrvågnes, V. (2008). *Analyses and Characterization of Fossil Carbonaceous Materials for Silicon Production.* Faculty of Natural Sciences and Technology, Department of Material Science and Engineering. Trondheim: NTNU.

Schei, A., Tuset, J. K., & Tveit, H. (1998). *Production of High Silicon Alloys.* Trondheim, Norway: Tapir Forlag.

Sævarsdottir, G., & Bakken, J. (2010). Current distribution in submerged arc furnaces for silicon metal/ferrosilicon production. *Ferrosilicon Smelting*, 717-728.

Tangstad, M., Beukes, J. P., Steenkamp, J., & Ringdalen, E. (2019). Coal-based reducing agents in ferroalloys and silicon production. In *New Trends in Coal Conversion* (pp. 405-435). Elsevier.

Tranell, G., Andersson, M., Ringdalen, E., Ostrovski, O., & Steinmo, J. (2010). Reaction zones in a FeSi75 furnace - results from an industrial excavation. *The Twelth International Ferroalloys Congress*, (pp. 709-715). Helsinki.

Silicon for the Chemical and Solar Industry XV
Trondheim, Norway, June 15 – 18, 2020

Particulate matter and related airborne emissions from silicon and ferrosilicon production

Ida Teresia Kero [1)], Svend Gråbahl[1)], and Gabriella Tranell[2)]
1) Sintef Industry, Alfred Getz vei 2, NO-7465 Trondheim, Norway
2) Norwegian University of Science and Technology, Alfred Getz vei 2, NO-7491, Trondheim, Norway

Abstract

The management of airborne particulate matter (PM) emissions from silicon and ferrosilicon production is, in many ways, similar to the management of airborne PM emissions from other pyrometallurgical industries. Certain challenges are, however, highly branch specific. For example, the simultaneous production of silica dust and NO_X gas in the submerged arc furnace, especially in the furnace hood above the charge surface. The SiO reaction into SiO_2 is a highly exothermic reaction which promotes thermal NO_X production and may occur above the charge surface or in the tap-hole. Localized temperature control can only be achieved by limiting the extent of silica fume production through SiO(g) combustion. Hence, any SiO reducing measures will also be beneficial in terms of reducing NO_X emissions.
This conference article is an excerpt from the literature review article Airborne Emissions from Si/FeSi Production published in Journal of Metals (JOM) in 2017.

Introduction

The management of airborne particulate matter (PM, also known as dust) emissions from the production of metallurgical grade silicon (MG-Si) and ferrosilicon (FeSi) is, in many ways, similar to the management of airborne emissions from other metallurgical industries, such as other smelters, foundries and electrochemical metal production. Nonetheless, certain challenges are specific for the silicon alloy industry, such as the specific dust types generated and the management of NO_X emissions by furnace design and operation.

Airborne PM, originating from various sources in the metallurgical industry are a concern in terms of working environment and potential adverse health effects. The PM is also an important constituent in the diffuse emissions escaping the plants and may affect the air quality of the local, urban communities as well as the environment at large.

The PM produced in most metallurgical processes may be harmful if inhaled and exposure to high levels of particles has been linked to cancer, pneumonia, chronic obstructive pulmonary disease (COPD) and other respiratory and cardiovascular syndromes [1-8].

The SAF produces the largest amounts of PM, through combustion of escaping SiO gas from the furnace hot zone to SiO_2 above the charge surface. A typical metal yield of between 80-90% means that up to 10-20% of incoming Si-units in the furnace escape as fumed silica. [9-11]. However, furnace dust is efficiently collected from modern furnaces and therefore it does not normally contribute to the more problematic diffuse PM emission. Hence, PM management is an important issue from health and environmental perspectives but it is also an economic consideration in this industry, since the condensed silica fume may be sold as a valuable product (microsilica) if it can be collected and its quality guaranteed.

In addition, nitrogen oxide gas (NO and NO_2; often referred to as NO_X) will be generated at the furnace top, the tap-hole and in refining and casting operations where liquid Si is exposed to air. Nitrogen oxides are important emissions due to their role in the atmospheric reactions creating fine particles and may also contribute to acid rain. The focus of this article is the airborne PM and NO_X emissions from high silicon alloy production. Considering the simultaneous production of thermally generated silica PM and nitrogen oxide gas, this paper will discuss process understanding and the furnace operation which governs them both.

Silicon production and emissions

The submerged arc furnace (SAF) is the core process for MG-Si and FeSi production. Figure 1 schematically illustrates the production process steps and emission sources.

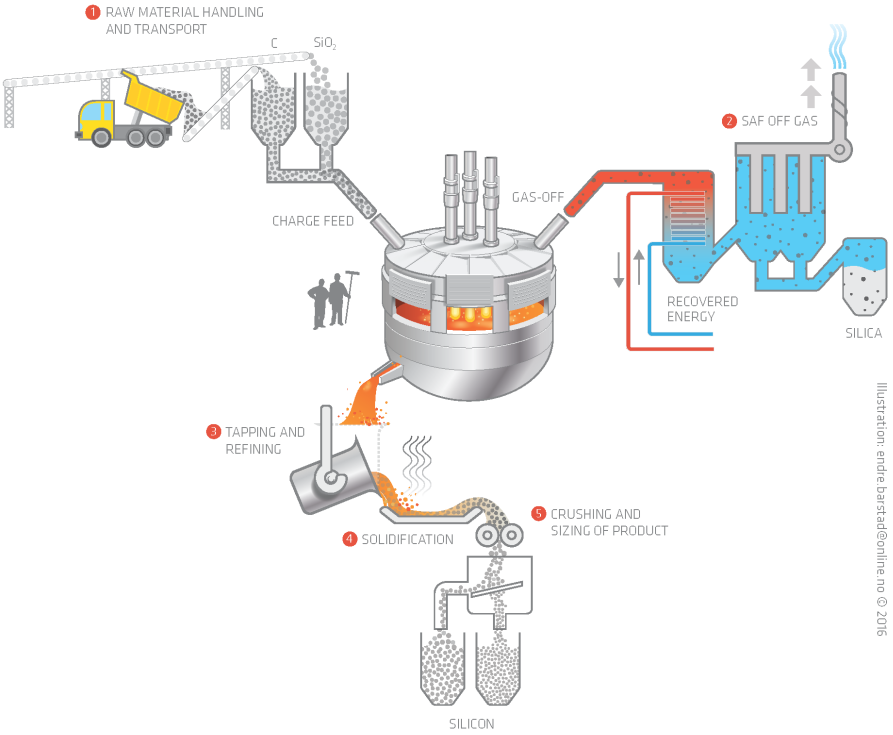


Figure 1: High silicon alloy production process and its primary emission sources. The figure is reproduced after an original by Schei et al.

The primary raw material for silicon production is quartz. In addition, iron ore pellets or scrap iron are included in the raw material mix to produce ferrosilicon. The raw materials and reductants are crushed and weighed before they are charged to the furnace. In the production of both MG-Si and FeSi alloys, the carbonaceous reductants are usually coal and coke, but bio-carbon (charcoal and wood chips) is also commonly used as primary or secondary carbon sources. The MG-Si or FeSi product is hereafter simply referred to as the silicon alloy. The raw silicon alloy is tapped from the furnace and refined in a slag process before it is cast in moulds for cooling. The solidified product is also crushed, sized, weighed and packed at the plant before it is sent to the customer.

The most commonly considered emission types, emission points and their origin, as discussed in the review article [12, 13], are listed in Table I.

Table 1: Emission types and their origins in the plant

Type	*Origin*	*Emission Point*
CO_2 and other GHG	Reductants	SAF
NO_X	Combustion	SAF, Tapping
SO_2	Reductants	SAF
Dioxin*	Reductants	SAF
PAH	Electrodes, Carbon Paste	SAF, Tapping
Heavy metals	All raw materials	SAF, Tapping, Refining
Mechanically formed PM	Solid material handling	Conveyor belts, mills, sieves, etc.
Thermally formed PM	Liquid alloy in contact with air	Tapping, refining, casting

*Levels from modern, semi-open furnaces are typically too low to be measured

Particulate matter: generation and characteristics

Almost all processes involved in silicon and high-silicon alloy production produces PM in some form. In this article, the terms particulate matter and dust are used as synonyms and primarily used for solid particles. The term aerosol includes both liquid and solid particles and the term fume relates to thermally generated aerosols.

While most gases are generated in the furnace itself, dust is generated in almost every step of the silicon production process. The transport and handling of raw materials, reductants and products at ambient conditions generates particulate matter (PM) through mechanical impact. These dust types are relatively coarse and their physical and chemical properties resemble those of the bulk material from which it formed.

Hot processes on the other hand, such as tapping, refining and casting, where liquid alloy comes into contact with air are sources of thermally generated PM. This dust is often referred to as fume and primarily consists of amorphous silica. Most of the hot processes are equipped with ventilation systems of various kinds. The collected off gases are typically transported through a system of filters and, in some plants, heat exchangers. The thermally generated PM collected in the filters, commercially termed “Microsilica” is often sold to be used as concrete filling material and a variety of other applications. Table II provides an overview of the PM sources and a rough estimate of their relative importance to indoor air PM concentration and to PM emissions out of the plant [14, 15].

Table 2: Estimated relative importance of dust sources in silicon smelters [14]

Actvity	*Share of emissions to outer environment (%)*	*Share of indoor air pollution (%)*
Raw material transport pre-storage	0-5	0
Raw material handling post-storage	0-5	5-10
Semi-closed furnace process	10-20	5-20
Tapping	20-40	30-50
Casting and liquid alloy handling	20-40	15-25
Solid alloy product handling	5-15	5-15
Microsilica packing and handling	0-5	5-15
Off gas system	5-10	0-5

It is clear from table 2 that the major sources of PM, both inside the plant and escaping the plant are those which involve the liquid alloy. Tapping, refining, casting and other operations where high-temperature liquid alloy is in contact with air produces a silica fume which has many similarities to the Microsilica [14, 16-21]. The dust which occurs during handling and transport of solid materials, such as the product and the raw materials, is fundamentally different from the thermally generated dust. The mechanically generated PM is typically coarser particles with physical and chemical properties similar to those of the material from which it was generated. Raw material handling and transport can, for example, produce airborne crystalline alpha-quartz which is a health hazard in its own right.

Figure 2 shows an SEM picture and a particle size distribution (obtained by Electrical Low Pressure Impactor, ELPI) for thermally generated fume particles from ferrosilicon tapping. The PM in the silicon alloy industry includes both fine (FP) and ultrafine particles (UFP), i.e. particles with aerodynamic diameters of < 2.5 μm and < 0.1 μm, respectively. UFP's represent a special case of particulate matter as the large surface area implies high reactivity and different physico-chemical properties than the larger particles [22-24]. Current administrative norms as well as other limits are established in mass concentration but UFPs give little contribution to the mass concentration [19, 20, 25].

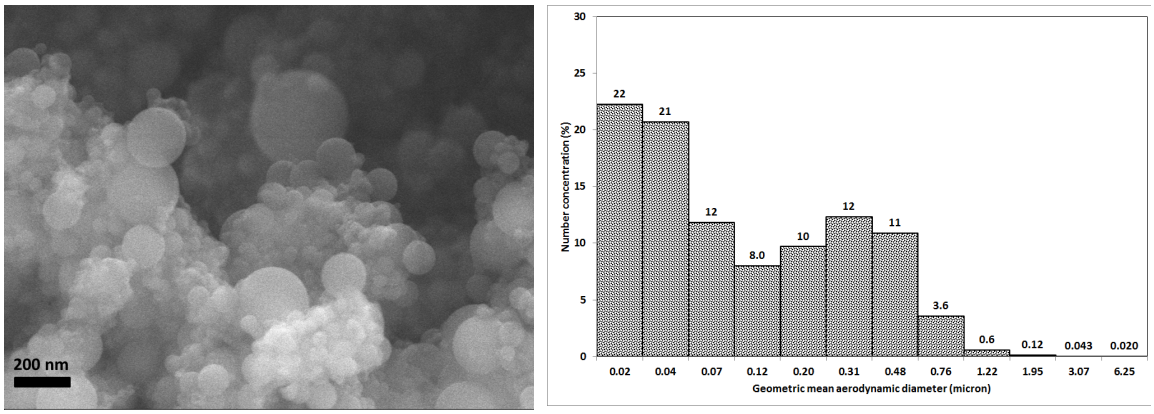


Figure 2: Fume from FeSi furnace tapping area. A) Scanning electron micrograph of the fume particles. B) Particle size distribution as measured by an electrical low pressure impactor. (Reproduced with permission from Kero et al. [20])

PM formation through active oxidation

Naess et al. [16, 26] studied the process by which the thermally generated silica PM forms in post-taphole operations and concluded that the main formation mechanism is the active oxidation of the liquid silicon alloy while a small fraction (< 1%) of dust particles would form by splashing (droplet expulsion) [21]. The active oxidation was found to occur in two steps where the silicon would first react with oxygen to form SiO gas on the liquid alloy surface. The SiO gas would then oxidize further to SiO_2 which ultimately condensates to form the dust particles [21, 27-29]. The kinetics of this process was found to be governed by oxygen diffusion through the boundary layer near the alloy surface. During oxidative ladle refining of MG-Si, the rate of fume formation was found to be particularly highly dependent on the large and dynamically moving alloy surface exposed to air [16, 30, 31]. Depending on the refining gas flowrate, typical PM amounts were between 0.8 – 1.7 kg SiO_2 per ton Si produced.

Heavy metals in the PM and flue gas

The concentrations of heavy metals and other trace elements in the PM and the flue gases has also been studied by Næss et al. [17, 18] At process temperatures of 1600°C or higher, certain metals such as Zn, Pb, Cd, Na, Mn and Fe go into the gas phase and may escape as metal vapour. When the off-gas temperature drops, the metal vapours are condensed and therefore often collected with the dust. Myrhaug and Tveit [11, 32] showed that a boiling point model can be used to predict whether an element is most likely to escape the SAF as gas, condensed silica fume or remain in the tapped metal. Næss et al. [18] showed that the boiling point model is applicable also to the fume of the oxygen-blown refining ladle, with some modifications due to the oxidation of elements.

Requirements for heavy metal emission control from silicon and ferrosilicon production are typically less stringent than for other ferroalloys, such as the Mn-, Ni- and Cr- based ferroalloys. The European, U.S. and other partners to the United Nations Environment

Program (UNEP) have put special emphasis on lead, cadmium and mercury [33] but chromium and arsenic are also included in the Norwegian legislation for emission control. Mercury is something of a special case among the airborne heavy metal emissions as international legislation has long been stringent with respect to Hg emissions [34]. In silicon alloy plants, the particulate control devices (e.g., fabric filter or wet scrubber) capture most of the mercury in particulate and oxidized forms. Emission estimations to air through the filter systems must cover both gaseous and particle-bound heavy metals. A major challenge in the estimation of heavy metal emissions is their low concentrations in the material flows. Some plants evaluate their heavy metal emissions by use of aggregated collection samples from the filter systems. Others still use emission factors for particle-bound emissions. Emission factors are generally based on the contents measured in the condensed silica fumes from the SAF. However, the concentrations of heavy metals in the dust generated in other operations can be quite different from the furnace fume and is generally assumed to have lower heavy metal contents. [17, 18]

NO_X: formation and management

Figure 3 illustrates the temperature dynamics of the three main NO_X formation mechanisms compared to typical process and operation temperatures for silicon alloy production. The fuel and thermal formation mechanisms are the dominant mechanisms in electric arc furnaces producing MG-Si and FeSi. Fuel NO_X is formed by oxidation of the nitrogen components present in the solid raw materials while thermal NO_X is formed by direct oxidation of nitrogen (from the air) at temperatures above 1400ºC. Such temperatures are frequently observed in the furnace hood [14, 37, 38].

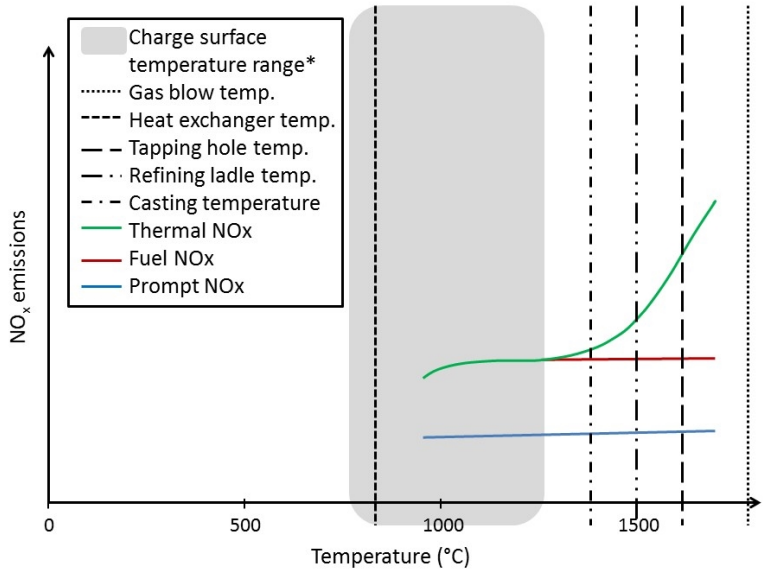


Figure 3: Temperature dependence of NO_X formation mechanisms compared to process temperatures in Si production. (Adaptation of original figure by DeNevers [39]) from FeSi furnace

Emission of NO_X always reports as NO_2, because NO is unstable and will react to NO_2. Measurements of PM and NO_X above the furnace charge and in the offgas show strong correlations. The SiO reaction into SiO_2 is a highly exothermic reaction and the combustion of gaseous SiO above the charge surface and in the tap-hole may increase the temperature, very locally. In these local high temperature zones, thermal NO_X production is promoted [14, 40]. The amount of SiO(g) released from the charge will therefore also influence NO_X formation and any SiO reducing measures will also be beneficial in terms of reducing NO_X emissions. The Norwegian Ferroalloy Association (FFF), SINTEF and the Norwegian University of Science and Technology (NTNU) have worked together on NO_X reducing strategies for nearly 20 years. The collaboration and joint efforts have resulted in many industrial initiatives and investments which have given positive NO_X reduction results. [38, 41, 42]. While some of this work is available through international journal and conference publications, a significant part of the results and achievements remain unpublished. We have been fortunate enough to obtain the permission from authors and industrial partners to include brief summaries of some of the major, unpublished findings and conclusions in this field.

Research initiatives have both focused on waste gas dynamics in general [43] and NO_X emissions in particular [44]. Efforts to understand the NO_X formation have shown that furnace design and furnace operating procedures, such as stoking and charging, heavily influence NO_X emissions [45-51]. Reported NO_X emission values vary greatly with typical values ranging from 500 to 1500 ton per site and year [52]. The NO_X production is inversely proportional to the silicon yield (low Si yield, high SiO losses), at least up to a certain level of silica fume formation. NO_X also forms during tapping, when an oxygen lance is used to open up the tapping channel to increase the metal flow out of the furnace [14, 53, 54]. The general correlation between SiO and NO_X emissions is illustrated in Figure 4.

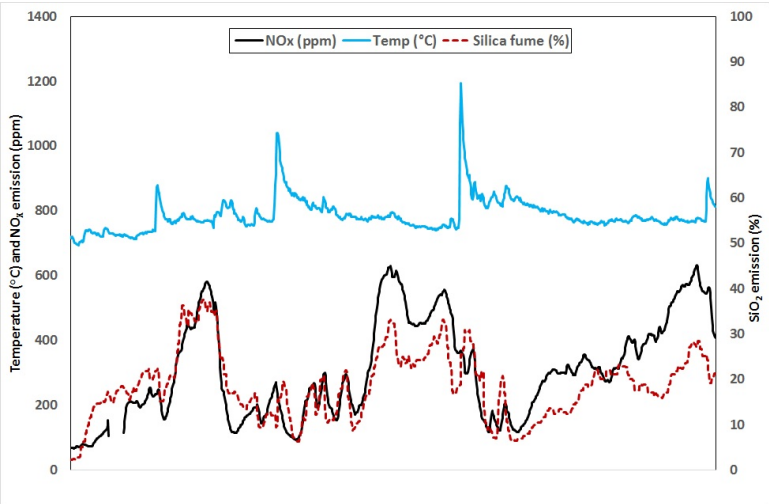


Figure 4: Correlation between furnace emissions of NO_X gas and SiO_2 fume with simultaneous temperature measurements. (Reproduced with permission from Grådahl et al. [37])

Slizovsky et al. [55] and Brede [56] have suggested a correlation between the NO_X formation and the moisture content of the furnace gas. Moisture is introduced through the raw materials and hence, will vary throughout the materials charging cycle. It is well-documented that the injection of water vapor into a combustion engine reduces the NO_X emissions. The steam increases the heat capacity (CP) of the off gas so that the temperature cannot exceed the limit for thermal NO_X production [57-59]. Although not validated, it is likely that this effect, in part at least, explains the observations made in the high silicon alloy production [38, 55, 56].

The effect of the furnace hood design and the inlet for false air on the NO_X emission has been thoroughly studied and modelled by Kamfjord [14] and others [60-62] but most of this work is not published. The main conclusions from the unpublished reports are that the amount of air and its flow path throughout the hood determines when, where and whether oxygen and nitrogen are mixed for sufficiently long time in a sufficiently hot zone to produce NO_X. Optimization of furnace hood designs is very complex, and the trial-and-error approach is both time- and cost consuming. Therefore, modelling capabilities are extremely valuable. Panjwani and Olsen [63] and Ravary et al. [64-68], have developed a modelling concept for predicting turbulent flows, heat transfer, combustion and NO_X formation in the furnace hood of a typical submerged arc furnace where silicon or ferrosilicon is produced. Their current concept is not sufficiently accurate to estimate the true NO_X emissions, but it predicts whether the NO_X emissions increases or decreases when changes are made in hood design or process operations.

The reduction of nitrous gas emissions is often divided into primary and secondary strategies. Secondary strategies include chemical reduction treatments for the flue gas from the furnace, such as selective reduction with ammonia (NH_3) or urea ($CO(NH_2)_2$) [69]. Primary strategies include modifications to the furnace operation, process management and/or the furnace system itself [70-72]. For silicon and ferrosilicon production, this translates into the following concrete actions [53, 73]:

- Reducing the combustion temperature through active cooling of the primary flame zone.
- Avoiding the "blowing" of SiO rich gas up through the charge surface.
- Frequent stoking and semi-continuous charging. Grådahl et al. [37] found that it was possible to reduce NO_X emissions from poorly operated furnaces by 50% if best practices were implemented.
- Recycling the flue gas to reduce excess air above the charge.

Polycyclic aromatic hydrocarbons, PAH

In the management of NO_X, close control of the flue gas temperature is paramount. It is, however, complicated by a kind of trade-off situation with respect to polycyclic aromatic hydrocarbons (PAH). Some PAH compounds are linked to cancer in humans and/or animals. The lighter compounds, with few aromatic rings, are gaseous at room temperature whereas the larger molecular compounds are liquid or solid and commonly occur in or on particles, for example soot.

PAH in the high silicon alloy production is formed through the combustion of reductants in the furnace and the baking of electrodes [74-79]. The formation of PAH is linked to soot formation which in turn is influenced by furnace design and operation and may vary greatly throughout the charging cycle [73]. PAHs are organic compounds that are destroyed in complete combustion and consequently, the semi-closed modern furnace types tend to have very low levels. These low levels are, in themselves, challenging with respect to measurements. Variation and uncertainty are often very high in PAH analysis and particularly so when concentrations are low. There are many additional reasons why PAH sampling and analysis is challenging. Firstly, there are numerous PAH components, so it is virtually impossible to measure them all. Norwegian authorities require measurements of the EPA-16 selection of PAH's while the European BAT documents focus on Benzo(a)pyrene. Secondly, the PAH's form and decompose in a dynamic manner so the concentrations are not constant. Thirdly, the boiling points of the PAH's vary greatly and therefore, PAH's can occur as gases, droplets or particles in an off-gas system and change between these states with temperature and other conditions.

Some industrial trials suggest that PAH emissions from ferrosilicon furnaces can be reduced if off gas temperatures are increased [37], as illustrated in Figure 5. The reference case (A) represents a traditional open furnace with batch charging. The second case (B) is a more enclosed furnace, equipped with feeding tubes through which the raw materials are fed in a semi-continuous manner (every minute). Case (C) represents the semi-closed furnace with average off gas temperatures raised from an average of 635°C to 812°C, by reducing the off-gas amount. The increased temperature leads to destruction of PAH and other organics but may also increase the formation of thermal NO_X.

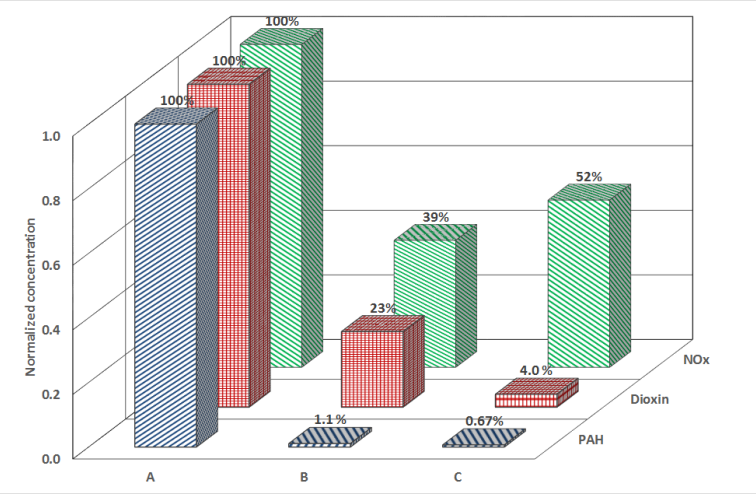


Figure 5: Off gas emissions of PAH, dioxin and NOx for A) a batch-fed, open SAF, B) a semi-closed SAF with semi-continuous charging and C) a semi-closed SAF with semi-continuous charging and off-gas temperatures > 800°C. (Reproduced with permission from Grådahl et al.[37]).

Conclusions

Measurements show strong correlations between PM and NO_X formation above the furnace charge. The SiO reaction into SiO_2 is a highly exothermic reaction which promotes thermal NO_X production and may occur above the charge surface or in the tap-hole. Localized temperature control can only be achieved by limiting the extent of silica fume production through SiO(g) combustion. Hence, any SiO reducing measures will also be beneficial in terms of reducing NO_X emissions.

The furnace design, flue gas management and furnace operating procedures, such as stoking and charging, influence NO_X emissions. Close flue gas temperature control is important for several reasons. One reason is that there may be a trade-off between PAH and NO_X management. PAH are destroyed at high temperatures and PAH emissions can be significantly reduced when off gas temperatures are kept above 800°C. PAH and heavy metals are simultaneously present as gases and particulate forms, and their distribution is highly temperature dependent. Their concentrations in the PM are very low which makes measurements extra challenging.

Acknowledgements

This article was enabled through funding from the Research Council of Norway through the center for research-driven innovation (SFI) Metal Production. The authors wish to thank Jens Christian Fjelldal, Dr. Edin Myrhaug and Dr. Nils Eivind Kamfjord at Elkem AS for comments and discussions.

References

1. Johnsen, H.L., *Lung Function, Respiratory Symptoms, and Occupational Exposure*, in Fakultetsdivisjon Akershus universitetssykehus. 2009, University of Oslo: Oslo.

2. Johnsen, H.L., et al., *Quantitative and Qualitative Assessment of Exposure among Employees in Norwegian Smelters*. Annals of Occupational Hygiene, 2008. **52**(7): p. 623-633.

3. Johnsen, H.L., et al., *Production of silicon alloys is associated with respiratory symptoms among employees in Norwegian smelters*. International Archives of Occupational and Environmental Health, 2008. **81**(4): p. 451-459.

4. Hobbesland, Å., H. Kjuus, and D.S. Thelle, *Mortality from nonmalignant respiratory diseases among male workers in Norwegian ferroalloy plants*. Scandinavian Journal of Work, Environment and Health, 1997. **23**(5): p. 342-350.

5. Hobbesland, Å., H. Kjuus, and D.S. Thelle, *Mortality from cardiovascular diseases and sudden death in ferroalloy plants*. Scandinavian Journal of Work, Environment and Health, 1997. 23(5): p. 334-341.

6. Søyseth, V., et al., *Incidence of airflow limitation among employees in Norwegian smelters*. American journal of industrial medicine, 2011. **54**(9): p. 707-713.

7. Søyseth, V., et al., *Prevalence of airflow limitation among employees in Norwegian smelters: a longitudinal study*. Occupational and environmental medicine, 2011. 68(1): p. 24-29.

8. Søyseth, V., H.L. Johnsen, and J. Kongerud, *Respiratory hazards of metal smelting*. Current Opinion in Pulmonary Medicine, 2013. **19**(2): p. 158-162.

9. Dingsøyr, E., M. Dåstøl, and W.C. Wedberg, *Particle size and particle size distribution of Elkem Microsilica and its relevance to technical application*, in The 5. European Symposium Particle Characterization. 1992: Nurnberg, Germany.
10. Kolderup, H., *Particle size distribution of fumes formed by ferrosilicon production*. Journal of the Air Pollution Control Association, 1977. 27(2): p. 127-130.
11. Myrhaug, E.H. and H. Tveit, *Material balances of trace elements in the ferrosilicon and silicon processes*, in 58th Electric Furnace Conference and 17th Process Technology Conference Proceedings. 2000, Iron & Steel Society: Warrendale, PA, USA. p. 591-604.
12. Kero, I., S. Grådahl, and G. Tranell, *Erratum to: Airborne Emissions from Si/FeSi Production*. Journal of Metals (JOM), 2017. **69**(2): p. 409.
13. Kero, I.T., S. Grådahl, and G. Tranell, *Airborne emissions from Si/FeSi production*. Journal of Metals (JOM), 2017. **69**(2): p. 365-380.
14. Kamfjord, N.E., *Mass and Energy Balances of the Silicon Process - Improved Emission Standards*, in Materials Science and Engineering. 2012, The Norwegian University of Science and Technology: Trondheim, Norway.
15. Best Available Techniques (BAT) Reference Document for the Non-Ferrous Metals Industries. 2014, Integrated Pollution Prevention and Control (IPPC).
16. Naess, M.K., *Mechanisms and kinetics of liquid silicon oxidation*, in Materials science and engineering. 2013, Norwegian University of Science and Technology: Trondheim, Norway.
17. Naess, M.K., I. Kero, and G. Tranell, *A new method for estimation of emissions and sources of measurements error in the silicon refining process*. JOM, 2013. **65**(8): p. 997-1006.
18. Naess, M.K., et al., *Element distribution in silicon refining – Thermodynamic model and industrial measurements*. JOM, 2014. **66**(11): p. 2343-2354.
19. Kero, I., M. Naess, and G. Tranell. *Fume characterization in the ferroalloy industry*. in INFACON XIII. 2013. Almaty, Kazakhstan.
20. Kero, I., M. Naess, and G. Tranell, *Particle size distributions of particulate emissions from the ferroalloy industry evaluated by electrical low pressure impactor (ELPI)*. Journal of Occupational and Environmental Hygiene, 2015. **12**(1): p. 37-44.
21. Naess, M.K., et al., *Mechanisms and kinetics of liquid silicon oxidation during industrial refining*. Oxidation of metals, 2012. **78**(3): p. 239-251.
22. Li, N., et al., *Ultrafine particulate pollutants induce oxidative stress and mitochondrial damage*. Environmental Health Perspectives, 2003. **111**(4): p. 455.
23. Monteiller, C., et al., *The pro-inflammatory effects of low-toxicity low-solubility particles, nanoparticles and fine particles, on epithelial cells in vitro: the role of surface area*. Occupational and Environmental Medicine, 2007. **54**: p. 609-615.
24. Vincent, J.H. and C.F. Clement, *Ultrafine particles in workplace atmospheres*. Philosophical Transactions: Mathematical, Physical and Engineering Sciences, 2000. **358**(1775): p. 2673-2682.
25. Kero, I.T. and R.B. Jørgensen, *Comparison of Three Realtime Measurement Methods for Airborne Ultrafine Particles in the Silicon Alloy Industry*. International Journal of Environmental Research and Public Health, 2016. **13**(9): p. 871-885.
26. Næss, M., et al., *Parameters Affecting the Rate and Product of Liquid Silicon Oxidation*. Oxidation of metals, 2014. **82**(5): p. 395-413.
27. Naess, M.K., G.M. Tranell, and N.E. Kamfjord. *Fugitive emissions related to oxidation of liquid silicon during ladle refining*. in 2nd International Symposium on High-Temperature Metallurgical Processing, TMS Annual Meeting & Exhibition. 2011. San Diego, CA, USA.
28. Naess, M.K., et al., *Active Oxidation of Liquid Silicon: Experimental Investigation of Kinetics*. Oxidation of metals, 2012. **78**(5-6): p. 363-376.
29. Naess, M.K., et al. *Experimental study of rate of silica fume formation from active oxidation of liquid silicon*. in INFACON XIII. 2013. Almaty, Kazakhstan.
30. Olsen, J.E., M. Næss, and G. Tranell, *CFD modeling of silica fume formation during refining of silicon metal*, in 8th International Conference on CFD in Oil & Gas - Metallurgical and Process Industries 2011: SINTEF/NTNU, Trondheim, Norway.
31. Olsen, J.E., M.K. Næss, and G. Tranell, *Understanding Fuming During Metal Refining by CFD*, in TMS Annual Meeting. 2012: Orlando, Florida, USA.

32. Tveit, H. and E. Myrhaug. *Important sub-processes in the silicon process. The behavior of trace elements*. in Silicon for the chemical industry, 5th, Tromsø, Norway. 2000. Tromsø, Norway: The Norwegian University of Science and Technology.
33. Aarhus Protocol on Heavy Metals Emissions - UNECE Convention on Long-range Transboundary Air Pollution. 1998, The United Nations Economic Commission for Europe (UNECE): Aarhus, Denmark.
34. Minamata Convention on Mercury, I.N. Committee, Editor. 2013, United Nations Environment Programme (UNEP): Geneva, Switzerland.
35. Haaland, D., M. Bruno, and T. Thomassen. *Mercury Removal from Off-gases at Tinfos Manganese Plante, Øye Smelteverk, Norway*. in INFACON IX - The Ninth International Ferroalloys Congress. 2001. Quebec, Canada: The Ferroalloys Association, Washington, USA.
36. Reference Document on Best Available Techniques in the Non Ferrous Metals Industries. 2001, Integrated Pollution Prevention and Control (IPPC).
37. Grådahl, S., et al. *Reduction of Emissions from Ferroalloy furnaces*. in INFACON XI. 2007. New Delhi, India: MacMillan.
38. Myrhaug, E.H., et al. *NOx Emissions from Silicon Production*. in Silicon for the Chemical and Solar Industry XI. 2012. Bergen-Ulvik, Norway: Fagtrykk AS/ The Norwegian University of Science and Technology.
39. De Nevers, N., Air pollution control engineering. 2010: Waveland Press.
40. Kamfjord, N.E., et al. *Mechanisms of NO Formation during SiO Combustion*. in 3rd International Symposium on High-Temperature Metallurgical Processing. 2012. Orlando, FL, USA: Wiley Online Library; John Wiley & Sons, Inc., Hoboken, NJ, USA.
41. Nikolaisen, P.I., *Slik kuttet Elkem utslipp tilsvarende 150.000 dieselbiler på rekordtid*, in Teknisk Ukeblad. 2014, Teknisk Ukeblad Media AS: Oslo, Norway.
42. Tveit, H. and B. Wittgens, *Grønnere Metallproduksjon*, in Dagens Næringsliv. 2014, Dagens Næringsliv AS: Oslo, Norway.
43. Johansen, S., et al., *Clogging of ferro-silicon furnace off-gas channels at high temperatures*, in Smelter Process Gas Handling and Treatment, T.J.A. Smith and C.J. Newman, Editors. 1992, The Minerals, Metals and Materials Society: San Diego, U.S.A. p. 7-18.
44. Johansen, S.T., et al. *Environmental aspects of Ferro-Silicon furnace operations-an investigation of waste gas dynamics*.(Revised edition). in INFACON VIII. 1998. Beijing, China.
45. Ravary, B. and S.T. Johansen. *2D modeling of the combustion and NOx formation in furnaces producing FeSi*. in 2nd International Conference on CFD in the Minerals and Process Industries. 1999. Melbourne, Australia: CSIRO.
46. Kamfjord, N.E., H. Tveit, and I. Solheim. *Pilot Scale Measurements of NOx Emissions from the Silicon Process*. in 3rd International Symposium on High-Temperature Metallurgical Processing. 2012. Orlando, FL, U.S.A.: Wiley Online Library; John Wiley & Sons, Inc., Hoboken, NJ, USA.
47. Solheim, I., R. Jensen, and N.E. Kamfjord, *Equipment for Pilot Scale Experiments of NOx-Emissions from the Silicon Process*, in 3rd International Symposium on High-Temperature Metallurgical Processing, Tao Jiang, et al., Editors. 2012, Wiley Online Library; John Wiley & Sons, Inc., Hoboken, NJ, USA: Orlando, Florida, USA.
48. Ravary, B., C. Colomb, and S. Johansen. *Modelling Combustion and Thermal NO_X Formation in Electric Arc Furnaces for the Production of Ferrosilicon and Silicon Metal*. in INFACON XI. 2007. New Delhi, India: MacMillan.
49. Panjwani, B., S. Andersson, and H. Midtdal. *Effect of Combustion on NOx Emissions*. in 8the International Conference on CFD in the Oil & Gas, Metallurgical and Process Industries. 2011. Trondheim, Norway: SINTEF.
50. Solheim, I. and N.E. Kamfjord. *NOx-emissions from the silicon process: Comparing wet and dry raw materials pilot scale experiment*. in INFACON XIII. 2013. Almaty, Kazakhstan.
51. Skreiberg, Ø., *Evaluation of detailed gas-phase chemical kintetics mechanisms for NOx modelling in biomass- and MSW combustion applications*. 2002, SINTEF: Trondheim, Norway.
52. Total emissions to air in Norway - The Norwegian PRTR. [cited 2016 February 1]; Available from: http://www.norskeutslipp.no/en/Frontpage/?SectorID=90.
53. Olsen, J.E., et al., *Status on NOx-Related Studies for the Norwegian Ferroalloy Industry*. 2012, SINTEF: Trondheim, Norway.

54. Kadkhodabeigi, M., *Modeling of Tapping Processes in Submerged Arc Furnaces*, in Faculty of Natural Sciences and Technology, Department of Materials Science and Engineering. 2011, Norwegian University of Science and Technology: Trondheim, Norway.
55. Slizovskiy, D., et al. *The Industrial Scale Study of the Effect of Charge Frequency and H2O Behaviour in the Off-gases on NOx emissions in Si Furnace*. in Silicon for the Chemical and Solar Industry XII. 2014. Trondheim, Norway: Fagtrykk Trondheim AS/ The Norwegian University of Science and Technology.
56. Brede, I., *Parameters Contributing to the Formation of NOx in the Silicon Furnace: The effect of the charging frequency and raw material composition on the formation of NO*. 2013, The Norwegian University of Science and Technology: Trondheim, Norway.
57. Ishida, M., H. Ueki, and D. Sakaguchi, *Prediction of NOx reduction rate due to port water injection in a DI diesel engine*. 1997, SAE Technical Paper.
58. Kannan, K. and M. Udayakumar, *NOx and HC emission control using water emulsified diesel in single cylinder diesel engine*. Journal of Engineering and Applied Sciences, 2009. **4**(8): p. 59-62.
59. Maiboom, A. and X. Tauzia, *NOx and PM emissions reduction on an automotive HSDI Diesel engine with water-in-diesel emulsion and EGR: An experimental study*. Fuel, 2011. **90**(11): p. 3179-3192.
60. Colomb, C. and B. Ravary, *Modelling combustion and thermal NOx formation in electric arc furnaces for the production of ferro-silicon and silicon-metal*. 2005, SINTEF: Trondheim, Norway.
61. Simonsen, A., *3D CFD simulation of NOx combustion - Comparison with experiments and evaluation of NOx reducing strategies*. 2008, SINTEF: Trondheim, Norway.
62. Solvang, B. and H. Midtdal, *A generic silicon furnace model for the investigation of NOx reduction strategies using CFD*. 2009, SINTEF: Trondheim, Norway.
63. Panjwani, B. and J. Olsen. *Combustion and mechanisms for NOx formation in ferrosilicon electric arc furnaces*. in European Combustion Meeting. 2013. Lund, Sweden: Lund University.
64. Bugge, M., et al., *A status on NOx related to waste combustion and pyro-metallurgical processes*. 2001, SINTEF: Trondheim, Norway.
65. Ravary, B. and M. Bugge, *Description and analysis of ferroalloy processes in connection with NOx formation* 2002, SINTEF: Trondheim, Norway.
66. Ravary, B., C. Colomb, and S.T. Johansen. *Modeling combustion and thermal NOx formation in electric arc furnaces for the production of ferro-silicon and silicon-metal*. in INFACON XI. 2007. New Delhi, India.
67. Ravary, B., S. Grådahl, and M. Bugge, *Analysis of NOx formation in electric arc furnaces producing ferro-silicon and silicon metal*. 2005, SINTEF: Trondheim, Norway.
68. Ravary, B. and K. Tang, *SiO combustion in furnaces for ferroalloy production and its influence on NOx formation* 2003, SINTEF: Trondheim, Norway.
69. Forzatti, P., *Present status and perspectives in de-NOx SCR catalysis*. Applied Catalysis A: General, 2001. **222**(1–2): p. 221-236.
70. Echterhof, T. and H. Pfeifer, *Measurement and Control of NOx Emissions at Two AC Electric Arc Furnaces*. ISIJ International, 2011. **51**(10): p. 1631-1636.

Carbon fibers – alternative to graphite core in composite technology?

Robert Becker[1)], Stefan Bauer[2)]
1) Rheinfelden Carbon
2) RW Silicium

Abstract

Electrodes in form of a composite system have been used for more than 20 years. A graphite core in the middle forms the suspension for less costly søderbergpaste. This system was an economic way to safe costs and enabled larger electrode diameters compared with prebaked electrodes**.** Graphite price explosion, availability and quality problems set a question mark on composite technology. Concept for our research was to find economic alternatives to the graphite core. The high thermal conductivity of the graphite is hindering the use of non-toxic electrode paste in large composite furnaces. Using a construction of carbon fibers was successful tested over a 3 month period in a 15MW furnace using non-toxic electrode paste.

Technical Basics

The following points should be considered when developing new electrodes for the Si production:

- Silicon production is a continuous process. Interruption causes mechanical and thermal stress.
- Iron input has to be minimized.
- Current distribution should be symmetric.
- Paste gets solid at 500°C. Electrical conduction starts at 700°C.
- Mechanical strength of the holding system must be reliable at temperatures above 1000°C. Construction steel (ST 37) failed as a link in the system.
- The graphite core in the center is a good approach as long as it stays in position. When leaving the center, problems came up with this rigid system. Bending forces, asymmetric baking and risk for breakages. A flexible device like a rope or chain in the center of the Söderbergpaste should be less critical in operation.
- The thermal conductivity of the graphite core is too high for the use of the non-toxic paste. Steep isotherms and overbaking (solid paste above the contact clamps) has to be avoided.

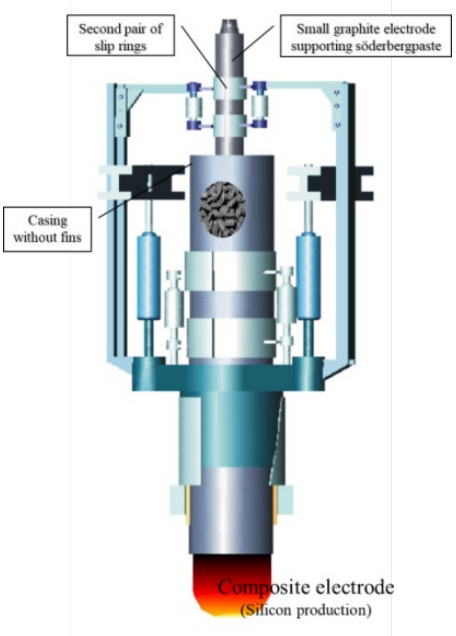


Figure 1: composite electrode with graphite core

From the spectrum of materials withstanding these temperatures carbon was our choice. Carbon fibers are designed for tensile strength and this was the feature we needed. Carbon fibers are good conductors for electricity and heat, however due to the small dimensions we did not expect noteworthy effects on the isotherms.

Carbon fibers

Our choice of carbon fiber material was the PAN fiber with the following characteristics:

- Heat resistant in oxygen free atmosphere
- Excellent tensile strength
- Low elasticity
- The fibers are very brittle and bending of the fibers should be limited.

Tight braided ropes and knots to link elements failed as the losses in tensile strength are enormous. Silicon production is a continuous process and we needed an endless carbon rope. Mechanical winches or friction based spill winches are not optimal to control the rope as the damage to the fibers is significant. It was found that best solution for this application is a loose braided carbon fiber material rope stitch sewn with carbon fibers to a loop. (See Fig. 2). The Kevlar bandage is covering the overlapping and sewn part of the sling which is centered and positioned to carry the next sling. (See Fig. 3).In use, the sling chain is easy to hang on a crane hook or, like in our test set-up, fixed by a simple strong steel bolt. Loops can be connected in the following way forming an endless carbon fiber holding.

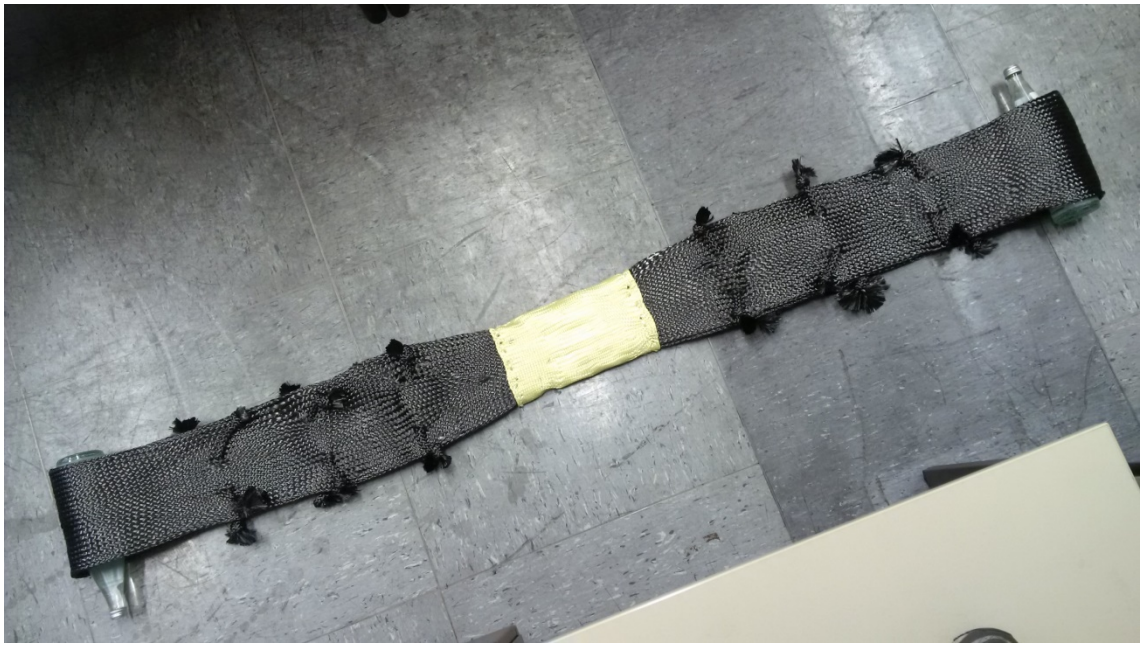


Figure 2: Sling ready for use in furnace. Braided ropes, each 20 cm, gives additional grip to the electrode paste. The center is fixed by a Kevlar bandage. Tensile strength of this construction is 500 KN or 50t. Slings with 100t tensile strength are realized and available.

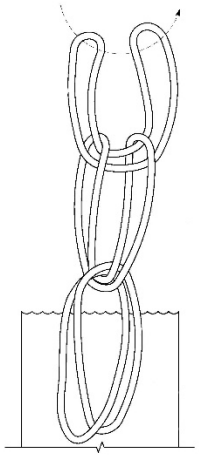


Figure 3: connecting the loops

Experimental design

The test was carried out in a small production furnace (18 MW) with existing composite technology. To keep costs low, we tried to use existing equipment and keep the furnace running without production losses. Of course there is room for improvements but our main objective was to find out the following answers:

- Is carbon fiber capable to run under furnace conditions?
- Has the fiber construction enough grip in baked electrode paste?
- Is this system working with non-toxic LIMAK paste?
- Are there risks of green breakages or overbaking? Where is the 500°C isotherm located?
- What is the economic benefit compared to graphite?

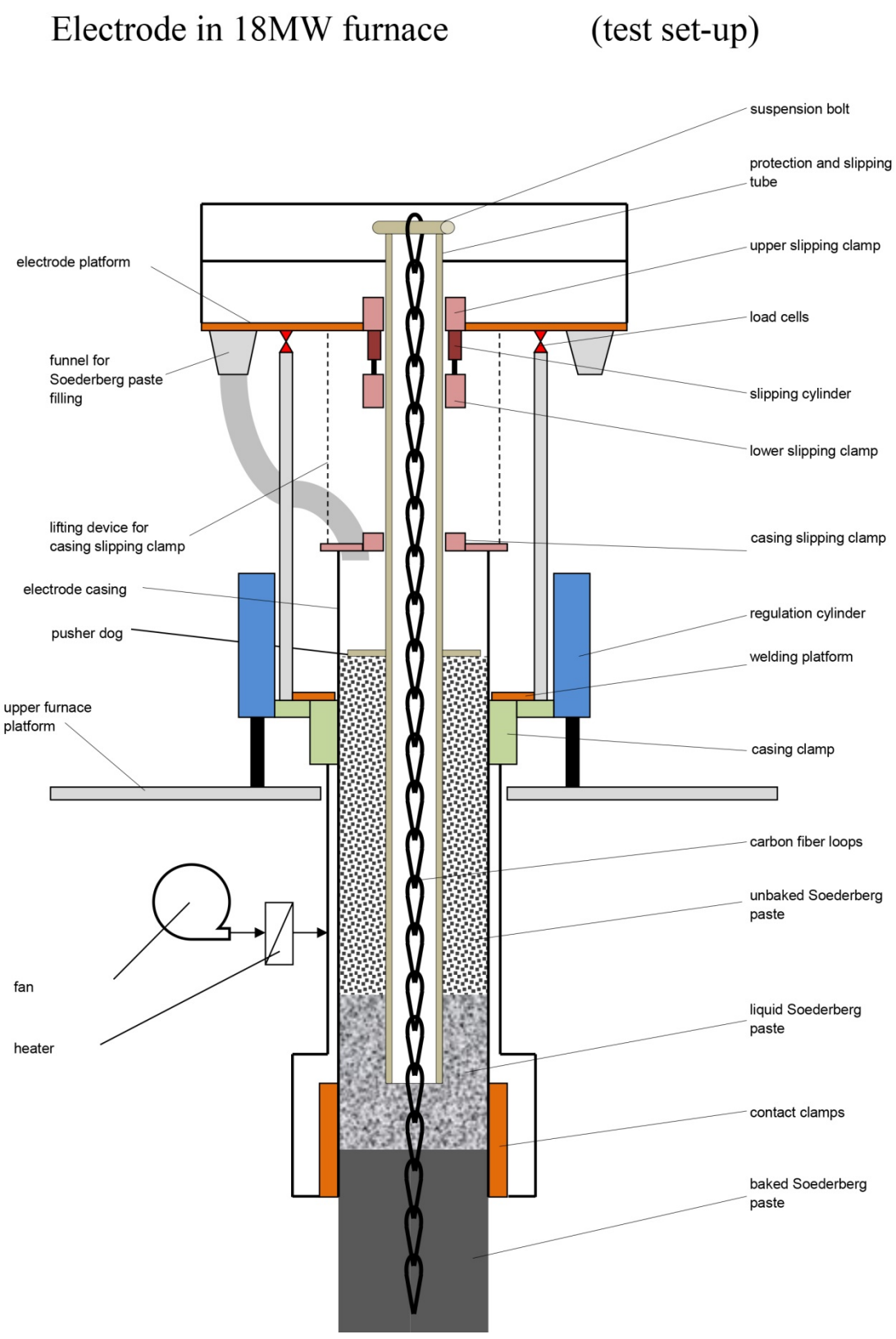


Figure 4: Furnace cross section

In the test set-up a grooved tube is replacing the graphite electrode. Material for this tube can be various, aluminum, steel, different alloys etc.

- This tube is held by the same clamp and moving system used for the graphite core before.
- A bolt is carrying the sling chain and the complete electrode
- Moving the electrode can be done by the slipping clamps via the steel tube.
- The carbon fibers of the sling chain are fully shielded by the tube from sharp edged Söderberg briquettes.
- Entering the liquid zone at 200°C the fibers are protected against oxidation.

Converting the electrode from graphite to fiber system could be done without considerable interruptions of production. All technical modifications were done with the own workshop.

Practical tests at 18 MVA furnace

A continuous practical test of the carbon fiber system was performed over a period of 3,5 month on one column of a 18MVA furnace. Electrode diameter was 1016mm. The size of the replaced graphite core was 400mm. Prior to the trial at the furnace, some simple tests on the strength of the fibers were performed as seen in Figure 5.



Figure 5: Forklift truck (5.5 t) hanging on a carbon fiber rope chain

The transfer of graphite electrode to carbon fiber was made by using a standard transportation pin.



Figure 6: Transportation pin as transfer element

The shielding tube was brought in by welding together shorter pieces over a period of a few days. No changes at all had to be made on the existing slipping system. Typically the patented system is a „ready to use“ equipment.



Figure 7: Shielding tube in position

Furnace operation was quite normal during the test. Baking of the electrode was observed using the Cavigli voltage between core and casing. Slipping by gravitation did not always work properly as the electrode weight was very low on this small furnace with short

column. Additional slipping of casing was sometimes necessary to bring the system back to equilibrium.

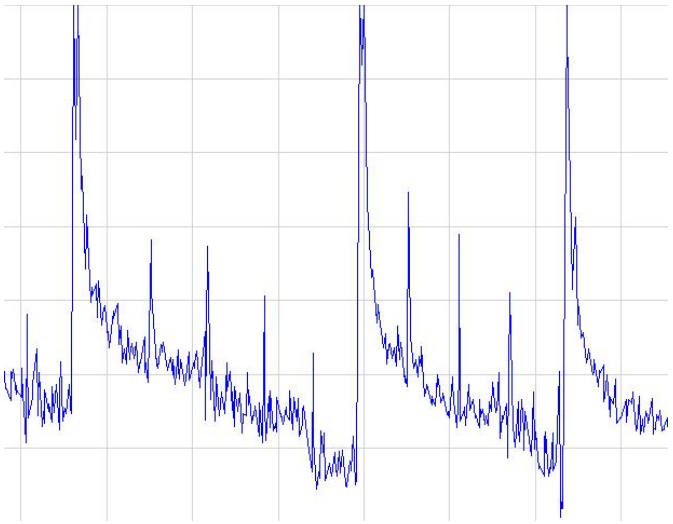


Figure 8: Cavigli voltage trend

The overall consumption of electrode length was about 115m during the test period. As one carbon fiber rope measures 1m in operating length, about 115 pieces of rope were used.
As the test was performed during the period of extraordinary high graphite prices during 2018 (up to 10.000 €/mt), the savings with the carbon fiber electrode were more than 200.000 € in total.

Résumé

PAN Carbon fiber is absolute capable to carry the electrode in electric arc furnaces for silicon production.
The isotherms are shaped more or less identically as in standard Söderberg furnaces. The top of the electrode with the fiber bundle in the center is the 500°C isotherm. See Figure 9 below.



Figure 9: Electrode stump ready for autopsy. Paste LIMAK (nontoxic paste). Liquid paste was removed and hence the surface is representing the 500°C isotherm.

The carbon fiber elements looked strong and undamaged down to the bottom of the electrode with no substantial gaps or holes inside. The rope chain is perfectly attached inside the baked paste as seen in Figure 10. Even when graphitized 50 cm above the electrode tip, the fiber construction is fully in shape. The braided ropes are in horizontal orientation and give additional contact to the electrode matrix.



Figure 10: Rectangular block from the center of the electrode stump. The block is showing the contact of 2 slings and the baked paste surrounding this area. The Kevlar fabric is carbonized - leaving a small gap between the 2 slings. This is substantial to avoid thermal stress to the system.

Conclusion

Carbon fiber is definitely a good and economic alternative for composite technology. This test was done in a small furnace with a low budget approach. In larger furnaces with longer and heavier electrodes, slipping is much easier and can be regulated by paste properties. If necessary to push down the electrode it's easy to install additional equipment or use aluminium shielding tubes. In our opinion this will not be necessary.

Some of the critical points in composite technology could be solved. The rope will always stay in the center. Baking is more homogeneous, isotherms are less steep and overbaking is solved. Using non-toxic paste is perfect adapted to this technology.

References

1. M. Cavigli, *Self-baking electrode structure and method of operating same*, US3624261A,
2. J. Bullon et al., *The New Compound Electrode: Current Situation and Thermoelectric Studies,* Infacon 8 proceedings 1998, p398

Silicon for the Chemical and Solar Industry XV
Trondheim, Norway, June 15 – 18, 2020

Effect of melting properties of quartz on industrial Si and FeSi production

Eli Ringdalen[1)], Sarina Bao[1)], and Halvard Tveit[2)]
1) SINTEF, Trondheim Norway
2) Elkem, Norway and NTNU, Norway

Abstract

The effect of melting properties of quartz is discussed based on estimated temperature distribution in industrial furnaces combined with measured melting properties for various quartz sources.

Softning and melting properties for four industrial quartz sources have been investigated in a sessile drop apparatus in both nonisothermal experiments and with holding temperatures of 1730ºC, 1750 ºC and 1775 ºC. This showed that quartz needs superheating to achieve complete melting and that it takes long time to melt particles even with temperatures above the melting point of SiO_2. Time needed for complete melting increases with decreasing temperature and is much longer than the time needed for heating the particle. Heating rates of 2, 5.5 and 10 ºC/min have been investigated. With higher heating rates higher temperature is needed to obtain complete melting. Recorded melting temperatures were similar in Ar and CO atmosphere

Time needed to achieve complete melting varies considerably between the different quartz sources. This difference is expected to affect behaviour of different quartz sources in industrial FeSi and Si furnaces. The effect depends on the temperature profile in the industrial furnaces. A comparison of melting properties of quartz with the temperature profile in a industrial Si furnace indicates that most of the furnace volume is filled with softened or partly molten SiO_2. Use of, and change between, different quartz sources are expected to affect furnace performance in industrial Si and FeSi production

Introduction

Metallurgical silicon (Si) and ferrosilicon (FeSi) are produced in submerged arc furnaces (SAF), where the main raw materials are quartz plus carbon reductants such as coke, coal,

charcoal, and woodchips. For FeSi production, iron sources are added. Electrical energy, around 11-13 MWh/ton alloy for Si production, is another important input factor. This is supplied through the electrode. The reduction of silica to Si takes place by the overall reaction (1). In industrial furnaces, the reactions take place in several steps as described by Schei et al. [1].

$$SiO_2 + 2C = Si + 2CO \qquad \Delta H°_{2000°C} = 687 \text{ kJ/mol} \qquad (1)$$

Both a high silicon yield and a stable furnace operation are needed to achieve good results and low energy consumption. These are both affected by the properties of the raw materials used. Knowledge about the effect of carbon properties has led to improvement in furnace operation. Increased knowledge about quartz properties are expected to give further improvements in furnace operation and reduce specific energy consumption and CO_2 emissions.

Quartz in the silicon process

The silicon process

Furnace excavations during the last years [2] have established a schematic picture of inner structure of a Si furnace, given in Figure 1.

.

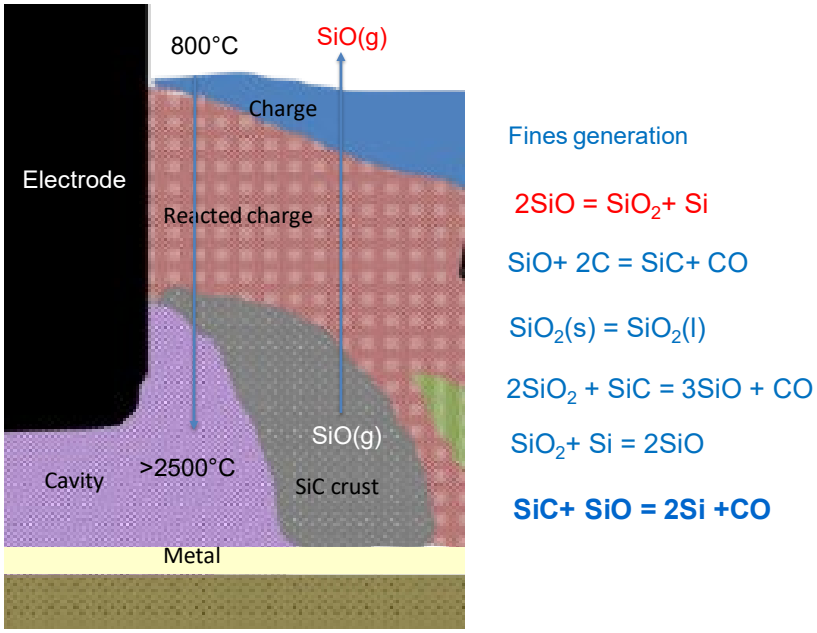


Figure 1 Inner structure of Si-furnace and the reactions that take place in different parts of the furnace.

The raw materials are fed to the top of the charge mixture where the temperature is around 700-1300 °C [3]. Liquid Si, at approximately 1800 ºC [4], is tapped at the bottom of the furnace. Off-gas composed mainly of CO and SiO leaves the charge at the charge top where it burns to CO_2 and SiO_2. To obtain a high silicon yield, the off gas must have a low SiO-content. To obtain a good furnace performance, there must be an even gas flow and a good charge permeability in the furnace.

Quartz descend down in the furnace and is reduced to SiO by reaction (5) and (6). The produced SiO is further reduced to SiC by reaction (4) in the upper parts of the furnace or to Si by reaction (7) in the high temperature zone. SiO gas that is not consumed by reaction (4) will be captured in the charge by reaction (2) and (3) or escape the charge mixture and lead to decreased Si-yield.

$$2SiO\ (g) = SiO_2(s,l) + Si(l) \quad \Delta H^o_{1800°C} = -\ 606\ kJ/mol \qquad (2)$$

$$3SiO(g) + CO(g) = 2SiO_2(s,l) + SiC(s) \quad \Delta H^o_{1800°C} = -\ 606\ kJ/mol \qquad (3)$$

$$2C(s) + SiO(g) = SiC(s) + CO(g) \quad \Delta H^o_{1800°C} = -78\ kJ/mol \qquad (4)$$

$$SiO_2(s,l) + Si(l) = 2SiO\ (g) \quad \Delta H^o_{2000°C} = 599\ kJ/mol \qquad (5)$$

$$2SiO_2(s,l) + SiC\ (s) = 3SiO\ (g) + CO\ (g) \quad \Delta H^o_{2000°C} = 1364\ kJ/mol \qquad (6)$$

$$SiC\ (s) + SiO\ (g) = 2\ Si(l) + CO\ (g) \quad \Delta H^o_{2000°C} = 167\ kJ/mol \qquad (7)$$

All enthalpy values are calculated by HSC[5]

An effective production of Si requires that the reactions with SiO_2, reactions (5) and (6) in the upper part of the furnace are slow and governed by kinetics while the reaction between SiO-gas and carbon, reaction (4) is fast and close to equilibrium. The final production of Si in the lower part of the furnace, equation (7) is not much investigated, but a fast reaction rate will be an advantage.

At what depth in the furnace the different reactions take place, depend on the temperature profile in the furnace. This vary with furnace design and produced alloy quality as well as furnace operation and distance from the electrodes. An average heating rate of 5.5 ºC/min and a material flow of around 0.3m /hour has earlier been estimated [6] as normal for Si furnaces. Modelled temperature profiles for selected Si and FeSi-furnaces [7][10] indicate that the temperature does not increase linearly with increasing furnace depth. The raw materials are heated fast up to around 1600ºC in the upper part of the furnace. In most

of the furnace volume above the crater zone, the temperature is between around 1600 °C and 1800 °C. The heating is here much slower around 0.5 ºC/min.

Quartz in the Si -process

Use of quartz from different sources or change been quartz sources will affect the furnace performance. This has been reported orally from different producers but is also documented from the operations of Dow Corning in Brazil [8]. The effects of quartz will depend on temperature profile in a given furnace and also interact with this. Modelled temperature profiles for 3 different furnaces [9],[10] have been published and will be used as a basis for the discussion. They will later be shown in Figure 7.

Quartz may affect furnace performance by having an impact on:

- Downwards flow of material
- Upwards flow of gases
- Rates for reaction involving SiO_2, especially SiO production
- Energy and temperature distribution in the furnace

To obtain an even and good upwards gas flow, the charge mixture must not contain too much fines. Quartz will decrepitate to fines during heating, both by heating in the charge mixture and by thermal shock when it meets the charge surface that has a temperature of 700-1300 °C [3],[11]. Amount of fines that is generated vary strongly with quartz source [12]. Laboratory experiments and modelling [13] indicates that the quartz fines itself will not be the main factor determining the permeability and gas pressure in the furnace. Clogging of particles by SiO-condensates are believed to be more important, although this is not documented. The larger surface areas of fines compared to lump material will present an opportunity for both more SiO-condensation, faster heat transfer and higher reaction rates. Decrepitation and fines generation of quartz may through this mechanism affect furnace performance.

Stable furnace operation requires a stable downwards flow of raw materials. Formation of and clogging of materials by SiO-condensation, reactions (2) and (3) will affect the flow. The flow will also be affected by softning and melting of quartz and changes in its viscosity. Melting properties vary between different quartz sources[9]. This is discussed more in detail in next chapter. The observed differences in melting properties between different quartz sources may thus give variations in furnace performance depending on quartz source.

To obtain a high Si-yield escape of SiO gas from charge top must be minimised. Quartz must thus react in the lower part of the furnace and supply SiO to the Si-production by reaction (7) there. Surplus SiO gas that ascend through the charge should preferably react to SiC by reaction (4) or be captured by reaction (2) and (3). Reactions (5) and (6) that produces SiO gas must then take place in the lower part of the furnace. To obtain this these reactions should have a low reaction rate at the lower temperatures found in the upper parts of the furnace and relatively high reaction rates in the high temperature zone. Parameters that might affect the reaction rate are temperature, gas phase, particle size, contact area towards other phases, structure and SiO_2 polymorph.

During heating quartz will transform to different SiO_2 polymorphs: α-quartz→ β-quartz→ amorphous SiO_2→ cristobalite→ molten SiO_2. The rate for the transformation and thus the amount of each polymorphs at a certain time and temperature vary considerably between quartz sources[14], [15]. Reaction (6) between SiO_2 and SiC seems not to be affected by amount of cristobalite[16] or amount of amorphous phase [17]. Reaction (5) between SiO_2 and Si seems to have similar reaction rate as reaction (6) [18]. It is indicated that the rate for the reaction are different before, during and after melting[19]. Reduction of quartz to SiO will based on this not depend on rate for phase transformations in quartz but may vary due to differences in particle sizes or in melting properties. This need to be further investigated. It can not be excluded that extent of SiO-producing reactions at a given temperature in a Si-furnace will vary with quartz source. This can then affect both Si-yield and temperature distribution in the furnace.

Final reduction to Si, reaction (7) is, contrary to final reduction in most other processes, not the most energy demanding reaction in silicon production. Reduction to the intermediate product, SiO by reaction (5) or (6) require more than 5 times as much energy. Excess SiO react back to SiO_2 by the exothermic reactions (2) or (3) in the upper part of the furnace. Energy is through this "SiO-circulation" transported from the lower to the upper part of the furnace. The temperature distribution in the furnace will be a consequence of this. Energy consumed or developed at a certain depth depend on the extent of reactions with SiO_2. Since reaction rates depend on the temperature there will be close interaction between reaction rates and temperature distribution that will affect how much SiO that is captured in the charge. Variations in rates for reactions with SiO_2 may through this affect energy consumption, temperature distribution and SiO capture in the Si furnace.

Changes in quartz during heating

Several properties of quartz are expected to change during heating. This can be changes in cracks, composition of gangue minerals, water inclusions, texture and others. Thermal

stability, phase changes, melting and changes in viscosity are properties where changes during heating have been shown to vary between quartz sources at temperature of interest for Si-production.

Shock heating of quartz when it meets the charge top in the silicon furnace will lead to varying degrees of disintegration depending on quartz source[12]. Generated quartz fines are not the main cause for uneven gas flow in the furnace [13]. The smaller quartz particles will be heated faster, can melt faster and also have a larger specific surface area that can enhance rates for reactions with SiO_2

Quartz, the low temperature polymorph of SiO_2, will at 573 °C (1 atm) change to β-quartz by a fast and reconstructive transformation. The further transformation to tridymite described in the established SiO_2 phase diagram [20], is as discussed in [21], debated. Transformation to the high temperature polymorph β-cristobalite is slow and goes through an amorphous phase[14]. Quartz, amorphous silica and cristobalite have been found to occur together in quartz kept for relatively long time at temperatures at 1500 ºC to 1700 ºC [14,15,22]. The relative amounts vary considerably between different quartz sources [15]. Rate for phase transformation is one of the properties where it is large variations between quartz sources. It is suspected to be one of the causes behind the effect of quartz source on furnace performance. Phase transformations in SiO_2 has been shown to not be the main cause for fines generation due to thermal shock [14]. Amount of different phases will not affect the rate for SiO generation from SiO_2 reacting with SiC [16] or from SiO_2 reacting with Si [18]. Phase transformation may affect softning and melting properties of quartz and through this both material flow and reaction rates. This is not yet investigated.

Liquid silica has a viscosity, around $2 \cdot 10^7$ Poise at the melting temperature and will then behave nearly as a solid. The viscosity will as shown in Figure 2 [24] decrease rapidly with increasing temperature and be around $5x10^4$ Poise at 2000 ºC. Other constituents may affect the viscosity. Reactions rates and how easily silica drain down in furnace is expected to increase with decreased viscosity.

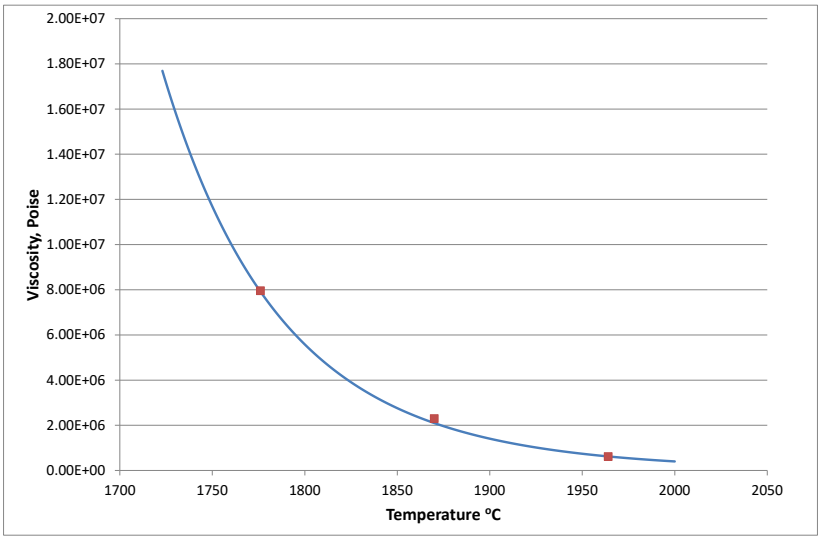


Figure 2 Viscosity of molten silica. Calculated by FactSage by Dalaker and Tang

Under equilibrium conditions, pure SiO_2 will melt at around 1720 °C. Cristobalite is the stable solid phase at this temperature. Content of common minor constituents in quartz, such as Na_2O, FeO, CaO and Al_2O_3 have been reported to both change the rate of the solid-state phase transformations [23] and to decrease the solidus temperature. Liquid phase will then start to form at temperature below 1720 °C and liquid and solid will coexists in a melting interval. Melting properties has been shown to vary considerably between different quartz sources [24]. This has further been studied in the current work . Melting properties of quartz is expected to affect both material and gas flow in the furnace as well as reaction rates and, through this, energy and temperature distribution.

Melting properties of quartz

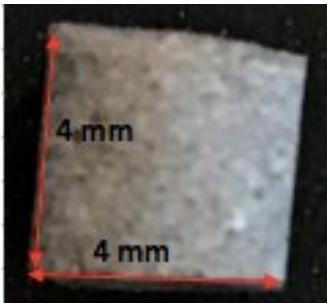
Investigations

Melting properties of four different quartz types, A, B, C and D all used in production of metallurgical silicon were investigated . Results earlier published by Nordnes[10] and by Ringdalen[9] are a part of the same investigations and are here presented together with newer results. Melting properties were studied in a sessile drop furnace by the method described by Ringdalen [9]. Three tests were run for each quartz source. A 4x4 mm quartz cylinder was heated with 300 °C/min from room temperature until 900 °C and 67 °C/min from 900 °C to 1500 °C. From 1500 °C the sample was heated with either 2 °C/min, 5,5 °C/min or 10 °C/min. Melting was investigated by two different methods:

- Non-isothermal heating where temperature for softning and for complete melting with a certain heating rate was determined
- Isothermal heating where time needed for complete melting when held at a designated temperature, 1730 °C, 1750 °C or 1775 °C, was recorded. This was

studied with different heating rates up to holding temperature. For all samples softning started at lower temperature than the holding temperature.

Temperature for *Softening* is determined as the temperature when the shape of the sample has lost the sharp edges. Temperature for *Final melting* is determined as the temperature when the droplet is round. Start temperature for softening is difficult to observe and where there are large differences in softening temperatures between parallels, the lowest temperature is normally regarded as most reliable. Examples of images are shown in Figure 3.



Sample before heating


Sample at softening temperature


Completely molten sample

Figure 3 Example of sample shapes, before heating, at softening and when completely molten.[10]

The experiments were run either in Ar or in CO atmosphere, mostly in Ar.

In the sessile drop set-up, the thermocouple, type C, is not protected. It is thus a risk for degradation of the thermocouples and drifting in measured values. To correct for this, temperature for melting of Fe was measured regularly and difference between measured value and melting temperature for Fe (1538 °C) was used as a correction factor for further measurements. It was assumed that for each thermocouple deviation from correct temperature increased linearly with amount of tests. Temperatures between the calibration measurements were corrected based on this. In the current work 4 different thermocouples with various ages were used in 46 tests. It was found that the thermocouples degrade with 1.2- 2.3 °C per test in Ar atmosphere and with around 8 °C in each test in CO. In the newer earlier unpublished results the temperatures are corrected for this deviation while for data form earlier experiments [9], [10] the original measured values are used. The temperature corrections did not change the main conclusions from the results. The temperatures were corrected after the experiments. Holding temperatures in the isothermal experiments are thus, in the cases where the temperatures are corrected, different from designated temperature and varies between experiments.

Modelling of heating of quartz particles [10] have shown that for a 4 mm particle only 1 second was needed from the surface was heated to 1765 °C and until the centre of the particle had the same temperature. The quartz samples will thus in this context have a uniform temperature distribution. For a 100 mm particle the temperature in the centre is 1735 °C when the surface has temperature of 1765 °C for non-isothermal experiments.

Melting properties of different quartz sources

The four investigated quartz sources have, as seen in Figure 4, different melting behaviour. Softning and melting temperatures for different quartz sources heated in Ar with 5.5 °C/min are here compared. Results from all parallels for both isothermal and non-isothermal experiments are included. Softning temperatures for all quartz sources were lower than the melting point of quartz and thus lower than the holding temperatures used in the experiments. Softning temperatures from both isothermal and non-isothermal experiments can then be compared.

The holding temperature of 1730 °C is close to the melting point of SiO_2. The quartz may, due to the uncertainties in temperature measurements, in some cases have been held at temperatures below its melting point. Recorded times for complete melting at 1730 °C may thus not be reliable and are not used in further discussions. They are included since they too show the general trend that long time is needed for complete melting at low temperatures.

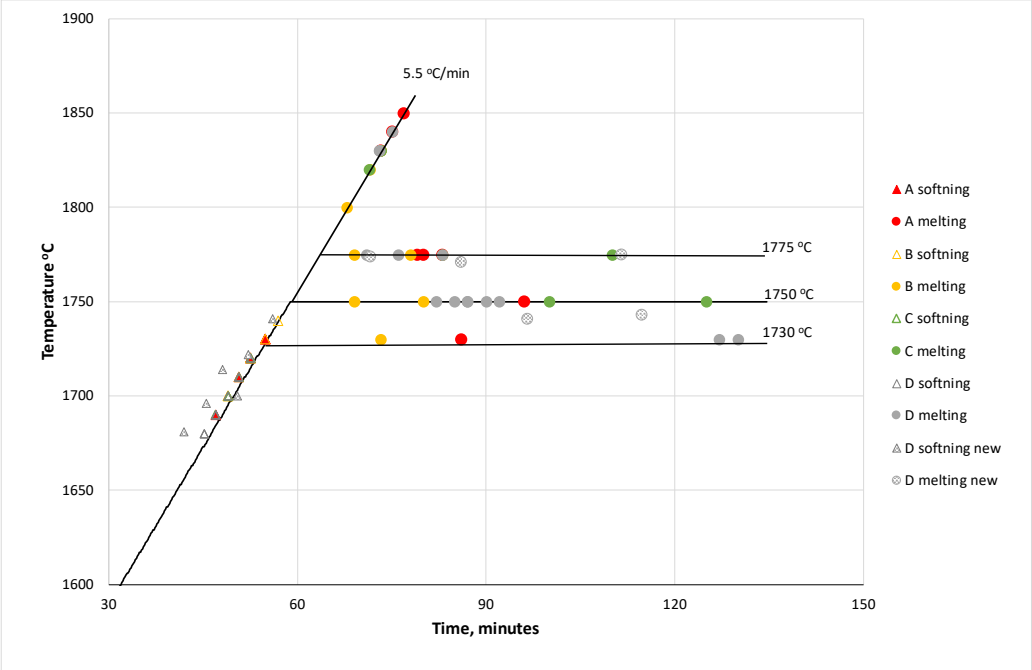


Figure 4. Softening and melting of various quartz in Ar with 5.5°C/min heating. The new samples for quartz D are with corrected temperatures

The main information from these investigations is that melting of quartz either needs superheating or long time. At 1750 °C which is clearly above the melting point for quartz, quartz B needs between 10 and 20 minutes from it reaches 1750 °C and until it is completely molten. Quartz C needs between 60 and 75 minutes to become completely molten at this temperature. With higher temperature, the melting goes faster and at 1775 °C, quartz C is completely molten 35-55 minutes after 1775 °C is reached. With continuous heating at 5.5 °C/minute the quartz sources need to be heated above 1800 °C before they are completely molten. Required temperature vary between quartz sources. Quartz B that needs shortest time to melt at 1750 and 1775 °C have the lowest temperature for complete melting, while quartz A that need longest time to melt have highest temperature for complete melting. Quartz D has an abnormal behaviour. This indicates that the decrease in time needed for melting with increasing temperature vary between quartz sources. Other parameters in addition to temperature may thus be of importance for this. The observed high melting temperatures during continuous heating with 5.5 °C/minute, above 1800 °C for all the quartz types, reflects the time needed for melting under these conditions.

All quartz sources start to soften at lower temperatures than the melting temperature for quartz, mostly around 1680-1720 °C. With continuous heating at 5.5 °C/ min it is a temperature interval of 100-150 °C from quartz starts to soften and until it is completely molten. Softened and partly molten quartz thus exist together in a large temperature interval.

Quartz is an inhomogeneous material. The observed relatively large scatter between the investigated parallels are thus not unexpected. The uncertainty in determination of temperature for softning gives an additional uncertainty for this parameter. Differences in temperatures for complete melting between the quartz sources are large enough to describe general trends in spite of this.

Effect of heating rate

Both softning temperature and temperature for complete melting vary with heating rate. as shown in Figure 5. There is large scatter in the data, but they indicate that for quartz D higher heating rate give higher softning temperature and slightly higher temperature for complete melting For quartz B there are no clear differences. Effect of heating rate may thus vary with quartz source. There are too much scatter in the data set to make any clear conclusions about effect of heating rate. More data will be needed to do this With a heating rate of 2°C/min the highest recorded temperature for complete melting for quartz D was 1843 °C while it with a heating rate of 10 °C/min was 1893 °C. Highest

recorded temperature for softning of quartz D were 1690 °C with heating at 2 °C/min and 1760 °C with heating at 10 °C/min. Also for quartz B the temperatures for softning and for complete melting was higher with heating at 10 °C/min. than with 2 °C/min. There were no clear differences in softning and melting temperatures between heating with 10 °C/min. and with 2 °C/min.

The decrease in melting temperatures with lower heating rate is assumed to be a result of the longer time needed for the materials to reach the temperature and consequently longer time exposed to the higher temperature. The mechanism behind this is not known. It can thus not be excluded that heating rates or time exposed at high temperatures affects other properties that are of importance for melting properties

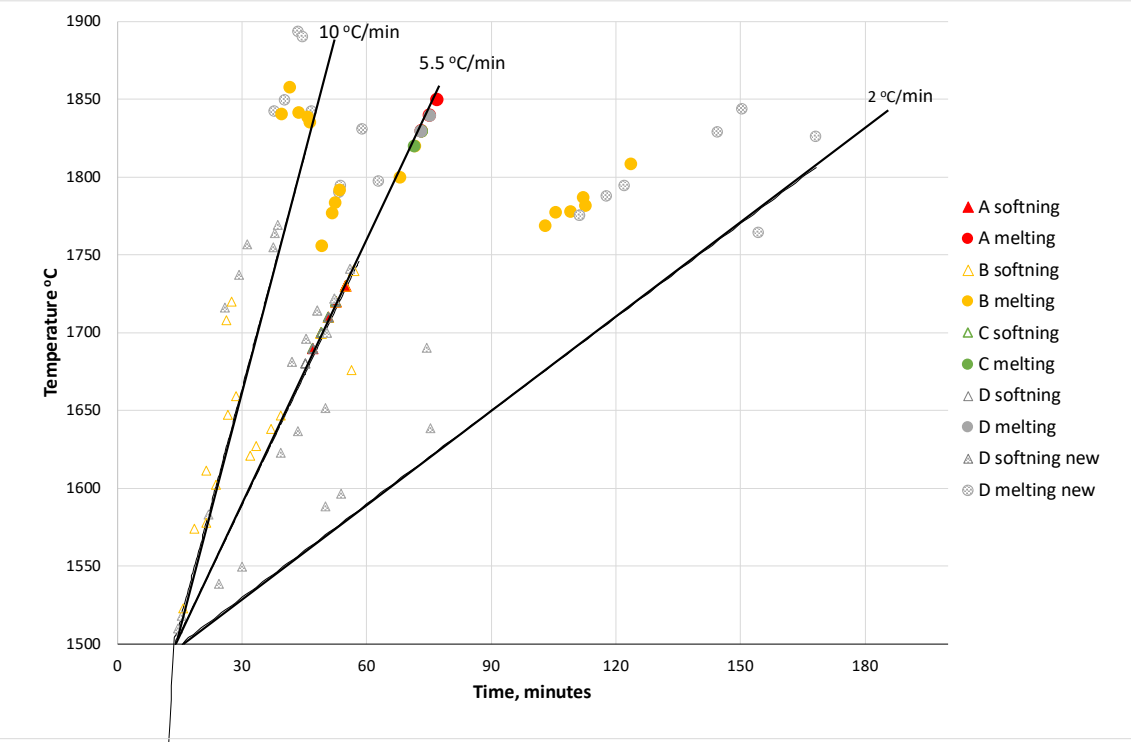


Figure 5 Softening and melting temperature with heating of 10, 5.5 and 2°C/min. The experiments with 2°C/min and 10°C/min and the experiments marked as new are all with corrected temperatures.

Effect of gas atmosphere

During melting in industrial Si-furnaces, quartz is exposed to a mixture of CO and SiO gas. Comparison of melting properties for quartz D in CO and Ar atmosphere illustrated in Figure 6 shows that the gas atmosphere, Ar versus CO, will not affect the melting properties. The melting experiments done in Argon (Ar) atmosphere are thus relevant for conditions in Si-furnaces

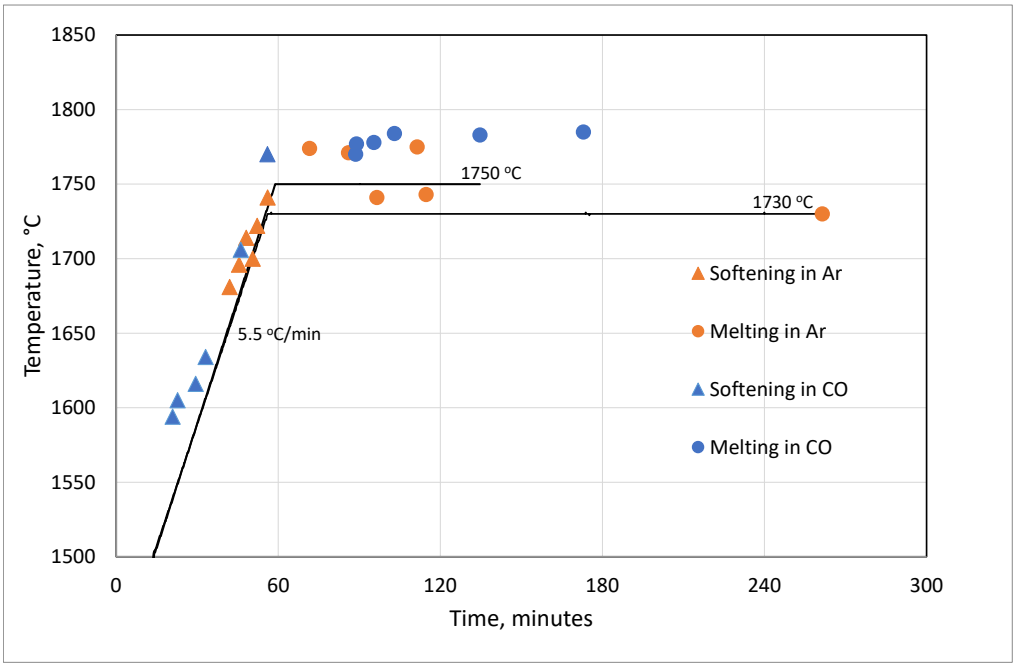


Figure 6 Softening and melting temperature of Quartz D in CO and Ar atmosphere

Discussion - Effect of quartz source on furnace performance

The observed differences in melting properties of quartz raise questions both about the mechanism behind these difference and about their effects on furnace operation.

The long time, up to more than 2 hours, or the high superheating, up to around 100 °C, needed to melt quartz was unexpected. Modelling of heat transfer in the investigated quartz particles showed that the time needed to melt the investigated quartz particles were several magnitudes longer than the time it took to heat it. So it must be governed by another mechanism. Ainslie[25] showed superheating of quartz of up to 300 °C before melting which is in line with the results presented here. He mainly attributed this to the high viscosity of molten silica. Crystal structure of SiO_2, amount of cristobalite, seemed in addition to impurities to affect the required superheating. This could be a reason for the observed differences in melting properties between various quartz sources in the current investigations. To have a better understanding of the mechanism for melting of quartz and the quartz properties that govern this, further investigation are needed.

Melting of quartz particles will give a larger contact area towards adjacent solid particles as SiC and for the dispersion of SiO_2 in a Si-melt. Polymorph of SiO_2 will not affect the rate for reaction (6) between SiO_2 and SiC [16] or for reaction (5) between SiO_2 and Si [18]. The increased contact area after melting is expected to increase the rate for these reactions. SiO generation may thus be higher in the part of the furnace where SiO_2 is

molten. Softened silica and molten silica with too high viscosity to drain down in the furnace will also bind particles together and affect flow of materials and gases in industrial furnaces.

In industrial Si furnaces most of the furnace volume above the cavity , have a temperature between 1600 °C and 1800 °C [7] . Quartz start to soften around 1600 °C and is not fully molten until around 1800 °C. The temperatures vary with quartz source. Most of the furnace volume is thus filled with softened and partly molten quartz, The depth where quartz start to soften and where it becomes fully molten and consequently how much of the volume that is filled with partly molten silica depend on quartz source [9],[10]. Depth in a Si furnace for start softning and for complete melting for different quartz sources are in Figure 7 shown together with the temperature profiles.

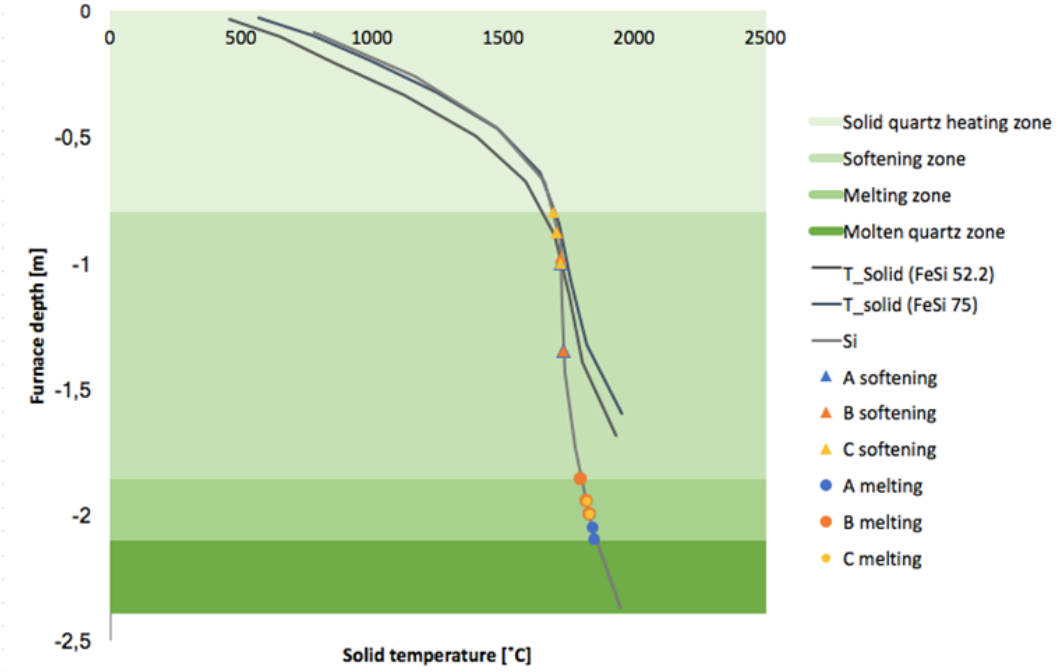


Figure 7 Modelled temperature profiles for selected industrial FeSi and Si furnaces with depth in the Si-furnace for softening and melting of different quartz sources All parallel in experiments from Nordnes are included[10].

To be able to compare the different quartz sources, depths were calculated based on softning and melting temperatures found in experiments with a heating rate of 5.5 °C/min. With the slower heating rates that occur in industrial furnaces, quartz will as shown above start to soften and become completely molten at lower temperatures. This will shift the depth for the transitions slightly upwards, but most of the furnace will also in this case be filled with partly molten silica. The exact temperature profile in the furnace and the flow of the materials in meters pr. minute at different depth will also strongly affect at which depth in the furnace SiO_2 will soften and melt and also interact with this.

Above 1600 °C, the temperature in the Si-furnace, changes slowly with increasing depth. Relatively small differences in melting properties between different quartz sources will therefore strongly affect at which depth quartz starts to soften and how much of the furnace that is filled with partly molten silica. A change of quartz source will change the distribution of theese zones. The transition period until a new distribution of soften and molten material are established might be expected to affect operational parameters of the furnace.

Partly molten quartz can affect both gas and material flow and reaction rates. A softened or half molten surface of quartz particles is sticky and will glue particles together. This will reduce gas permeability in the charge and may change gas distribution. This is normally assumed to be of minor importance compared with the blockage of gas transport due to condensation of SiO gas. The same is to some degree also the case for the transport of charge materials down in the furnace.

Partly molten and molten silica that sticks to and partly cover carbon or SiC and other charge materials will have a larger contact area with these materials. This may increase rates for the reactions with silica, reaction (5) and (6). [26, 27]. To obtain a high Si-yield these SiO producing reactions should take place at high temperatures low down in the furnace where the produced SiO-gas can further react with SiC to Si. The SiO producing reactions and especially reaction (6) between SiO and SiC are highly endothermic while reaction (2) and (3) consuming excess SiO-gas are strongly exothermic. Temperature distribution in the furnace will due to this be strongly affect by which depth in the furnace these reactions take place. Melting of silica will thus affect the temperature distribution in the furnace. The change of temperature profile and depth for the reaction zones in the furnace due to such changes are expected to give a period with instabilities.

Molten silica with a good draining down to the SiC-crust and crater zone will facilitate high production rate of SiO in these zones where the final production of Si from SiO-gas takes place by reaction (7) from around 1800 °C and upwards. Silica sources that need a high temperature and long time to be completely molten, may not react completely in the high temperature zone and contribute to build up of unreacted materials in the furnace as described in furnace excavations [2].

Based on these considerations a quartz source with a high softening temperature, small temperature difference between softening and melting and that melts relatively fast and are completely molten at around 1800 °C could be expected to be beneficial for furnace operation. Change between quartz sources with different melting properties may give periods with instabilities in furnace operation.

Conclusions

Quartz particles will not melt immediately when they reach the melting point of SiO_2. They will start to soften below the melting temperature and need long holding time or large superheating before they are completely molten. At 1750 °C a 4 mm particle may need up to 2 hours to become completely molten. The time needed vary between different quartz sources. It decreases with increasing holding temperature. A decrease with decreasing rates for heating up to holding temperature is indicated, but may depend on quartz source. With a heating rate of 5.5 °C/min quartz must be heated to around 1800 °C before it is completely molten. This is well above the melting point of SiO_2 of around 1720°C. Quartz softens around 1700 °C, e.g. below the melting point of SiO_2. With higher heating rates, higher temperatures are required to obtain complete melting. The melting properties are similar in Ar and CO gas atmospheres.

In industrial SAF furnaces for Si and FeSi production most of the furnace volume are filled with softened and partly molten SiO_2. Charge temperature are according to modelled temperature distribution in furnaces between 1650 °C and 1800 °C for most of the furnace volume. Measured melting properties show that SiO_2 will soften and melt in this temperature range. The exact furnace depth where solid quartz starts to soften and where it is completely molten vary with quartz source. Change of quartz source used in the furnace will change amount and distribution of partly molten and molten silica in the furnace. A change of quartz source will thus give a transition period until the new distribution of these are established.

Depth and volume of solid, partly molten, and completely molten quartz are expected to affect the conditions for transport of solids downwards and the flow of gas upwards in the furnace as well as the reactions with quartz. Since reactions with quartz produces SiO through highly exothermic reactions, melting properties may also affect temperature distribution in the furnace.

Other quartz properties as fines formation or rate for transformation to cristobalite that seems to have little direct effect on furnace performance, may have an effect on melting and melting properties of quartz and through this affect furnace performance.

Acknowledgements

This work has been funded by Elkem ASA and the Research Council of Norway through the RCN project 256788 High-temp Quartz. They are both acknowledged.

References

1 Anders Schei, Johan K Tuset, Halvard Tveit, Production of High Silicon Alloys, Tapir forlag, Trondheim, Norway, 1998, ISBN: 82-519-1317-9.

2 Michael Ksiazek, Merete Tangstad, Eli Ringdalen, Five furnaces five different stories, Silicon for the Chemical and Solar Industry XIII, Kristiansand, Norway, 2016

3 S. T. Johansen, H. Tveit, S. Grådahl, A. Valderhaug, and J. A. Byberg, "Environmental Aspects of Ferro-Silicon Furnace Operations-An Investigation of Waste Gas Dynamics,", INFACON 8, Bejing China 1998

4 Michael Ksiazek et al. Measurement of metal temperature during tapping of an industrial FeSi furnace; Furnace tapping conference, South Africa, 2018.

5 HSC, Outotec Finland

6 Halvard Tveit, Elkem: Personal communication

7 A Hammervold, Cybernetica: Simulated temperature profiles using FeSiMod. Elkems proprietary simulation model for FeSi/Si processes. Elkem University 2017

8 K Aasly, V. Doshaj: Assessment of production performance of quartz in Si-furnace, Silicon for the Chemical and Solar Industry XIII, Kristiansand, Norway, 2016

9 E. Ringdalen, et al., Melting properties of quartz and its effect on industrial Si and FeSi production, in International Congress and Exhibition: Non- ferrous metals and minerals. 16-20, September 2019: Russia.

10 Elisabeth Nordnes: Softening and Melting Properties of Quartz, MSc thesis NTNU, Trondheim, Norway, 2019

11 Eli Ringdalen and Merete Tangstad, Reaction Mechanisms in Carbothermic Production of Silicon, Study of Selected Reactions, Proceedings of International Smelting Technology Symposium (Incorporating the 6th advances in sulphide smelting) held during TMS 2012, Editors: Jerome P Downey, Thomas P Battle, Jesse F White p. 195 – 204. ISBN 978-1-11829-116-0

12 Karin Fjeldstad Jusnes, Merete Tangstad, Eli Ringdalen: Cracks, Disintegration and Phases transformations in Quartz, Silicon for the Chemical and Solar Industry 14, Svolvær, Norway, 2018

13 Hanne Edfeldt: Pressure drop in charge mixture in silicon production, MSc- thesis, NTNU, Trondheim, Norway 2020.

14 Karin Jusnes, Merete Tangstad, Eli Ringdalen: Phase transformations in quartz used in silicon and ferrosilicon production: Met Trans B To be published 2020

15 Eli Ringdalen, Changes in quartz during heating and the possible effects on Si production; JOM (The Journal of the Minerals, Metals&Materials society (TMS) October 2014, ISSN 1047 -4838, DOI 10.1007/11837-014-1149-y

16 Merete Tangstad, Jafar Safarian, Sarina Bao, Eli Ringdalen and Aasgeir Valderhaug: Reaction Rates of $2SiO_2+SiC=3SiO+CO$ in Pellets at Elevated Temperatures, AMMS Vol 3, Issue 2, July 2019, AMMS.MS.ID.000558. 3(2).2019, Crimson Publishers, ISSN: 2578-0255

17 Marit B Folstad: Effect of Different Polymorphs of SiO2 on the reaction between SiO2 and SiC in Si-production. MSc thesis, June 2019, NTNU, Trondheim, Norway

18 Caroline Sindland: Reactivity of $Si+SiO_2$ mixtures, Specialisation project, Fall 2019, NTNU, Trondheim, Norway

19 S. Bao, M. Tangstad, K. Tang, and E. Ringdalen, Production of SiO-Gas in the Silicon Process, Infacon 13, Almaty, Kazakhstan June 9–12,2013.

20 Kurt Aasly: Properties and behaviour of quartz for the silicon process. PhD thesis 2008:236, NTNU Trondheim, Norway 2008, ISBN 978-82-471-1163-5

21 S. J. Stevens, R. J. Hand, and J. H. Sharp. The polymorphism of silica. Journal of Materials Science, 32:2929{35, 1997.

22 Marthe E Kjelstadli: Kinetics and Mechanism of Phase Transformation from Quartz to Cristobalite, MSc thesis, NTNU, Trondheim, Norway, 2016

23 R.C. Breneman, J.W. Halloran: Kinetics of Cristobalite formation in Sintered Silica: Journal of American Ceramic Society, 1-7 (2014), DOI 10.1111/jace.12889

24 E. Ringdalen, M Tangstad: Softening and melting of SiO_2, an important parameter for reactions with quartz in Si-production. 10th International Conference on Molten Slags, Fluxes and Salts (MOLTEN16) TMS (The Minerals, Metals & Materials Society), 2016

25 N. G. Ainslie, J. D. Mackenzie, and D. Turnbull. Melting kinetics of quartz and cristobalite. Journal of Physical Chemistry, 65(10):1718–1724, 1961. ISSN 00223654.

26 Vegard Andersen: Investigation of thermal properties of quartz for the silicon industry under reducing atmosphere: Project work TMT 4500, NTNU, Norway, 2009

27 Jafar Safarian et al: Interaction of silica and silicon carbide in silicon process, Presentation at The 10th International Conference on Molten Slags, Fluxes and Salts (MOLTEN16) TMS (The Minerals, Metals & Materials Society), 2016

Silicon for the Chemical and Solar Industry XV
Trondheim, Norway, June 15 – 18, 2020

Slag in the Tapping Area in a Si Furnace

M. B. Folstad[1)], M. Ksiazek C[2)], M. Tangstad[1)]
1) NTNU
2) SINTEF

Abstract

In 2019 a Si furnace was excavated and valuable tap-hole samples including the areas next to the tapping channel was collected from three different tap-holes. This paper presents comparison of observations and slag composition analyses from these three tap-holes. Visually, all tap-hole areas look similar. Closest to the Si channel is a green layer that consists of slag and SiC particles. Next is a grey layer that has larger SiC particles in addition to slag and some Al_2O_3. The slag is mainly of the SiO_2-CaO-Al_2O_3 system in various compositions, and the variations within the same tap-hole is in the same size range as between the separate tap-hole samples. From the liquidus and solidus temperatures it is found that the slag is liquid inside the furnace in the tap-hole area. The viscosities are found to decrease with increasing amount of CaO, the effect increases with increasing amount of SiO_2.

Introduction

Metallurgical silicon (Si) is produced industrially by carbothermic reduction of quartz (SiO_2) in a submerged arc furnace. The main literature describing the Si production process is Schei et al [1]. The overall reaction can be written as reaction 1, but the actual process is more complex.

$$SiO_2 + 2C = Si + 2CO_g \quad (1)$$

Figure 1 summarises the interior of a silicon furnace. However, the exact geometry will depend on the operation history. Condensate of Si, SiO_2 and SiC sticks the charge together and creates a void below the charge as the raw materials are consumed. The cavities surround the three electrode tips and are separated by charge materials in various states of conversion. SiO and CO gas fills the cavity, in addition to some other high temperature

gas species. It should be mentioned that earlier excavations [2]–[4] have found the size of the cavities to vary and will in some furnaces only be small gas channels. In the lower parts of the cavity walls are porous SiC, partly filled with molten Si. Since the SiC crystals are sintered together or grown into larger geometries, they make the upper part of the deposit firm enough to create a wall. Above the SiC, the materials close to the inner surface of the wall are heated enough to have some reaction. The materials closer to the furnace shell are rather inactive.

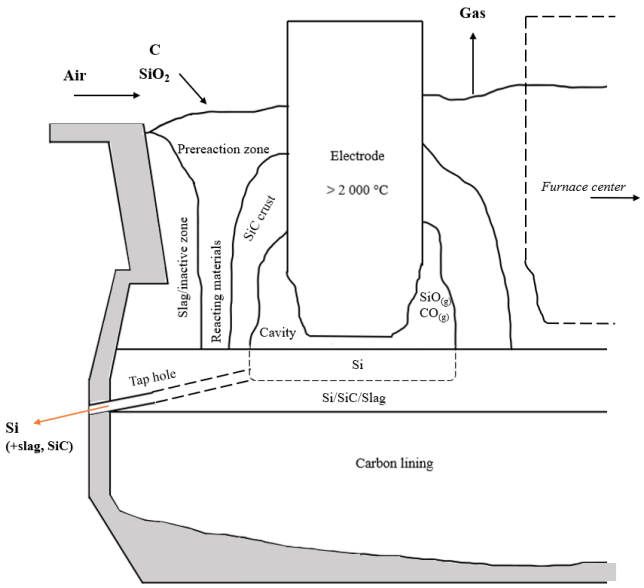


Figure 1 Schematic figure illustrating the interior of a Si furnace.

In a silicon furnace there is also several oxide impurities present, *slag*. Slag is typically found along the furnace walls all the way up to the charge top, in a thick layer at the furnace bottom and in the tap-hole area. One of the main differences found between the different Si furnaces is the extent of slag [2]. In some furnaces it is found large amounts of slag, while others have almost no slag accumulated in the furnace. Slag will affect the furnace operation. Slag that are pushed up in the low temperature zone in the furnace will start to solidify. In that way it will have the same impact as the condensed layer, it will stop the raw materials from descending and reacting further down in the furnace, and the reaction route will be narrower. The slag layer at the bottom will affect the tapping process. Unlike some other metallurgical production processes that have separate tap-holes for slag, it is only one common tap-hole in Si production. The tappers must work their way through the slag layer to the silicon bath. Since the slag is more viscous than silicon, it will clog the tap-hole and the tappers must work to keep the tap hole and the runner “clean”. Some of the slag will also be tapped together with the silicon.

The slag present in a Si furnace mainly consists of the SiO_2-CaO-Al_2O_3 system. Figure 2 shows the phase diagram of this system. Different compositions of these three oxides will affect the properties. Slag of mainly SiO_2 and Al_2O_3 have a high viscosity, while addition of CaO to the system will lower the viscosity so that the slag flow more easily through the furnace. Addition of CaO will also in most compositions lower the liquidus temperature.

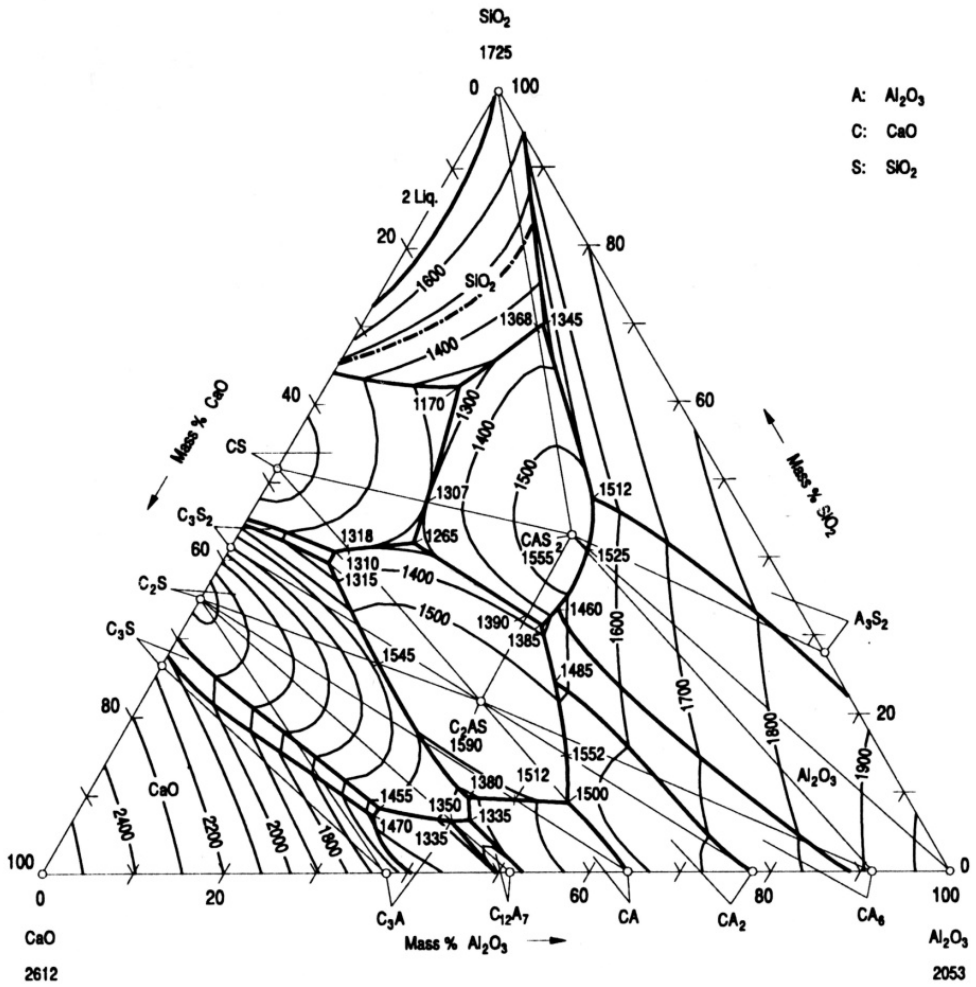


Figure 2 SiO_2-CaO-Al_2O_3 ternary phase diagram [7].

Si production has earlier been considered as a slag free process and the slag have therefore not been the focus during many of the earlier excavations. Nell and Joubert [5] analysed digout samples from tap-hole areas of a FeSi furnace, Bø [6] analysed slag samples from an excavation at Wacker Chemicals and Tangstad et al. [4] analysed a slag sample from the bottom SiC/slag layer from the excavation at Elkem Thamshavn. Their results are summarised the SiO_2-CaO-Al_2O_3 ternary phase diagram in Figure 3.

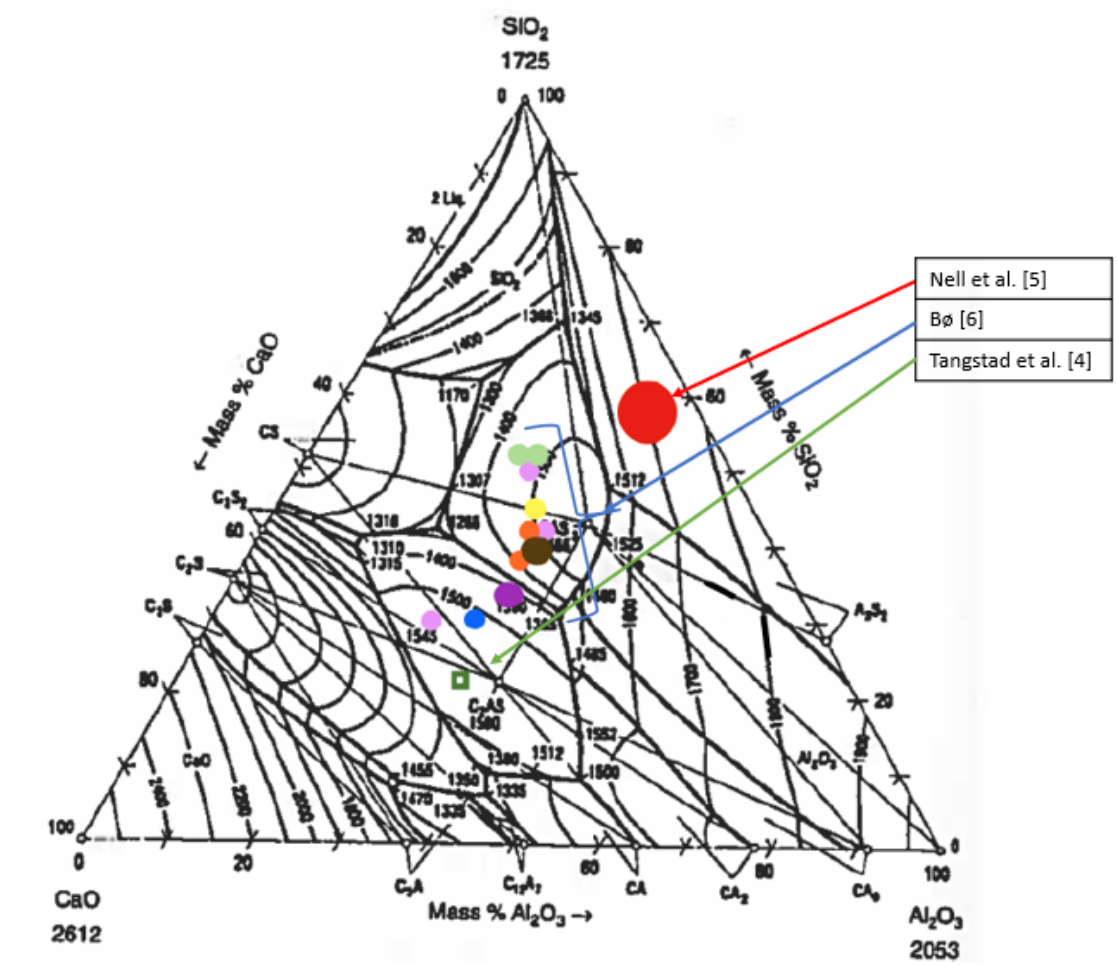


Figure 3 Comparison of slag analyses reported by Nell and Joubert [5], Bø [6] and Tangstad et al. [4].

Results and discussion

A Si producing furnace in Norway was excavated in 2019. The furnace was burned down before shut-down, and the excavation of the materials inside the furnace started three days after. The furnace has seven tap-holes. Samples from three different tap-holes A, B and C, including parts of the Si tapping channel together with the zones around was collected. Tap-hole C was last tapped before the excavation. The samples are studied and analysed with EPMA (Electron Probe Micro Analyzer) and EDS (Energy-dispersive X-ray Spectrometer). It should be mentioned that the samples from the furnace in this study has a higher amount of Al than the average Norwegian Si plant.

Zones around Si tapping channel

Visually, the zones around all the tap-holes appear similar. Figure 4 shows pictures of collected tap-hole samples. Closest to the Si channel is an approximately 5-15 cm thick green layer with slag and SiC particles. In addition, some SiO_2 is observed in this zone. Next is a dark grey area. This layer has larger SiC particles in addition to some slag and Al_2O_3. In both layers there is also some Si droplets. Earlier studies [1] have proposed that green colour slag have more Al_2O_3. This have not been confirmed in this study. In this study it is believed that the colour is more dependent on the size and amount of the SiC particles. From the composition analyses it can be seen that there are no significant difference between the slag composition in the green zone and the dark grey zone. Figure 5 shows two EPMA images from different coloured area and illustrates the different appearance of the SiC particles.

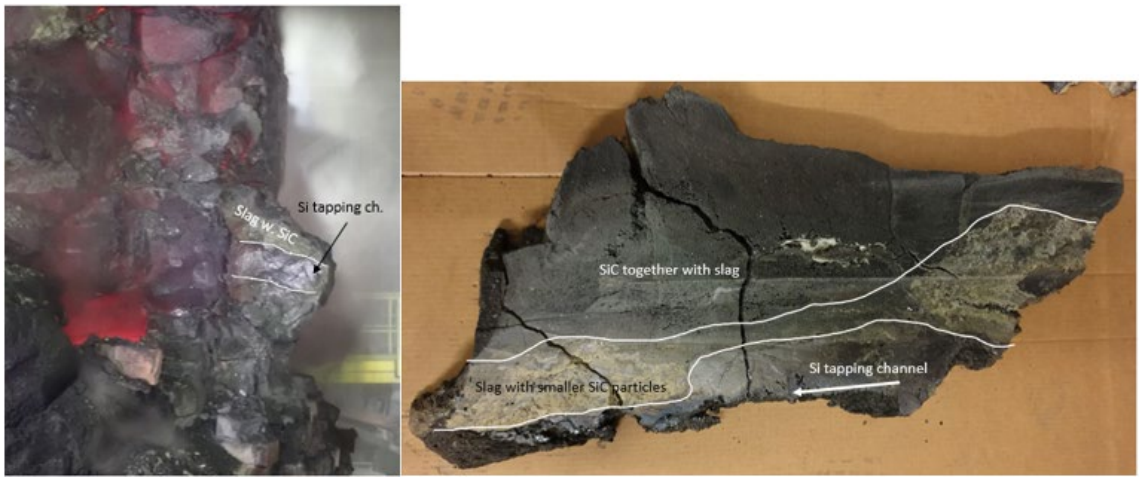


Figure 4 Slag samples collected from the Si furnace. The picture to the left is sample from tap-hole C, while the right picture is a cut-out plate from sample collected from tap-hole A. The material content in the layers are indicated on the picture. The arrow below "Si tapping channel" in the right picture gives the tapping direction.

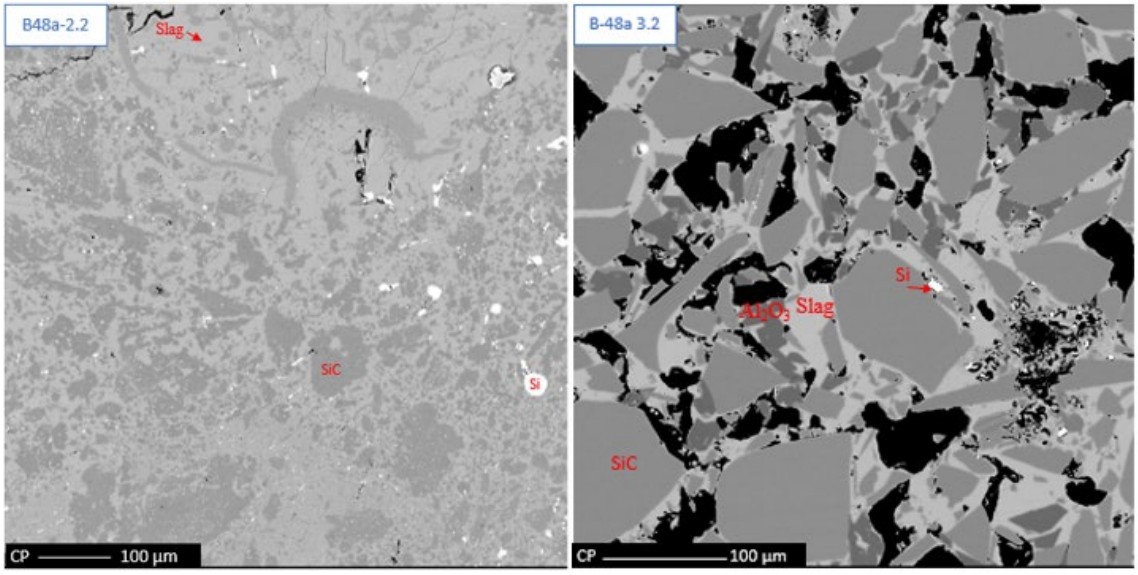


Figure 5 Microstructure of two samples from the same tap-hole sample. The left image is from the green coloured area and contains smaller SiC particles. The right image is from the grey coloured area.

Slag Analyses

The left figure in Figure 6 shows the analysed slag samples for all three tap-hole areas placed in the SiO_2-CaO-Al_2O_3 ternary phase diagram. Different shapes of the points are used to separate the different tap-holes. The slag compositions for these three tap-holes does not vary significantly, and the variations within the same tap-hole is in the same size range as between the separate tap-hole samples. For tap-hole A and C, samples were collected where the position above and below the Si tapping channel was known, shown in the right phase diagram in Figure 6. From those it can be observed a higher content of SiO_2 above the Si tapping channel. The CaO/Al_2O_3 relationship is approximately the same, ~1/1, for almost all slag analysed. Tap-hole C was last tapped before shut-down. The furnace was burned down before shut-down, but it is not observed any visual differences or found any significant differences in the slag analyses from tap-hole A and B. Burning down the furnace may result in larger amount of slag and/or other accumulated matter in the furnace in the area around the last tapped tap-hole. This was not found in this study.

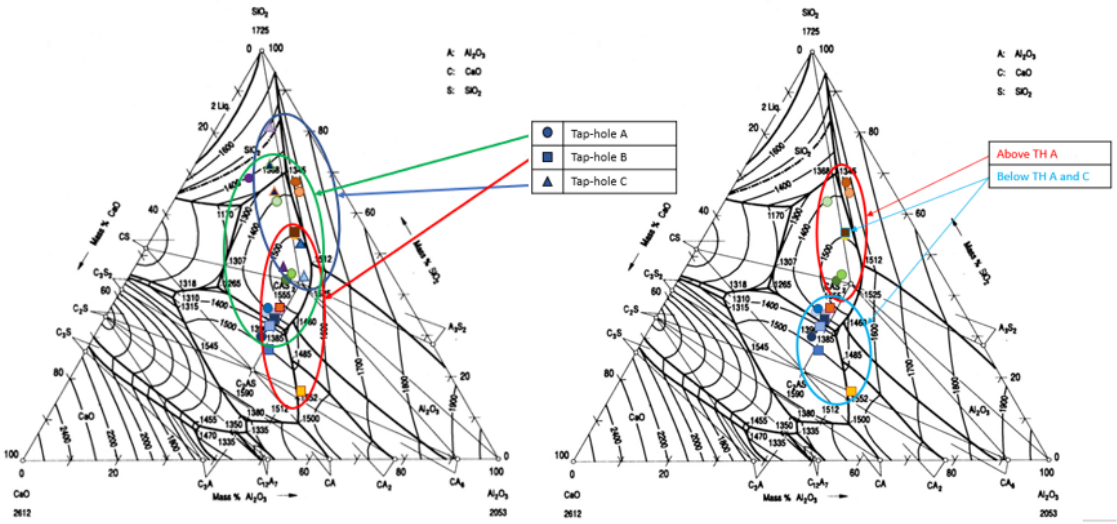


Figure 6 Samples from tap-hole A, B and C summarised in the SiO_2-CaO-Al_2O_3 ternary phase diagram to the left. In the right phase diagram, the circles separate the analysed samples from tap-hole A and C into above and below the tapping channel.

Resent temperature measurements of the tapped silicon in the tap-hole have found temperatures up to 1835 °C [8]. Table 1 lists the lowest and highest liquidus and solidus temperatures for the slag in the different tap-holes, and from this it can be concluded that all the slag was most likely liquid in the furnace tapping zone. SiC has a much higher melting temperature around 2700 °C, and solid SiC particles will therefore be present in the liquid slag phase inside the furnace.

Table 1 The lowest and highest liquidus and solidus temperatures found for the slag analysed from three different tap-holes.

Tap-hole no.	$T_{liquidus}$ *[°C]*	$T_{solidus}$ *[°C]*
A	1390-1540	1170-1512
B	1265-1610	1265-1585
C	1400-1550	1170-1512

For the samples with known position in the furnace it was found a higher content of SiO_2 above the Si tapping channel. A higher content of SiO_2 increases the viscosity. Figure 7 gives the viscosity at 1500 °C and 1800 °C with increasing amount of SiO_2 in a logarithmic scale. The viscosity area is shown in the SiO_2-CaO-Al_2O_3 ternary phase diagram to the right in the figure. The graph confirms an increasing viscosity with increasing amount of SiO_2, and the effect increases with increasing amount of SiO_2. This

gives that the slag over the Si tapping channel has a higher viscosity than the slag found in the lower parts. The difference is significant, also at 1800 °C. From the viscosity graphs it should also be noticed the great effect of temperature. It is of highly importance to have correct temperature measurements to know how to best operate with the slag in the tap-hole area. A lower slag viscosity is preferable to avoid accumulation in the furnace. Many plants add calcium in form of limestone to the process to obtain slag with a lower viscosity. Higher content of CaO gives a lower viscosity and makes the slag descend more easily through the furnace. Molten Si at 1500-1800 °C has viscosities of 0.004-0.005 Poise [9] and is possible to separate from the slag. It must be mentioned that the SiC particles will also increase the total viscosity of the slag, and hence the overall viscosity will be higher than the figure depicts.

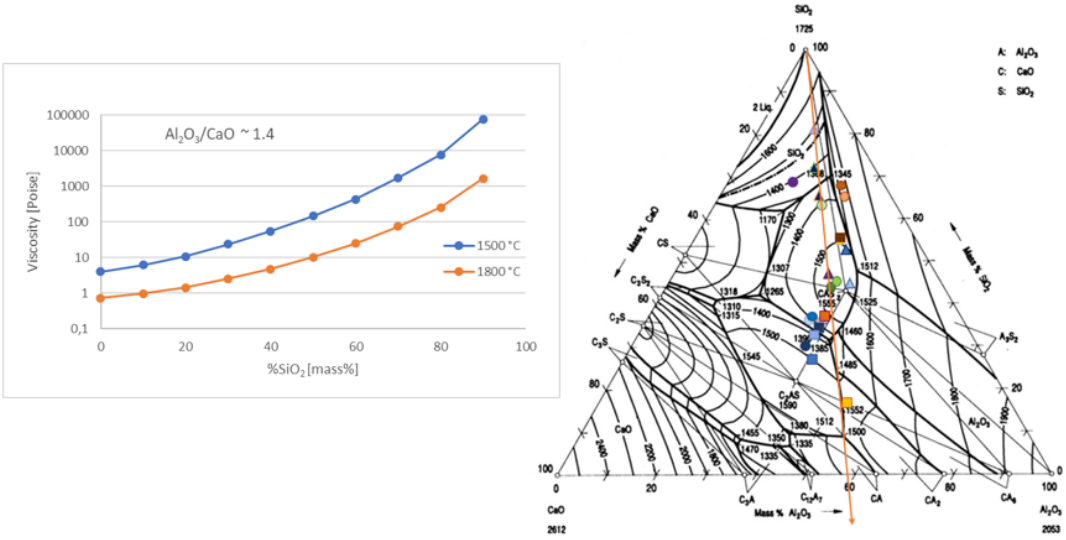


Figure 7 Viscosity versus %SiO_2 at temperature 1500 °C and 1800 °C. The Al_2O_3/CaO relationship is kept constant 1.4. The orange arrow in the ternary diagram gives the analysed area. The viscosity is calculated using FactSage7.3.

Conclusion

- Visually, the zones around all the tap-holes appear similar with a green zone closest to the Si tapping channel followed by a dark grey area. In this study it is believed that the colour is dependent on the size and amount of the SiC particles.
- The slag compositions for the three tap-holes does not vary significantly, and the variations within the same tap-hole is in the same size range as between the separate tap-hole samples.
- All slag collected from the tap-hole areas analysed in this study were in liquid state inside the furnace in the tapping area.

- Increasing amount of SiO_2 to the SiO_2-CaO-Al_2O_3 slag system increases the viscosity, and the effect increases with increasing amount of SiO_2.
- The slag samples with known position over the Si tapping channel contains a higher amount of SiO_2 than the samples with known position below, and will hence have a higher viscosity.

Acknowledgements

The authors would like to thank The Norwegian Ferroalloy Research Assosiation (FFF) and the Norwegian Research Council (NRC) are appreciated for their financial support through the KBN project Controlled tapping, project no 267621.

References

1. A. Schei, J. Kr. Tuset, and H. Tveit, *Production of High Silicon Alloy*. Trondheim: Tapir, 1998.
2. M. Ksiazek, M. Tangstad, and E. Ringdalen, *Five Furnaces Five Different Stories*, Silicon for the Chemical and Solar Industry XIII, 2013, p. 33–42.
3. K. F. Jusnes, *Excavation of a FeSi75 furnace at Finnfjord*, 2018.
4. M. Tangstad, M. Ksiazek, and J. E. Andersen, *Zones and Materials in the Si Furnace*, Silicon for the Chemical and Solar Industry XII, 2014.
5. J. Nell and C. Joubert, *Phase Chemistry of Digout Samples from a Ferrosilicon Furnace*, INFACON XIII, 2013, p. 265–272
6. S.M. Bø, "Phases and Zones in the Silicon Furnace," Master Thesis Norwegian University of Science and Technology, 2016.
7. V. D. Eisenhüttenleute, *Slag Atlas*. Verlag Stahleisen, 1995.
8. T. Werner, *As-tapped liquid silicon temperatures*, Master Thesis Norwegian University of Science and Technology, 2019.
9. M.J. Assael, J. Brillo, S.V. Stankus, J. Wu, W.A. Wakeham, Reference Data for the Density and Viscosity of Liquid Cadmium, Cobalt, Gallium, Indium, Mercury, Silicon, Thallium, and Zinc, Journal of Physical and Chemical Reference Data, 2012

Silicon for the Chemical and Solar Industry XV
Trondheim, Norway, June 15 – 18, 2020

SisAl – A New Process for Production of Silicon

Gabriella Tranell[1)], Jafar Safarian[1)], and Maria Wallin[1)]

1)Department of Materials Science and Engineering, Norwegian University of Science and Technology

Abstract

The integrated SisAl process, patented by NTNU, represents an environmentally and economically sustainable alternative to today's carbothermic reduction process in the Submerged Arc Furnace (SAF), allowing Si production in an increasingly carbon-lean world. The process utilizes secondary raw materials such as difficult Al scrap and dross as replacements for the carbon reductants used in today's SAF process, without direct CO_2 emissions, producing both Si alloy and an CaO-Al_2O_3-based slag from which metallurgical grade- or high-purity alumina, may be recovered. Quartz fines and Si refining sculls can be valorised as alternative silica raw materials to quartz lumps, enabling utilization of low-cost raw materials unsuitable for traditional Si production. The SisAl process will reduce material yield losses substantially, enhance valorisation of waste and by-product streams, at a 3 times lower energy consumption and radically lower emissions of CO_2 and other harmful pollutants. SisAl represents a strong contribution to "circularity" through industrial symbiosis where the aluminium industry acts as both a raw material supplier and end user to the silicon industry. The process has been demonstrated in both laboratory and small pilot scale and will be further developed through a project funded under the EC H2020 research program.

Introduction

Europe is a large producer of both **Silicon (Si)** and **Aluminium (Al**), two materials with extensive use in almost all modern society applications. The market for Si is linked to that of Al as approximately 50% of the global metallurgical grade silicon (MG-Si) consumption is used as aluminium alloying additive[1]. Si was added to the EU's list of Critical Raw Materials in 2014[2]. While Europe only makes 300-350.000 tonnes (10-12%) of the 2.9 million tonnes/year MG-Si produced globally - it uses a quarter of the world production[3]. The absence of substitutes for the wide range of Si end-uses and the dominant role of China enhances its critical character for Europe. With all current MG-Si production in Europe and internationally being carbothermic, the strong European focus to lower its greenhouse gas (GHG) emissions means that the silicon sector is exposed to a high risk of future carbon leakage.

Aluminium is primarily produced with the Hall-Héroult process by electrolysis of alumina (Al_2O_3) generated from bauxite ore through the Bayer process. While currently operated with carbon anodes resulting in significant CO_2 emissions from the process, new developments suggest that CO_2-free aluminium production may soon be within reach[4]. This development will put further pressure on suppliers to the Al industry -such as Si alloy producers - to lower their own carbon footprint. In the handling and processing of

(liquid) aluminium, there are different secondary product streams. One of the most significant losses of metal is in the formation of dross – an Al/Al_2O_3 mixture containing up to 80% Al metal. Processing and recovery of Al metal from dross, as well as avoidance of solid waste deposition, is important to the Al industry due to the lost value and the environmental impact. The total production of primary Al in Europe is about 4 M tonnes per year, generating about 60.000-80.000 tonnes of dross annually. Efficient recycling of scrap aluminium is high on the circular economy agenda for Europe but also for Al producers, as recycling reduces process emissions and creates economic value. While approximately 4.5 M tonnes of Al is recycled every year in Europe[5], since 2002 the EU has been a net exporter of aluminium scrap, particularly scrap that is challenging to recycle (coatings etc.), with typically between 500.000-600.000 tonnes exported annually[6]. Recycling of end-of-life Al scrap is however not without challenges and often increases the amount of dross generated during metal re-melting as compared to primary Al handling.

The SisAl process patented by NTNU[7] , links the production of Si and Al by utilizing secondary raw materials such as Al scrap and dross as replacements for the carbon reductants used in today's SAF process, without direct CO_2 emissions. Quartz fines and Si refining sculls can be valorised as alternative silica raw materials to quartz lumps, enabling utilization of low-cost raw materials unsuitable for traditional Si production. The SisAl process will reduce material yield losses substantially, enhance valorisation of waste and by-product streams, at a theoretically three times lower energy consumption. The SisAl approach represents a strong contribution to "circularity" through industrial symbiosis where the aluminium industry acts as both a raw material supplier and end user to the silicon industry. The European Commission, through the EU Horizon 2020 research programme, recently granted a 4 year, €14.5M budget pilot project, "SisAl Pilot", to bring the process to > TRL 7 through a partnership between Si- and Al industries and suppliers, SME´s, universities and institutes across Europe, the US and South Africa.

SisAl Process Concept

MG-Si is currently produced through carbothermic reduction of quartz in SAF with an electrical energy consumption of 11-13 MWh/tonne Si and a typical carbon material (coal, charcoal, woodchips) consumption of 2.5 tonnes/tonne Si. The CO gas produced in the furnace is combusted above the charge to CO_2 giving the process a direct CO_2 emission of approximately 5 tonnes/ tonne Si. The Si yield (typically 85-92% Si metal with respect to input Si in SiO_2), is determined by the mode of operation and the carbon material properties, with the rest of SiO_2-unit inputs ending up as micro-silica in the furnace off-gas. The furnace off-gas principally has the same energy content as that electrically supplied to the furnace. The only possible SiO_2 raw material to achieve gas permeability in the SAF is lump quartz. This is a serious restriction for the process in terms of resource efficiency with 5-15 wt% of on-site quartz being too fine to be used and hence sieved off prior to entering the furnace. This comes in addition to the losses to fines created during quartz mining. The raw metal produced in the SAF is tapped into a ladle where dissolved Ca and Al is refined by oxidation, resulting in the Si metal-infused (20-

30% Si) Al_2O_3-CaO-SiO_2 slag by-product (sculls), typically representing a yield-loss of up to 8% Si (on top of SiO_2 fuming losses).

The SisAl concept involves entirely different principles. In this process, Al scrap and dross are used to metallothermically (rather than carbothermically) reduce quartz to silicon. The integrated SisAl process, explained below, is shown in Figure 1.

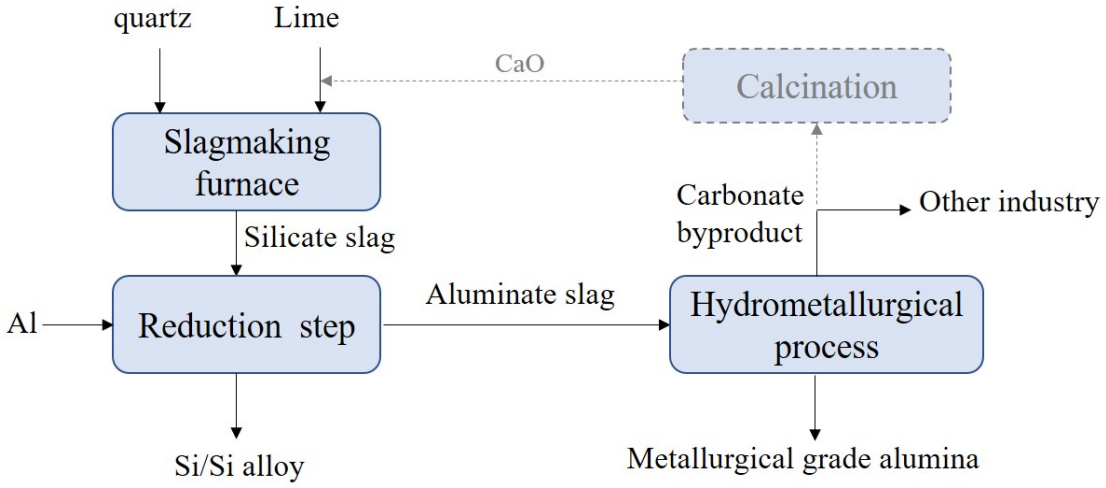


Figure 1. Schematic representation of the SisAl process

Summarised, the SisAl process consists of the following steps:

1. Combining silicon dioxide (preferably as less costly fines /fine material rather than lump) and calcium oxide in a vessel at a temperature sufficient to form a molten calcium silicate slag
2. Introducing a source of aluminium metal (Al scrap, dross etc.) to reduce the calcium silicate slag to Si metal and form a calcium aluminate slag; subsequently separating the Si metal from the calcium aluminate slag. The overall reaction for this main process step can be written as:

$$SiO_2 + 4/3Al = Si(l) + 2/3Al_2O_3 \qquad \Delta H_{1550^\circ C} = -174.8 \text{ kJ /mol} \qquad (1)$$

From the overall chemical reaction above there should be 4/3 mol of Al to one mol of Si present. This reduction reaction is advantageous as it yields liquid silicon at much lower temperatures around 1500-1600˚C compared to silicon production in a SAF, where MG-Si is formed at around 2000˚C. As this reaction is exothermic, limited energy needs to be supplied as the heat of reaction melts the Al scrap or dross added into the reduction-refining step. Depending on the raw material purity and mix, as well as operational choices, different Si compositions can be produced i.e. MG-Si and Al-Si.

3. Separating CaO and Al_2O_3 in the slag to individual compounds through a hydrometallurgical process. The hydrometallurgical process (a modification of the

hydrometallurgical step in the "Pedersen Process"[8]) typically involves the treatment of the slag with an aqueous sodium carbonate solution. A calcium carbonate precipitate is generated, which can be filtered from the remaining materials and calcined to generate calcium oxide. The filtrate is a saturated sodium aluminate solution, out of which solid aluminium hydroxide can be precipitated. In addition, if the aforementioned solution is treated with CO_2 gas, an aqueous solution is generated, containing $NaCO_3$ and NaOH (which is recycled to the slag digestion step). Calcination of the precipitated hydroxide yields high quality alumina. The alumina may have a purity of above 99% or more, since it is produced from the treatment of a high purity $CaO\text{-}Al_2O_3$ slag and is hence of a quality (and morphology) suitable for, among other applications, high purity aluminium production. Process step 3) is optional. Alternatively, the calcium aluminate slag formed in process step 2) can be sold to the market for use in e.g the EAF steelmaking industry. Furthermore, the aluminium hydroxide formed in process step 3) can be refined into high purity alumina for sapphire production and use in light emitting diodes or as an element in separators for Li-ion batteries.

The main electric energy use for steps 1 and 2 above is the production of slag, with a theoretical required electrical energy requirement of around 2 kWh per kg silicon product. The subsequent aluminothermic reduction of silica (step 2) does not require significant electrical consumption due to the exothermic reaction. Some of the raw materials, such as the Si sculls, can be added directly to the process, as the slag has already been formed.

The main advantages of this new integrated process are the following:

- The SisAl process achieves a lower environmental footprint by using secondary Al (with a low lifecycle CO_2 footprint) rather than carbon for reducing SiO_2 to Si, with a theoretical third of the energy consumption and a higher yield (no losses through SiO emission) than the SAF process. The SisAl process generates minimal NO_x, dust, PAH and SO_2.
- The SisAl process valorises dross material from the aluminium process and end-of-life, low value scrap into primary alumina feed for the Al electrolysis process or other high-end alumina uses
- The SisAl process is very versatile both in raw materials and products:
  - It can use quartz mining fines and fine (pure) quartz, which is not possible in the SAF Si process.
  - Recovers Si, Al_2O_3 and CaO from Si sculls, currently sold as a by-product, providing synergy with the SAF
  - Al dross/scrap ratio can be varied to make different qualities or replaced with high purity Al to produce pure Si
- By recycling CaO from the intermediate slag by-product, which is a possibility, the only raw material consumed in the SisAl process are quartz and aluminium.

Experimental Validation of the Aluminothermic Reduction of SiO_2 in Slag

A key step in the SisAl process is the aluminothermic reduction of silica in the $CaO\text{-}SiO_2$ slag to form a Si-alloy and a $CaO\text{-}Al_2O_3$ rich slag. Under equilibrium conditions, the Ca and concentrations in the Si-alloy will naturally reflect the slag composition for any given

metal/slag ratio. The equilibrium Al- and Ca- iso-concentration lines in liquid Si alloy at 1600°C is superimposed on the ternary Al_2O_3-CaO-SiO_2 phase diagram calculated by FACTSage 7.1[9], using the FToxid (slag) and the SINTEF ferroalloy databases, shown in Figure 2.

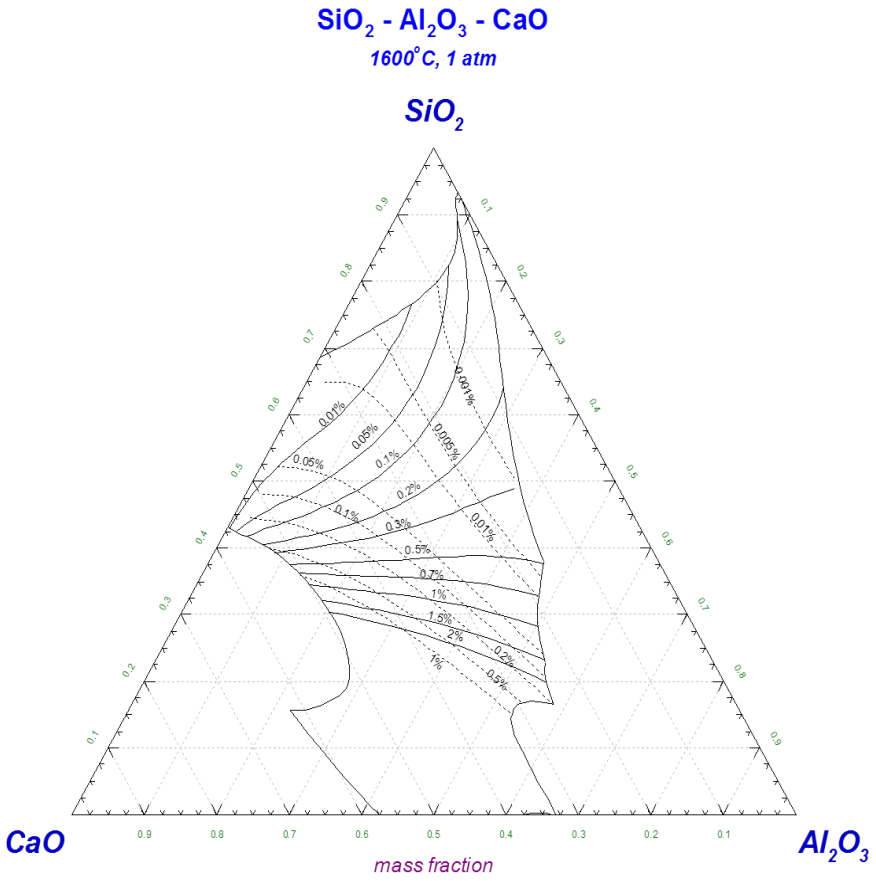


Figure 2. Calculated iso-concentration lines for Al (solid lines) and Ca (dotted lines) in equilibrium with a Si alloy at 1600°C.

The SisAl process and its reaction products were validated in laboratory and pilot scale as described below.

Laboratory scale trials

A large number of smaller, proof of concept laboratory trials have been carried out with different starting CaO/SiO_2 ratios in the slag and different stoichiometries and types of Al reductant (Al metal, Al dross) [7, 10]. As an example, a mixture of CaO+SiO_2 powders with molar ratio of CaO/SiO_2=0.67 was prepared (4 kg mixture). The mixture was heated up and smelted in a graphite crucible, while the temperature in crucible was continuously measured by a thermocouple. The smelting was performed in an induction furnace in a

closed chamber under controlled continuous argon (+99.999%) gas flow. The mixture became molten at temperatures between 1600˚C and 1650˚C, and the temperature stabilized to around 1600˚C. Pure aluminum metal was added to the liquid slag for the reduction of silicon oxide of the slag. The amount of Al was 90% of the stoichiometric ratio to reduce the majority of SiO_2 of the slag. The reaction started immediately through the contact of Al with slag through reaction (1) and the temperature of the melt increased rapidly to higher temperatures (1700˚C-1800 ˚C) during the Al addition and for a period after Al addition, before dropping to lower temperatures. The crucible containing metal and slag phases was cooled down after 30 minutes holding at elevated temperatures from the time Al addition was completed. The solidified metal and slag phases were separated and their chemical compositions determined using ICP-MS. The chemical compositions of the two phases were as follows:

- Alloy: 88.2%Si, 7.5%Ca, 4.1%Al
- Slag: 39.1%CaO, 56.0%Al_2O_3, 4.9%SiO_2

As seen above, we obtain a calcium-aluminate slag which is relatively low in SiO_2, and the majority of SiO_2 has been reduced to Si metal so that the alloy phase is silicon containing Ca and Al. The compositions of these phases are outside the region where data in the thermodynamic databases are considered reliable. This alloy phase is challenging to analyse in a representative manor due to the significant presence of precipitated intermetallic phases.

In order to lower the Ca and Al concentration of the alloy, one may envisage the SisAl process where slag and alloy are produced and reacted in a counter-current mode. To illustrate the result of such process implementation, the above produced metal (around 1 kg) was combined with a molten CaO-SiO_2 slag (CaO/SiO_2= 0.67) using the same approach as described above, with slag/metal mass ratio as 2/1. The process was again carried out at 1600˚C for 30 minutes, and the melts were cooled down and solidified in the crucible. Chemical analysis of the alloy and slag after the test result in compositions of:

- Alloy: 99.2%Si, 0.6%Ca, 0.2%Al
- Slag: 39.2%CaO, 57.5%SiO_2, 3.3%Al_2O_3

As noted from Figure 2, the Ca concentration is higher and the Al concentration lower than what is predicted by thermodynamic modelling for these phases in equilibrium but within the range of error expected at the scale of the current experiment.

Pilot scale trials

Pilot experiments have also been carried out at Elkem´s demonstration facilities in Kristiansand, Norway. The furnace used was a 300 kW induction furnace that was fitted with a specially ordered graphite crucible from Tanso (ø=600 mm, h=850 mm). The crucible was fixated with refractory cement in the furnace (Figure. 3a) and slowly heated over 24 hours to prepare for the experiments. A frame carrying a graphite impeller for stirring the melt was mounted on the furnace top (Figure 3b).



Figure 3 a) Crucible set in furnace **b)** Furnace fitted with frame for stirring

The stoichiometry for the charge mixture was such that a slag with a remaining content of approximately 5% SiO_2 would be achieved. As a basis for the experiment, a pre-made 48 wt%CaO-52wt%SiO_2 slag (Figure 4a) was used. The aluminum reductant used were pure Al bars (Figure 4b).



Figure 4 **a)** CaO-SiO_2 slag **b)** Al bars

230 kg of the CaO-SiO_2 slag was gradually melted (at effects from 50 – 200 kW) and an additional 10 kg of CaO powder added. This took approximately 6 hours. T=1660°C and power at 150 kW was recorded when the Al addition started. Aluminium bars, 60 kg, approximately 5 kg at a time were added over the course of 1 h. The temperature rose to 1720°C in the first 10 min and the furnace effect was turned down from 150 kW to 0W and then gradually turned up to 80-120 kW over the course of the Al addition to keep T at around 1550- 1580°C. The melt was continuously stirred with the graphite impeller. The melt was very calm – no boiling, gas eruptions or fuming. Samples are taken under way of metal/slag. The frame with impeller was lifted off before tapping started (1 h after

start Al addition). A visible pool of metal was observed at the centre top of the crucible. The furnace was tapped (Figure 5) by pouring into prepared moulds. Si is tapped first (Figure 6a) and subsequently slag in a second mold. (Figure 6b).



Figure 5. Removal of impeller and furnace tapping



Figure 6. a) Tapped metal **b)** Tapped slag

After cooling for 1h, the slag started to decrepitate, resulting in a powdery material. Samples of tapped slag and metal were taken and analysed by ICP. Although the composition of the alloy was not within the calibration region of the analysis and non-representative samples (due to the hardness of the alloy) analysed, a preliminary composition of the alloy and slag were measured as:

- Alloy: 40.5%Si, 5.1%Ca, 54.5%Al
- Slag: 50.6%CaO, 27%SiO_2, 27.8%Al_2O_3

Although the experiment was generally behaving as expected (calm, no smoking or foaming/boiling), it is clear that the design/stirring of the reactor was not effective/sufficient to reduce all the intended SiO_2 within the timeframe of the experiment and to establish equilibrium conditions. In future trials, more effective mixing and reductant addition practises will be applied.

Validation of Alumina recovery from the SisAl slag

The Pedersen hydrometallurgical process for producing alumina from calcium aluminate slags has been significantly studied at NTNU in recent years [11-14]. The produced slag from a laboratory scale trial was treated through the Pedersen hydrometallurgical process for alumina recovery. In this case, 20 g slag powder from the first step of the laboratory scale trial was digested by a solution made of 60g Na_2CO_3 and 20 g NaOH added to one liter of distilled water at 45°C. The digestion was done in a beaker stirred by a magnet with 250 rpm for three hours. The leaching yielded a solution with 9.61 g/L Al as measured by ICP-MS, with around 95% Al extraction, which was used later for alumina precipitation.

The precipitation of aluminum hydroxide from the solution was done through carbonation by the injection of Ar-30%CO_2 mixture into the solution. The precipitation step was done at room temperature and the temperature increased slightly from 21 to 23°C during the one-hour process. The precipitate was separated from the solution through filtration and was washed by distilled water and dried. The XRD analysis of the produced powder indicated a product of Bayerite and Gibbsite, which are to polyforms of $Al(OH)_3$. The particle size of the produced powder was measured, and it indicated a d50 of 31 microns, as found from the curve in Fig. 4. The size of the product can be controlled in the precipitation step with optimizing the process conditions.

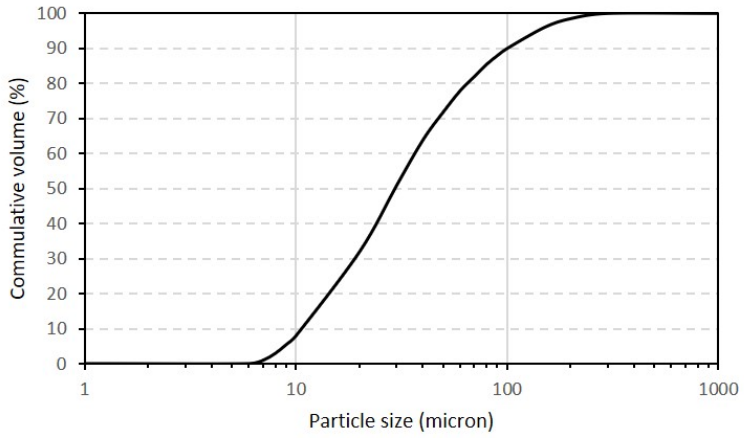


Figure 7. The particle size distribution of precipitated $Al(OH)_3$.

Conclusions

- A new integrated aluminothermic process to produce commercial silicon grades (the "SisAl" process) and metallurgical grade alumina was demonstrated in laboratory and pilot scale with successful results.
- The process has no direct CO_2 emissions, virtually no SiO losses to gas and an electric energy consumption theoretically less than 1/3 of the current SAF-based process.
- The SisAl process provides the possibility to valorise secondary industrial streams from the metallurgical industry such as SiO_2 fines, Si refining slags/skulls, Al scrap, Al dross etc to produce commercial grade Si-alloys. From a raw materials utilisation perspective, this is well aligned with current international sustainable development goals.

The SisAl process will be further developed in the EU H2020 funded pilot project "SisAl Pilot", in collaboration with industrial partners in the Si- and Al industries, SMEs and academia.

References

1. Roskill Market Report 2017. https://roskill.com/news/outlook-silicon-metal-diverges-sharply-ferrosilicon/
2. Communication from the commission to the european parliament, the council, the european economic and social committee and the committee of the regions on the 2017 list of Critical Raw Materials for the EU, COM (2017) 490
3. Roskill Market Reports, 2019 https://roskill.com/market-report/silicon-ferrosilicon/
4. V. Christ, *Elysis- the aluminium industry revolution at our doorstep*, TMS 2019, Keynote, 11 March 2019
5. European Aluminium. Data for recycling of Al scrap in Europe. https://www.european-aluminium.eu/media/1836/20170323-sustainability-performance-report.pdf
6. European Aluminium. Data for export of Aluminium scrap from Europe. www.european-aluminium.eu/data/recycling-data/recycling-eu-net-exports-of-aluminium-scrap/
7. J. Safarian, G. Tranell, European Patent No. 17826484.2 (3554998)
8. J. Safarian, Leiv Kolbeinsen, *Sustainability of alumina production from bauxite*, Sustainable Industrial Processing Summit and Exhibition, Nov. 6-10, 2016, Henan, China, Vol. 5, p 75-82.
9. Bale et al, "FactSage thermochemical software and databases, 2010–2016", CALPHAD
10. I. Meling, *Recycling and utilization of secondary aluminium products*, Masterthesis, NTNU, 2018

11. F. I. Azof, M. Vafeias, D. Panias, J. Safarian, *The leachability of a ternary CaO-Al_2O_3-SiO_2 slag produced from smelting-reduction of low-grade bauxite for alumina recovery*, Hydrometallurgy, **191**, 2020, p 105-184.
12. F. I. Azof, Y. Yang, D. Panias, L. Kolbeinsen, J. Safarian, *Leaching characteristics and mechanism of the synthetic calcium-aluminium slags for alumina recovery,* Hydrometallurgy **185**, 2019, p273-290.
13. F. I. Azof, L. Kolbeinsen, J. Safarian, *Kinetics of the leaching of alumina-containing slag for alumina recovery*, Proceeding of European Metallurgical Conference, EMC 2019, **2**, p511-526.
14. E. Nedkvitne, *Leaching and precipitation experiments related to the Pedersen Process*, Master thesis at NTNU, 2019.

New Philosophy for Metal Production in a Green Environment

Bjørn Sandberg[1)], Ragnar Tronstad[1,2)]
1) Styrhuset AS,
2) Eyde Cluster

Abstract

A huge number of scientific studies and industrial improvement work have these days focus on reducing CO_2 emission from process industry both by CCUS (carbon capture use and storing), by changing reductant from fossil carbon to biocarbon/ hydrogen or by developing/using new process technology. This paper describes a "new" zero CO_2 emission philosophy for metal production. The process is exemplified by magnesiothermic production of silicon from forsterite clustered with Norsk Hydro's process for magnesium production.

Project background

During the last 20 years focus on CO_2 emission has increased in transport sector. Electrical cars and ferries have been tested and put into daily operation, and today a majority of new cars sold in Norway are fully electrical or hybrids. The same trends are also seen in the industry and Statoil started as early as 1996 to return CO_2 from platform in the North Sea back to the subsea formations. The land-based industry has followed and Norcem, Norway, ran test programs at their cement plant in Brevik and developed a concept together with suppliers of CO_2 catch equipment which is becoming a standard for the cement industry. Other parts of the industry have focused on replacing fossil carbon, as reductant and fuel, by biocarbon. However, there are limitations for some industries that make it difficult to remove sufficient amounts of CO_2 to reach the European New Deal goals for 2030. The silicon industry is one example where carbon as reductant cannot be replaced by hydrogen and the raw materials must have sufficient strength to withstand the charge pressure without disintegration. Present technology also needs mechanical assistance to force the charge through the furnace, and this is made possible by open furnace operation. The CO_2 concentration of the emitted fume is therefore low due to mix in with air, and this make CO_2 catch technologies inefficient and expensive.

This paper focusses new philosophies for metal production when renewable power is available.

Process idea

Background

Norsk Hydro has developed a process for production of magnesium based on electrolysis of magnesium chloride. The input raw material for the process was originally based on sea-water magnesia converted to chloride. However, with the access to a much cheaper raw material from China – magnesia – (Mg_2CO_3) Hydro's plant in Becancour Canada was build based on this starting material. As the Chinese set out to become leading supplier of magnesium globally based on access to cheap domestic materials and efficient supply chain (for the competing Pidgeon process), Hydro decided to abandon magnesium production in 2006.
The company AMG was some 20 years ago developing a process for production of precipitated silica based on dissolving silicate materials in hydrochloric acid. One such material was the magnesium-silicate-rich mineral olivine which "theoretically" consists of Forsterite, a magnesium silicate ($2MgO \cdot SiO_2$) containing some 7 % iron silicate (Fayalite - $2FeO \cdot SiO_2$) as "impurity". As this process yields magnesium chloride in addition to precipitated silica, AMG partnered with Hydro to establish the company SilMag in 2008 at Herøya, Norway. In spite of successful (small) pilot scale production of precipitated silica and magnesium chloride, SilMag failed to attract investors for large scale production of the precipitated silica. One will observe that a successful outcome would have resulted in a "CO_2-free" production of magnesium provided that the electrolysis is based on renewable energy like hydroelectric power.

Mineral conditioning/synthetic minerals.

The direct dissolution of minerals – like olivine, which consists of a number of mineralogical phases including phases containing crystal water – may take place under pretty tough conditions (pH, temperature, pressure, time etc.). As the incoming mineralogical phases may also vary – including a range of impurity elements – leaching of olivine may prove an expensive challenge.
One way to circumvent this may be to "pre-condition" the mineral. In the case of olivine – which is basically of forsteritic overall composition – one way of conditioning would be to fuse the mineral in a submerged arc furnace where the iron impurity elements (Fe, Ni, Cr, Mn) of the fayalite will be reduced at the carbon electrode to metal/alloy (leaving a small CO_2 footprint). To avoid reduction of excessive silica in the melt, some MgO will be added to ensure a melt of "pure" forsterite. As a result, one would expect a faster, easier dissolution process.
Such principles may also apply for other silicate minerals, including optimisation of composition (Fig. 1).

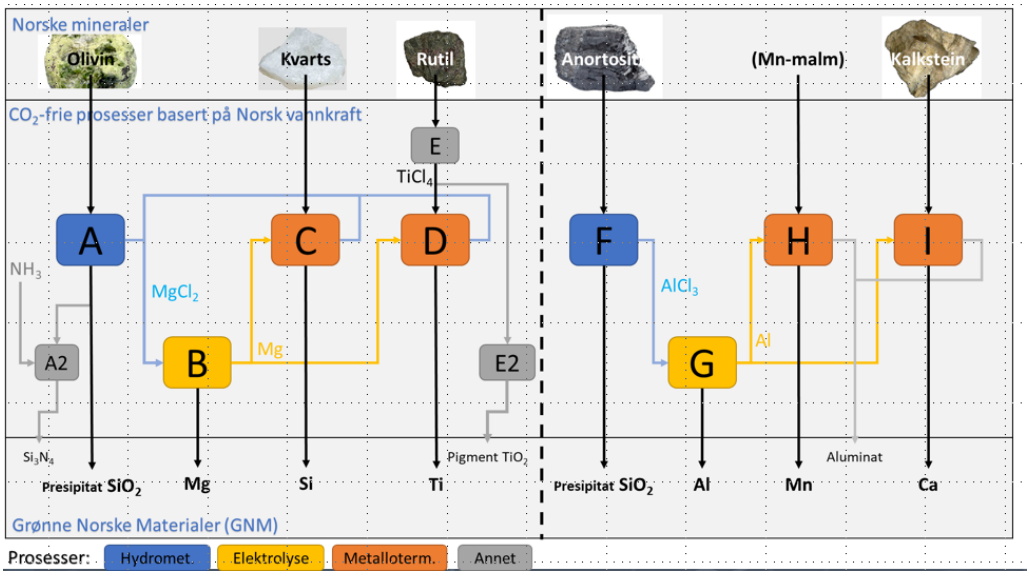


Figure 1: Alternative use of Norwegian minerals (exemplified by Olivine/ Quartz/ Rutile/Anorthosite/Manganese-ore/Limestone) in "CO_2-free" metal production (exemplified by process technologies; hydrometallurgy/electrolysis/metallothermic reduction/other).

Fusion of minerals has a relatively low energy input (1-3 kWh/kg).
An application for funding of development of a "CO_2 free" magnesium process including the above steps have been submitted to EU under the Horizon 2020 framework by Sintef/NorMag (SilMag).

Silicon production by magnesiothermic reduction

At the onset of the "Solar revolution" some 20 years ago there became quickly a silicon shortage, and several companies/research institutions rushed to develop new technologies for production of solar grade silicon. One route was reduction of quartz sand with magnesium powder (thermite reaction). Apart from a few publications, no significant volumes appeared on the market.
Similarly, 15 year later, at the onset of the "Battery revolution", the magnesiothermic reduction of quartz attracted renewed interest, this time especially for the potential nano-sized silicon particles that can be obtained through this reaction.
Once again, it is reaction between SiO_2 (quartz sand, fumed silica, silica fume) and magnesium that has attracted interest.
Under various process conditions (temp./mixing ratio, oxygen access etc.) a number of reactions and reaction products may occur (like Mg_2Si and $2MgO.SiO_2$ -fosterite).Our proposal is thus quite simple: Instead of reducing quartz with magnesium, one will actually reduce forsterite (as produced from olivine) with magnesium (1):

$$2MgO \cdot SiO_2 + 2\ Mg \Rightarrow 4MgO + Si \qquad (1)$$

The resulting MgO is dissolved in HCl and silicon removed. The magnesium chloride is returned to the Hydro electrolysis process whereafter half of the magnesium is returned to the reduction of fosterite, the other half for commercial applications (Fig. 2).

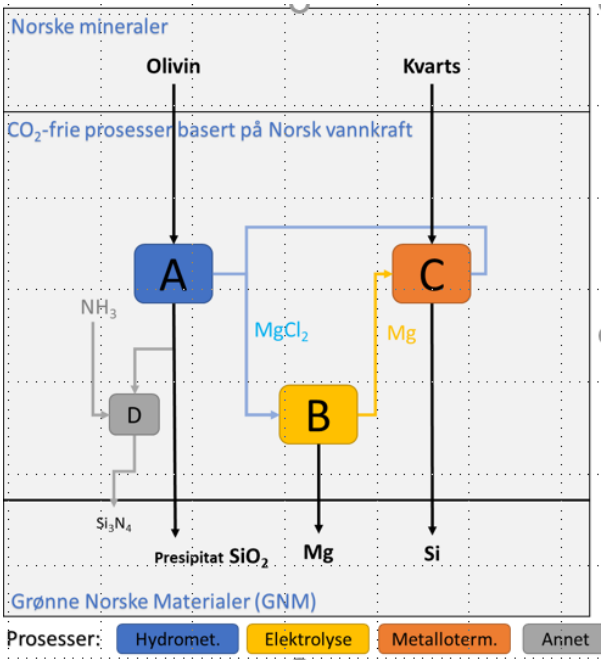


Figure 2: Metallothermic production of Si with full utilization of by-products

In this concept, all components (except oxygen) of the mineral olivine will be converted to saleable metals with no waste.
The silicon is produced with a recyclable reductant.

Ongoing activities

Development of the magnesium project is run as a separate project managed by NorSil. The silicon project has started with the main goal to evaluate the potentials for the described process compared to present process with CCS. Both cost, energy consumption and carbon footprint will be studied. Results from this work will be published this autumn.

Acknowledgement

The project is included in the Eyde Cluster portfolio and financially supported by Gassnova.

Silicon for the Chemical and Solar Industry XV
Trondheim, Norway, June 15 – 18, 2020

Advanced insights into the stoichiometry and kinetics of the reaction of silicon in HF/HNO_3 and $HF/HNO_3/H_2SiF_6$ mixtures

Anja Rietig, Thomas Langner, and Jörg Acker
Brandenburg University of Technology Cottbus-Senftenberg, Department of Physical Chemistry, 01968 Senftenberg, Germany

Abstract

The stoichiometry and kinetics of wet chemical etching of silicon in HF/HNO_3 and $HF/HNO_3/H_2SiF_6$ mixtures was investigated. The side reactions and main reaction pathways were identified by quantifying all reaction products. The relationship between the concentration of undissociated HNO_3 and the consumption of HNO_3, as well as the formation of H_2 as a function of the mixing ratios were found by varying the etching mixture composition systematically.

Based on the etching rates determined, kinetic models for the reaction- and diffusion-controlled reaction mechanism are presented as well as the interrelation between the etchant composition and the transition between reaction- and diffusion-controlled etching.

Introduction

Wet chemical etching of Si in HF/HNO_3 or $HF/HNO_3/H_2SiF_6$ mixtures is a widely used process in the semiconductor and solar industry. The process is used for the removal of saw damage and texturing of the Si surfaces. The first studies on the HF/HNO_3 system were carried out by Robbins and Schwartz [1-4]. They divided the process into two steps: (i) The oxidation of the Si with HNO_3 to SiO_2, in which the HNO_3 is reduced to NO, and (ii) the dissolution of the SiO_2 by HF. Equation 1 describes the overall reaction.

$$3\,Si + 4\,HNO_3 + 18\,HF \longrightarrow 3\,H_2SiF_6 + 4\,NO + 8\,H_2O \qquad (1)$$

By contrast, Turner described the dissolution of Si in HF/HNO_3 as an electrochemical process, in which anode and cathode reactions take place at separate positions on the Si surface [5]. The two models have in common that NO, H_2SiF_6 and H_2O are considered as the only products of the reaction.

However, more recent studies have shown that these models do not represent the actual reaction process, nor do they describe the stoichiometry of the reaction sufficiently, since

numerous other reaction products have been detected. In addition to the formation of H_2 [8,13], many other reduction products of HNO_3, such as NO_2, N_2O_4 [7,11], N_2O [7,8], N_2O_3 [9], NH_4^+ ions [12] and N_2 [23] were identified.

Based on the data of Steinert et al. [9-12] and a first quantitative study of the formation of H_2 as a function of the etching bath composition by Hoffmann et al. [13], Acker et al. [14] established a first mass and electron balance for the oxidation of silicon. However, the balance contains a considerable gap between the amount of N-species consumed and formed, because only the dissolved species NH_4^+ and NO_2^-, representing a sum parameters for dissolved N(III) species, were quantified. The gap in the balance is caused by several unquantified nitrogen oxide compounds, which evolve mainly as gases from the etching solution. These compounds, summarized as "non-detected N-species," contribute almost half of the electrons to the oxidation of Si oxidation in the model presented.

Rietig et al. succeeded in quantifying the gaseous products and proved that the majority of the reaction products detected are products of side reactions of the reduction of HNO_3 and the formation of NH_4^+ [23]. The major conclusion was that H_2SiF_6, H_2O, NO and H_2 are the only primary reaction products formed in the dissolution of Si according to the overall equation (Eq. 2).

$$\mathrm{Si} + \frac{z}{3}\,\mathrm{HNO_3} + 6\,\mathrm{HF} \longrightarrow \mathrm{H_2SiF_6} + \frac{4-z}{2}\mathrm{H_2} + \frac{z}{3}\mathrm{NO} + \frac{2}{3}z\,\mathrm{H_2O} \qquad (2)$$

The parameter z ranges between $2 \leq z \leq 4$ and describes the number of electrons accepted by the N atom of HNO_3. The limit $z = 4$ leads to the overall equation (Eq. 1) postulated by Robbins and Schwartz [1-4], while at the lower limit $z = 2$, exactly 1 mol H_2 per mole of dissolved Si is formed, which corresponds to the stoichiometry of etching in diluted HF at low current densities.

Robbins and Schwartz found a functional relationship between the etching kinetics and the composition of the etching bath in their studies [1-4]. The oxidation of Si in HF-rich mixtures turned out to be rate-determining ($E_A \approx 45$ kJ mol^{-1}), while the dissolution of Si in HNO_3-rich mixtures is rate-determining and controlled by diffusion ($E_A \approx 17$ kJ mol^{-1}). Furthermore, they showed an increase in etching rates and the elimination of the characteristic induction period when nitrite salts were added to the etching solution. They concluded that the HNO_2 concentration in the boundary layer must first exceed a limit to start the reaction. Since the HNO_2 required is constantly reproduced in the reaction by an equilibrium between HNO_2 and various dissolved N-oxides, the reaction was considered autocatalytic by Abel and Schmid, however, without any experimental evidence [6].

Steinert et al. investigated how different compositions of the mixture change the formation of N(III) species (chromatographically determined as the sum parameter NO_2^-) and the dissolution rates with varying temperature and level of stirring of the etching mixture during the reaction [9-11]. They found a linear relationship between the NO_2^-

concentration and etching rate in HF-rich mixtures up to a threshold from which the etching rate remained constant. In addition, they demonstrated a reduction of the etching rate with increased stirring speed, which was explained by the removal of the reactive N(III) species from the Si surface. A correlation was found between the etching rate and a Raman signal at 2245 cm^{-1}, which can be assigned to the complex $N_4O_6^{2+}$ [15]. The formation of the complex $N_4O_6^{2+}$ as an adduct of ($NO_3^- \cdot 3NO^+$) finally motivated Steinert to classify the nitrosyl cation NO^+ as a rate-determining species. The impact of an excess of N(III) species in the etching mixture has been extensively investigated, but only a few investigations have been carried out on freshly prepared etching mixtures. Meinel et al. found that the etching rate of the saw-damaged area is considerably higher than the bulk etching rate [16]. This increase in reactivity in the saw-damaged areas was caused by lattice strain in the silicon crystal [17]. However, since the etching solutions previously investigated vary both the HNO_3 and the HF concentration, the data are not suitable for establishing a functional relationship between the composition of the etching mixture and the etching rate in a kinetic model. Only a few papers, which are all exclusively based on the HNO_3 content in the mixture, offer mathematical relationships for the dissolution rate over time [18, 19]. Assuming a diffusion-controlled etching mechanism due to the high HNO_3 content in $HF/HNO_3/H_2SiF_6$ mixtures used for industrial texturing of solar wafers, Blocks carried out numerous etching experiments to find a kinetic model dominated by the minor component HF [20]. He tested both the second (b = 2) and the fourth order reaction (b = 4) for HF in the model (Eq. 3), while the first order (a = 1) was used for undissociated HNO_3. The impact of H_2SiF_6 on the mixture was considered negligible.

$$r \approx \left(\frac{d\mathrm{n(Si)}}{d\mathrm{t}} \right) = k_\mathrm{i}(\mathrm{T}) \cdot [\mathrm{HNO_3,undiss}]^\mathrm{a} \cdot [\mathrm{HF}]^\mathrm{b} \qquad (3)$$

The temperature-dependent rate constant $k_i(T)$ is given by the Arrhenius law. Although both models (b = 2, b = 4) showed a linearization of individually selected data sets, neither of the models could explain all concentrations. Blocks suggested that the model (Eq. 3) would have to be extended by a term involving the reactive N(III) species ($k_j(T) \cdot [N(III)]^c \cdot [HF]^b$) [20]. Although wide concentration ranges of the three acids were covered, Blocks' data did not include enough mixtures with at least two constant components. It is, therefore, difficult to make a reliable prediction about the kinetic model.

In order to get a functional relationship between the etching kinetics and the composition of the etching bath, a systematic variation of the different components must be carried out to adequately describe the changes between the two reaction mechanisms already characterized.

Experimental

Reagents

All etching mixtures were prepared by weighing the starting materials HNO_3 (67% (w/w), p.a., Merck), HF (48% (w/w), p.a., Merck), H_2SiF_6 (45% (w/w), pure, Fluorchemie Dohna) and distilled H_2O (18 MΩ cm^{-1}). The etching experiments were performed using pieces of Si(100) wafer (thickness 508 µm, p-type, < 5 mΩ cm^{-1}) from Silchem GmbH Freiberg, Germany.

In order to compare the quantities used, even though the density differs between the etchant mixtures, the concentrations of all components are given as specific molar partial quantities q_i, defined as follows.

$$q_i = \frac{n_i}{m} \qquad (4),$$

where i describes the component in the etching mixture, n_i its absolute amount of substance and m the total mass of the etching solution.

Analytical methods and instrumentation

The nitrate concentration was determined by ion chromatography (881 Compact IC pro, Deutsche Metrohm GmbH) after aqueous dilution with a factor of ≥ 4800 (depending on the composition of the etching mixture) in a triple determination. The separation was performed at 35 °C in an eluent flow of 0.7 mL min^{-1} (1 mmol L^{-1} $NaHCO_3$ / 3.2 mmol L^{-1} Na_2CO_3) on a 250 x 4.0 mm ASupp5 column (Deutsche Metrohm GmbH). A conductivity detection was carried out after a chemical conductivity suppression. The determination of the ammonium ions was also performed by ion chromatography (761 Compact IC, Deutsche Metrohm GmbH) in aqueous dilution with a factor of 360 via direct conductivity detection after separation at room temperature and an eluent flow of 1.5 mL min^{-1} (4 mmol L^{-1} HNO_3 in 30% methanol) on a 150 x 4.1 mm PRP-X200 column (Hamilton). Matrix-matched 10-point calibrations, which were prepared from single element standards (1 g L^{-1}, Supelco), were used for quantification for all IC analyses.

The concentration of undissociated HNO_3 in the etching mixture was determined, according to the method of Langner et al. [24], by means of Raman spectroscopy (DXR SmartRaman, Thermo Scientific). The excitation wavelength of the laser was 532 nm and the laser power 10 mW.

The gaseous reaction products H_2 and NO_x were determined by means of a quadrupole mass spectrometer with a Faraday detector (GSD 320 OmniStar, Pfeiffer Vacuum GmbH). An argon stream of 45 mL min^{-1} (Ar 6.0, Linde AG) flows continuously through the reaction triple-neck flask. The mass spectrometer removes 2 sccm from the reaction gas stream via a T-connection, while most of the reaction gas is supplied into the exhaust gas. The calibration of N_2, O_2 and Ar was done by measuring the compressed air. H_2O was calibrated by measuring the ambient air via the relative air moisture. NO and NO_2

were calibrated using calibration gases (15% NO in Ar, 10% NO_2 in Ar, Westfalen AG) and N_2O as pure substance (99%, Fackelmann). The calibration of H_2 was performed as a multipoint calibration by dissolving different masses of Zn (p.a., granulated, Merck) in hydrochloric acid solutions of different concentrations (diluted from HCl, 37% (w/w), p.a., Merck). A detailed description of the quantification method is given in [23].

Etching experiments

A defined amount of etching mixture was weighed into a PFA flask for each experiment and tempered to the required reaction temperature using a cryostat (MPC-K12 CC2, Huber Kältemaschinen GmbH). The mixtures were stirred at 360 rpm during the whole reaction time. Well-defined squares of silicon pieces of different lengths, each 508-µm thick (p-type, < 5 $m\Omega \cdot cm^{-1}$, (100), Silchem GmbH Freiberg, Germany) were dissolved in the etching mixture and the process temperature was recorded at 5-s intervals using a PTFE-coated PT-100 temperature sensor.

Determination of etching rates

The etching or dissolution rates are derived from the slope of the conversion curves. The conversion curve for dissolving a Si piece, i.e. the cumulated dissolved mass of silicon with the reaction time, is calculated with the help of Newton's cooling law. The latter states a proportional cooling to the temperature difference to the ambient area. Assuming that the composition of the etching bath does not change during the experiment, the cooling down process can be described as follows.

$$T' = \frac{dT}{dt} = k \cdot \left(T_t - T_U \right) \tag{5}$$

After solving the differential equation, the value for the cooling rate k can be determined by plotting the logarithmic term. T_U describes the surrounding temperature. Using equidistant values for t and solving the equation according to the temperature of the etching mixture at the time t (T_t), the cooling down rate results as a function of the bath temperature:

$$\left(\frac{dT}{dt} \right) = f\left(T_t \right) \tag{6}$$

The slope observed in these time intervals is corrected by the cooling rate at the corresponding bath temperature. This correction provides a temperature profile that corresponds to an adiabatic reaction process with an acceptable approximation. Since the conversion and temperature curves are linear to each other in an adiabatic reaction process, the conversion curve for dissolving the Si piece can be described as follows.

$$\chi = \frac{T_{adia(t)} - T_{start}}{T_{adia(max)} - T_{start}} \tag{7}$$

The dissolution rate r_{diss} is normalized to the twice-surface area of the Si-piece to ensure comparability between the etching rates of differently sized Si-pieces. The edges can

usually be neglected. The etching rate r_{etch} [nm s^{-1}] and the dissolution rate r_{diss} [mg min^{-1} cm^{-2}] frequently used are related in the following way, whereby all values must be entered in SI units,

$$r_{etch} = \frac{2 \cdot 10^7}{60 \cdot \rho_{Si}} \cdot r_{diss} \approx 143 \cdot r_{diss} \quad (8),$$

with $r_{etch}\left[\mathrm{nm \cdot s^{-1}}\right] = \frac{(m_1 - m_2)}{\rho_{Si} \cdot A_G} \cdot \frac{1}{t_{etch}} \cdot 10^6$ and $r_{diss}\left[\mathrm{mg \cdot min^{-1} \cdot cm^{-2}}\right] = \frac{(m_1 - m_2)}{2A_G} \cdot \frac{60}{t_{etch}} \cdot 10^{-1}$.

The major advantage of the method of determining the etching rate by temperature is that the dissolution rates can be determined solely for the bulk Si and for different mixtures at identical reaction temperatures. The words etching rate and dissolution rate are often used synonymously throughout the paper.

Results and discussion

Stoichiometric studies

Several studies were carried out using an etching mixture containing 15 mol kg^{-1} HF and 2 mol kg^{-1} HNO_3 with the aim of complete quantification of all reaction gas phase constituents. One Si piece was dissolved in the etching mixture after the other, and the gas phase was analyzed by means of mass spectrometry (MS). Sampling of the etching mixture was carried out when no more gaseous by-products could be detected in the inert gas flow, so that the etching mixture was mainly free of dissolved NO_x. It was found that the consumption of HF and HNO_3 leads to a significant increase in H_2 formation, and that the absolute amounts of H_2 formed and Si dissolved does not yield to a linear relationship. It is necessary to carry out the experiments in a quasi-stationarity state to gain information about the H_2 formation per mole of dissolved Si as a function of the etching bath composition. This means utilizing an infinite excess of etching mixture and an etch regime that leads to the lowest possible temperature increase in the reaction bath. The impact on the H_2 formation per mole of Si dissolved is shown in Figure 1 for mixtures with 15 mol kg^{-1} HF/ 2 mol kg^{-1} HNO_3 and 6 mol kg^{-1} HF/ 5 mol kg^{-1} HNO_3 as a function of the ratio between the etching bath volume and the Si dissolved therein (V_{etch} : m_{Si} [mL mg^{-1}]). The experiments show that constant stoichiometric ratios between H_2 and Si are found only from a ratio of V_{etch} : $m_{Si} \geq 0.75$ mL mg^{-1}. The $n(H_2)$: n(Si) ratio is 70% lower than the data of Hoffmann et al. [13], that are based on a ratio of 0.13 mL mg^{-1}. At the same time, the results of [13] were integrated into the mass and electron balance published by Acker et al., where deviating ratios between the etching mixture and dissolved Si were used in parallel experiments for the determination of N(III) species and the NH_4^+ formed as well as the HNO_3 consumption [14].

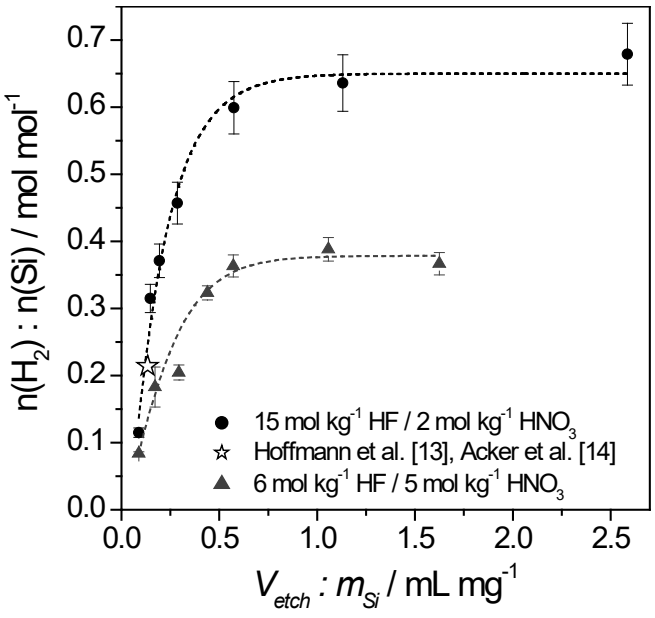


Figure 1: Formation of hydrogen during the dissolution of Si in 15 mol kg^{-1} HF/ 2 mol kg^{-1} HNO_3 and 6 mol kg^{-1} HF/ 5 mol kg^{-1} HNO_3 at 20 °C as a function of the ratio of the etchant volume to the mass of dissolved Si.

In addition to the consumption of acids during the dissolving process, the formation and accumulation of the N(III) species N_2O_3 in the etching mixture also shows an influence on the $n(H_2) : n(Si)$ ratio. The oxidation of Si via the dissolved intermediate N_2O_3 is a competitive reaction to the oxidation under the formation of H_2. This could be shown by selective enrichment with N_2O_3 in a mixture of otherwise constant composition in [23]. Furthermore, Rietig et al. demonstrated by selective enrichment experiments of the etching mixtures with different NO_x that the formation of this "excess" of N_2O_3 occurs in a series of side reactions [23]. At first, it was shown that the NO_2 often detected, that outgassed from N_2O_4 [8-13], is not a direct reaction product of Si dissolution. It turned out to be formed in a side reaction between gaseous NO (Eq. 1) and HNO_3 in the etching mixture.

$$2\ NO + 4\ HNO_3 \longrightarrow 3\ N_2O_4 + 2\ H_2O \qquad (9)$$

The N_2O_4 which accumulates in the etching mixture subsequently combines with further NO to form N_2O_3, which is in equilibrium with HNO_2 in an acidic, aqueous solution.

$$N_2O_4 + 2\ NO \longrightarrow 2\ N_2O_3 \xrightleftharpoons{H^+/H_2O} 4\ HNO_2 \qquad (10)$$

The side reaction (Eq. 9) also particularly shows that the entire consumption of HNO_3 in the overall reaction cannot be exclusively attributed to the oxidation of Si. The experiments carried out as a function of the $V_{etch} : m_{Si}$ ratio also underline this conclusion. With increasing reaction volume and, thus, increasing absolute content of HNO_3 in the etching mixture, the HNO_3 consumption per mol of dissolved Si (Fig. 2, left) increases while, simultaneously, the ratio of $n(NO) : n(NO_2)$ decreases. Consequently, more of the NO formed in the reaction is oxidized by HNO_3 to NO_2 or N_2O_4.

If an "excess" of N_2O_3, measured by ion chromatography as the sum parameter NO_2^-, is enriched at a constant reaction volume according to the side reactions Eq. 9 – 10, the consumption of NO_3^- per mole of dissolved Si decreases (Fig. 2, right). This indicates that the oxidation of Si by the intermediate HNO_2 not only competes with the formation of H_2 but also with the oxidation by HNO_3.

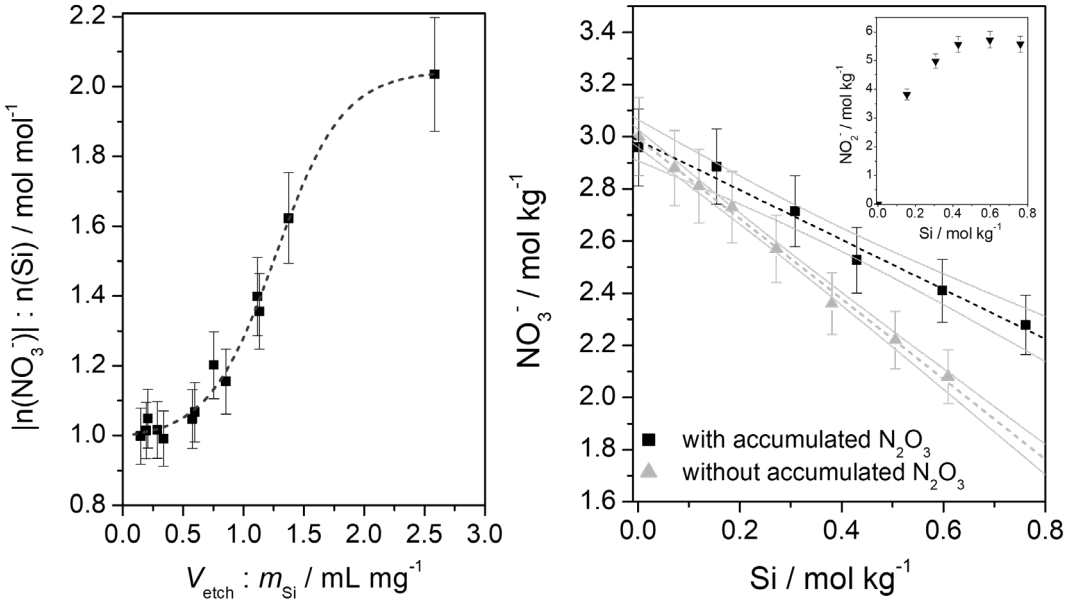
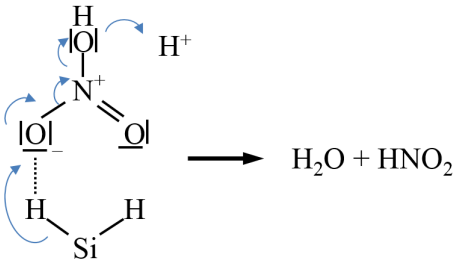


Figure 2: Consumption of NO_3^- during the dissolution of Si in 15 mol kg^{-1} HF and 2 mol kg^{-1} HNO_3 as a function of V_{etch} : m_{Si} (left); trends in NO_3^- concentration with increasing Si content with and without enrichment of N_2O_3 in a mixture of 15 mol kg^{-1} HF/ 3 mol kg^{-1} HNO_3 with $V_{etch}:m_{Si}$ = 0.25 mL mg^{-1} (right)

The intermediate HNO_2 has already been identified by Robbins and Schwartz [1-4] as the most important species for the etching process. They described the formation of HNO_2 and its concentration in the boundary layer at the Si surface as the determining step to overcome the induction period. The validity of this assumption and that the intermediate is not only formed in the side reaction is shown in a series of experiments by Rietig et al., in which H_2O_2 was added to the etching mixture in order to immediately re-oxidize formed HNO_2 to HNO_3 [23]. It was found that the etching reaction did not start, even with etching mixtures of high concentration. Etching rates that correspond to those of the HF/H_2O_2 [21] system could be observed only at reaction times of several minutes.
A direct formation of HNO_2 can only be explained by a reaction of the molecule of the undissociated HNO_3 with the Si-H termination at the Si surface, whose thermodynamic driving force is the elimination of H_2O. (Scheme 1)



Scheme 1: Schematic formation of HNO_2 at the Si-H termination of the Si surface with a molecule of undissociated HNO_3.

Consequently, the undissociated HNO_3 can be identified as the initial key species in the etching process, from which the especially important intermediate HNO_2 is directly formed. This is also in accordance with the investigations of Berg in the 1950s, who identified the undissociated HNO_3 as the reactive species when dissolving various metals in HNO_3 [22].

These findings allow, for the first time, to establish a functional relationship between the HNO_3 consumption and the composition of the etching mixture during the dissolution of Si in HF/HNO_3 mixtures. Acker et al. also found that the HNO_3 consumption in HF-rich etching mixtures is approximately 15% lower than in HNO_3-rich mixtures [14]. Systematic investigations of different etching mixtures with identical conditions showed a linear relationship between the NO_3^- consumption and the concentration of undissociated HNO_3 in the etching mixture (Fig. 3).

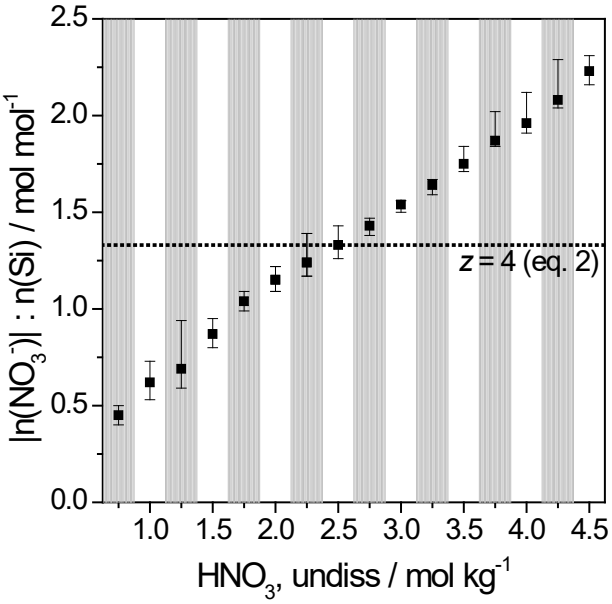


Figure 3: NO_3^- consumption per mole of Si as a function of concentration of undissociated HNO_3, obtained from experiments with etching mixture compositions of 15/1, 15/2, 15/3, 15/4, 12/4, 10/4, 8/4 and 6/4 (HF/HNO_3, each mol kg^{-1}) with accumulating N_2O_3

Figure 3 also shows that the Si oxidation at concentrations of ≤ 2.5 mol kg^{-1} of undissociated HNO_3 must be determined by the formation of H_2 (Eq. 2 with $z < 4$), whereas the nitrate consumption of the overall reaction for $q(HNO_3, \text{undissociated}) > 2.5$ mol kg^{-1} is mainly determined by side reactions, thus, the upper limit ($z = 4$) in Eq. 2 is clearly exceeded.

Based on these results, the dependence of H_2 formation on the HNO_3 content in the etching mixture, as described by Hoffmann et al. [13], also needs to be scrutinized. On the one hand, the exponentially decreasing H_2 formation with the HNO_3 content can easily be replaced by an exponentially increasing H_2 formation with the HF content, because the HF content is directly linked to HNO_3 content in the mixture due to the volume mixing (Eq. 11). On the other hand, the simultaneous change of both concentrations does not allow any conclusions to be made about the causality of the H_2 formation.

$$q_{HF} = \left(1 - \frac{q_{HNO_3}}{q^0_{HNO_3}}\right) \cdot q^0_{HF} \qquad (11)$$

In comparison with the data of Hoffmann et al. [13], Figure 4, left, shows the H_2 formation as a function of the HNO_3 content in the etching mixture in series of each constant HF concentration. It is seen that considerable amounts of H_2 are formed as long as the HF content is comparatively low even at high concentrations of HNO_3 in the etching mixture.

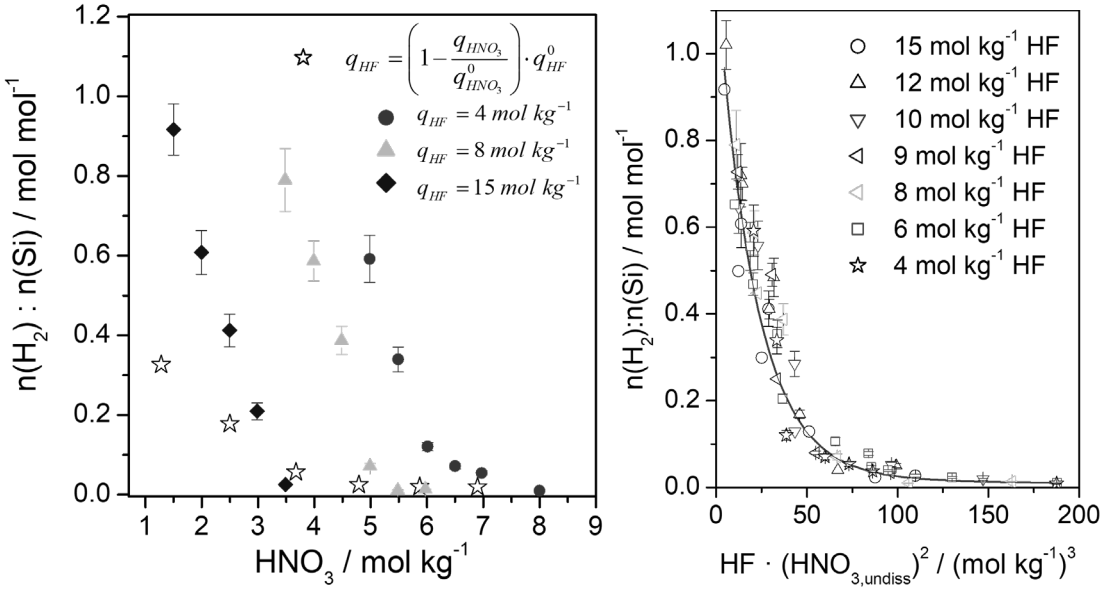


Figure 4: H_2 formation per mole of dissolved Si as a function of the HNO_3 concentration in the etching mixture (left); relationship between H_2 formation per mol of dissolved Si and the product of q(HF) and $q(HNO_3, \text{undiss})^2$ (right).

As has already been shown, the oxidation of Si by the H_2 formation is obviously in competition with both the oxidation with undissociated HNO_3 (and, thus to the HNO_2) and with excessive N_2O_3 contents in the etching mixture. Therefore, a simple plot of the

H_2 formation per mole of the dissolved Si as a function of the undissociated HNO_3 is not sufficient to describe all data.

Assuming that the transfer of a total of three electrons during the reduction of the undissociated HNO_3 to NO takes place via the intermediate HNO_2 (Eq. 12 – 14),

$$HNO_3 + 2H^+ \xrightarrow{Si} HNO_2 + H_2O + 2e^- \quad (12)$$

$$HNO_2 + H^+ \xrightarrow{Si} NO + H_2O + e^- \quad (13)$$

$$\overline{HNO_3 + 3H^+ \xrightarrow{Si} NO + 2H_2O + 3e^-} \quad (14)$$

in a first approximation, the concentration of HNO_2 in the etching mixture near the boundary layer can be described as the square of the concentration of undissociated HNO_3. By plotting the H_2 formation against the product of the HF and HNO_2 concentration, due to the competition for Si oxidation, an exponential decrease with increasing arguments is shown for the H_2 formation. Figure 4, right, shows the validity for a large set of quasi-stationary experiments with various compositions of the etchant mixture.

Kinetic Models

Similar to the stoichiometric data, the etching rate is also described in the literature only as a function of the HNO_3 content in the etching mixture [1-5, 11]. Series of experiments were carried out in which the concentrations of HF and HNO_3 were kept constant and only the concentration of H_2SiF_6 was varied. The addition of H_2SiF_6 to the etching mixture reduces the degree of dissociation of the HNO_3 [24], so that the concentration of undissociated HNO_3 varies with the varying H_2SiF_6 content. The etching rates applied for mixtures with 4 mol kg^{-1} HNO_3/ 3.5 mol kg^{-1} HF/ 0.2 to 1.3 mol kg^{-1} H_2SiF_6 (corresponding to mass fractions of 25% HNO_3, 7% HF and 3 to 19% H_2SiF_6) are shown on the left side of Figure 5 as a function of the concentration of undissociated HNO_3. The etching rates at ϑ_{Start} = 23 °C were determined in freshly prepared etching solutions for both stirred and unstirred experiments.

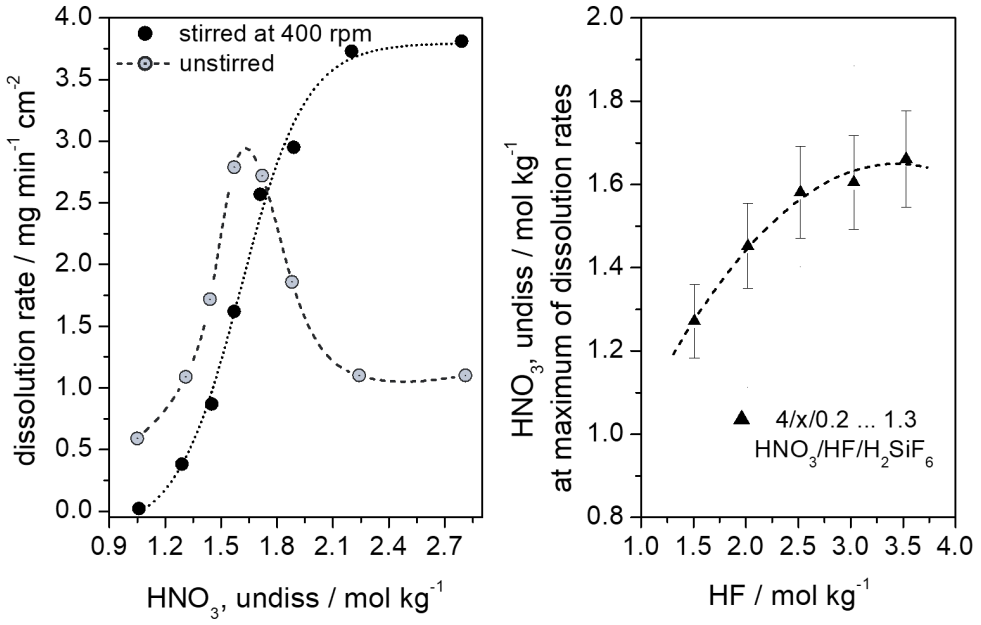


Figure 5: Comparison of the dissolution rates ($\vartheta_{start} = 23$ °C; $m_{etch}:m_{Si} = 0.2$, $\Delta d_{Si} = 100$ µm on both sides) as a function of q(HNO_3, undiss.) for ternary mixtures with 4 mol kg^{-1} HNO_3, 3.5 mol kg^{-1} HF, 0.2...1.3 mol kg^{-1} H_2SiF_6 under stirring at 400 rpm and without stirring (left); shifts of the etching rate maxima positions with the HF content in various ternary etching mixtures (right)

The etching rates determined (Figure 5, left) indicate a change in the reaction mechanism with the concentration of undissociated HNO_3. Looking first at the etching rates determined without stirring the mixture, the etching rate increases with the increasing content of undissociated HNO_3 until a local maximum is reached at approximately 1.65 mol kg^{-1}. If the concentration of undissociated HNO_3 is further increased, then the etching rate decreases again. A comparison with the dissolution rates determined under stirring initially shows that significantly lower etching rates occur at low concentrations of undissociated HNO_3 than in the experiments without stirring. The intense agitation of the solution reduces the concentration of the reactive species HNO_2 on the Si surface and the etching rate decreases. This is in good agreement with the data of Steinert et al. [9]. The etching rate increases with the increasing concentration of undissociated HNO_3 until, finally, the dissolution rate is independent of q(HNO_3, undiss). Remarkably, the inflection point of the function r_{diss}*([HNO₃, undiss.])* corresponds to the maximum of the etching rate with no agitation influence. Above the inflection point, the stirred etching mixtures show significantly higher etching rates than those in the experiments without stirring. These results are in good agreement with the data of Steinert et al. for HNO_3-rich etching mixtures, in which the mass transport of the reactive species HF to the silicon surface underlines the model of a diffusion-controlled etching process by increasing the etching rate with increasing stirring rate [11].

Identical experiments performed with varying HF concentrations show a comparable behavior. It was observed that not only an increase of the maximum etching rate but also a shift towards higher concentrations of undissociated HNO_3 occurs with an increasing HF concentration (Figure 5, right). That indicates that the etching rates are determined by both the HF concentration and the concentration of undissociated HNO_3 in which one of the components must have a higher impact. These dependencies can also be shown analogously for binary HF/HNO_3 mixtures, in which the variation of the concentration of undissociated HNO_3 proceeds via the absolute concentration of HNO_3 at a constant HF content.

Looking first at the diffusion-controlled range of the reaction for the stirred experiments, in which the etching rates do not change despite an increasing concentration of undissociated HNO_3. Here, it becomes clear that the dissolution rate is only determined by the HF content in the etching mixture (Fig. 6, left). Since this relationship is also unaffected by H_2SiF_6 in the etching mixture, Eq. 3 is generally simplified to Eq. 15

$$r \approx \left(\frac{d\mathrm{n(Si)}}{d\mathrm{t}} \right) = k_{\mathrm{HF}}(\mathrm{T}) \cdot [\mathrm{HF}]^{\mathrm{l}} \qquad (15),$$

so that a simple 1st order reaction kinetics is obtained.

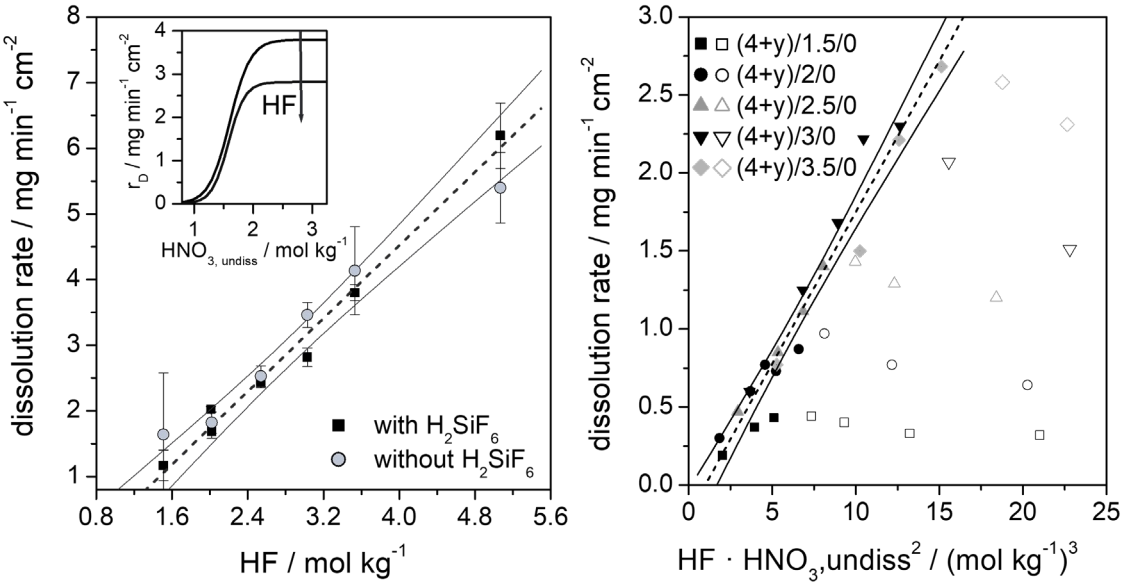


Figure 6: Correlation of etching rates in the diffusion-controlled reaction mechanism with the HF concentration in the etching mixture (left); plot of the etching rates in binary mixtures in the kinetic model (Eq. 16, filled symbols) of the reaction-controlled mechanism (right).

However, the kinetic model is slightly more complicated for the reaction-controlled area. While HF still determines the absolute level of the etching rate, the undissociated HNO_3 determines the local slope of the etching rate, i.e. simplifies the curvature of the function.

Assuming, in analogy to the stoichiometric considerations of the H_2 formation, that the concentration of the key species HNO_2 can be described as the square of the concentration of undissociated HNO_3 in a first approximation, all data up to the maximum of the etching rates (Figure 5, left) can be described by the following relationship (Eq. 16, Fig. 6, right). Always presuming that the experiments are performed in a state of quasi-stationarity, i.e. without an excess of N_2O_3,

$$r \approx \left(\frac{d\mathrm{n(Si)}}{d\mathrm{t}} \right) = k_\mathrm{i}(\mathrm{T}) \cdot [\mathrm{HNO_3,undiss}]^2 \cdot [\mathrm{HF}]^1 \qquad (16)$$

It is, therefore, not surprising that etching mixtures with HF/HNO_3 ratios in a reaction-controlled etching process (HF-rich, e.g. 15 mol kg^{-1} HF/ 1 to 3.5 mol kg^{-1} HNO_3) always show a correlation between etching rate and H_2 formation.

Conclusion

The dissolution of Si in HF/HNO_3 and $HF/HNO_3/H_2SiF_6$ acid mixtures was investigated in the present study. Special attention was paid to the complete quantification of the gaseous reaction products, which were quantified using quadrupole MS. It was found that there is a relationship between the etching bath volume used and the dissolved mass of Si. The analysis of the reaction gases shows a reduced H_2 formation per mole of dissolved Si with decreasing etching bath volume with the same mass of dissolved Si. This results in the conclusion that the oxidation of Si by accumulated N_2O_3 is in competition with the Si oxidation under H_2 formation. Furthermore, it is shown that both the consumption of nitrate ions per mol of dissolved Si increases and the ratio between the NO and NO_2 formed decreases with increasing etching bath volume. This underlines the findings from previous investigations that the formation of NO_2 is only a side reaction and that the consumption of HNO_3 over the reaction time is not solely attributable to Si oxidation. By systematically varying the concentrations of individual acids in the etching mixture, it was possible to find a correlation between the composition of the etching bath and the consumption of HNO_3 and H_2 formation. While the consumption of HNO_3 depends only on the concentration of undissociated HNO_3 in the etching mixture, both the intermediate HNO_2 and the HF are responsible for the amount of H_2 that is formed. The intermediate HNO_2 is approximated with the square of the undissociated HNO_3, which is causative for its formation and can be interpreted as the initial key species in the etching process.

It was revealed by systematic variations of the concentrations of individual acids in the etching mixture that an increasing concentration of undissociated HNO_3 leads to a change in the reaction mechanism, which is completely independent of the HF content in the mixture. Thereby, the maximum etching rates determined in unstirred experiments correspond to the inflection point of the etching rate function in stirred mixtures. These maxima show a linear shift towards higher $q(\mathrm{HF}) : q(\mathrm{HNO_3,\ undiss.})$ ratios with increasing HF content. The etching rate in the diffusion-controlled region of the reaction is solely dependent on the HF content of the etching mixture. However, there is a linear

dependence between the etching rates and the formation of H_2 in ranges of concentrations for the reaction-controlled mechanism. Consequently, a kinetic model can be assumed that is dominated by the undissociated HNO_3 or the intermediate HNO_2, while the HF plays only a minor role in the reaction rate.

References

1. H. Robbins and B. Schwartz, J. Electrochem. Soc, **106 (6)**, 1959, 505-508
2. H. Robbins and B. Schwartz, J. Electrochem. Soc., **107 (2)**, 1960, 108–111
3. H. Robbins and B. Schwartz, J. Electrochem. Soc., **108 (4)**, 1961, 365–372
4. H. Robbins and B. Schwartz, J. Electrochem. Soc., **123 (12)**, 1970, 1903–1909
5. D. R. Turner, J. Electrochem. Soc., **107 (10)**, 1960, 810–816
6. E. Abel and H. Schmid, Z. Phys. Chem., Stoechiom. Verwandtschaftsl., **132**, 1928, 55–77.
7. W. Weinreich, Diploma Thesis, Technische Universität Bergakademie Freiberg, 2005
8. E. S. Kooij, K. Butter, J. J. Kelly, Electrochem. Solid State, **2 (4)**, 1999, 178–180
9. M. Steinert, J. Acker, A. Henßge, K. Wetzig, J. Electrochem. Soc., **152 (12)**, 2005, 843–850
10. M. Steinert, J. Acker, M. Krause, S. Oswald, K. Wetzig, J. Phys. Chem. B, **110 (23)**, 2006, 11377–11382
11. M. Steinert, J. Acker, S. Oswald, K. Wetzig, J. Phys. Chem. C, **111 (5)**, 2007, 2133–2140
12. M. Steinert, J. Acker and K. Wetzig, J. Phys. Chem. C, **112 (3)**, 2008, 14139–14144
13. V. Hoffmann, M. Steinert, J. Acker, J. Anal. At. Spectrom., **26**, 2011, 1990–1996
14. J. Acker, A. Rietig, M. Steinert, V. Hoffmann, J. Phys. Chem. C, **116**, 2012, 20380–20388.
15. J. E. Harrar, L. P. Rigdon and S. F. Rice, J. Raman Spectrosc., **28**, 1997, 891–899.
16. B. Meinel, T. Koschwitz, C. Blocks, J. Acker, Materials Science in Semiconductor Processing **26**, 2014, 93–100
17. T. Langner, T. Sieber, J. Acker, ACS Appl. Nano Mater. **1**, 2018, 4135−4144
18. R.J. Archer, J. Phys. Chem. Solids Pergamon Press **14**, 1960, 104-110.
19. G. Di Francia, A. Citarella, Journal of Applied Physics, **77(7)**, 1995, 3549 - 3551.
20. C. Blocks, Bachelor Thesis, Lausitz University of Applied Science, 2013
21. C. Gondek, M. Lippold, I. Röver, K. Bohmhammel, E. Kroke, J. Phys. Chem. C, **118 (4)**, 2014, 2044−2051.
22. Berg T. G. O., Zeitschrift für anorganische und allgemeine Chemie **265**, 1951, 332-337
23. A. Rietig, T. Langner, J. Acker, Phys. Chem. Chem. Phys., **21**, 2019, 22002-22013
24. T. Langner, A. Rietig, J. Acker, J Raman Spectrosc. **51**, 2020; 366–372

Silicon for the Chemical and Solar Industry XV
Trondheim, Norway, June 15 – 18, 2020

Activation of silicon in the hydrochlorination process

Jan-Otto Hoel and Harry Morten Rong
Elkem ASA, Elkem Silicon Materials, Fossegrenda 13, 7038 Trondheim

Abstract

The activation of silicon in the hydrochlorination process has been studied.

It has been found that the negative effect of manganese is due to the addition of oxygen to the reactor (in the form of the surface oxygen on the silicon particles) and that manganese is transferring the oxygen to the already active areas on the silicon and blocking these sites for reaction. The oxygen leaves the reactor as high boiling compounds, but Mn will slow down this removal of oxygen. Without addition of oxygen to the reactor the manganese has no negative effect.

Aluminum is improving the reaction rate in both a manganese containing and manganese free system. Aluminum is only important in the activation of the silicon. When the silicon is activated, aluminum seem to have no effect. In continuous reactors, always some new silicon is added and therefore some aluminum is always required in the activation.

Introduction

The hydrochlorination process (HC) to produce trichlorosilane (TCS; $HSiCl_3$) by reaction of ground metallurgical grade silicon, hydrogen and silicon tetrachloride (STC; $SiCl_4$) is presented by the overall equilibrium reaction:

$$Si\ (s) + 2H_2\ (g) + 3SiCl_4\ (g) = 4HSiCl_3\ (g) \quad (1)$$

The HC reaction is an equilibrium reaction that has a maximum TCS yield determined by the thermodynamics given by the operating conditions. The available thermodynamic data for the reaction products is not accurate, resulting in a wide range of calculated equilibrium values for TCS selectivity. The equilibrium data used in this work was obtained by applying very long residence time in the reactor [1, unpublished work]. Our equilibrium TCS selectivity is slightly higher than data presented by Ingle and Peffley [2]. For more details of the HC process confer Crawford et al. [3].

In the HC process STC is consumed to produce TCS. Typically, the reactivity of a process is reported by the how fast one product is produced or how fast a reactant is consumed. In the HC process it is typical to report the TCS selectivity in the product gas (Equation

2). The amounts of other products produced in the HC process is typically about 1% and therefore the TCS selectivity of the process is proportional to the reactivity of the silicon.

$$[\text{TCS selectivity}] = \frac{[\text{molar fraction TCS}]}{[\text{molar fraction TCS}] + [\text{molar fraction STC}]} \quad (2)$$

Another method for calculating the reactivity of the process is to measure the amount of STC consumed (STC conversion) in the process like for instance used by Colomb [4] (Equation 3). Colomb also included the possibility to recycle HCl from the Siemens reactor in his formula.

$$[\text{STC conversion}] = \frac{3 \times [\text{molar flow TCS out}]}{(4 \times [\text{molar flow STC in}]) + [\text{molar flow HCl in}]} \quad (3)$$

In small laboratory reactors the residence time (the time the STC is in contact with the silicon powder) is much shorter (1.5 seconds) than in an industrial reactor that typically is designed to have a residence time of 60 seconds. Due to the shorter residence time the test results from a laboratory reactor can only be used as a guideline for what will happen in the industrial reactor. If a process has enough time it will eventually reach equilibrium conditions.

Experimental

The apparatus

The experiments are made in a laboratory scale continuous fluidized bed reactor. See Figure 1. Liquid STC is evaporated and mixed with hydrogen and argon. The argon is used as an internal standard for the product gas analysis. The reactant gases are fed into the reactor where they react with the fluidized Si particles. The product gases and the remaining reactant gases go through a dust trap and a dust filter before entering the sampling system. The sampling system sends small portions of the product gas into the Gas Chromatograph (GC) every 17 minutes, while most of the product stream goes further to a pressure controlling valve. This valve controls the pressure by regulating the gas output. The addition system adds fresh Si pneumatically from the top. This system is automated and controls the Si amount in the reactor by monitoring the pressure drop through the reactor.

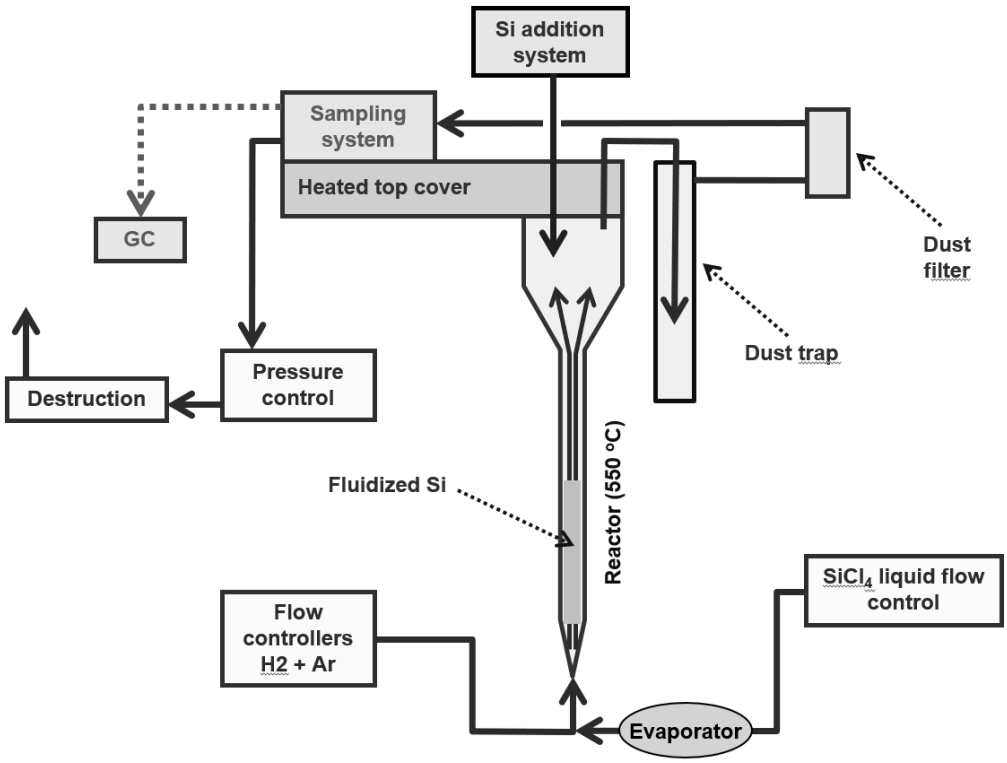


Figure 1: The layout of the hydrochlorination (HC) lab scale reactor

Experimental conditions

Physical conditions

The experiments are carried out at 550°C and at a pressure of 10 bar (absolute). The superficial gas velocity is 4.9 cm/sec, giving an estimated interstitial gas velocity of 8.7 cm/sec and a residence time of 1.5 seconds. The gas velocity is slightly lower than in industrial reactors, but the particle size is finer, giving similar fluidization conditions. The fluidization regime is bubbling bed.

Reactor mass

The reactor is loaded with 10g Si with a particle size of 125-250 microns. The silicon is crushed, milled and sieved in ambient air. No specific action has been taken to reduce the exposure to oxygen and humidity. It is quite common that the silicon is exposed to air and humidity after sizing. The effect of pre-drying the silicon has been studied and found to have no effect on the HC performance. New Si is continuously added to replace the consumed Si, keeping 10g Si in the reactor at all time. Experiments both with Cu catalyst and without Cu catalyst have been run. The Cu catalyst is added as a master alloy made from high purity Si and Cu. This master alloy is mixed with the Si sample to get the desired level of Cu. The start-up mix contains 0.8wt% Cu and the mix added during run contains 0.1wt% Cu.

Gas chromatograph measurements

All selectivity measurements and the other quantified gas analyses are produced by a Varian 3900 gas chromatograph (GC). The GC is equipped with a packed column (30% QF1, 80/100 Chromosorb PAW) and a thermal conductivity detector (TCD). The product gas is sampled about each 17 minutes. Figure 2 shows a typical chromatogram. In this paper, all TCS selectivities are reported according to equation (2).

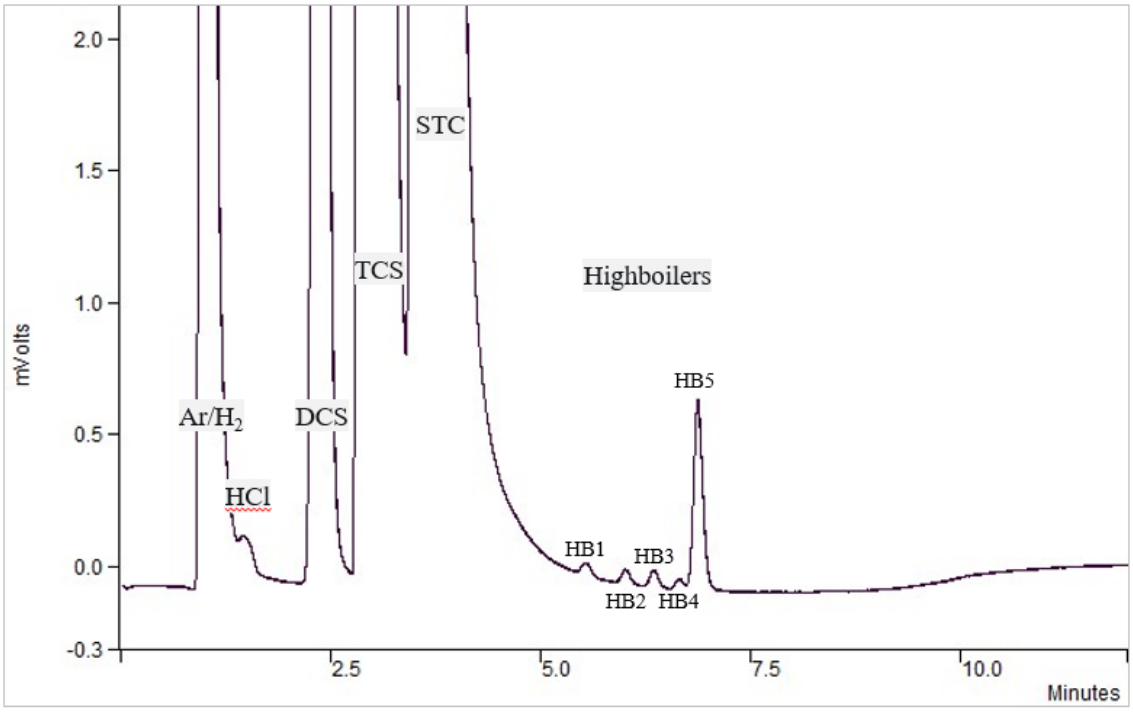


Figure 2: Sample chromatogram from the HC process

FTIR measurements

When more info or more frequent measurements of the product gas is needed, a Cary 660 FTIR gas analyzer (FTIR, Fourier Transform Infra-Red) is connected to the apparatus. The product gas is continuously fed through the gas cell (Cyclone C2). The gas cell is heated to 200°C to avoid condensation. The IR beam has 16 passes through the cell, giving an optical pathway of 2m. With the current set-up, the FTIR can make several analyses each minute. Figure 3 shows a typical IR spectrum.

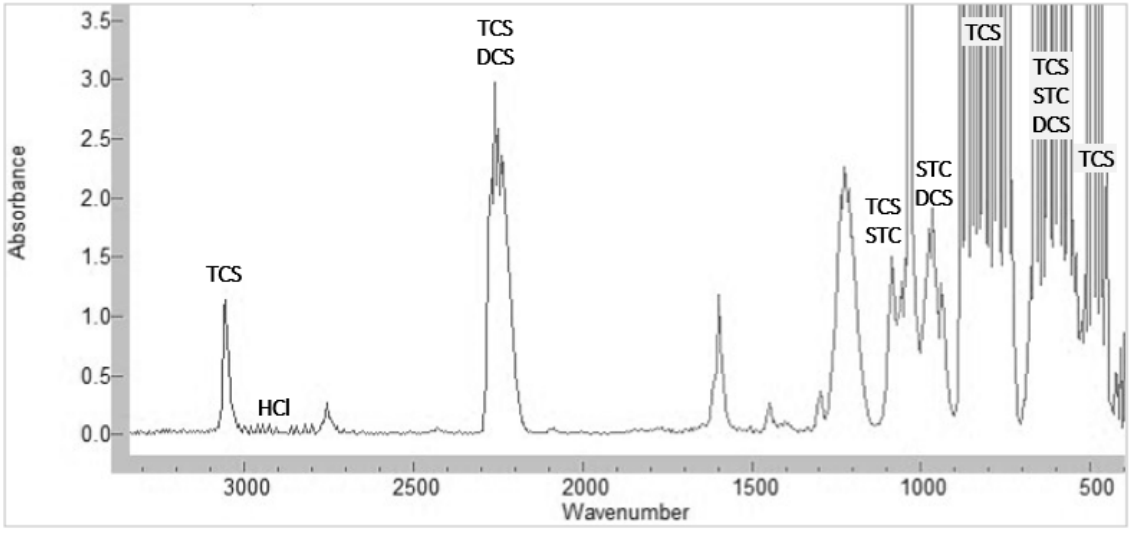


Figure 3: Sample spectrum of the product gas from the HC process. Each gas species has several peaks. Many of the peaks represent more than one gas species.

Results and discussions

Comparing different Si qualities

When comparing different Si qualities, it is important to make long runs where several reactor volumes of silicon are consumed. This will ensure that non-volatile trace elements are accumulated in the reactor to reveal the effect of accumulation of these elements.

Figure 4 shows six runs of Silgrain® compared with two different silicon qualities. There is a large difference in the performance which can be correlated to the content of Mn in the samples. Mn has shown to be strongly negative in presence of Cu catalyst [5]. The six runs of Silgrain®, over two years, show that the reproducibility of the apparatus is good.

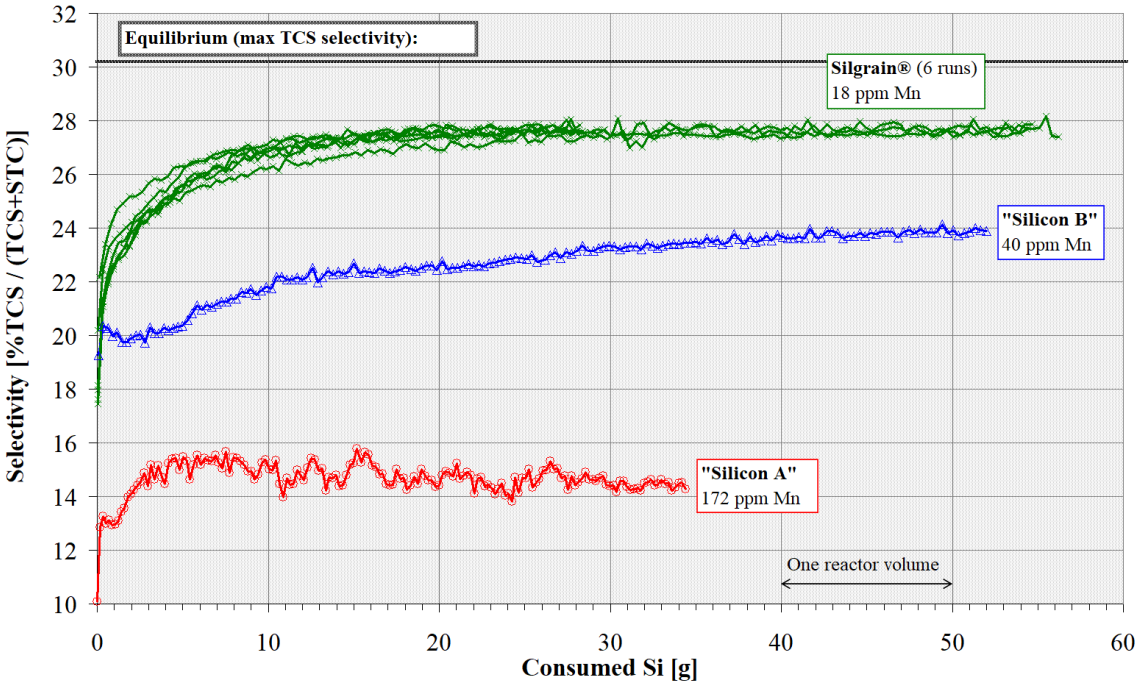


Figure 4: Three different silicon samples. The x-axis shows the amount of consumed Si, where 10 g is equal to 1 reactor volume. The y-axis shows the measured TCS selectivity.

An unexpected effect of stopping the Si addition

Synthetic Si samples were made by alloying high purity Si with specific trace elements. This was done to study effects and synergy effects of these trace elements. Table 1 shows the contents of the synthetic samples relevant for this publication.

Sample		Syntetic-1	Syntetic-2	Syntetic-3	Syntetic-4	Syntetic-5
Description		High purity Si	High purity Si +Fe	High purity Si +Fe +Al	High purity Si +Fe +Al +Mn	High purity Si +Fe +Al +Ca
Al	%	-	-	0.157	0.158	0.160
Ca	%	-	-	-	-	0.023
Fe	%	-	0.245	0.310	0.275	0.277
Mn	ppm	-	-	-	160	-

Table 1: Contents of the synthetic samples

Figure 5 shows two experiments with a sample of high purity Si alloyed with Fe, Al and Mn (Synthetic-4). When running one of those experiments, the addition system failed after consuming 4g of Si (along the x-axis). After this addition stop, the TCS selectivity increased dramatically. This was a totally unexpected behavior and had to be checked in more detail. The experiment and the Si addition were restarted, and at 15g Si consumed, the conditions are back to normal. After 18g Si consumed, the Si addition was stopped intentionally to reproduce this effect. As seen, the TCS selectivity again increased dramatically. It has earlier been observed that an unstable Si addition gives varying TCS

selectivity (reactivity). This is probably the same effect as described above, but in a smaller scale.

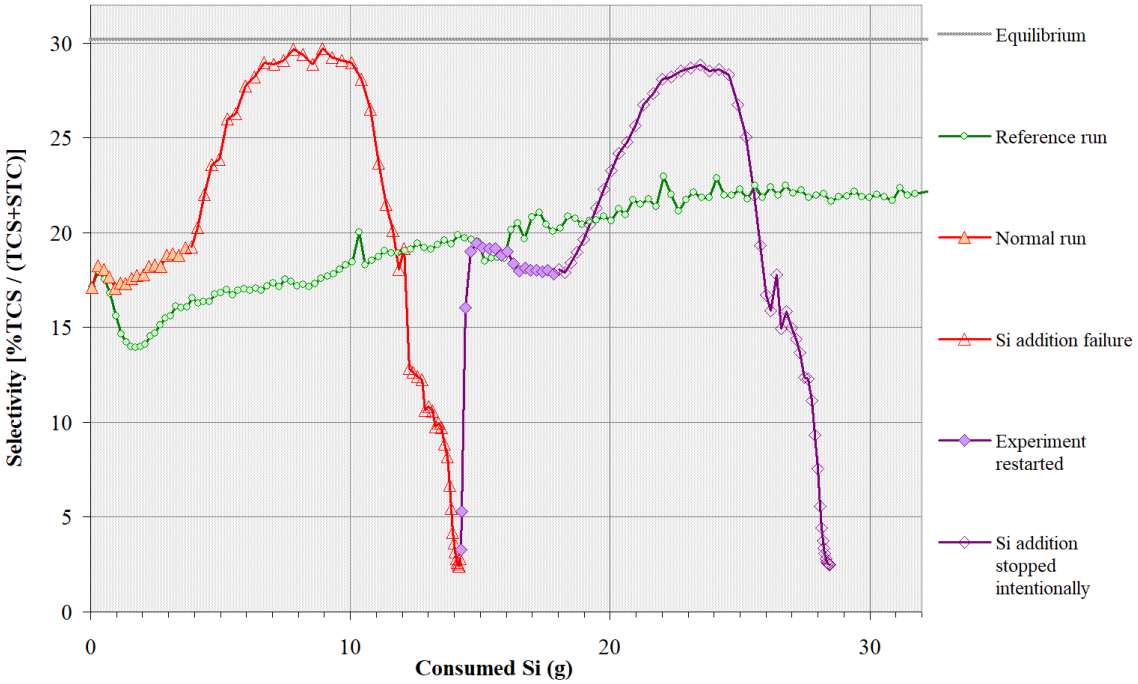


Figure 5: Two runs that should have been equal, but the Si addition failed after consuming 4g of Si. This gave an unexpected increase in TCS selectivity.

Stopping the silicon addition had an immediate positive effect on the reactivity (giving higher TCS selectivity) in the system. This effect was also observed with high purity silicon, showing that the negative effect of adding silicon is caused by the oxide layer present on the silicon surface. Two experiments, shown in Figure 6, were made to check if the effect is dependent on the addition rate of Si. Both experiments were started with the Mn containing sample (Synthetic-4), but with a change to pure Si (Synthetic-1) after 17g consumed Si, giving the same amount of accumulated Mn in the reactor.

In experiment 1, the Si amount was increased from 7 to 10g over a 20 minutes period. The TCS selectivity decreased dramatically, not only during those 20 minutes but also the next 2 hours before starting to recover.

In the experiment 2, the increase from 7 to 10g lasted for 6 hours. The TCS selectivity remains high all the time.

At the end of the experiments, both have similar conditions: The reactor contains 10g Si, the amount of Mn is equal and other elements in the reactor are equal. Still, the TCS selectivity is very different.

When adding Silicon powder with an oxide layer to the reactor, an important step of the activation of the silicon is to remove this oxide layer. Our hypothesis is that a good reacting Si mass removes this oxide layer faster than a poor reacting Si mass. Therefore, a good reacting mass can cope with the added oxide if it is not added too fast. If too much

oxide is added to the reactor, the reactivity will decrease, and longer time is required for the system to recover.

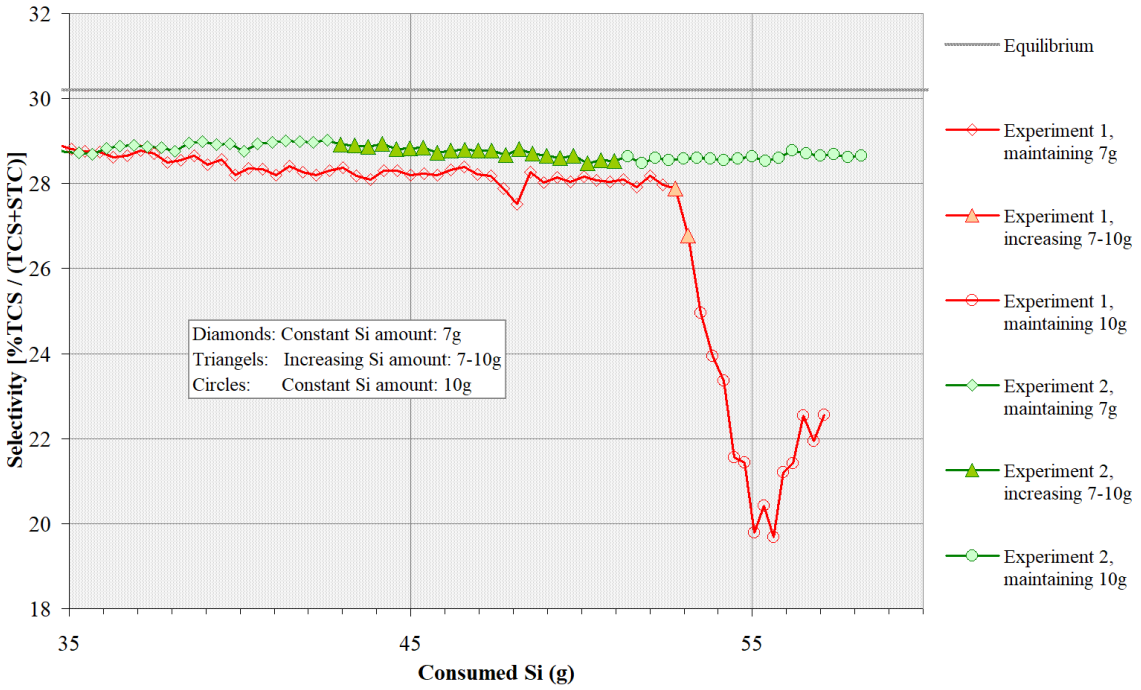


Figure 6: Two experiments where the Si amount is increased from 7g to 10g. In experiment 1, the Si amount is increased fast. In experiment 2 it is increased slowly.

A silicon particle added to the reactor with an oxide layer will not react before the oxide layer is removed. Therefore, adding new particles that are not reacting should have minor influence on the reactivity of the system. However, as shown above, we see a sharp decrease when the new silicon particles are added showing that the oxide layer reacts quickly with the gases in the reactor (TCS, STC or both) and start to block (oxidize) the active areas that are producing TCS.

We have found that Mn and Cu plays an important role in the activation of the silicon. Cu catalyst have been tested as Si-Cu alloy and CuCl, giving the same effect. The negative effect of Si addition is almost absent when running without Mn in the system. The negative effect of Si addition is also almost absent when running without Cu catalyst. The mechanism of Mn and Cu is unknown, but our hypothesis is that Mn helps to distribute oxide from newly added Si particles to Cu-Si phases which are already reacting. Cu is a natural trace element in silicon, and it is typical to find Cu values up to 100 ppm by some silicon producers. The Cu will accumulate strongly in the reactor and the negative effect of Cu and Mn is observed despite that Cu catalyst is not added by purpose.

The oxide layer on the Si particles will leave the reactor as an oxygen containing gas species or alternatively accumulate in the reactor as an oxide of other elements. To check this, we started to look for gas species that follows the addition of Si rather than the reactivity in the reactor.

Removal of oxide from the Si surfaces

When Silicon is added to the reactor, it has a layer of oxide on the surfaces. This oxide layer is attacked by the STC/TCS as soon as the Si particle is added. The oxygen is transported out of the reactor as different oxygen containing gas species. Those species are assumed to be mainly highboilers with the structure $H_XCl_{(3-X)}Si\text{-}O\text{-}SiH_YCl_{(3-Y)}$, where X and Y is in the range 0-3.

To examine if any products could be oxygen containing, large amounts of Si (1-2 g) have been added intentionally. Sampling with GC and FTIR have been made shortly after the addition. Some products are typically high during the start-up of the experiment and decrease as the experiment proceeds.

It was observed that the 2nd high boiler in the GC chromatogram (highboiler-2) seems to follow the addition of silicon and not the reactivity. The correlation with silicon addition and the other high boilers is not so clear and will be studied further.

Figure 7 shows the TCS selectivity and the production of highboiler-2 (Figure 2) in a continuous run with the Fe and Al containing sample (Synthetic 3). The production flow of "Highboiler-2" is relatively high during the first hour. After 5 hours, the production has been reduced to 1/3 of the initial production. The silicon is added as small batches with intervals of several minutes. If the GC sample is taken shortly after a Si addition, it will give a higher value in the Higboiler-2.

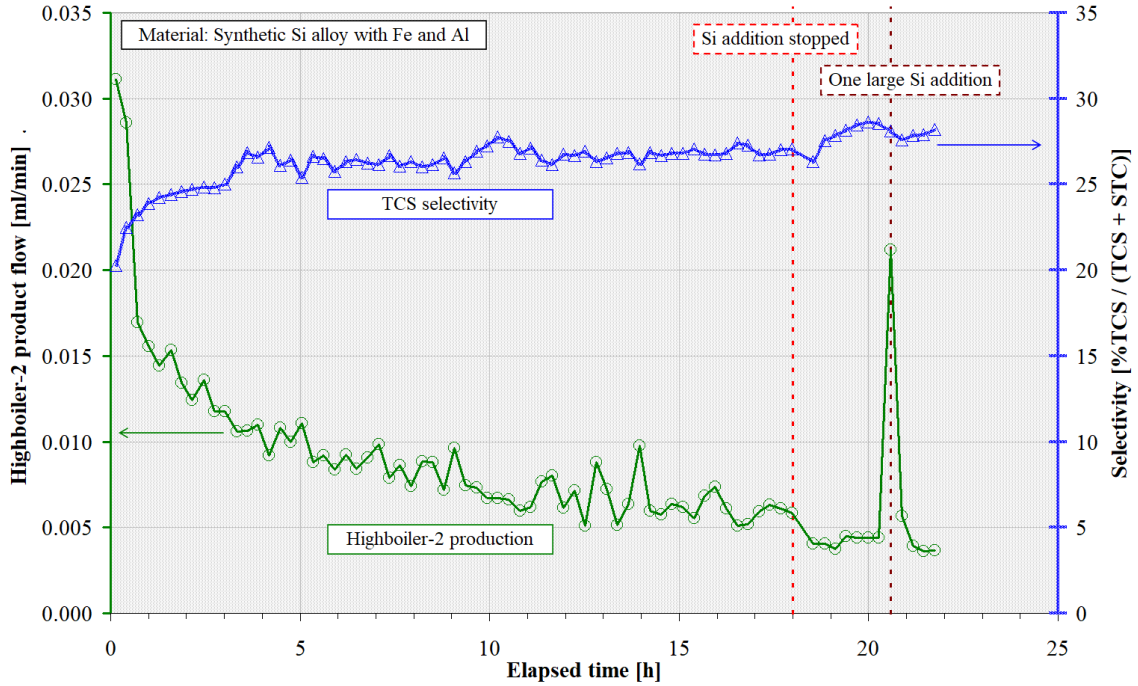


Figure 7: Sample run showing TCS selectivity (right y-axis) and contents of the oxygen containing gas species "Highboiler-2" (left y-axis) as function of time.

After 18.0 hours, the Si addition is stopped. This reduces the production of "Highboiler-2" even more and reduces the instability. After 20.5 hours elapsed time, one large single addition of Si is made resulting in a significantly increased amount of the "Highboiler-

2". This indicates strongly that the "Highboiler-2" is an oxygen containing compound. The other high boilers could also be oxygen containing but the relationship is not so clear as observed for "Highboiler 2".

Figure 8 shows FTIR spectra with different timings related to the same large addition as described above. The effect of the Si addition is visible as a shoulder in the valley around wavenumber 1130 sec^{-1}. The lowest graph is sampled just before addition. The highest is sampled 20 seconds after addition. The next samplings are after 110 and 180 seconds and show a gradual decrease of the shoulder against a level equal to the sampling just before addition. This shoulder peak is probably caused by the oxygen containing "Highboiler-2" species. It cannot be excluded that this signal is also caused by other oxygen containing high boilers.

With intention of going to the extreme, a large amount of quartz powder was added to the reactor while sampling with the FTIR. As seen in figure 9, this gave a huge response on the FTIR around wavenumber 1130 sec^{-1}. The lowest graph is sampled just before the addition. The highest peak is from the sampling taken 25 sec after the addition. The other samplings in descending order are taken after 85 seconds, 2.0 minutes and 3.5 minutes.

The increased production of the oxygen containing highboiler happens within the first half minute after the Si and its oxide layer are added, and the duration is only of the order of a few minutes. This indicates that it is only the surface of the quartz, perhaps the OH groups, that are reacting in the process.

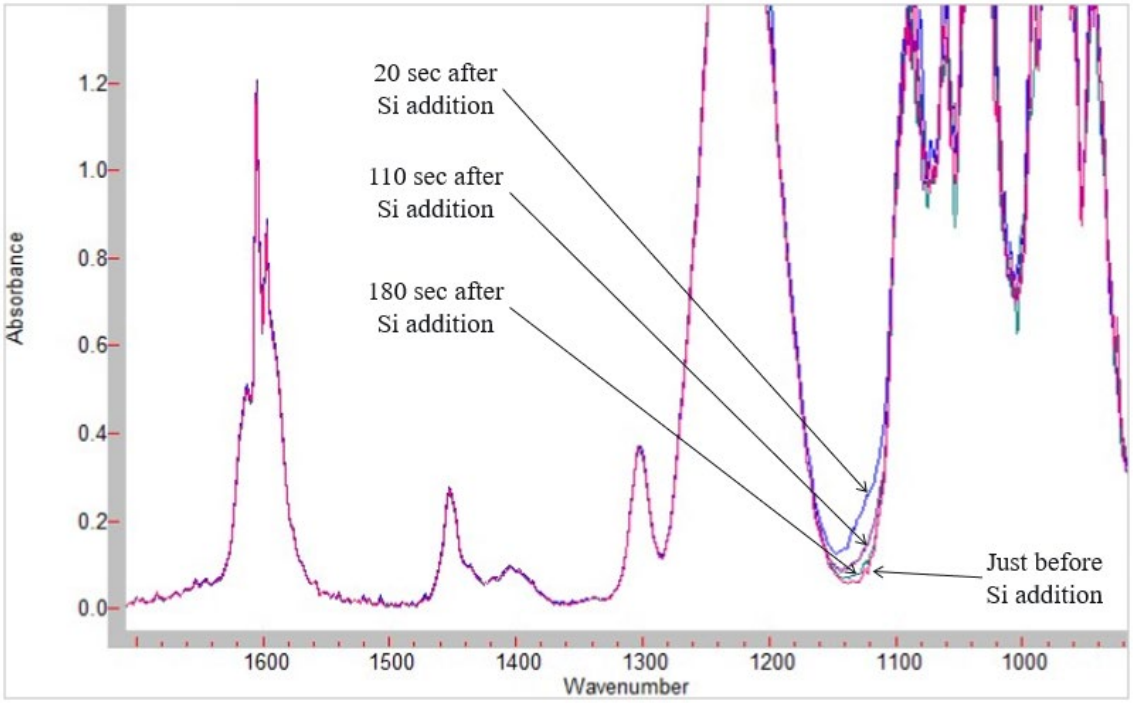


Figure 8: A part of FTIR spectra at different timings related to one large addition of Si

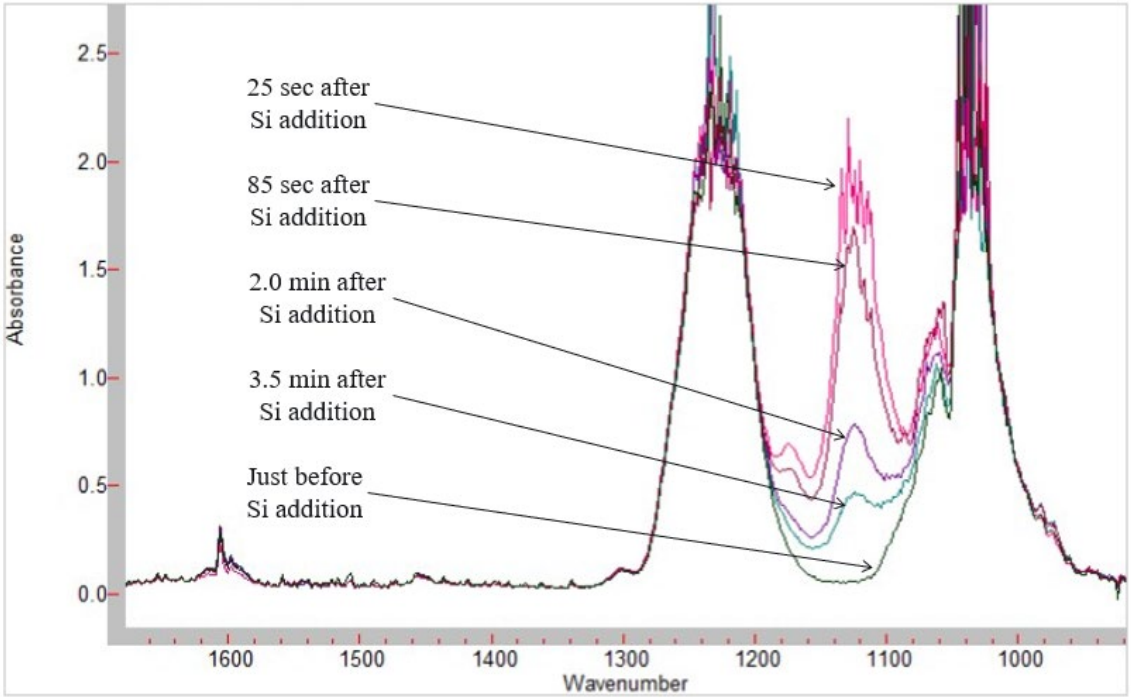


Figure 9: FTIR spectra at different timings related to one large addition of quartz

Effect of Al in the activation of silicon

During a run with continuous addition of silicon, an activation process will always occur as new silicon is added to the reactor all the time. To study the activation itself, it is favorable to make batch runs instead of continuous runs. This will ensure that all silicon in the reactor is at the same stage in the activation process. The slope of the graph will tell us how fast the silicon activates in the reactor.

Four different synthetic samples have been compared in the batch runs with samples made from high purity Si and intentionally added Fe, Al, Ca, and/or Mn. Therefore, the alloys have a high purity except the elements alloyed intentionally. See Table 1.

As seen in Figure 10, the two samples with Al (Synthetic-3 and -5) starts at 3 times higher initial TCS selectivity than the two samples without Al (Synthetic-1 and -2), while the difference after 4-5 hours is only minor. This indicates that Al is very important for the initial activation, but not important for the already activated Si particles. Sørheim [6] proposed that Al makes the oxide layer porous by the formation of AlOCl. In this work, it is shown that the removal of oxygen also occurs in the absence of aluminum.

However, it is important to bear in mind that this initial activation always occurs in a continuous reactor. Thus, Al anyway is important in a continuous process. Referring to the chapter above about the negative effect of adding Si, this means that this effect will be less for samples containing enough Al, as Al speeds up the activation.

It should also be noted that activation of the samples Synthetic-3 and -5 are equal, showing that Ca has no effect on the activation.

It is also interesting to note that when all silicon has been consumed, there is still some TCS production in the reactor. This is due to the gas phase reaction between STC and

hydrogen, producing TCS and HCl. This is confirmed both with GC and FTIR by the detection of HCl.

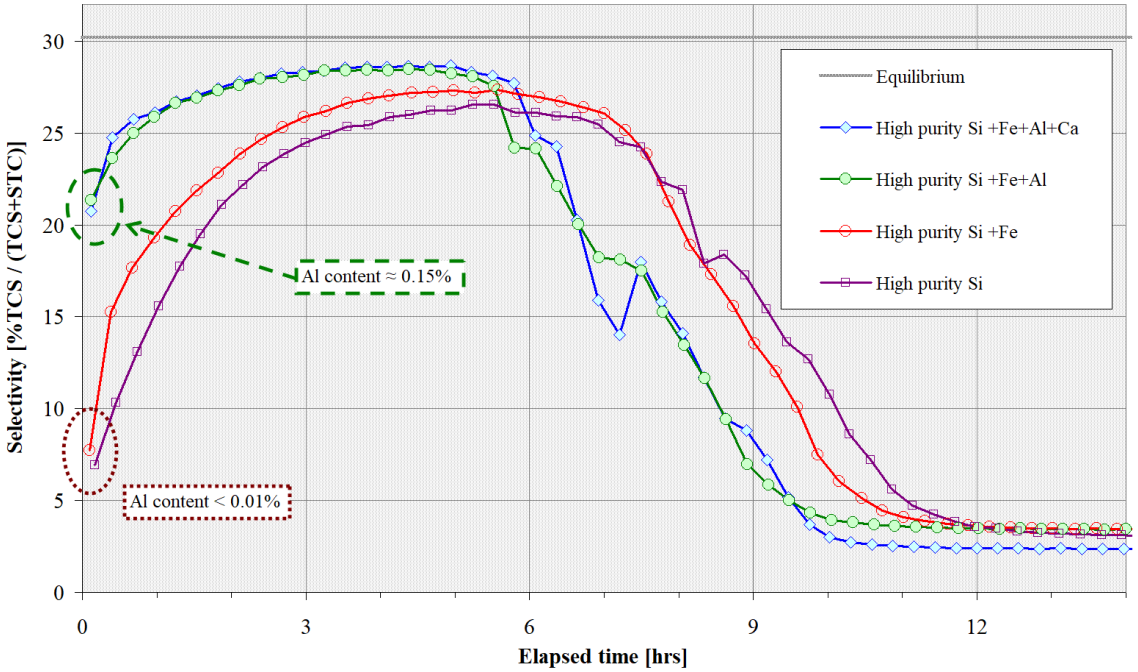


Figure 10: Batch experiments with synthetic samples.

Figure 11 shows the synthetic sample without trace elements (Synthetic-1) and the sample with Fe, Al, and Ca (Synthetic-5) with and without extra additions of Mn. As seen, Mn slows down the activation significantly. The additions of Mn to sample Synthetic-5 even cause the selectivity to decrease the first 2-3 hours. The graph shows two similar runs of Synthetic-5 with addition of 190 ppm Mn to show the reproducibility.

It should be noted that the experiments with 190 ppm Mn end up at about the same max selectivity as the experiments without. This means that the main negative effect of Mn is to slow down the activation. In a continuous process, poor activation will slow down the all-over reaction, as the reactor always will contain recently added Si particles. The combination of high Mn content and low Al content will give a poor TCS selectivity in the continuously operated process based on these results.

In Figure 12, the effect of alloying Mn into the material is compared to Mn added as metallic powder. The initial selectivity is the same for both ways of adding Mn. In the alloyed Mn experiments, the selectivity starts to increase rapidly after 2-3 hours up to the same level as the sample without Mn, while the experiments with Mn added as powder need more time to activate. The reason is not known but is probably connected to the availability of Mn and how Mn appear in the Si mass.

Figure 13 shows two experiments with Synthetic 2, where one is without Cu catalyst and one is with Cu catalyst. As seen, the experiment without Cu catalyst has a significantly lower reactivity and is never becoming fully activated. This confirms the catalytic effect of Cu, which is very strong in systems with a low Mn content (below 50 ppm).

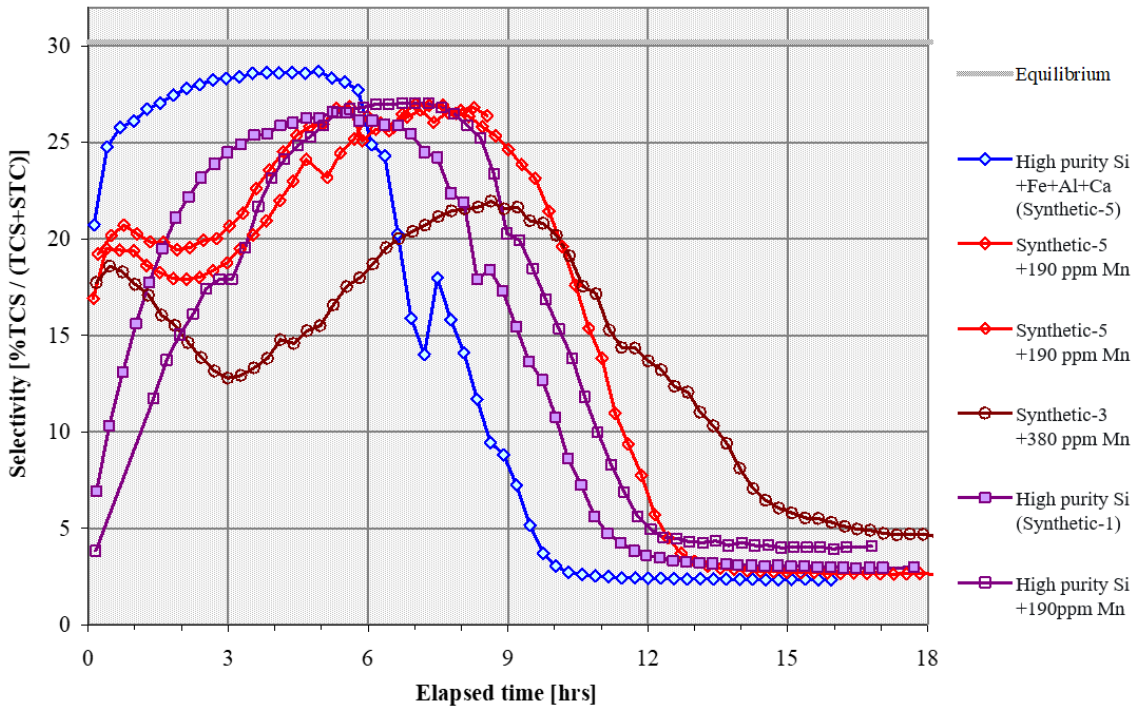


Figure 11: Batch experiments: Synthetic samples with additions of metallic Mn powder.

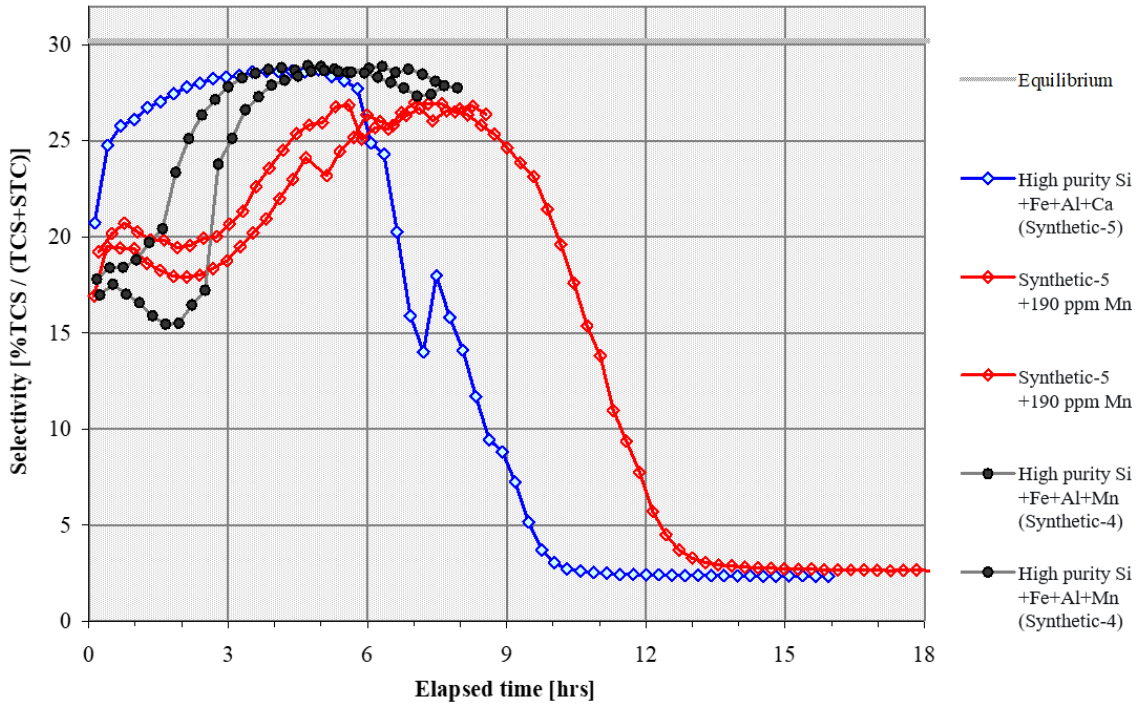


Figure 12: Batch experiments: Mn as an alloy compound versus Mn added as metallic powder.

As showed in Figure 11 and 12, all samples end up at about the same maximum selectivity when the activation is complete. One exception from that is the experiment with 380 ppm Mn in Figure 11. This high Mn content is in the high end for commercially available silicon qualities. Mn accumulates strongly in the reactor mass, and values above 380 ppm Mn are reached after a few days of operation. This again shows the importance of running experiments with continuous addition of Si when the aim is to compare Si qualities. In batch experiments, the effects of continuous activation and accumulation of trace elements will be lost.

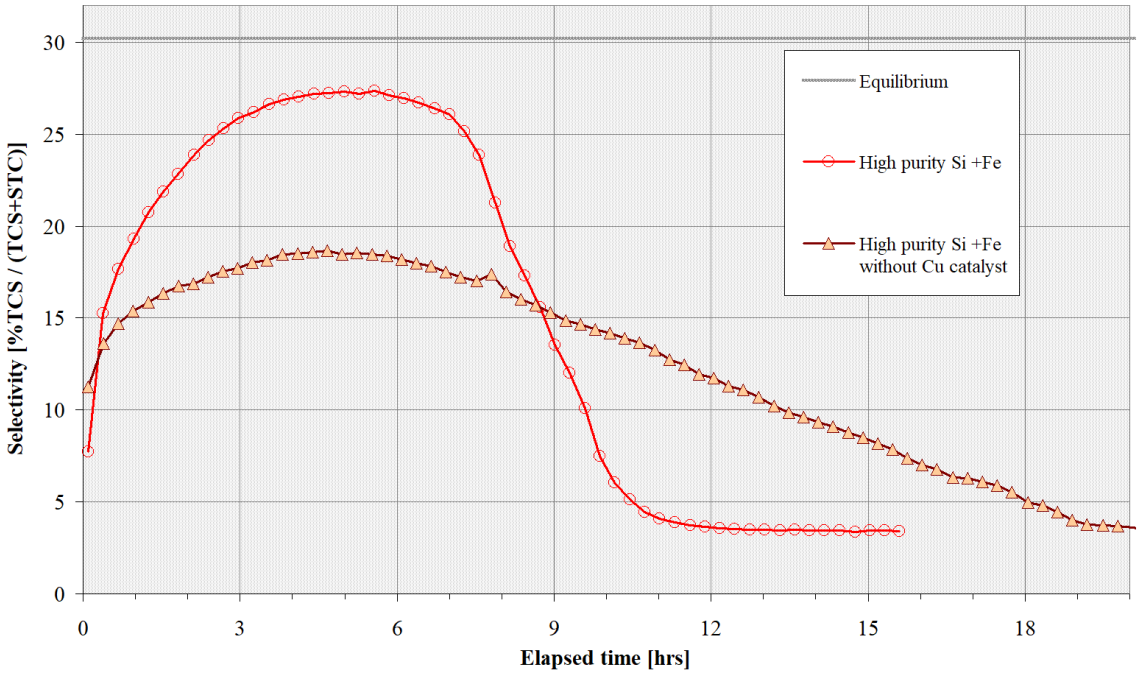


Figure 13: Batch experiments: One experiment with Cu catalyst versus one experiment without Cu catalyst.

Summary

It has previously been shown that manganese has a negative influence on the production rate of trichlorosilane in the presence of a copper catalyst [5].

In this work it is shown that the negative effect of manganese is due to the addition of oxygen to the reactor (in the form of the surface oxygen on the silicon particles) and that manganese is transferring the oxygen to the already active areas on the silicon and blocking these sites for reaction. The oxygen leaves the reactor as high boiling compounds, but Mn will slow down this removal of oxygen. Without addition of oxygen to the reactor the manganese has no negative effect.

Aluminum is improving the reaction rate in both a manganese containing and manganese free system. Aluminum is only important in the activation of the silicon. When the silicon is activated, aluminum seems to have no effect. In continuous reactors, always some new silicon is added and therefore some aluminum is always required in the activation. The worst combination seems to be low aluminum, high manganese and high copper.

Copper catalyst is increasing the reactivity in low manganese systems, but turns into a poison if the manganese content is high.

References

[1] J.O. Hoel, G. Andersen, T. Røe, and H. Rong, Maximizing Trichlorosilane Production in the Reaction Between Silicon, Silicon Tetrachloride and Hydrogen, Silicon for the Chemical and Solar Industry XI, Bergen -Ulvik, Norway, June 25 - 29, 2012, p 157

[2] W. M. Ingle and M. S. Peffley, Kinetics of the hydrogenation of silicon tetrachloride. Journal of the Electrochemical Society, 132, 1985, p 1236.

[3] A. Crawford, Cost saving of using a metallurgical grade silicon with higher trichlorosilane yield in the hydrochlorination based polysilicon process, Silicon for the Chemical and Solar Industry XIII, Kristiansand, Norway, June 13 - 16, 2016, p 201

[4] M. Colomb, S. Palanki, N.D. Sylvester, Experimental verification of scalable model for the hydrochlorination reaction in a pilot-scale fluidized bed reactor, Powder Technology 301 (2016), p 989

[5] World patent no. 2007035108A1, Method for production of trichlorosilane and silicon in use for production of trichlorosilane, Priority 2005-09-22, publication 2007-03-29

[6] H. Sørheim, The influence of intermetallic phases on the production of methylchlorosilanes, Doctoral thesis at NTH, Norges Tekniske Høgskole, Trondheim, Norway 1994

Reactivity of HCl at the Si(100)-c(4x2) reconstructed surface: a DFT study.

Ingeborg-Helene Svenum[1)], and Sylvain Guottebrouze[1)], Francesca L. Bleken[1, *)]
1) *SINTEF Industry, P. O. Box 4760 Torgarden,* 7465 Trondheim, Norway
**) Corresponding author: francesca.l.bleken@sintef.no*

Abstract

The interaction of H, Cl and HCl with a Si(100) surface was modelled with Density Functional Theory, with and without a single Fe atom impurity close to the surface. The presence of Fe on the surface affects silicon surface reactivity. Fe has a positive effect on the formation of Si vacancy in the surface. However, the effect of Fe on the adsorption of H, Cl and HCl is negative, leading to a lower adsorption energy compared to the pure Si surface.

Introduction

The conventional commercial process for producing high purity silicon is based on the Siemens process, in which purified trichlorosilane (TCS) is obtained from metallurgical grade Silicon (MG-Si). Silicon is then deposited by thermal decomposition of TCS in the presence of large amounts of hydrogen (H_2) [1]. TCS can be produced by reacting anhydrous HCl(g) with MG-Si in the direct hydrochlorination process [2].

$$\text{MG-Si (s)} + 3\ \text{HCl (g)} \rightarrow \text{SiHCl}_3\ \text{(g)} + \text{H}_2\ \text{(g)} \qquad (1)$$

The product composition varies widely depending on process conditions, and at 575 K in a fluidized bed reactor the selectivity towards TCS is about 90 %, with silicon tetrachloride (STC) as main biproduct [3]. TCS is then purified by distillation before being processed to the high purity Si according to the following two reactions [3]:

$$4\ \text{SiHCl}_3\ \text{(g)} \rightarrow \text{Si (s)} + 3\ \text{SiCl}_4\ \text{(g)} + 2\text{H}_2\ \text{(g)} \qquad (2)$$

$$\text{SiHCl}_3\ \text{(g)} + \text{H}_2 \rightarrow \text{Si (s)} + 3\ \text{HCl (g)} \qquad (3)$$

STC in not only the main by-product in the TCS production, it is also a major by-product in the deposition reaction seen in equation (2). TCS also forms Si(s) upon reduction with H_2 (equation (3)), but this is hampered by a very slow deposition rate, at 1/3 of the deposition rate in the Siemens process [3]. Due to this reaction the off gas from the reactor will contain some HCl which in turn can be used to quantify the silicon produced by this

reaction. While equations (1), (2) and (3) represent the overall reactions correctly they do not convey the complicated mechanisms of the reactions. The large majority of published experimental research is focused on the production of Si(s) from chlorinated silane in the gas phase, and even though the experimental setups are geared towards Si deposition these studies are also relevant for the (reverse) formation on $SiHCl_3$.

Fe is normally the main impurity present in MG-Si, and the effect of Fe containing intermetallics and impurities in the Si crystals on the direct chlorination process is therefore highly relevant. Tests show that the presence of iron has a negative effect on both the reactivity of HCl and the selectivity towards $SiHCl_3$, but results indicating a negligible influence of Fe have also been reported [[4] and references therein]. Investigation at the atomic scale on the effect of Fe atoms on the reactivity of the Si surface have, to the best of our knowledge, not been reported. Understanding the interaction of H, Cl and HCl with the Si surface and the effect of Fe is an essential starting point for proper analysis of the full reaction.

Computational investigations of the chemical system based on quantum chemical (QM) methods is a powerful addition to the experimental toolbox, which can help elucidate the chemical interactions at the atomic scale. With QM methods, the electronic structure of the system is solved, making the study of breaking and forming of bonds available. Density Functional Theory (DFT) is a branch of QM in which the electronic density in the system is optimized instead of the wavefunction of the system. Sholl and Steckel [5] provide a thorough and easily comprehensible introduction to QM and DFT for the interested reader. An example in which DFT has been used to predict and understand heterogeneous reactions of industrial relevance is the work of Nørskov et al. in which the reactivity of Ru nanoparticles as catalysts for the synthesis of ammonia was studied. First, size and shape of Ru nanoparticles were predicted as well as the reactivity of the different Ru atoms on the surface. An overall prediction of the catalytic activity was made based on DFT, which were later confirmed by experimental tests at industrial conditions [6].

Quantum chemical studies have been performed on the interaction of H_2, Cl and HCl with Si surfaces [7-20]. Note that while most published studies are focused on the reverse reaction, i.e. the deposition of Si(s), any obtained reaction path is also valid for the forward reaction due to the principle of microscopic reversibility. Both cluster model studies in which a part of the surface is cut out and simulated as a (large) cluster [7-9, 19, 20] and periodic boundary condition (PBC) studies [10-12] in which a small part of the surface is repeated infinitely in all directions have been reported. Computational studies indicate that the preferred mechanisms for adsorption of H_2 and HCl differ. The H_2 molecules desorbing from Si(111) and Si(100) show very similar behaviour, suggesting a common predominating mechanism and transition state for both surfaces [13]. This

mechanism is a two-dimer (surface Si dimers are shown in Figure 1) pathway in which the H atoms come from two Si atoms on adjacent dimers [7, 13]. In contrast, HCl pairwise intradimer pathway seems less activated though this may depend on surface coverage [7, 20]. Highly accurate, beyond DFT, PBC studies of the intra and inter dimer adsorption of H_2 recently published show a very small difference in barrier between the two mechanisms at low surface coverage [11], in contrast to earlier cluster studies at similar high level of theory based on Coupled Cluster single-double and perturbative triple (CCSD(T)) [7]. Because of the limited size of the cluster model, this suggests that PBC can describe some aspects of the system more realistically. While both cluster and PBC studies show a marked difference in results from DFT and CCSD(T) for the reaction of H_2 with the Si surface, differences between CCSD(T) and DFT for HCl (cluster model) were negligible [7]. Also, the energy barriers for the HCl reaction were very low compared to the corresponding H_2 reaction. Another PBC study, however has found barrierless adsorption for both H_2 and HCl [12], which is surprising for H_2 in light of the results mentioned above. Evidence for the barrierless adsorption of HCl both on dimer and interdimer has been shown by Guo et al. [10].

The aim of this study is to investigate the formation of SiH_xCl_{4-x} from Si(s) and HCl(g) by quantum chemical methods. In the present study a Si(100) surface with periodic boundary conditions was chosen as a model for Si calculating DFT with the robust and widely used PBE functional. The surface unit cell size was chosen to allow for a c(4x2) reconstruction of the surface. This idealised model allows for a one parameter investigation of the effect of a single Fe atom impurity on adsorption and reaction properties. Here we present initial results on the reconstruction and energetics of the Si(100) surface upon reaction with H, Cl and HCl, as well as the effect of a single Fe atom impurity at the surface.

Computational details

Density Functional Theory as implemented in Vienna Ab initio Simulation Package (VASP) version 5.4 [21, 22] was employed to investigate the reactivity of Si towards HCl, H and Cl. The exchange-correlation energy was calculated using the general gradient approximation (GGA) with the Perdew-Burke-Ernzerhof (PBE) functional [23], and a plane wave cut-off energy of 550 eV was employed.

Prior to surface construction the Si crystal structure was optimized using a 12x12x12 Γ-centred k-point grid. The calculated lattice constant is 5.469 Å, close to the experimental value of 5.431 Å [24]. The Si(100)-c(4x2) surface was chosen as model for the Si surface, giving a surface area of $(15.468Å)^2$. The Si(100)-c(4x2) surface was represented by an eight layers slab with 8 Si atoms within each layer. The bottom Si atoms were terminated

by hydrogen, which were initially relaxed while all the Si atoms were fixated. During further structural optimization, the hydrogen atoms and the bottom two Si layers were kept fixed. In order to investigate adsorption of HCl, Cl or H, the adsorbate was initially placed above high symmetry sites at the Si(100)-c(4x2) model surface as described in more detail below. Both the adsorbate and the top six layers of Si atoms were free to relax during structural optimization. The structures were optimized until the forces acting on each atom were below 0.02 eV/Å and with a convergence criterion for the electronic self-consistent loop of 1×10^{-6} eV. Transition states were explored by climbing image nudged elastic band (CI-NEB) calculation. Spin polarization was included in calculations with Fe.

Results and discussion

Surface reconstruction

The Si(100) surface reconstructs by pairing up the top-most atom [25] thus forming rows of 'valleys' and 'hills' observed already in 1959 with LEED [26], and this is reproduced well with DFT, as seen in Figure 1. The surface prior to reconstruction is shown at the top, and the pairing of the atoms in the topmost layer is shown in the middle. Further tilting of the atom pairs is highly stabilising, favoured by around 0.255 eV/Si-pair in this study, a somewhat higher value than early reports of 0.14 eV calculated with the much

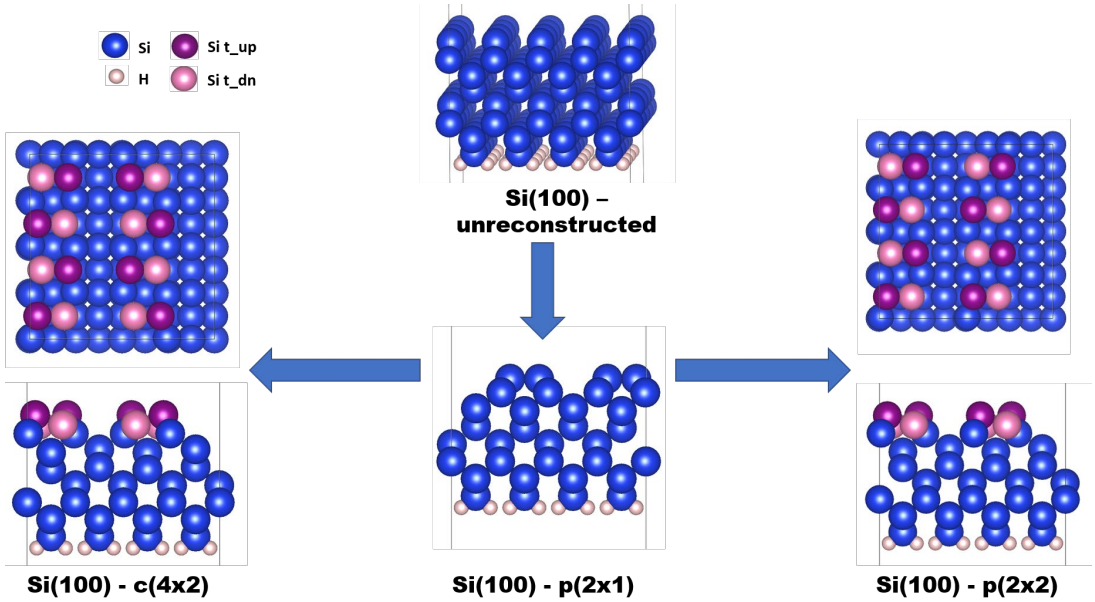


Figure 1: Surface reconstruction of the Si(100) surface. The top-layer of the reconstructed surface are colour coded according to height of atom. The lower part of the surface is H-terminated.

less accurate LDA functional [27]. Two such possible highly symmetrical sequences in the tilting was investigated, and the c(4x2) conformation was found slightly more stable. The p(2x1) and the c(4x2) conformations are mainly observed at room temperature and lower temperature, respectively [25]. The c(4x2) surface was therefore used as basis for further studies. Note, however that the difference in energy for the two buckled surface configurations is very small (0.7 meV/Si pair). In reality elastic coupling leads to alternate buckling of the Si dimers, but subjected to fast dynamic flipping already at room temperature [[13] and refs. therein], although it is probable that the c(4x2) conformation is still dominant [28]. In the optimized surface structure, the bond length of the dimers is 2.36 Å, almost identical to the 2.37 Å in the optimized bulk structure. The vertical height difference of the two atoms in the tilted pair is 0.77Å. These values are in close agreement with the experimental Si-Si dimer bond length of 2.2-2.4 Å [29, 30], the Si-Si distance in bulk (2.35 Å) [13], and the vertical height difference of 0.72 Å [30].

Figure 2 shows the different high-symmetry adsorption sites for the Si(100)-c(4x2) surface. There are 8 top-up atoms and 8 top-down atoms. Several sites are possible bridging between atom pairs: between to Si of the same dimer (one down and one up), between two adjacent dimers along the same hill, or between to dimers across the valley. Two possibilities were identified for the latter, either between to Si atoms pointing up or two pointing down. Lastly, two different 'hollow' sites, placed in the middle of a quadrilateral defined by four Si-atoms in the top layer, as seen in Figure 2.

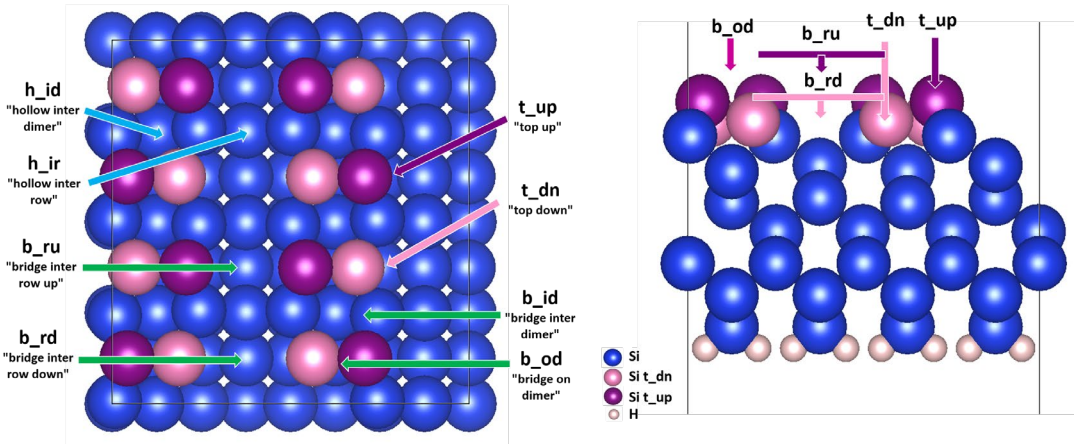


Figure 2: Surface sites of the reconstructed Si(100)-c(4x2) surface with Si-pairs flipped opposite to each other across the parallel rows. Sites of type (h): hollow between four atoms, (b) bridge between two atoms, (t) on top of an atom. The number of equivalent sites are: t_up: 8, t_dn: 8, b_od: 8, b_id: 16, b_ru: 4, b_rd: 4, h_id: 8, h_ir: 8. [id: inter-dimer, od: on-dimer, rd: inter-row dimer]

Formation of a Si vacancy on Si(100)-c(4x2)

The removal of one Si atom at the Si-surface introduces defects that may make the remaining surface more reactive compared to the ideal surface. Furthermore, the energy required to form such a vacancy gives an indication on the energy required to extract one Si by HCl to form $SiCl_xH_{4-x}$ (x=0-4). The energy penalty associated with the formation of a Si vacancy can be described by

$$E_{vac} = E_{surf\_1vac} - (E_{surf} - E_{Si\_bulk}) \quad (4)$$

where E_{surf} is the total energy of the up-flip reconstructed Si(100)-c(4x2) surface, E_{surf_1vac} is the total energy of the same surface with one Si vacancy and E_{Si_bulk} is the total energy of one bulk Si atom. The energy for introducing a vacancy in the Si(100)-c(4x2) surface is relatively high as illustrated in Figure 3. Vacancy formation in the third and fourth layers below a 'valley' is highly endoergic, requiring 3.7-3.9 eV per vacancy. In contrast the surface can more easily stabilize a vacancy in the same layers but situated below the topmost silicon pairs, i.e. the 'hill', with energy requirements of 1.7-2.0 eV per vacancy. Removal of Si from the two topmost layers has an energy cost between 1.2 and 1.5 eV. Removal of the up atom in the Si pair in the top layer (l1_t) required the least energy, closely followed by an atom in the second layer. That removing the topmost atom is least endoergic agrees with this atom being the least stabilized by the tilting of the Si pair during surface reconstruction. There is only one type of atom position in the second layer, between a up and a down Si atom on two adjacent Si pairs and slightly more towards the 'valley'. Interestingly, removing this atom in the second layer has the same energy penalty as removing the topmost atom of the Si pair. Inspection of the final structure reveals that the closest Si t_up moves into the vacancy and the resulting structure is identical to l1_t.

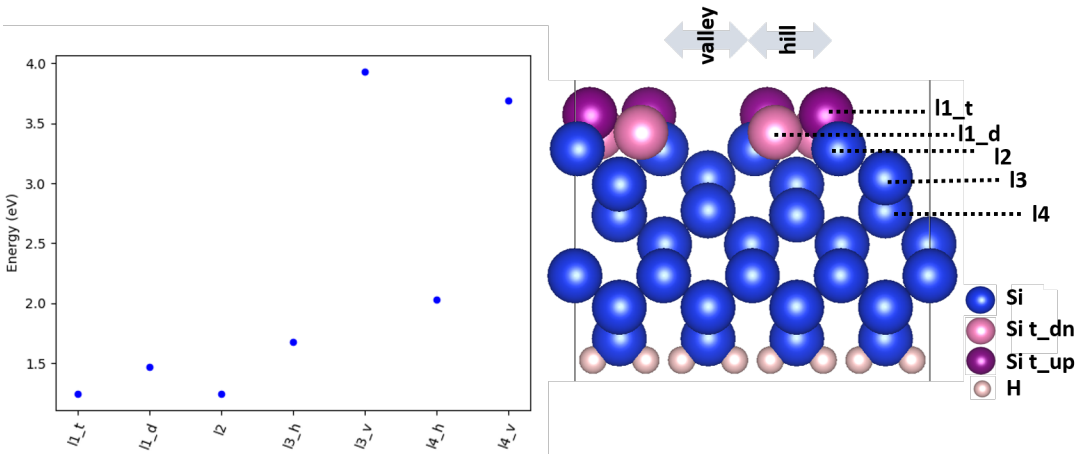


Figure 3: Energy penalty for the formation of a Si vacancy at the Si(100)-c(4x2) surface.

Both the Si t_up and Si t_dn atoms move slightly towards the middle of the original pair when the neighbour is removed. The Si t_up, however, does not completely go into the vacated Si t_dn position, but stays a little higher. Thus, removal of the Si t_dn requires more energy (by ~0.2 eV) than Si t_up. This result indicates an energy barrier for Si hopping at the surface, although this can be expected to be small.

Adsorption of single Cl, H or HCl on Si(100)-c(4x2)

The adsorption energies of H and Cl are listed in Table 1, where negative values indicate that the adsorption is energetically favourable. The adsorption energies are calculated with reference to H_2 and/or HCl in the gas phase, as follows:

$$E_{ads\_H} = E_{surf+H} - (E_{surf} + 0.5E_{H2}) \quad (5)$$

$$E_{ads\_Cl} = E_{surf+Cl} - (E_{surf} + E_{HCl} - 0.5E_{H2}) \quad (6)$$

$$E_{ads\_HCl} = E_{surf+HCl} - (E_{surf} + E_{HCl}) \quad (7)$$

where E_{surf+X} (X is H, Cl or HCl) is the total energy of the Si surface with an adsorbate and E_Y (Y is H_2 or HCl) is the total energy of gas phase species.

Table 1 Adsorption energies of H and Cl on Si(100)-c(4x2)

Site	E_{ads_H} (eV)	E_{ads_Cl} (eV)
b_id	1.02	moves to t_dn
b_od	0.60	moves to t_dn
b_rd	1.50	0.13
b_ru	1.74	-0.14
h_id	1.54	0.26
h_ir	1.41	0.35
t_dn	-0.58	-1.24
t_up	-0.76	-1.41

Hydrogen adsorption is only favourable at the top sites as shown in Table 1, with preference for the t_up sites by 0.18 eV compared to the t_dn sites. The adsorption energy of H in the t_up site is -0.76 eV. Chlorine also adsorbs preferentially in the t_up site with an energy of -1.41 eV. The adsorption geometry of H or Cl is not directly on top of the Si atom due to the covalent nature of the Si-Si/Cl/H bonds. H or Cl is tilted away from the surface normal towards the 'valley' area of the reconstructed Si(100)-c(4x2) surface. The resulting coordination around the Si atom is close to tetrahedral, in as similar manner as illustrated for dissociative adsorption of HCl in Figure 4. A stronger binding to H for the Si in t_up position compared to the t_dn position goes hand in hand with the t_up position being less stable than the t_dn position as inferred by the formation of vacancies (see above). This trend is the same for the adsorption of a single Cl atom, with 0.19 eV in difference. Upon adsorption of one Cl the tilting of the Si pair is reduced to almost nothing, and in both cases the atom with Cl attached is very slightly elevated compared to the other. The

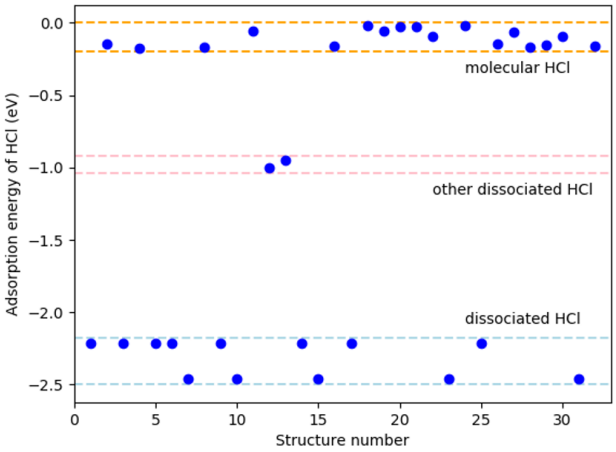


Figure 4: Energies of adsorption of HCl. The most stable adsorption was obtained with dissociated HCl.

same is true for the two starting position that moved to the t_dn adsorption site, and for H adsorbed on t_dn and t_up. Note also that the Cl adsorbed between two up Si atoms across the valley (b_ru) is slightly energetically stable, and the two Si-up the Cl coordinates to come across the valley come closer to each other (with the Cl between them). While we do not report on diffusion properties, we note that this position may be relevant for Cl hopping across the valley on the Si(100) surface.

Adsorption of HCl was studied by placing HCl in different orientation above the high symmetry sites. HCl were initially placed with the H-Cl bond parallel or perpendicular to the surface normal. For the latter case, configurations with H or Cl pointing down toward the surface were investigated. Depending on the orientation and distance to the surface, the results show that HCl can adsorb both molecularly and dissociatively. The most favourable configuration with an adsorption energy of 2.46 eV, is when H and Cl occupies a Si dimer (on-dimer adsorption), as illustrated in Figure 5. This is close to previous calculated values of -2.38 eV [10] and -2.48 eV [12]. Upon adsorption the Si-pair adjust its position, and there is no longer a clear-cut difference between 'up'-atom and 'down'-atom. This is in agreement with results found in literature which actually observe that the flipping can be reversed , e.g. [31]. H and Cl situated in top sites on two different Si dimers is ~0.25 eV less stable, also in agreement with Guo et al. who report 0.20 eV and 0.29 eV lower stability than on-dimer for adjacent inter-row and inter-dimer, respectively [10]. Molecular HCl, on the other hand, binds weakly with adsorption energies of -0.03 to -0.17 eV. It should be noted that while the present study does not reveal reaction mechanisms, Guo et al. show experimentally that inter-dimer adsorption is most abundant below 265 K and they explain this computationally with charge transfer directing the

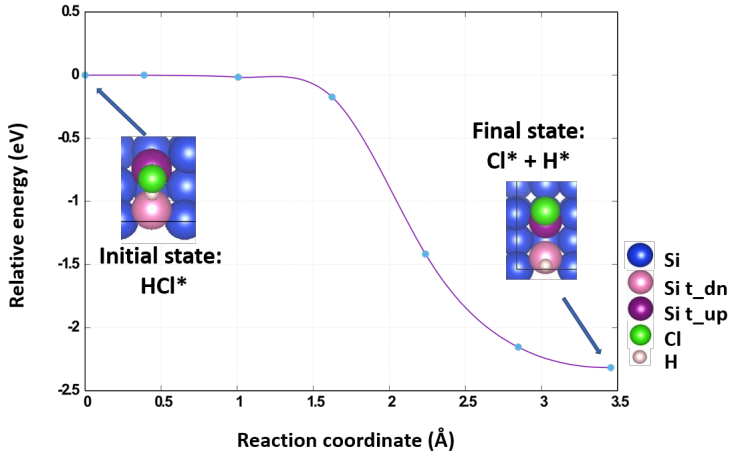


Figure 5: Energy profile of dissociative adsorption of HCl from weakly adsorbed

adsorption towards inter-dimer instead of on-dimer even though the latter is energetically more favourable.

As many of the HCl ends up in dissociated adsorption configurations, it can be expected that the energy barrier for dissociation is low. From the literature it is previously predicted that the activation energy for adsorption of HCl is negligible [7, 10]. Here, CI-NEB calculations were performed to evaluate the dissociation barrier of HCl. The calculation was started with both HCl far from the surface and at the surface in a weakly adsorbed state as given in Figure 4. Five images were used between the initial stated (adsorbed HCl or HCl far from the surface) to the final state (dissociatively adsorbed HCl). In both cases the dissociation is found to be barrierless as shown for the case of weakly adsorbed HCl in Figure **5**, demonstrating that HCl will readily dissociate at the Si(100)-c(4x2) surface. The presented results on the interaction of a single H, Cl and HCl with Si(100) agree with literature and provide a good starting point for the study of Fe impurities in the surface.

Effect Fe single atom impurity at the Si(100)-c(4x2) surface

In order to study the effect of a single Fe atom added at the surface on the reactivity of Si-atoms with HCl, the preferential position of Fe atoms at the surface was investigated. Three possible methods of single Fe-atom insertion to the system were investigated: (1) Fe-adsorbed on the adsorption positions identified in Figure 2 similarly to the adsorption of Cl and H described above, indicated with blue in Figure 6; (2) One Si atom was replaced by an Fe atom (green in Figure 6); and (3) the Fe atom was added interstitially at the height of the second layer, indicated by magenta (l2_b and l2_h) in Figure 6. The left panel in Figure 6 reports the energy of the optimized structure with the Fe atoms with

respect to the optimized Si(100) surface and optimized Fe bulk. The energy of Fe insertion is defined as

$$E_{\text{Fe-insertion}} = E_{\text{surf+Fe}} - E_{\text{surf}} - 1\ E_{\text{Fe-bulk}}\ (+\ 1\ E_{\text{Si-bulk}}) \qquad (8)$$

where $E_{\text{surf+Fe}}$ is the total energy of the Si surface with an additional Fe atom and $E_{\text{Fe-bulk}}$ is the energy of on bulk Fe atom. For systems with one less Si atom in the surface (i.e., for system where Si is replaced by Fe) the energy of a Si bulk atom ($E_{\text{Si-bulk}}$) is taken as reference value for the single Si atom**.**

Adsorption on top of the surface (blue in Figure 6) shows that adsorbing a single Fe atom on top of the surface is unstable compared to Fe in its most stable form (α-Fe). However, local minima were found for all possible sites, and Fe adsorbed on a hollow site between is the energetically most stable, as shown in Figure 6. However, the height of the Fe atom is slightly below the upper most Si atoms. The height/depth of the Fe atoms is shown in the right panel of Figure 6. For the most stable adsorbed conformation, h_id, this is below the height of the Si t_up position (Si t_up) and only marginally above the height of Si in the t_dn position (Si t_dn). The size of the bullet in Figure 6 is proportional to the coordination number, and generally Fe atoms surrounded by more (Si) atoms are more stable, as expected. h_id has 7 atoms in the first coordination sphere, although b_rd has one more even though being less stable. The structures represented by violet dots in Figure 6 have the same total number of atoms as the blue, but in this case the Fe is initially placed interstitially, i.e. below the top layer. One of these structures, l2_b shown in Figure

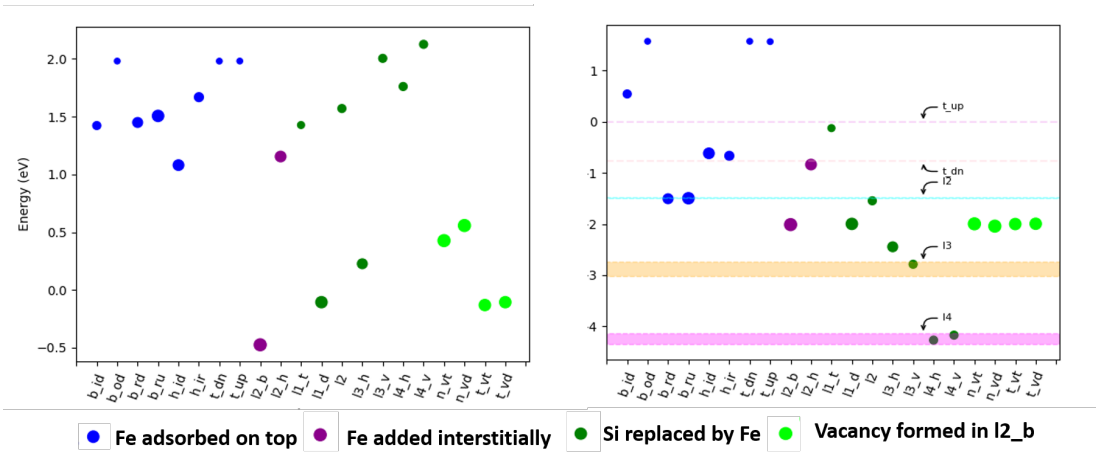


Figure 6: Left: Energetics for the insertion of single Fe atom defects in and on the Si(100) structure. *Blue*: systems in which Fe was adsorbed on the top (naming according to **Figure 2**). *Magenta*: Fe added interstitially. *Green*: One Si atom replaced by an Fe atom. *Lime*: One vacancy introduced on top layer of most stable system (l2_b, magenta). The number denotes at which layer the replacement took place initially, _t and _d indicate replacement of top or down atoms in the Si par of layer 1, _h and _v indicate replacement in the 'valley' or the 'hill' in the structure. The size of the bullet indicates the number of nearest neighbours (coordination numbers).

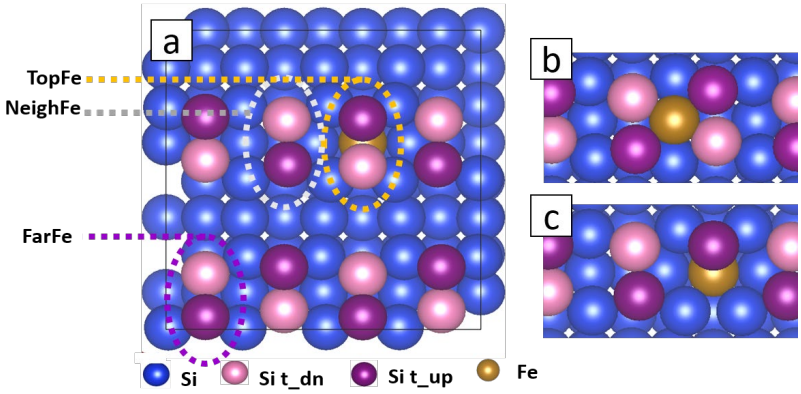


Figure 7: Local structures with Fe defects inserted subsurface. (a) l2_b, Fe is added interstitially directly below a complete Si pair. (b) l2_h, Fe is added interstitially between two Si pairs. (c) The lower laying Si (Si t_dn) was initially exchanged with Fe, but moved subsurface to the same position as in (a) leaving a vacancy in the initial Si t_dn position. Three Si-pairs at different distances from Fe are identified as in (a).

7 (a), stands out as particularly stable, and is indeed energetically more favourable than having the Fe in bulk shown by the negative energy of formation. This Fe atom is positioned directly below a Si pair. Upon insertion of Fe the tilting of the Si-pair above ceases with the Si t_dn moving to the same height as Si t_up. The height of the Fe atom in this most stable configuration is slightly below the second layer of Si atoms (Figure 6 right). In contrast, the interstitial configuration in which the Fe is placed below layer 1, but between two neighbouring pairs (l2_h) was not particularly stable. To summarize, the most stable structure with Fe atoms added and no Si vacancies, was with Fe placed interstitially directly below a top layer silicon pair giving the highest coordination number observed of 9 (referred to as Fe-Si(100)-c(4x2)).

The green bullets in Figure 6 show the energy of formation and height of Fe atom relative to Si t_up of Si(100) surfaces containing one Fe atom and with one Si atom less than the reference Si(100) surface, i.e. one with one Si vacancy. The dark green bullets are for systems in which Si atoms were directly replaced by an Fe atom, denoted by layer number. _t and _d for top or down atom in Si pair of layer one, and _v and _h according to position in the valley (between the Si pair ridges) or in a hill (below layer 1 Si pairs), respectively. Clearly forcing the Fe atom into a Si position far into the structure (layer 3 and 4) is not particularly stable. Here the surrounding Si structure is close to the Si bulk which is an optimal structure for Si, but not for the metallic Fe which prefers a closer packing. When replacing Si atoms closer to the surface with Fe the energy of the system is drastically reduced if the new structure optimizes to a rearrangement in which the Fe atoms gains a larger number of Si neighbours. This is the case for l1_d and l3_h, with coordination numbers for Fe of 8 and 6, respectively. Interestingly there is a large difference in energy, position and number of atoms depending on which of the Si-pair atoms is replaced, with the down position being by far the most stable. A closer look at

these structures reveals that while the Fe in the Si t_up position stays adsorbed on top, the Fe in the down position optimizes by going below the Si-pair positions, as shown in Figure 7c. Note that this is identical to the most stable structure found with all initial Si, in which the Fe is placed interstitially below the Si-pair, with the exception of one of the atoms in the Si-pair being removed. Fe in Si forms separate iron silicide phases and in $FeSi_2$, the Fe atom is coordinated to 8 Si atoms as in the most stable Fe position reported here.

Formation of a Si vacancy Fe-Si(100)-c(4x2)

Four structures with a surface Si vacancy were made from the most stable l2_b, by removing Si t_up and Si t_dn either on the Si pair directly above the Fe (see Figure 7) or the neighbouring pair. The energy and geometry data for these structures are included as lime green bullets in Figure 6. The surfaces with vacancies directly above the Fe atoms are significantly more stable than with vacancies on the neighbour Si pair. Note also that while the remaining Si atom of a pair is coordinated to the Fe, its position remains roughly unchanged, it moves significantly towards the geometrical middle of the original pair for a neighbour. Removal of one Si on top of Fe requires ~0.35 eV on top and ~1 eV on the neighbouring pair, which in both cases is significantly lower than the formation of a vacancy on the pure Si(100) surface of ~1.2 eV at the lowest (see Figure 3). This indicates that Fe has a positive effect on Si removal from the Si(100)-c(4x2) surface.

Adsorption of single Cl, H or HCl on Fe-Si(100)-c(4x2)

The adsorption energy of H or Cl at the Fe-Si(100)-c(4x2) surface is calculated according to equations (5) to (7), with E_{surf} being the total energy of the Fe-Si(100)-c(4x2) surface. As the top sites provided the most energetically stable adsorption sites, only top sites were investigated for adsorption of H and Cl for the Fe-Si(100)-c(4x2) system. Adsorption at top sites on three different Si dimers was investigated as seen in Figure 7: [TopFe]: The Si dimer directly above Fe (t_dn_{TopFe}, t_up_{TopFe}), [NeighFe]: Si dimers neighbouring TopFe ($t\_dn_{NeighFe}$, $t\_up_{NeighFe}$) and [FarFe]: Si dimer on row without Fe the farthest away from TopFe a within the limitations of the unit cell (t_dn_{FarFe}, t_up_{FarFe}).

The adsorption energies of H and Cl are listed in Table 2. The adsorption of H and Cl are strongly affected by the presence of Fe. In the case of H, the adsorption in top sites of the Si dimer directly above Fe becomes energetically unfavourable. H prefers the sites far away from Fe, and the adsorption energy is reduced at Si top sites neighbouring Fe. The trend is similar for Cl, where the strongest adsorption is found in top sites far from Fe.

Table 2 Adsorption energies of H and Cl on Si(100)-c(4x2) with Fe

Site	E_{ads_H} (eV)	E_{ads_Cl} (eV)
t_dn$_{overFe}$	0.05	-0.56
t_up$_{overFe}$	0.14	-0.58
t_dn$_{neighbouringFe}$	-0.55	-1.24
t_up$_{neighbouringFe}$	-0.58	-1.25
t_dn$_{awayFe}$	-0.73	-1.42
t_up$_{awayFe}$	-0.66	-1.31

The adsorption energetics are similar to that of the pure Si(100)-c(4x2) surface at top sites far from Fe. These results indicate that while the effect of Fe is not long-range it has some effect beyond the immediate neighbours.

Adsorption of HCl was calculated at using similar initial configurations as for the pure Si(100)-c(4x2) surface (described above). Additional configurations were included to account for the different sites due to the presence of Fe (dimers topFe, neighFe and farFe). The adsorption energy for various configurations of HCl on the Fe-Si(100)-c(4x2) surface is plotted in Figure 8. As in the case of the pure Si(100)-c(4x2) surface, both molecularly and dissociated HCl is obtained. Molecular HCl has adsorption energies in the range of -0.02 to -0.21 eV. There is a clear distinction between the adsorption energies of HCl close to the Fe impurity and far from it. Dissociated HCl situated at the same dimer far from the Fe impurity has an adsorption energy of -2.41 eV, close to the value obtained for the pure Si(100)-c(4x2) surface. Adsorption on two different dimers away from Fe, has an adsorption energy of -2.17 eV and dissociated HCl situated on the dimer neighbouring Fe is close in energy (-2.20 eV). Dissociated HCl situated at the Si dimer directly above Fe has an adsorption energy of 1.00 eV, largely destabilised (about 1.4 eV), compared to HCl situated at the same dimer far from Fe. Fe not only influences the bond strength of dissociated HCl, but also the activation of HCl. Preliminary results indicate an energy barrier for dissociation of HCl

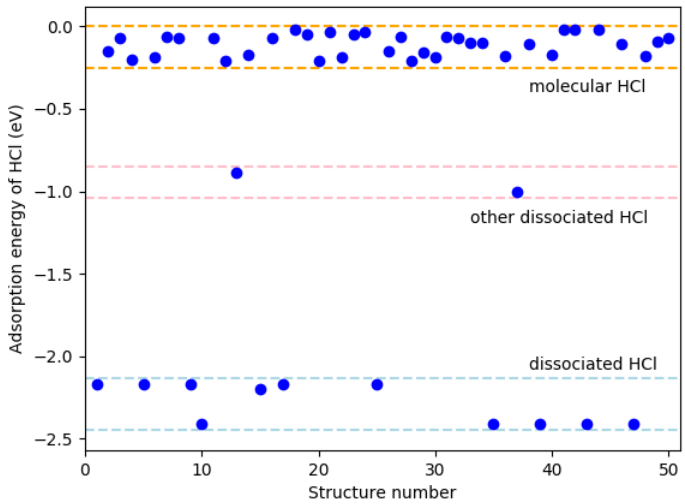


Figure 8: HCl adsorption energies for the Fe-Si(100)-c(4x2) surface.

over an Si dimer above Fe, in contrast to the non-activated process predicted for the pure Si(100)-c(4x2) surface.

It is evident that the introduction of one Fe impurity in the surface close to the top layer significantly reduces the adsorption energies of H, Cl and dissociated HCl to the coordinated Si atoms on the surface. For H, the adsorption is even unfavourable at these sites. This indicates that the presence of Fe will alter the reactivity. Experimental results have not been conclusive on the effect of iron, with reports varying between a negative effect on reactivity and selectivity towards $SiHCl_3$ and negligible effects of Fe. The preliminary results in the present study indicate that there will be an effect on coverage, and also that the dissociation of HCl will be affected. However, the height of this barrier will determine whether the reaction is significantly hindered at relevant reaction conditions. Since the interaction of surface Si with H, Cl and HCl is energetically altered with the presence of Fe, alterations in the energetics for the formation of the direct chlorination products are to be expected. However, this should be subject of further studies.

Conclusions

Quantum mechanical calculations using DFT have been applied to the Si(100) system. The Si(100) surface is known to reconstruct, and the calculations show a slight preference for the c(4x2) compared to the p(2x2) surface configuration agreeing with literature findings. The adsorption of H, Cl and HCl was investigated on the Si(100)-c(4x2) surface, where Si top sites are the energetically preferred adsorption sites. HCl can adsorb molecularly or dissociatively on this surface. However, the dissociation of HCl was found to be barrierless. Dissociated HCl is energetically favoured when adsorbed at top sites of the same Si dimer

A Fe impurity atom has a positive effect on the removal of Si atoms from the Si(100)-c(4x2) surface, where the energy penalty for formation of a Si vacancy is considerably lower (~0.75 eV) when Fe is present. However, Fe has a negative effect on the adsorption of H or Cl. H adsorption is no longer energetically stable at Si top sites directly in contact with the Fe impurity. The effect of Fe on the adsorption of H and Cl is not limited to the Si in close contact with Fe, but also adsorption at Si sites not directly bonded to the Fe impurity is weakened. The adsorption energetics is close to that of the pure system at Si sites further away from Fe. Both molecular and dissociated HCl is found, and the trend for the dissociated molecule is similar to that of the individual species. The adsorption is largely destabilised at Si sites directly bonded to Fe, and the binding strength increases at sites away from Fe. The results also indicate that Fe induces an energy barrier for HCl dissociation for Si sites directly bonded to Fe.

Acknowledgements

The present work has been carried out as part of project HECSI supported by the Norwegian Research Council (project No. 295861) and Elkem ASA. The authors acknowledge a generous grant of computing resources from the Research Council of Norway under the UNINETT Sigma2 program (account no. NN9462k). The authors also acknowledge Harry Rong and Torbjørn Røe for fruitful discussions.

References

1. Yasuda, K. and T.H. Okabe, *Solar-grade silicon production by metallothermic reduction.* JOM, 2010. **62**(12): p. 94-101.
2. O'Mara, W.C., R.B. Herring, and L.P. Hunt, *Handbook of Semiconductor Silicon Technology*. 1990: Elsevier.
3. Yasuda, K., K. Morita, and T.H. Okabe, *Processes for Production of Solar-Grade Silicon Using Hydrogen Reduction and/or Thermal Decomposition.* Energy Technology, 2014. **2**(2): p. 141-154.
4. Gaal, S., R. Shafer, and S. Stachowiak. *The Effect of Minor Elements on the Production of Trichlorosilane by Direct Chlorination*. in *Silicon for the Chemical and Solar Industry XIV*. 2018. Svolvær, Norway.
5. Sholl, D.S. and J.A. Steckel, *Density Functional Theory*. 2009.
6. Honkala, K., A. Hellman, I.N. Remediakis, A. Logadottir, A. Carlsson, S. Dahl, C.H. Christensen, and J.K. Nørskov, *Ammonia Synthesis from First-Principles Calculations.* Science, 2005. **307**(5709): p. 555-558.
7. Cavallotti, C., *Reactivity of Silicon Surfaces in the Presence of Adsorbed Hydrogen and Chlorine.* Chemical Vapor Deposition, 2010. **16**(10-12): p. 329-335.
8. Kunioshi, N., K. Anzai, H. Ushijima, and A. Fuwa, *Effects of cluster size on calculation of activation energies of silicon surface reactions with H2 and HCl.* Journal of Crystal Growth, 2015. **418**: p. 115-119.
9. Kunioshi, N., S. Hagino, A. Fuwa, and K. Yamaguchi, *Novel pathways for elimination of chlorine atoms from growing Si(100) surfaces in CVD reactors.* Applied Surface Science, 2018. **441**: p. 773-779.
10. Guo, S.Y., M. Ebrahimi, I.R. McNab, and J.C. Polanyi, *Charge-Transfer in Silicon Governs the Pattern of Dissociative Attachment of Hydrogen Halides: HCl, HBr, and HI.* The Journal of Physical Chemistry C, 2016. **120**(39): p. 22414-22420.
11. Tsatsoulis, T., S. Sakong, A. Gross, and A. Grueneis, *Reaction energetics of hydrogen on the Si(100) surface revisited: a periodic many-electron theory study.* arXiv.org, e-Print Arch., Condens. Matter, 2018: p. 1-12.
12. Yadav, S. and C.V. Singh, *Molecular adsorption and surface formation reactions of HCl, H2 and chlorosilanes on Si(100)-c(4 × 2) with applications for high purity silicon production.* Applied Surface Science, 2019. **475**: p. 124-134.
13. Dürr, M. and U. Höfer, *Dissociative adsorption of molecular hydrogen on silicon surfaces.* Surf. Sci. Rep., 2006. **61**(12): p. 465-526.
14. Lee, L.-Q. and P.-L. Cao, *Cl-Cl interaction and chlorine adsorption mechanism on Si(100)2*1.* Journal of Physics: Condensed Matter, 1994. **6**(31): p. 6169-6175.
15. Radny, M.W., P.V. Smith, and P.L. Cao, *An ab initio Hartree-Fock/density functional study of the cluster simulated Si(111)7 × 7:Cl adsorption system.* Surface Science, 1996. **365**(1): p. 15-28.
16. Ricca, A. and C.B. Musgrave, *Theoretical study of the Cl-passivated Si(111) surface.* Surface Science, 1999. **430**(1): p. 116-125.
17. Rosenow, P. and R. Tonner, *Extent of hydrogen coverage of Si(001) under chemical vapor deposition conditions from ab initio approaches.* The Journal of Chemical Physics, 2016. **144**(20): p. 204706.
18. Sakurai, S. and T. Nakayama, *Cl adsorption process on Si(111) surfaces.* Surface Science, 2001. **493**(1): p. 143-147.
19. Anzai, K., N. Kunioshi, and A. Fuwa, *Analysis of the dynamics of reactions of SiCl2 at Si(100) surfaces.* Applied Surface Science, 2017. **392**: p. 410-417.

20. Kunioshi, N., Y. Fujimura, A. Fuwa, and K. Yamaguchi, *Dynamics of reactions inhibiting epitaxial growth of Si(100) surfaces via interaction with hydrogen chloride.* Computational Materials Science, 2018. **155**: p. 28-35.
21. Kresse, G. and J. Furthmüller, *Efficient iterative schemes for ab initio total-energy calculations using a plane-wave basis set.* Physical Review B, 1996. **54**(16): p. 11169-11186.
22. Kresse, G. and J. Furthmüller, *Efficiency of ab-initio total energy calculations for metals and semiconductors using a plane-wave basis set.* Computational Materials Science, 1996. **6**(1): p. 15-50.
23. Perdew, J.P., K. Burke, and M. Ernzerhof, *Generalized Gradient Approximation Made Simple [Phys. Rev. Lett. 77, 3865 (1996)].* Physical Review Letters, 1997. **78**(7): p. 1396-1396.
24. Becker, P., P. Scyfried, and H. Siegert, *The lattice parameter of highly pure silicon single crystals.* Zeitschrift für Physik B Condensed Matter, 1982. **48**(1): p. 17-21.
25. Bent, S.F., *Chapter 5 - Semiconductor Surface Chemistry*, in *Chemical Bonding at Surfaces and Interfaces*, A. Nilsson, L.G.M. Pettersson, and J.K. Nørskov, Editors. 2008, Elsevier: Amsterdam. p. 323-395.
26. Schlier, R.E. and H.E. Farnsworth, *Structure and Adsorption Characteristics of Clean Surfaces of Germanium and Silicon.* The Journal of Chemical Physics, 1959. **30**(4): p. 917-926.
27. Krüger, P. and J. Pollmann, *Dimer Reconstruction of Diamond, Si, and Ge (001) Surfaces.* Physical Review Letters, 1995. **74**(7): p. 1155-1158.
28. Guo, C.-S., K. Hermann, and Y. Zhao, *Dynamics and Energetics of Reconstruction at the Si(100) Surface.* The Journal of Physical Chemistry C, 2014. **118**(44): p. 25614-25619.
29. Bullock, E.L., R. Gunnella, L. Patthey, T. Abukawa, S. Kono, C.R. Natoli, and L.S.O. Johansson, *Surface Core-Level Photoelectron Diffraction from Si Dimers at the Si(001)-($2\ifmmode\times\else\texttimes\fi{}1$) Surface.* Physical Review Letters, 1995. **74**(14): p. 2756-2759.
30. Over, H., J. Wasserfall, W. Ranke, C. Ambiatello, R. Sawitzki, D. Wolf, and W. Moritz, *Surface atomic geometry of Si(001)-(2\ifmmode\times\else\texttimes\fi{}1): A low-energy electron-diffraction structure analysis.* Physical Review B, 1997. **55**(7): p. 4731-4736.
31. Wang, C.-G., K. Huang, and W. Ji, *Dissociative adsorption of CH3X (X = Br and Cl) on a silicon(100) surface revisited by density functional theory.* The Journal of Chemical Physics, 2014. **141**(17): p. 174701.

Silicon for the Chemical and Solar Industry XV
Trondheim, Norway, June 15 – 18, 2020

Effects of Shortening a Pilot-Scale Hydrochlorination Reactor with Catalytic Considerations and Comparison to Mathematical Model Predictions

Matthias A. Colomb[1)], Esteban J. Romano[1)], and Srinivas Palanki[2)]
1) Mitsubishi Polysilicon America Corp., Theodore, AL 36582
2) Dan F. Smith Department of Chemical Engineering, Lamar University, Beaumont, TX 77710

Abstract

In the hydrochlorination reaction, silicon tetrachloride (STC), metallurgical silicon, and hydrogen are converted to trichlorosilane (TCS) at about 540°C. Previously, a pilot-scale reactor was used to study the yield of TCS produced by the hydrochlorination reaction. The yield observed by experimentation compared favorably with a scalable mathematical model developed to predict the rate of TCS conversion. The model predicted that 90% of the final amount of TCS produced was achieved after the reactant gas traveled a quarter of the vertical distance in the reaction section of the reactor. The pilot-scale reactor was shortened to verify the model predictions. In addition, some catalytic effects on the reaction were studied.

Introduction

In the polysilicon industry, trichlorosilane (TCS) is passed over a circuit of polysilicon seed rods heated to about 1000°C to produce ultra-pure polysilicon. The TCS feed gas for the polysilicon reactors can be produced by the direct chlorination of metallurgical grade silicon by hydrogen chloride (HCl). This process is typically carried out in a fluidized bed reactor and produces a byproduct of silicon tetrachloride (STC) in the amount of 4-8 mol % in the product stream, depending on operating conditions, as shown in Eqs. 1 and 2.

$$Si_{mg}(s) + 3HCl(g) \leftrightharpoons SiHCl_3(g) + H_2(g) \quad (1)$$

$$SiHCl_3(g) + HCl(g) \leftrightharpoons SiCl_4(g) + H_2(g) \quad (2)$$

STC is similarly created as a byproduct of producing polysilicon rods whose process is approximated by Eqs. 3-5.

$$SiHCl_3(g) + H_2(g) \leftrightharpoons Si(s) + 3HCl(g) \quad (3)$$

$$SiHCl_3(g) + HCl(g) \leftrightharpoons SiCl_4(g) + H_2(g) \quad (4)$$

$$SiHCl_3(g) + H_2(g) \leftrightharpoons SiH_2Cl_2(g) + HCl(g) \quad (5)$$

The amount of STC in the product stream is between 1-5 mol % depending on batch time and operating conditions.

There is a limited market for the sale of STC to produce fumed silica and optical fibers. Inventory of STC in the manufacture of polysilicon must be carefully managed and can result in reduced production of polysilicon if stores reach maximum capacity. For these reasons, it is desirable to convert STC to the TCS feed stock for the polysilicon reactors by the hydrochlorination process as described in a two-step process by Mui and Seyferth in Eqs. 6-8 [1].

$$SiCl_4(g) + H_2(g) \leftrightharpoons SiHCl_3(g) + HCl(g) \quad (6)$$

$$Si_{mg}(s) + 3HCl(g) \leftrightharpoons SiHCl_3(g) + H_2(g) \quad (7)$$

$$(Overall)\ Si_{mg}(s) + 3SiCl_4(g) + 2H_2(g) \leftrightharpoons 4SiHCl_3(g) \quad (8)$$

The hydrochlorination process can be used to reduce STC stores, produce TCS as a feed stock for the polysilicon reactors or for liquid sales, and reduce consumption of metallurgical silicon.

Previous Studies

A pilot-scale reactor was designed by Colomb *et al.* for information critical to the design of an industrial-scale reactor [2]. The TCS yield from the pilot-scale reactor was predicted with a mathematical model. The scalable mathematical model accounts for the hydrodynamics in a fluidized bed reactor and is based on the modeling framework of Kunii and Levenspiel [3]. The mathematical model for the hydrochlorination reaction in a fluidized bed was verified with the TCS yield published in the laboratory-scale work of Cygon [4] and Sill [5] resulting in differences between predicted TCS yield from experimentally observed TCS yield of less than ±6% [6]. The effect of HCl addition in the experiments of Cygon [4] and Sill [5] was studied by Becker [7] in the range of 2-6 mol % addition in the feed, which encompasses the range studied for the experiments in

this manuscript. Furthermore, the model was validated on the pilot-scale reactor of Colomb *et al.* The model was adjusted by changing the bubble size model from that of Yasui and Johanson [8], appropriate for laboratory-scale reactors, to Werther's[9], appropriate for pilot-scale and some industrial-scale reactors. In addition, the pilot-scale model used thermocouples along the bed height to account for energy losses from the reaction and to the environment; a change from the isothermal assumption used for the laboratory-scale work. No further adjustments were necessary to model the pilot-scale system and the difference between experimentally observed yield and yield predicted by the model was less than ±7%.

The mathematical model results predicted that 90% of the final TCS conversion on a mole basis was achieved a quarter of the distance up the 5.48 m tall reactor as shown in Figure 1 [2].

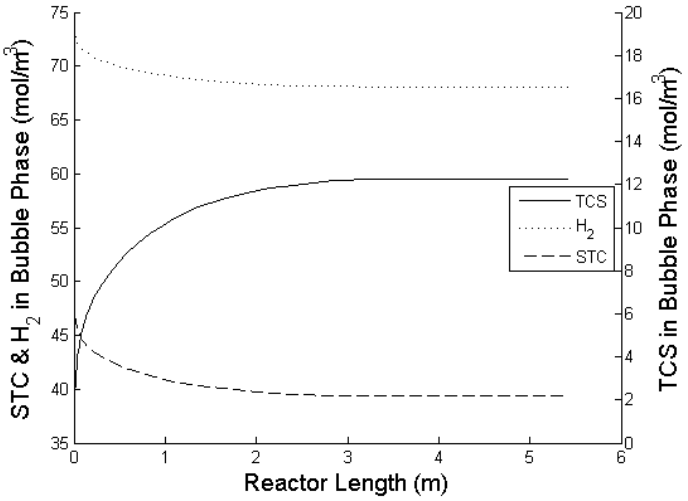


Figure 1: TCS conversion in reactor versus vertical bed height.

The model showed a shortened design would be adequate for targeted conversion. A shortened reactor would also serve to further validate the mathematical model.

Two previously unpublished experiments were conducted in this reactor without copper catalyst and are shown in Table 1.

Table 1: Hydrochlorination experiments conducted without catalyst.

Exp	Temp Bottom ($°C$)	Bottom Press (PSIG)	Molar Ratio (H_2/STC)	x_{HCl} (mol%)	W_{Cu} (wt%)	u_0 (m/s)	F_{TCS} (Norm)	Y_{TCS} (mol%)
1	457	116	0.99	3.5	0	0.111	0.865	15.1
2	512	116	1.08	3.5	0	0.119	1.00	18.3

For the experiments shown in Table 1 and subsequent experiments conducted for this manuscript, the hydrogen used for the reaction was from a recovery stream and contained some HCl (15,000-50,000 PPM), TCS (1500-2000 PPM), and dichlorosilane (700-3000 PPM). The intent of these experiments was to study the effect of temperature on TCS yield without copper catalyst while holding other important parameters nearly constant. The pressure at the bottom of the reactor was kept at 116 psig. The molar ratio of hydrogen to STC was kept close to the target of 1. The molar fraction of HCl (x_{HCl}) in the feed was 3.5%. There was a small variation in superficial velocity (u_0) from 0.111 to 0.119 m/s because of the change in feed temperature. The results of the experiment were the normalized mass flow rate of TCS (F_{TCS}) and the yield of TCS (Y_{TCS}). The reactor yield of TCS was calculated with the equation presented by Becker [7].

$$Y_{SiHCl_3} = \frac{3\dot{n}_{SiHCl_3,OUT}*100}{4\dot{n}_{SiCl_4,IN}+\dot{n}_{HCl,IN}} \quad (9)$$

Surprisingly, the expected reduction in TCS yield was not observed and conversion was comparable to the copper(II) chloride catalyzed experiments of Colomb *et al.* [2].

A decision was made to shorten the reaction section of the pilot-scale reactor to determine if the reaction was proceeding as quickly as shown by the model, to investigate the TCS yield achieved without added copper(II) chloride catalyst, and to test a new copper catalyst with improved material handling properties and less health hazards.

Experimental

The hydrochlorination system of Colomb *et al.* was used for the current study [2]. The reaction section and internals of the fluidized bed were physically shortened to 25% of their original length from 5.48 m to 1.37 m. No other modifications were made to the system shown in Figure 2.

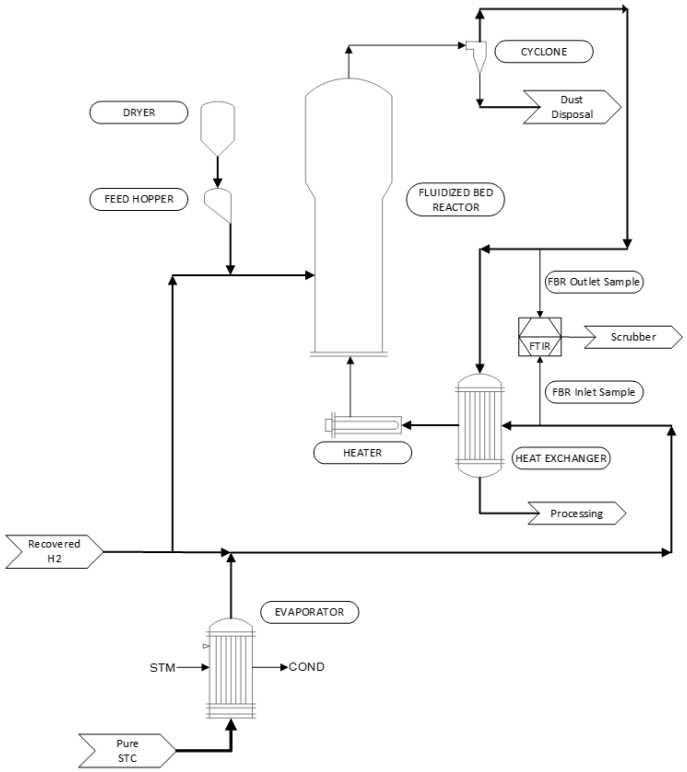


Figure 2: Process flow diagram of hydrochlorination system

For the previous studies and for the current study, the metallurgical grade silicon utilized was Silgrain from the Elkem Silicon Materials Company and was fed batch-wise to the reactor from a line 0.833 m in height in the reaction section of the fluidized bed reactor. The hydrogen used for the reaction was from a recovery stream and contained some HCl (15,000-50,000 PPM), TCS (1500-2000 PPM), and dichlorosilane (700-3000 PPM). The chemical composition of the inlet stream varied by less than 10% for each constituent in the time frame of each experimental trial. Pure STC was vaporized in an evaporator and blended with the hydrogen stream, heated to reaction temperature, and fed to the reactor through a distributor plate.

The inlet and exhaust stream composition of the hydrochlorination system was determined by an FTIR calibrated by Colomb *et al*. for high concentrations of chlorosilanes [10]. The STC concentration in the feed was determined by mass flow controller as it was considered to be more accurate. In addition to the FTIR utilized in previous studies, another FTIR was used for one experiment to verify the accuracy of results. The new FTIR was an MKS model MultiGas 2030 which was calibrated for a broad range of HCl, DCS, TCS, and STC by the Prism Analytical Technologies Company. The FTIR was equipped with an MKS custom built 2cm cell, which contained a mirror outside of the process gas stream. This was determined to be a necessity as chlorosilanes quickly fouled the mirror of the standard cell. There were no fouling problems after installation of the custom cell and the cell temperature control environment was superior to that of the original FTIR system.

Mathematical Model

The mathematical model of Colomb *et al.* was used to predict the yield of TCS from the pilot-scale reactor and to serve as a basis for recommending an industrial-scale design [2]. The model is based on the fluidized bed reactor model of Kunii and Levenspiel because the modeling parameters are physically reasonable and can be accurately scaled-up [3]. The model accounts for reacting gas (STC and Hydrogen) entering the reactor through a distributor as tiny bubbles and coalescing as they travel up to form larger bubbles. The bubbles cause mass transfer inefficiencies. The reaction kinetics are dependent on the iron inherently present in metallurgical grade silicon ($r_{Fe_xSi_y}$) and a parallel reaction with copper if added as a catalyst ($r_{Cu_xSi_y}$) as detailed by Becker [9]. The model of Colomb *et al.* [2] is shown in Eq. 10.

$$-u_0 \frac{dC_{ib}}{dz} = f_b \varrho_{si} v_i (\gamma_{Fe} r_{Fe_xSi_y} + \gamma_{Cu} r_{Cu_xSi_y})_b + \delta K_{be}(C_{ib} - C_{ie}) \quad (10)$$

For the equation *i* represents the chemical species either STC, hydrogen, or TCS and *b* stands for the bubble phase. Eq. 10 accounts for the consumption of a reactant or production of product chemical species of concentration *C* in the bubble phase by chemical reaction and by mass transfer to the emulsion phase *e*. The rate of mass transfer of chemicals to the emulsion phase is shown in Eq. 11.

$$\delta K_{be}(C_{ib} - C_{ie}) \cong f_e \varrho_{si} v_i (\gamma_{Fe} r_{Fe_xSi_y} + \gamma_{Cu} r_{Cu_xSi_y})_e \quad (11)$$

The mass transfer of chemicals from the bubble phase to the emulsion phase is approximately equal to its rate of consumption or production in the emulsion phase.

Bubble rise velocity, the fraction of the bed in bubbles, and mass transfer coefficient (K_{be}) are strong functions of bubble size. Bubbles are small in size at the distributor and grow as they coalesce as they travel up the reactor. To capture these changing dynamics, Werther's [8] bubble model was combined with the Kunii and Levenspiel [3] model to accurately describe the changing hydrodynamics along the bed height in the manner described by Colomb *et al.* [2].

The reactor yield of TCS was calculated with Eq. 9 as found in the "Previous Studies" section. The accuracy of the modeling results were determined by comparing the experimental TCS yield results as determined by FTIR with the results predicted by the model as shown in Eq. 13.

$$\%Diff = \frac{(Y_{TCS,EXP} - Y_{TCS,PRED}) * 100}{Y_{TCS,EXP}} \quad (13)$$

The model was used without modification, unless otherwise noted, to study the conversion of STC to TCS in the shortened conversion reactor

Results and Discussion

Before the reactor was shortened, two tests (Experiments 1 and 2) were performed without added copper catalyst. Subsequently, three experiments were conducted in the shortened reactor to study the effects of the shortened bed height and copper catalyst. Experiment 3 in the shortened reactor was also conducted without copper catalyst. Experiments 4, 5A, and 5B were performed with copper alloyed metallurgical silicon from the Elkem Silicon Materials Company. The alloyed silicon contained 2.5% copper by weight and was blended in a ribbon mixer with Silgrain metallurgical silicon for a final copper weight of 0.1%. Experiments 5A and 5B were from the same reactor trial; however, outlet gas composition was studied by different FTIR analyzers. Experiment 5B was studied with a new FTIR analyzer as explained in the "Experimental" section. The experimental conditions along with the observed results by FTIR and those predicted by the mathematical model are included in Table 2.

Table 2: Hydrochlorination reactor experimental results versus initial model predictions.

Exp	Reactor Length	Temp Heater ($^{\circ}C$)	Bottom Press (PSIG)	Molar Ratio (H_2/STC)	x_{HCl} (mol%)	W_{Cu} (wt%)	u_0 (m/s)	F_{TCS} (Norm)	Y_{TCS} (mol%)	Y_{TCS} Pred (mol%)
1	Long	457	116	0.99	3.5	0	0.111	0.768	15.1	11.1
2	Long	512	116	1.08	3.5	0	0.119	0.888	18.3	15.2
3	Short	552	112	1.41	2.2	0	0.147	1.00	20.6	14.5
4	Short	454	111	1.29	2.8	0.1	0.123	0.637	13.1	8.4
5A	Short	531	112	1.22	2.8	0.1	0.140	0.925	18.1	14.1
5B	Short	542	112	1.23	2.8	0.1	0.140	0.983	19.5	14.8

Catalytic Effects

Surprisingly, there was no reduction in TCS yield in Experiment 1-3, given other parameters like temperature, even though no copper catalyst was added. Further, shortening the reactor did not reduce TCS yield in Experiments 3-5. The mathematical model predicted much less TCS yield and a possible explanation follows. According to Mui, hydrochlorination preferentially occurs in the silicon where there is a silicon iron complex Fe_xSi_y [11]. Lehnen's experiments were conducted in a fused silica lined reactor to preclude known catalytic effects of a steel walled reactor [12]. His work with iron oxide catalyzed hydrochlorination also showed increased TCS yield in certain reaction conditions. For these reasons, it is theorized that the reaction is catalyzed by the iron in the reactor walls, internals, and distributor. The internals are constructed of 316 stainless steel and the distributor is made of 304 stainless steel, while the material of construction of the reactor is confidential. This catalytic effect of iron reactor parts explanation would also support the observation of no reduction in conversion given a shortened reactor length.

It was shown in the modeling work of Colomb et al. that the fractional iron weight (γ_{Fe}) in the metallurgical silicon also includes a reactivity coefficient as a lumped parameter when HCl is included in the feed gas to account for increased reactivity [6]. The increase in reactivity is thought to occur by the action of HCl on the silicon surface as it rapidly removes the less reactive oxidized silicon layer thereby exposing sites of reactive silicon iron complexes. This lumped parameter needs to be suitably adjusted in the mathematical model to account for higher reactivity when more iron is present in the reactor due to the presence of internals made of stainless steel. In Colomb et al. [6], the reactor studied was a laboratory-scale reactor and a value of 0.0058 was used for this lumped parameter. The model predictions with this value for our pilot-scale reactor are shown in Table 2. Since the pilot-scale reactor has iron parts exposed to the reaction such as internals, it is expected that the lumped parameter that captures the fractional iron weight and reactivity needs to be adjusted. This parameter value was adjusted to a value of 0.055 in the mathematical model until TCS yield in Experiment 2 reached an equilibrium value. The modeled TCS yield increased from a value of 15.2 to 17.5 while the value calculated from the FTIR was 18.3. The adjusted value for the iron to silicon fraction used in the mathematical model was subsequently used to model all the experiments and the results are shown in Table 3.

Table 3: Hydrochlorination experiment results versus modified model predictions.

Exp	Reactor Length	Temp Heater ($^{\circ}C$)	Y_{TCS} (mol%)	Y_{TCS} Pred (w/ γ_{Fe}=0.055) (mol%)	Diff (%)
1	Long	457	15.1	15.7	-3.9
2	Long	512	18.3	17.5	4.3
3	Short	552	20.6	19.3	6.5
4	Short	454	13.1	13.9	-6.5
5A	Short	531	18.1	18.1	-0.2
5B	Short	542	19.5	18.5	5.1

With the adjustment to the iron fraction of catalyst, the model predicted experimental TCS yield (Y_{TCS}(Pred w/γ_{Fe}=0.055)) with less than ±7% difference from the TCS yield as measured by FTIR (Y_{TCS}). The consumption and production rate of the hydrochlorination chemicals are shown for Experiment 3 in Figure 2.

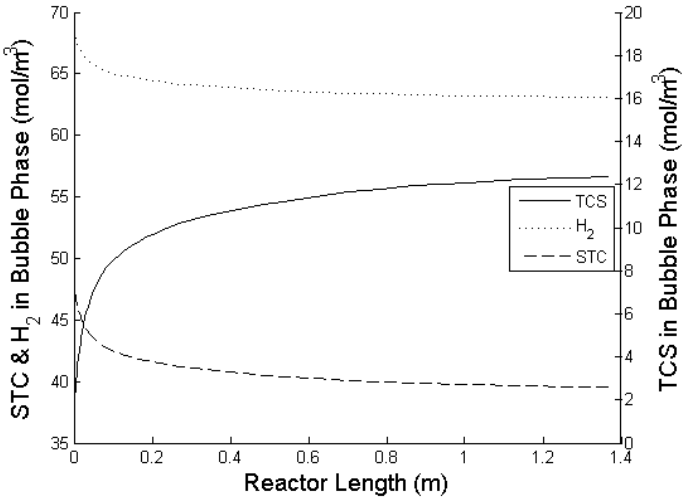


Figure 2: Hydrochlorination reaction progress versus bed height in shortened reactor.

The surface area of iron of the reactor, internals, and distributor to weight of metallurgical silicon in the reactor is an important parameter to consider for scale-up calculations. The ratio for the pilot-scale reactor was calculated to be 0.041m^2/kg. This ratio would need to be maintained for an industrial-scale design to justify using the adjusted iron to silicon weight ratio of 0.055, and even then its use for scale-up design should be considered judiciously. Fortunately, the other parameters of the model are physically reasonable and can be adjusted for an industrial-scale design.

Experiments 3-5 were conducted with a copper alloyed metallurgical silicon catalyst from the Elkem Silicon Materials Company. Unfortunately, the catalytic effect attributed to the iron parts of the pilot-scale reactor was so strong that the model did not show a significant change in TCS yield when the kinetics of the copper catalyst were incorporated. For this reason, the effect of the copper alloyed metallurgical silicon catalyst could not be evaluated in this study.

Analytical Results

To help validate the calibration of the original FTIR and the adjustment of the iron to silicon ratio to a value of 0.055, a second FTIR was purchased to analyze the exhaust stream of the hydrochlorination reactor and is described in the “Experimental” section. In the time required to switch the sample system from the original analyzer to the new analyzer, the bottom temperature of fluidized bed reactor increased from 531 to 542 °C. Given this temperature increase, the model predicted an increase of TCS yield from 18.1 to 18.5 mol%. The TCS yield as calculated with data from the new FTIR was 19.5 mol% representing a difference of 7.7% from the value of the original FTIR and a difference of 5.1% from the modeled value. Because the difference in values were both

less than 10%, the calibration of the original FTIR and the adjustment of the value of iron to silicon ratio were considered validated.

Conclusions

A pilot-scale reactor was tested without copper catalyst addition and then shortened to one quarter of its original length to study mass transfer and catalytic effects. As expected from the original testing, shortening the reactor did not reduce TCS yield. Surprisingly, the removal of the copper(II) chloride catalyst did not decrease TCS yield in either the original reactor or the shortened reactor. It was concluded that iron in the reactor walls, internals, and distributor are acting as a catalyst. With an adjustment to the iron to silicon weight fraction in the reaction kinetics of the mathematical model, TCS yield was predicted for all five experiments with less than ±7% difference compared to yield calculated by FTIR analysis. A new FTIR was successfully used to validate the original FTIR calibration and to confirm the TCS yield of the hydrochlorination system.

Notation

C	**component concentration, mol^1m^{-3}**
F_{TCS}	**TCS mass flow rate normalized to the data set**
f	**volume of solids per volume of bed**
K	**gas interchange coefficient, s^{-1}**
$\dot{n}$	**molar flow rate, mol^1s^{-1}**
r	**reaction rate, $mol^1s^{-1}kg_{cat}^{-1}$**
u_0	**superficial velocity, m^1s^{-1}**
v	**stoichiometric coefficient**
x_{HCl}	**molar fraction of HCl in the feed**
Y_{SiHCl_3}	**yield of TCS, *see Eq.9*, %**
Y_{TCS}	**yield of TCS as measured by FTIR, %**
$Y_{TCS,\ PRED}$	**yield of TCS as predicted by mathematical model with value of γ_{FE} in silicon doubled in the model**
$Y_{TCS,\ PRED}$ $(\gamma_{FE=0.055})$	**yield of TCS as predicted by mathematical model with value of γ_{FE} set to 0.055 in the model to account for catalytic effect of reactor's iron parts**
z	**reactor height, m**

Greek letters

δ	**bed fraction in bubbles**
ε	**fraction of voids in the bed**
γ	**fractional weight of catalyst**
ϱ	**density, kg^1m^{-3}**

Subscripts

b	**bubble phase**
Cu_xSi_y	**copper catalysed reaction**
e	**emulsion phase**
Fe_xSi_y	**iron catalysed reaction**
i	**component (*STC*, H_2, *TCS*)**
IN	**actual feed stream**
mg	**metallurgical grade silicon**
OUT	**product stream**
Si	**silicon**

References

1. J. Mui, and D. Seyferth, The hydrogenation of $SiCl_4$, Final Report, JPL Contract 955382, 1981.
2. Colomb, M. A., Palanki, S., and Sylvester, N. D., Experimental verification of scalable model for the hydrochlorination reaction in a pilot-scale fluidized bed reactor, Powder Technology, pp. 989-998, Vol. 301, (2016).
3. Kunii, D., and Levenspiel, O., *Fluidization Engineering*, 2nd ed., Butterworth-Heinemann, Newton, MA (1991).
4. Cygon, P., Reaction Studies for the Hydrochlorination of Silicon in a Laboratory Fluidized Bed System, Diss., U of Cologne, (1999).
5. Sill, T., Buchholz, S., Weber, R., and Mleczko, L., *Thermodynamic, Mechanistic and Reaction Engineering Aspects of Hydrochlorination of Silicon*, Silicon for the Chemical Industry V, Trondheim, Norway (2000).
6. Colomb, M. A., Palanki, S., and Sylvester, N. D., *Modeling the Hydrochlorination Reaction in a Laboratory-Scale Fluidized Bed Reactor*, Powder Technology, pp. 242-250, Vol. 292, (2016). G.
7. Yasui, L.N. Johanson, Characteristics of gas pockets in fluidized beds, AICHE J. 4 (4) (1958) 445–452.
8. Werther, J., *Scale-up Modeling for Fluidized Bed Reactors*, Chem. Eng. Sci., pp.2457-2462, Vol. 47, No. 9-11, (1992).
9. Becker, F., Modeling and Simulations of Hydrochlorination of Silicon to Trichlorosilane for the Development of a Technical Fluidized Bed Reactor, Diss., RWTH Aachen U, (2005).
10. Colomb, M. A., Palanki, S., and Sylvester, N. D. "FTIR Calibration for Detection of High Concentration Chlorosilanes in a Pilot-scale Hydrochlorination Reactor and Comparison with Modeling Results." Silicon for the Chemical and Solar Industry XIV, pp. 217-230, (2018).
11. Mui, J., *Investigation of the Hydrochlorination of $SiCl_4$*, Final report., JPL Contract 956061, (1983).

12. Lehnen, R., Studies on Hydrochlorination of Metallurgical Silicon and SiCl4 and H2 in a Laboratory Fixed Bed Reactor; Final report for the project "High-Purity Silicon for Photovoltaic Solar Energy Systems "of Bayer AG; (2000).

Characterization of carbonaceous compounds formed in the methylchlorosilanes synthesis

Eugénie Blaser [1)], Cécile Rosier [2)], Michel Huet [2)], Christophe Geantet[1)], Stéphane Loridant [1)]

1) Univ Lyon, Université Claude Bernard-Lyon 1, CNRS, IRCELYON-UMR 5256, 2av.A.Einstein, F-69626 Villeurbanne Cedex, France

2) ELKEM SILICONES – 55 av Frères Perret 69190 SAINT FONS - France

Abstract

The methylchlorosilanes synthesis, also called the Direct Synthesis (DS), suffers from a side-reaction during which the methyl chloride (CH_3Cl) reagent cracks and forms carbonaceous compounds. This carbon deposits on the active sites and deactivates the copper-based catalyst. Until now, investigations of the carbon formation were mainly done by the characterizations of lab reaction bed masses without studying its representativeness for the industrial scale. In order to get a full characterization study, reaction bed masses were recovered at different times of the DS from industrial and lab reactors and compared. XRD was used to follow the evolution of crystalline copper. The carbonaceous formation and transformation were studied by Raman, GCxGC-MS and elemental analysis of carbon and hydrogen (C and H). SEM-EDX was used to determine the relationship between copper and carbon content. The results showed that, for both origins, carbon and metallic copper are present in the reaction bed masses at the very beginning of the DS. Metallic copper may either be formed from the silicon (Si) consumption in the Cu_3Si active phase or from the reduction of CuCl by CH_3Cl. As metallic copper and carbon are formed at the same time, it is suggested that Cu contributes to the CH_3Cl cracking and formation of carbon (more precisely formation of tars). After a given time, disordered graphite is formed and remains disordered. However, no relationship was established between the copper and carbon amount by SEM-EDX.

Introduction

Since the silicones discovery in the first part of the 20th century, these compounds are more and more used for the chemical industry and for the everyday life. Interests in silicone are due to their chemical and physical properties such as good chemical and thermal inertness, biocompatibity, hydrophobicity and organophobicity. The physical properties of silicones can be tuned by formulation processes offering a wide range of applications: cosmetics, automotive, kitchenware…

The synthesis of silicones starts with the reduction of SiO_2 into Si. It is then converted into methylchlorosilanes $(CH_3)_xSiCl_y$ (MCS) which is called the Direct Synthesis (DS) or Rochow-Müller reaction (Eq. 1). For the silicones synthesis, the main desired MCS is $(CH_3)_2SiCl_2$.

$$Si(s) + 2\ CH_3Cl(g) = (CH_3)_2SiCl_2(l) \quad (1)$$

$(CH_3)_2SiCl_2$ undergoes hydroxylation followed by polymerization to produce silicones. The industrial synthesis of $(CH_3)_2SiCl_2$ is performed continuously in fluidized-bed reactors. Solid silicon, ground to a desired particle size distribution, is mixed with gaseous CH_3Cl. The temperature and pressure respectively range between 265-310 °C and 2-7 bar [1]. Copper based catalyst is needed to obtain high yield of $(CH_3)_2SiCl_2$ and reproducible results [2]. Promoters like Zn [3], Sn [3], Al [4] and P [5] could be used to increase the yield of $(CH_3)_2SiCl_2$.

In this process, the copper catalyst and Si are both solid. Copper diffuses over and through the Si particles to form Cu_3Si, the active phases for $(CH_3)_2SiCl_2$ synthesis [2,6,7]. However, other methylchlorosilanes are formed such as $(CH_3)HSiCl_2$, $(CH_3)_3SiCl$, disilanes…

Side-reaction occurs during the MCS synthesis called the CH_3Cl cracking. Previous experiences and data suggest that CH_3Cl cracking within the industrial MCS synthesis process results in formation of:

- Low boiling hydrocarbon gases (mainly CH_4, C_2H_6, C_3H_8, C_4H_{10}…), HCl and H_2,
- Hydrocarbon tars, which are viscous liquids acting like a glue and gathering the solid particles of hydrocarbons [8].
- Solid carbon (sometimes referred as coke),
- Excess formation of MCS by-products such as $(CH_3)SiCl_3$ and $(CH_3)HSiCl_2$.

It must be noted that C is an impurity of fresh silicon entering in the MCS synthesis with feed silicon as SiC. This source of carbon is not the topic of this present work.

Solid hydrocarbons and tars are mainly on the reaction bed masses, composed of Si, copper based catalyst and promoters. These hydrocarbons reduce the productivity of $(CH_3)_2SiCl_2$ and are partly responsible for the mass deactivation [9]. Some publications point out the origins of the CH_3Cl cracking: high temperatures ($T > 600$ °C) [10], presence of metallic copper [7,11], $AlCl_3$ [9], $FeCl_3$ [9]. However, only few publications deal with the characterization of the reaction bed masses of lab and industrial reactions to understand the formation and transformation of carbon and active phases.

The purpose of this present work was to study the evolution of reaction bed masses in industry and laboratory reactors. Samples were recovered from the reactional mixture during DS. The aims were to determine:

- The formation and evolution of tars hydrocarbons and coke. Tars were extracted by CH_2Cl_2 and analyzed by GCxGC-MS. The structure of coke was determined by Raman Spectroscopy. The amount of hydrocarbons on the surface and in the bulk were respectively determined by SEM-EDX and elemental analysis of C and H.
- The formation and evolution of active phases for the CH_3Cl cracking. XRD and SEM-EDX were used for the study of the inorganic phases.

Materials and methods

Materials and experimental conditions for the methylchlorosilanes syntheses.

The chemicals used for the DS were provided by Elkem Silicones. The details about the chemicals are confidential.

Laboratory Direct Synthesis (DS)

For the lab-scale reactor, the Direct Synthesis (DS) was performed in a stirred reactor at pressure and temperature respectively ranged between 2 and 7 bar and 265 and 310 °C. A pure CH_3Cl was continuously introduced in the reactor. The reaction bed masses consisted of Si particles, CuCl catalyst with Zn and Sn promoters. The solid mass was introduced at the beginning of the reaction and no further addition of fresh masses was done. Four samples were removed during the DS at 1, 3, 10 and 16 h. Table 1 summarizes the time sampling of each sample and the corresponding step of the synthesis. Each sample is referred by a labelling corresponding to its origin (laboratory or industry) and the hour of sampling. For the lab-scale, the MCS activity was recorded throughout the reaction. Figure 1 gives the evolution of the MCS activity as function of the reaction time. The red full circles correspond to the activity when samples of reaction bed masses were removed.

The pilote used for the MCS synthesis did not enable to continuously recover the reaction bed masses during the synthesis, and, therefore, the reaction was stopped to do so. The process of sampling was as follows: reaction was stopped and the reactor was flushed under N_2 until the room temperature was reached inside the reactor. The buffer loading was open and few grams of reaction bed masses were removed at ambient atmosphere using a syringe. The reactor then was heated up and flushed with N_2. When the working temperature was reached, CH_3Cl was introduced.

Table 1: Hours of samplings for the laboratory and industrial reactors.

	Industry	Laboratory
Sampling hours	10 h (I-10)	1 h (L-1) → activation
	15 h (I-15)	3 h (L-3) → High MCS activity
	24 h (I-24)	10 h (L-10) → Deactivation
	43 h (I-43)	16 h (L-16) → Deactivation
	57 h (I-57)	

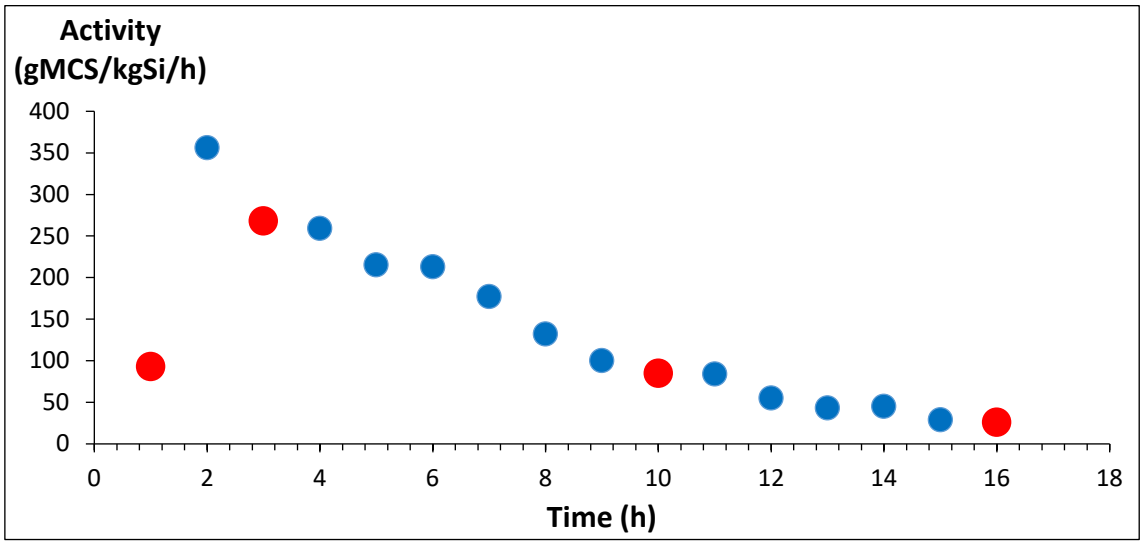


Figure 1: Activity of MCS as function of time for the lab-scale synthesis. The red markers correspond to the activity when samples of reaction bed masses were removed.

Industrial DS

The industrial DS is performed in continuous fluidized bed reactors at pressure and temperature respectively ranged between 2 and 7 bar and 265 and 310 °C. The reaction bed masses consisted of Si particles, CuCl catalyst with Zn and Sn promoters. Silicon, catalyst and promoters used in the experimental study are the same as those used at industrial scale. Five samples were recovered: before 10 h and then at 15, 24, 43 and 57 h (Table 1). Samples were removed at the working temperature under inert atmosphere and then store under ambient atmosphere. It should be noted that the sampling times given above do not correspond to the ages of the masses: since this is a continuous process, fresh masses are mixed with aged ones, so the masses recovered were composed of particles with a wide range of age.

Characterization analyses

Raman spectroscopy

Raman spectra were performed in ambient atmosphere with a LabRam HR (Jobin Yvon-Horiba) spectrometer. The exciting line at 633 nm of a He-Ne laser was used. The power measured at the sample was 1 mW. A microscope objective with magnification x50 focused the incident beam and recollected the scattered light which was spatially dispersed with a 300 lines/mm diffraction grating. The spatial resolution was 4 microns and the spectral resolution was 4 cm^{-1}. Mappings were performed recording around 30 spectra per sample on a surface of hundreds μm^2. Each mapping was treated with the NGSLabSpec software (Jobin Yvon-Horiba) to calculate the mean spectrum which was considered as statistical and used to compare the sample with each other.

Comprehensive Gas Chromatography (GCxGC-MS)

Tars were extracted from ca 1 g of reaction bed masses. The masses were introduced in a 25x80 mm cellulose thimble and fully immerged in 50 mL of methylene chloride

(CH_2Cl_2), purchased from Merck. A Randall extractor (VELP scientifica) was used to perform the extraction as follows:

- Immersion in CH_2Cl_2 heated to reflux at 40 °C for 1 h,
- Recovery for 30 min: the reflux was stopped and 90% of the solvent was vaporized,
- Cooling to room temperature for 20 min,
- The remaining solvent was vaporized at room temperature.

Tars extracted was diluted into 1-2 ml THF and analyzed by GCxGC-MS from Agilent Technologies 5975B. In this work, the following columns were used for:

- Primary column: ZB-35 (30 m x 0.25 mm x 0.18 µm),
- Secondary column: DB-1 (2 m x 0.10 mm x 0.10 µm).

The chemicals at the outlet of the primary column were collected and injected into the secondary column by a thermal modulator.

X-Ray Diffraction (XRD)

Samples were crushed and sieved under 50 µm before XRD analyses to avoid preferential orientations. Poly(methyl methacrylate) supports were used to analyze masses in a Bruker D8 Advance 25 diffractometer. The X-rays source, used with a power of 1.75 kW, was composed of a tungsten cathode and a copper anode. The K_α ray of copper was selected with a nickel filter. The acquisition conditions were as follows: from 4 to 80° with an interval of 0.02 ° and 0.5 second per point. Crystallites size was determined measuring the width at half maximum of bands and using the Debye-Scherrer equation.

As metallic copper is reported to be active for the CH_3Cl cracking, focus was put on the metallic copper content in the reaction bed masses which was determined by XRD. This technique enables to discriminate metallic copper from other copper phases. Previous calibration of metallic copper was done by mixing and crushing three powders Si, Cu and TiO_2-anatase (used as an internal standard) to obtain homogeneous samples. Cu and TiO_2 were respectively provided by Alfa-Aesar (42455) and Sigma-Aldrich (637254) while Si was provided by Elkem Silicones. The copper powder was chosen because its particles sizes were similar to the ones of copper in reaction bed masses (20 - 50 nm). The (111) diffraction peak of TiO_2 and Cu were integrated and the ratio of these areas was used for the calibration.

Scanning electron microscope – Energy Dispersive X-ray spectrometry (SEM-EDX)

The instrument used for SEM analysis was ESEM FEG, XL30, brand FEI (15 kV) with a high vacuum. Samples were deposited on a carbon film before analysis.

Elemental analysis of Carbon, Hydrogen, Nitrogen and Sulphur (CHNS)

All the CHNS analysis were performed with a Thermo Scientific, Flash 2000 organic elemental analyzer. Between 1 and 5 mg of desired sample measured on a microbalance, were introduced in a soft cup of tin (Sn). C, H, N and S were then oxidized to 1800 °C. SO_3 and NO_x reduced into SO_2 and N_2. CO_2, H_2O, SO_2 and N_2 were separated by a PTFE packed column (2 m, 6x5 mm) and detected by thermal conductivity detector (TCD).
The limited of the detection for the carbon weight content was 0.1 wt% and range of precision on the carbon masses and carbon weight content are 0.04 g and 0.03 wt%, respectively.

Results and discussion

Laboratory masses

The lab-scale the DS is semi-continuous: solid mass was introduced in the reactor at the beginning of the reaction and no further fresh mass was added during the DS. As silicon was consumed throughout the reaction, there is an increase in the content of chemical elements not consumed by the DS or by the side-reactions. In order to study the formation of carbon, only the variation of mass is studied and not the weight content.

The carbon masses in the four samples from laboratory, determined by CHNS, are reported in Table 2. The carbon formation is the highest one during the deactivation step, which was expected since carbon caused the deactivation [9,12]. Carbon is already present in L-1, meaning that this source of deactivation is already in the masses from the beginning of the reaction. Previous measurement of carbon in the fresh silicon were done by Inductively Coupled Plasma (ICP) but are not detailed in this work. They reported a weight content of carbon of 200 ppm which is under the detection limit of CHNS.

Table 2: Carbon mass in the reaction bed masses from lab-scale DS.

Sample	Sampling time (h)	Carbon mass (g)
L-1	1	0.1
L-3	3	0.1
L-10	10	0.2
L-16	16	0.3

Figure 2 displays the Raman spectra of the four samples and does not show any signal before 3 h whereas two bands are observed from 10 h:

- The first band at 1580 cm^{-1} is called the G-band (E_{2g} symmetry) of graphite structure with sp^2 carbon network [13].
- The second band, near 1350 cm^{-1}, is related to defects or heteroatoms present in graphitic plans and is called the D-band [12]. This second band is present for disordered graphite.

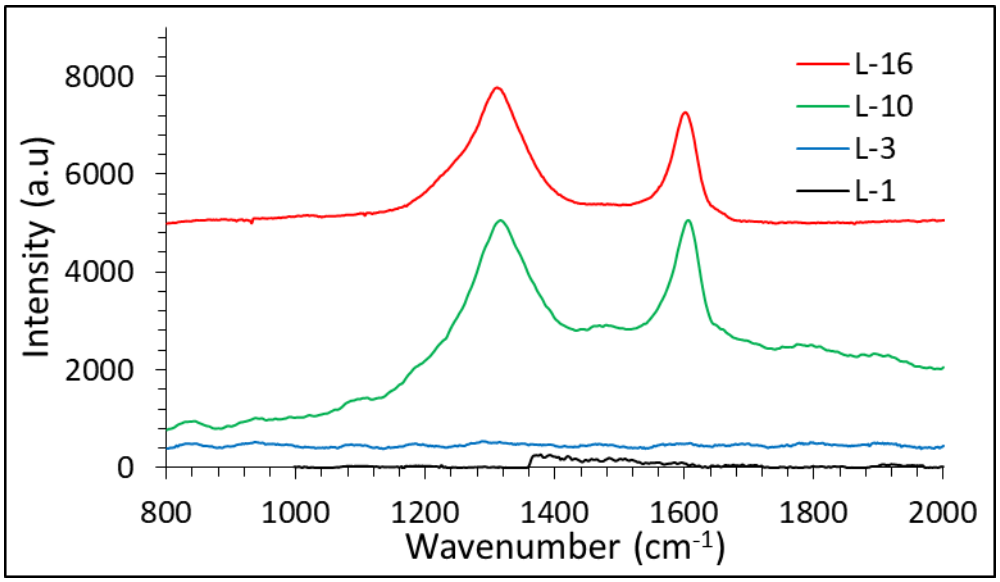


Figure 2: Raman spectra on reaction bed masses removed from the laboratory reactor.

Thus, the solid carbon is partly composed of disordered graphite formed during the deactivation step. Disordered graphite corresponds to graphite with defect or heteroatoms. The $\frac{Area\ (D1\ band)}{Area\ (G\ band)}$ ratio provides information on the disorder degree of graphite. These ratios, given in Figure 3, are similar for L-10 and L-16 suggesting that the structure of graphite does not change after its formation.

Table 3: $\frac{\boldsymbol{Area\ (D1\ band)}}{\boldsymbol{Area\ (G\ band)}}$ ratio of the two samples of the deactivation step.

Sample	Sampling time (h)	$\frac{\boldsymbol{Area\ (D\ band)}}{\boldsymbol{Area\ (G\ band)}}$
L-10	10	2.6
L-16	16	2.8

Based on the elemental analysis of CHNS, carbon containing compounds are present in the reaction bed masses from the activation step. Based on the Raman spectroscopy disordered graphite is formed only during the deactivation step and it is suggested that the carbon containing compounds turn into graphite during the deactivation. The nature of the carbon containing compounds will be investigated in the Industrial masses section.

To understand the role of metallic copper in the carbon formation, the masses of crystalline Cu were determined by XRD, the total mass of copper determined by X-Ray Fluorescence (XRF) and the $\frac{mass\ of\ metallic\ Cu}{total\ mass\ of\ Cu}$ ratio are reported in Table 4 for the four samples. Metallic copper is mainly formed during the activation and at the end of the deactivation steps. The crystallite size ranges between 20 and 30 nm, determined by the Debye-Scherrer equation.

Table 4: Mass of metallic copper in the reaction bed masses from the DS at lab-scale.

Sample	Sampling time (h)	$\frac{mass\ of\ metallic\ Cu}{total\ mass\ of\ Cu} \times 100$
L-1	1	25
L-3	3	44
L-10	10	40
L-16	16	65

Metallic copper could be formed from:

- The reduction of CuCl, the copper precursor used for the MCS synthesis. The reduction of CuCl into Cu was already reported [13] but no mechanism was established. However, it may be suggested that CuCl reduces with reactants such as CH_3Cl, CH_4 or H_2. Note that H_2 and CH_4 are produced from the CH_3Cl cracking.
- The Cu_3Si active phase [2,6,7], after Si consumption as previously reported [14].

Table 5 reports the hypothetic reduction reactions at 300 °C. The thermodynamic calculations indicate that reduction of CuCl with CH_4 and H_2 is less likely to occur at the working temperature of the DS as $\Delta_rG°$ (T=300 °C) > 0. Based on these reactions, the reduction of CuCl with CH_3Cl leads to the carbon and hydrocarbons (i.e CH_4) formation. This gives a first explanation on the origin of carbon and is consistent with the above results: metallic copper and carbon are formed at the same time.

Table 5: Enthalpies and Free enthalpies at 300 °C of hypothetical reduction reactions of CuCl into Cu.

Reactions	$\Delta_rH°$ (T=300 °C) (kJ/mol)	$\Delta_rG°$ (T=300 °C) (kJ/mol)
$CuCl + \frac{1}{2} CH_3Cl \rightarrow Cu + \frac{1}{2} C + \frac{3}{2} HCl$	26.8	-32.6
$CuCl + CH_3Cl \rightarrow Cu + \frac{3}{4} C + \frac{1}{4} CH_4 + 2\ HCl$	2.2	-63.3
$CuCl + CH_3Cl \rightarrow Cu + C + 2\ HCl + \frac{1}{2} H_2$	17.4	-70.0
$CuCl + CH_3Cl \rightarrow Cu + \frac{2}{3} C + \frac{1}{3} CH_4 + \frac{5}{3} HCl + \frac{1}{6} Cl_2$	25.2	-43.3
$CuCl + \frac{1}{4} CH_4 \rightarrow Cu + \frac{1}{4} C + HCl$	51.4	6.2
$CuCl + \frac{1}{2} H_2 \rightarrow Cu + HCl$	36.2	4.8

As CH_4 is an indicator of CH_3Cl cracking and was monitored during the DS performed at lab-scale and Figure 3 shows the evolution of CH_4 formed per hour. The amount of CH_4 is the highest during the deactivation step, when the amount of solid carbon and

metallic copper are the highest ones as well (see Table 2 and Table 4). The increase of the CH_4 production may be caused by:

- Catalytic cracking of CH_3Cl on metallic copper,
- Catalytic cracking of CH_3Cl on the solid carbon if this one acts like a catalyst for the CH_3Cl cracking as already previously observed [15]

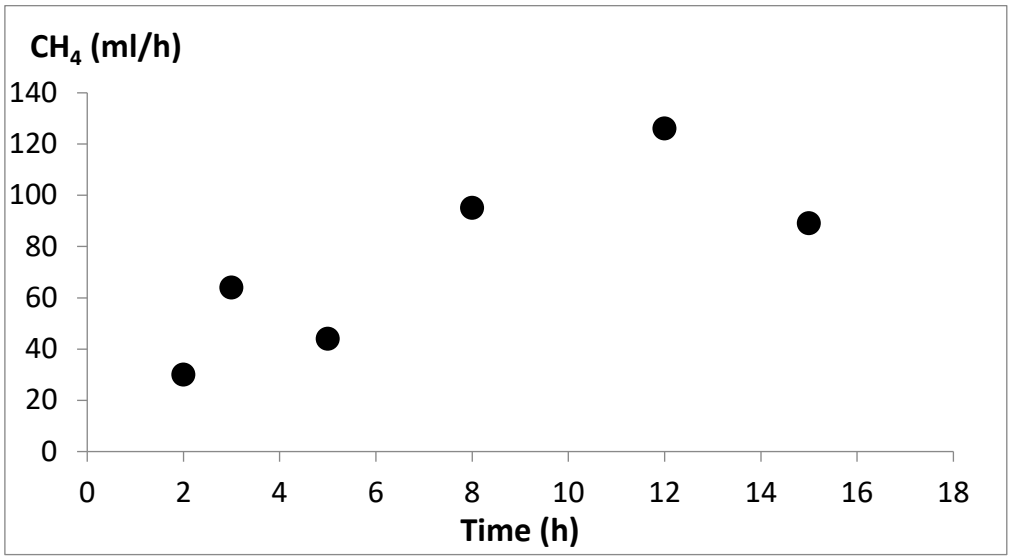


Figure 3: Formation of CH_4 as function of the reaction time.

Industrial masses

The carbon contents quantified by the elemental analyses CHNS on the five samples from industry are reported in Table 6. Carbon was detected in I-15, meaning that carbon was formed in the early stage of the DS, as in the laboratory synthesis. There is no tendency for the evolution of the carbon content with time which is probably due to the fact that the industrial process is continuous. For I-10 and I-57 samples, no carbon was detected by CHNS but it does not mean there is no carbon in the sample, the weight content of carbon is probably under the detection limit of 0.1 wt%.

Table 6: Carbon content in the reaction bed masses from industrial reactors.

Sample	Sampling time (h)	Carbon content (wt%)
I-10	10	0.0*
I-15	15	0.6
I-24	24	0.1
I-43	43	0.2
I-57	57	0.0*

*below the detection limit

SEM pictures of I-10, displayed in Figure 4, show a silicon particle partly consumed. 6 EDX analyses were performed on it, localisation of these spots are given by the red rectangles. They indicated 4.0 wt% of copper and 6.8 wt% of carbon, with respective

standard derivation of 0.6 wt% and 0.9 wt%. Even though the EDX analysis is known to be less accurate for carbon than for heavier chemical elements, it is still suitable to confirm the presence of carbon before 10 h, which could not be detected by CHNS.
As metallic copper is active for the CH_3Cl cracking, higher amount of C was expected on copper rich areas. In area copper rich with copper content of 4.0 wt%, the carbon content is 7.4 wt% while it is 5.3 wt% in area where the copper content is 0.4 wt%. Thus, it was not possible from EDX data to establish relationship between the copper and the carbon amount as carbon deposits on the all silicon surface. Similar observation was done with I-57. An explanation for this lack of correlation is as follows: CH_3Cl did crack on copper sites, leading to the carbon formation. This carbon spread over the silicon surface and fully covered it. This hypothesis is consistent if the amount of carbon is high enough to cover the all silicon surface. Considering carbon as monolayer of graphene, as the surface specific area of Si is 28 m^2/kg, the carbon content needed to fully cover 1 g of Si lower than 2 $x10^{-3}$ wt%. It is likely that the carbon content in I-10 is higher than 2 $x10^{-3}$ wt% but lower than the minimal carbon content detected by CHNS, which is 0.1 wt%.

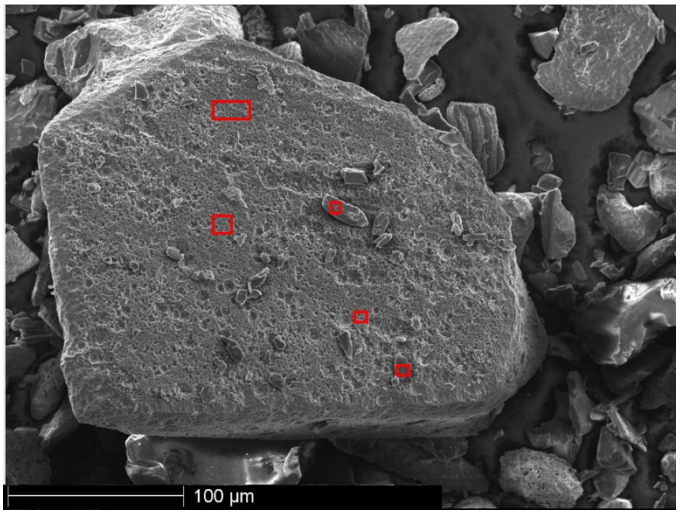


Figure 4: SEM pictures of I-10.

Structural characterization of solid carbon was obtained from Raman spectra plotted in Figure 5. No signal is observed for masses removed before 15 h. From 24 h, the two bands of disordered graphite are observed, revealing a delay between the formation of carbon containing compounds (observed by CHNS and SEM-EDX) and disordered graphite formation, already observed for the laboratory masses.

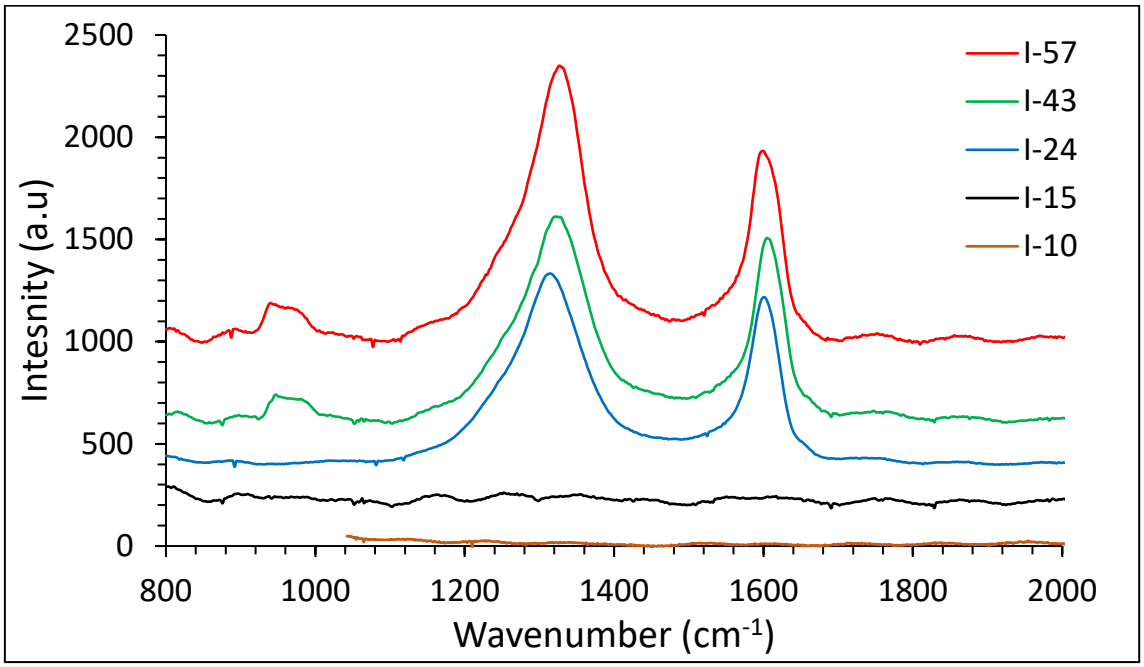


Figure 5: Raman spectra of the reaction bed masses from industrial reactor.

The $\frac{Area\ (D1\ band)}{Area\ (G\ band)}$ ratio determined for I-24, I-43 and I-57 and reported in of graphite. Moreover, the ratio determined for the industrial samples are similar to the ones of lab graphite. Thus, the nature and the evolution of disordered graphite are similar for both scales.

Table 7, does not change throughout the DS, revealing no evolution in the disordered degree of graphite. Moreover, the ratio determined for the industrial samples are similar to the ones of lab graphite. Thus, the nature and the evolution of disordered graphite are similar for both scales.

Table 7: Areas of G and D1-bands and area ratio determined from Raman spectra of industrial samples for Raman spectroscopy**.**

Sample	Sampling time (h)	G-Band Area (a.u)	D1-Band Area (a.u)	$\frac{Area\ (D1-band)}{Area\ (G-band)}$
I-24	24	56659	135361	2.4
I-43	43	62506	150905	2.4
I-57	57	58764	175580	3.0

Carbon containing compounds were observed for I-10 and I-15 while no disordered graphite was identified, suggesting that the containing compounds may correspond to hydrocarbon tars. The nature of these tars was investigated by GCxGC-MS and Figure 6 displays the 2D-chromatograph obtained for the I-24 tars with the localization of each type of organic molecules. Hydrocarbon tars are present in the five samples with the same

type of compounds: ramified and linear paraffins, olefins, linear polyunsaturated and cyclic hydrocarbons. As the industrial process is continuous, in each sample recovered, the particles are not in the same age. The longer the sampling time, the larger the range of the age is. Thus, it seems that disordered graphite is formed for samples with the largest range of particles age, suggesting that hydrocarbon tars are graphite precursors which underwent a process of polymerization, cyclization and dehydrogenation during the reaction. However, another explanation may be suggested for the delay in the graphite formation: it is possible that graphite was formed directly by the CH_3Cl cracking on active sites which were present in the reaction after a while.

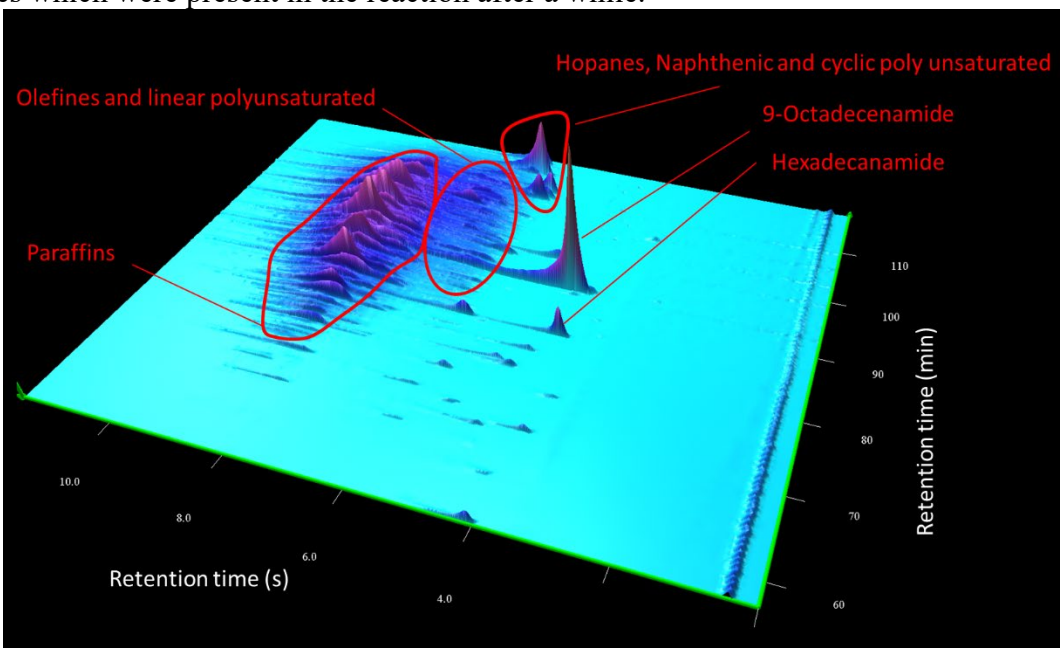


Figure 6: 3D chromatograph of tars I-24 extracted by CH_2Cl_2.

To understand the role of metallic copper in the tars and disordered graphite formation, XRD was undertaken. As well as the laboratory masses, the content of metallic copper and the total content of copper were determined for the industrial samples and reported in Table 8. Metallic copper was formed at the beginning of the DS, as in the laboratory masses. There is evolution tendency in the copper content during the DS, unlike the laboratory samples, which is probably due to the continuous introduction of copper masses in the industrial reactor. The crystallites size, determined by the Debye-Scherrer equation, ranges between 20-50 nm which corresponds to the copper particles size determined for the lab samples.

Table 8: Content of metallic copper in the reaction bed masses from industrial reactors.

Sample	Sampling time (h)	$\frac{mass\ of\ metallic\ Cu}{total\ mass\ of\ Cu} \times 100$
I-10	< 10	43
I-15	15	30
I-24	24	13
I-43	43	26
I-57	57	9

Conclusion

This report deals with the characterization of reaction bed masses recovered at different times of the DS at industrial and lab-scale. For both origins of reaction bed masses, carbon and metallic copper were formed at the very beginning of the synthesis. Carbon in the pristine masses corresponds to viscous liquid of hydrocarbon called tars. Cu comes from the reduction of the copper based catalyst CuCl. This reduction may be caused by:

- The reduction of CuCl into Cu with CH_3Cl as reducer. In this case, C and CH_4 may be formed as well.
- The Cu_3Si active phase [2,6,7], after Si consumption as previously reported [14].

After few hours, disordered graphite was formed for both industrial and lab-scale. It is believed that tars undergo polymerization, cyclization and dehydrogenation to form disordered graphite. However, another explanation is that active phases which convert CH_3Cl into graphite were present in the masses only after a while. Once graphite was formed, the degree of disorder does not change.

Formation of CH_4 was studied at lab-scale during the MCS synthesis. CH_4 was mainly formed during the deactivation step. Two hypotheses are suggested to explain this observation:

- Catalytic cracking of CH_3Cl on metallic copper,
- Catalytic cracking of CH_3Cl on the solid carbon [15].

Bibliography

1. B. Kanner, K. Lewis, *Catalyzed direct reactions of silicon,* Elsevier, 1993
2. R.J.H Voorhoeve, *Organosilanes: Precursor to silicones,* Elsevier, 1967, p 120-143
3. L. Gasper-Galvin, D. Sevenich, H. Friedrich, D. Rethwisch, *Role of metallic promoters in the direct synthesis of methylchlorosilanes.* Journal of Catalysis, **128,** 1991, p467-478
4. J. Bablin, A. Crawford, D. DeMoulpied, L. Lewis, *Effect of Low Aluminum Silicon on the Direct Process*, Industrial & Engineering Chemistry Research, **42**, 2003, p3555-3565

5. Olakangil, *Ph.D thesis: Effet of phosphorus and silicon purity on coke formation and reaction kinetics in the Direct Synthesis of Methylchlorosilanes,* 2002
6. D.H. Sun, B.E. Bent, *Chemistry of the Direct synthesis of the methylchlorosilanes from methyl + chlorine monolayers on a Cu_3Si surface.* Catalysis Letters, **46**, 1997, p127-132
7. T. Wessel, D. Rethwisch, *Activation of CuSi and CuZnSnSi contact masses for the direct synthesis of* methylchlorosilanes, Reaction Kinetics and Catalysis Letters, **58,** 1996, p7-12
8. M. Guisnet, P. Magnoux, *Coking and Deactivation of Zeolites,* Applied Catalysis, **54**, 1989, p1-27
9. J. Jokilk, V. Bazant, *Composés organiques du Si: influence de la composition du Si sur le synthèse directe des MCS,* Collection of Czechoslovak Chemical Communications, **26**, 1961, p417-426
10. M. Weissman, S. Benson, *Pyrolysis of Methyl Chloride, a Pathway in the Chlorine-Catalyzed Polymerization of Methane*, International Journal of Chemical Kinetics, **16**, 1984, p307-333
11. V. Bazant, *Direct Synthesis of Organo-Halogenosilanes,* Pure and Applied Chemistry*,* **13,** 1966, p313-326
12. W. Kalchauer, H. Straussberger, W. Streckel and J. Gross, *Process for the preparation of organochlorosilanes,* Patent 6,211,394 B1, April 2001.
13. M.A. Pimenta, G. Dressalhaus, M.S. Dressalhaus, L.G. Cançado, R. Saito, *Studying disorder in graphite-based system by Raman spectroscopy*, Physical Chemistry Chemical Physics, **9**, 2007, p1276-1290
14. M. Clarke, *The Direct Synthesis of Methylchlorosilanes*, Journal of Organometallic Chemistry, **376**, 1989, pp. 165-222.
15. E. Blaser, C.Rosier, M.Huet, C.Gentet, S. Loridant, *Catalytic cracking and thermalcracking of CH_3Cl occurring in the methychlorosilanes synthesis*, Silicon for the Chemical and Solar Industry XV, Trondheim, 2020.

Catalytic cracking and thermal cracking of CH_3Cl occurring in the methychlorosilanes synthesis.

Eugénie Blaser [1)], Cécile Rosier [2)], Michel Huet [2)] Christophe Geantet[1)], Stéphane Loridant [1)],

1) Univ Lyon, Université Claude Bernard-Lyon 1, CNRS, IRCELYON-UMR 5256, 2av.A.Einstein, F-69626 Villeurbanne Cedex, France

2) ELKEM SILICONES – 55 av Frères Perret 69190 SAINT FONS - France

Abstract

The methylchlorosilanes synthesis, also called the Direct Synthesis (DS), suffers from a side-reaction during which the methyl chloride (CH_3Cl) reagent forms carbonaceous compounds. This carbon deposits on the active sites and deactivates the copper-based catalyst.

This reports deals with the CH_3Cl cracking performed without the silicon reagent and the promoters. Two phenomena were studied: the thermal cracking and the cracking catalyzed by copper phases. For the thermal cracking, particles of silica were used to provide the surface needed for the radical CH_3Cl decomposition. For the catalytic cracking, four copper phases ($CuCl_2$, CuO_x, CuCl and Cu) were supported on black carbon and silica.

Results showed that the mechanism of CH_3Cl cracking is the same for the thermal and the catalytic cracking:

$$CH_3Cl\ (g) \rightarrow \tfrac{1}{2}\ CH_4\ (g) + \tfrac{1}{2}\ C(s) + HCl\ (g)$$

The thermal cracking starts between 400 and 450 °C, forming solid carbon which itself catalyzes the CH_3Cl decomposition. CuCl and Cu are both active phases for the CH_3Cl cracking. The evolution of copper phases depends on the support: metallic Cu was obtained for carbon support while CuCl was obtained for the silica support.

Introduction

Silicones are widely used for the chemical industry and for the everyday life in cosmetics for example or automotive, kitchenware… Their interests are due to their chemical and physical properties (good chemical and thermal inertness, biocompatibity, hydrophobicity and organophobicity).
Silicones are obtained from the reduction of SiO_2 into Si which is then converted into methylchlorosilanes $(CH_3)_xSiCl_y$ (MCS). This reaction is called the Direct Synthesis (DS) or Rochow reaction (Eq. 1) and for the silicones synthesis, the main desired MCS is $(CH_3)_2SiCl_2$.

$$Si(s) + 2\ CH_3Cl(s) \rightarrow (CH_3)_2SiCl_2(g) \quad (1)$$

Later on, $(CH_3)_2SiCl_2$ undergoes hydroxylation followed by polymerization to produce silicones. In the DS, solid silicon is mixed with gaseous CH_3Cl at temperature and pressure respectively range between 265-310 °C and 2-7 bar [1]. Copper based catalyst is needed to obtain high yield of dimethyldichlorosilanes $(CH_3)_2SiCl_2$ (referred as Me_2 in this report) and reproducible results [2]. Copper diffuses over and through the Si particles to form Cu_3Si, the active phases for $(CH_3)_2SiCl_2$ [3,4,5]. Promoters such as Zn, Sn [6], Al [7] and P [8] could be used to increase the yield of $(CH_3)_2SiCl_2$.
However, the DS suffers from a side-reaction during which the CH_3Cl reagent cracks and forms carbonaceous compounds such as CH_4 and solid carbon deposited on the reaction bed masses which reduces the productivity of Me_2 and is partly responsible for the mass deactivation [9].
Some publications point out two main origins for the CH_3Cl cracking:

- High temperatures (T > 600 °C) [10]. However, the reported mechanisms of thermal cracking were established with the experimental conditions far from the DS: in excess of H_2 [11], under oxidative conditions [12], with low pressure and high temperature (P < 0.05 atm and T < 790 °C) [13]. The conclusions may so not be representative of the thermal cracking in the DS.
- Metallic copper [5,11], $AlCl_3$ [9] and $FeCl_3$ [9], studied in the DS, are responsible for the CH_3Cl cracking. As the mechanisms involved for the DS and CH_3Cl cracking are poorly known, it is hard to draw proper conclusions about the exact role of the active phases and establish mechanisms of cracking. Therefore, few authors studied the cracking of CH_3Cl on Cu and CuCl without silicon [9, 14] and Jokilk and Bazant suggested the Eq.2 for the formation of CH_4 and carbon.

$$2\ CH_3Cl\ (g) + 2\ Cu\ (s) \rightarrow 2\ CuCl\ (s) + CH_4\ (g) + C\ (s) + H_2\ (g) \quad (2)$$

In this present work, thermal cracking and cracking of CH_3Cl on supported copper precursors were investigated, without Si to determine:

- The onset temperature and the mechanisms of the thermal cracking between 375 and 550 °C (at 375, 400, 450, 475, 500 and 550 °C) with experimental conditions as close as possible to the DS,

- The role of four copper precursors Cu, CuCl, $CuCl_2$ and CuO_x with and without carbon. Presence of carbon was reported to accelerate the deactivation [9] but the synergy between copper and carbon has not been studied yet to the best of our knowledge. Thus, copper were supported on black carbon and on silica. Characterization of the supported phases were done before and after the CH_3Cl cracking by X-Ray Diffraction (XRD).

For each cracking test, the selectivity values to CH_4, solid carbon, H_2 and other hydrocarbons with $C \leq 4$ were determined.

Experimental part

Material for the CH_3Cl thermal cracking

As the thermal cracking of CH_3Cl was reported to be a radical route [11], inert surface was needed to initiate the $CH_3^{\bullet}$ and $Cl^{\bullet}$ radicals. SiO_2-432 purchased from Grace Davison was used and the particles were crushed and sieved before the cracking tests to obtain a particle size distribution between 50 and 400 microns. Details about the support textural characterization are reported in Table 1.

Material and synthesis for the cracking of CH_3Cl on supported copper

The three copper precursors Cu, $CuCl_2$ and CuOx were either supported on black carbon (Vulcan 3 was purchased from Cabot) or on silica (SiO_2-432 purchased from Grace Davison) by incipient wetness impregnation using de-ionized water as solvent. Details about these supports are reported in Table 1. The copper content in the final mass was 3.5 wt%. After the incipient wetness impregnation, the compounds were dried at 120 °C for 2 h under N_2, crushed and sieved between 50 and 400 micrometers.

As CuCl is not soluble into water, it was mixed with the support and heated up to 400 °C, close to the CuCl melting point which is 430 °C [15] to melt CuCl and spread it on the support. The purpose was to simulate the behavior of CuCl for the DS where CuCl nearly melts on Si and diffuses all over the surface. XRD analyses confirmed the CuCl dispersion as the CuCl crystallites decreased after the heating.

Table 1: Textural characterizations of the supports Vulcan 3 and SiO_2-432.

Textural characterization	Vulcan 3	SiO_2-432
Specific surface area (m^2/g)	75	310
Porous volume (cm^3/g)	0.29	1.13
Microporous area (m^2/g)	8	37
Microporous volume (cm^3/g)	0.004	0.01
Pore size (nm)	10 à 100	5 à 18

The four copper precursors were obtained as follows:

- $CuCl_2$ was purchased from Alfa Aesar (n°10698, 99.99%),
- Cu was obtained by the reduction of supported $CuCl_2$ at T=550 °C for 2 h under 100 mls/min of reductive flow composed of H_2/Ar (10/90),
- CuCl was provided by Aldrich (n°1027390250, > 97.0%)
- Cu_2O/C was obtained by the pyrolysis of $Cu(NO_3)_2$/C at 400 °C for 2 h under 100 mls/min of Ar. $Cu(NO_3)_2$ was purchased from Acros Organics (n°405855000, 98%).
- CuO/SiO_2 was obtained by the calcination of $Cu(NO_3)_2$/SiO_2 at 500 °C for 2 h under air at 100 mls/min.

Experimental conditions for the CH_3Cl cracking tests

The CH_3Cl cracking tests were performed in a fixed-bed reactor with the following experimental conditions:

- Bed height of 3 cm,
- Bed diameter of 1 cm,
- The mass of loaded solid ranged between 0.75 and 1.0 g, with particles between 50 and 400 microns,
- Pressure of 0.4 MPa (similar to the DS),
- Six temperatures were set for the thermal cracking: 375, 400, 450, 475, 500 and 550 °C and the cracking on supported phases were always performed at 400 °C. Even though the DS is usually performed between 265-310 °C, the CH_3Cl cracking is a side-reaction so low activities were obtained at the temperature of the DS. To have a better understanding of the mechanisms of cracking and determine the active phases, high conversion are preferred, requiring temperatures higher than 310 °C.

The protocol for CH_3Cl cracking was as follows:

- The reactor was flushed under 100 mls/min of pure Ar at atmospheric pressure while temperature was increased from room temperature to 400 °C at a rate of 5 °C/min and maintained under Ar for 1 h.
- Argon flow was stopped and CH_3Cl/Ar (10/90) was mixed with N_2, with respective flow of 5.22 and 3.18 mls/min. With such flows, the contact time was 1 min corresponding to the contact time estimated for the DS in industry.
- The CH_3Cl cracking was performed until the steady step was reached, the reactions lasted from 10 to 30 h.
- After the cracking, the valves of CH_3Cl and N_2 were turned off and the reactor was flushed with 100 mls/min of Ar while the temperature was decreased to room temperature.

During the CH_3Cl cracking, the output gases N_2, CH_3Cl, H_2, CH_4, C_2H_6, C_2H_4, C_3H_8, C_3H_6, n-butane and isobutene were analyzed by Shimazu GC-2014 and treated with the Lab-Solutions software. The selectivity values to C_2, C_3 and C_4 were very low for each test (lower than 2 %) and, thus, only CH_4 and H_2 will be reported in this work.

In addition to the gases, the selectivity to carbon deposited on silica was determined by elemental analysis on carbon with a Thermo Scientific, Flash 200 organic elemental analyzer.
Concerning the black carbon support, the determination of the carbon selectivity was tricky as it required a discrimination between the carbon from the support and the carbon produced by the CH_3Cl cracking. Even though several methods were tried to determine the carbon selectivity, none of them were accurate enough to properly conclude. Thus, no carbon selectivity will so be given in this report for the CH_3Cl cracking on copper phases supported on black carbon.

The selectivity to A product was calculated by (eq.3).

$$\boldsymbol{Sel\,(A) = \frac{n(A)_{output}}{n(CH_3Cl)_{input} - n(CH_3Cl)_{output}} \times 100} \quad (3)$$

Where $n(A)_{output}$ corresponds to the amount of A product at the output of the fixed bed reactor and $n(CH_3Cl)_{input}$ and $n(CH_3Cl)_{output}$ correspond to the amount of CH_3Cl reagent on the input and output of the fixed bed reactor respectively.

The consumption rate of CH_3Cl was calculated by (eq.4)

$$r_{CH_3Cl\ consumption} = \frac{X(CH_3Cl) \times F(CH_3Cl)}{m_{Cu}} \quad (4)$$

Where $X(CH_3Cl)$ is the conversion of CH_3Cl, $F(CH_3Cl)$ is the input flow of CH_3Cl ($mol.s^{-1}$) and m_{Cu} is the mass of Cu in the supported phases (g).

Characterization of supported copper

X-Ray Diffraction (XRD)
Samples were crushed and sieved under 50 µm before XRD analyses to avoid preferential orientations. Poly(methyl methacrylate) supports were used to analyze masses in a Bruker D8 Advance 25 diffractometer. The X-rays source, used with a power of 1.75 kW, was composed of a tungsten cathode and a copper anode. The K_α ray of copper was selected with a nickel filter. The acquisition conditions were as follows: from 4 to 80° with an interval of 0.02° and 0.5 second per point. The crystallites size was determined measuring the width at half maximum of bands and using the Debye-Scherrer equation.

Inductively Coupled Plasma (ICP)
Supported Cu phases were dissolved into:
- H_2SO_4 + HNO_3 heated at 350 °C for the carbon support
- H_2SO_4 + HNO_3 + HF for the SiO_2 support

ICP-OES Activa Jobin Yvon was used to perform the analyses.

X-Ray Fluorescence (XRF)
The XRF analysis was performed with a Panalytical, Epsilon 4 instrument. A source of Ag was used. The calibration of copper was done using mixture of metallic Cu and Si, both from Elkem Silicones, with a weight content of copper ranging between 0.5 and 3.5 wt%.

Results and Discuss

Cracking of CH_3Cl on black carbon and silica

Before the tests of CH_3Cl cracking on copper phases, both supports were tested within the experimental conditions at T = 400 °C without supported copper. They led to a CH_3Cl conversion lower than 1 % meaning that supports have a very low activity for the CH_3Cl cracking.

The thermal cracking of CH_3Cl

The thermal cracking of CH_3Cl on SiO_2, studied for six temperatures from 375 to 550 °C, starts between 400 and 450 °C as displayed in Figure 1. As the thermal cracking of CH_3Cl does not occurs under 400 °C on SiO_2, it is suggested that there is not thermal cracking during the DS, performed around 300 °C. Results of cracking indicate that the higher the temperature is, the higher the CH_3Cl conversion and the rate of CH_3Cl consumption are, as reported in Table 2.

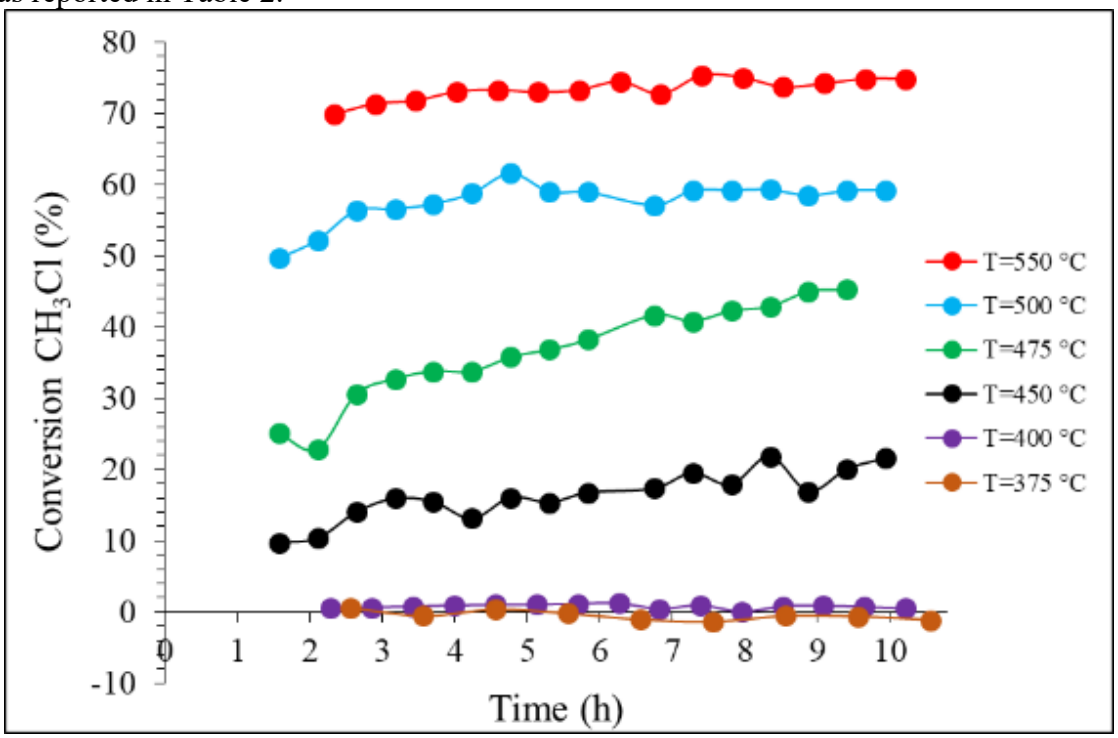


Figure 1: Evolution of CH_3Cl conversion as a function of time on stream for the reactor temperature 375, 400, 450, 475, 500, 550 °C on SiO_2.

Table 2: Rate of CH_3Cl consumption for the thermal decomposition of CH_3Cl.

Temperature (°C)	Rate of CH_3Cl consumption (mol $_{CH_3Cl}$/s) x 10^{-7}
450	0.7
475	1.5
500	2.0
550	2.5

Even though the temperature has an influence on the conversion, it has none on the products distribution as CH_4, C and H_2 have similar selectivity values for each temperature: 50 % for CH_4 and C and around 17% for H_2. The carbon obtained by thermal cracking will be referred as thermal carbon in the following. Other products were identified: C_2H_6, C_2H_4, C_3H_8 and C_3H_6 but with selectivity values lower than 2 %. Based on the product distribution, (Eq. 5) is suggested for the thermal cracking of CH_3Cl between 450 and 550 °C.

$$CH_3Cl\ (g) \rightarrow \tfrac{1}{2}\ CH_4\ (g) + \tfrac{1}{2}\ C(s) + HCl\ (g) \qquad (5)$$

Nevertheless, (Eq.5) is not consistent with the formation of H_2, observed for the thermal cracking. A hypothesis on the origin of H_2 could be the chlorination of the thermal carbon with HCl, as suggested in (Eq.6).

$$C\text{-}C\ (s) + 2\ HCl\ (s) \rightarrow 2\ C\text{-}Cl\ (s) + H_2\ (g) \qquad (6)$$

To validate such hypothesis, the chlorine content of the thermal carbon was determined by XRF: it ranged between 1.0 and 7.6 wt%, depending on the temperature and duration of cracking. This results is consistent with the hypothetical mechanism of chlorination of thermal carbon and formation of H_2.

The conversion of CH_3Cl increases throughout the reaction when cracking was performed at 450, 475 and 500 °C, as shown in Figure 1, suggesting an auto-catalytic effect which may be explained if the thermal carbon is active for the CH_3Cl cracking. Carbon, formed by the CH_3Cl cracking and deposited on the silica particles, may further catalyzes the CH_3Cl cracking. To determine whether the thermal carbon is active and the origin of this activity, two types of carbon were tested at 400 °C for the cracking:

- The black carbon Vulcan 3 appeared to be inactive,
- The thermal carbons obtained at 450, 500 and 550°C led to the CH_3Cl cracking and Figure 2 shows the CH_3Cl conversion at 400 °C on fresh silica and on thermal carbon obtained at 500 °C. While CH_3Cl did not crack on fresh silica at 400 °C, it did on aged masses, meaning that thermal carbon acts like a catalyst for the CH_3Cl cracking.

However, as black carbon is not active for the cracking, the origin of the activity of the thermal carbon may be the presence of Cl, previously identified by XRF. Cl may create acidic sites which catalyze the CH_3Cl cracking [16].

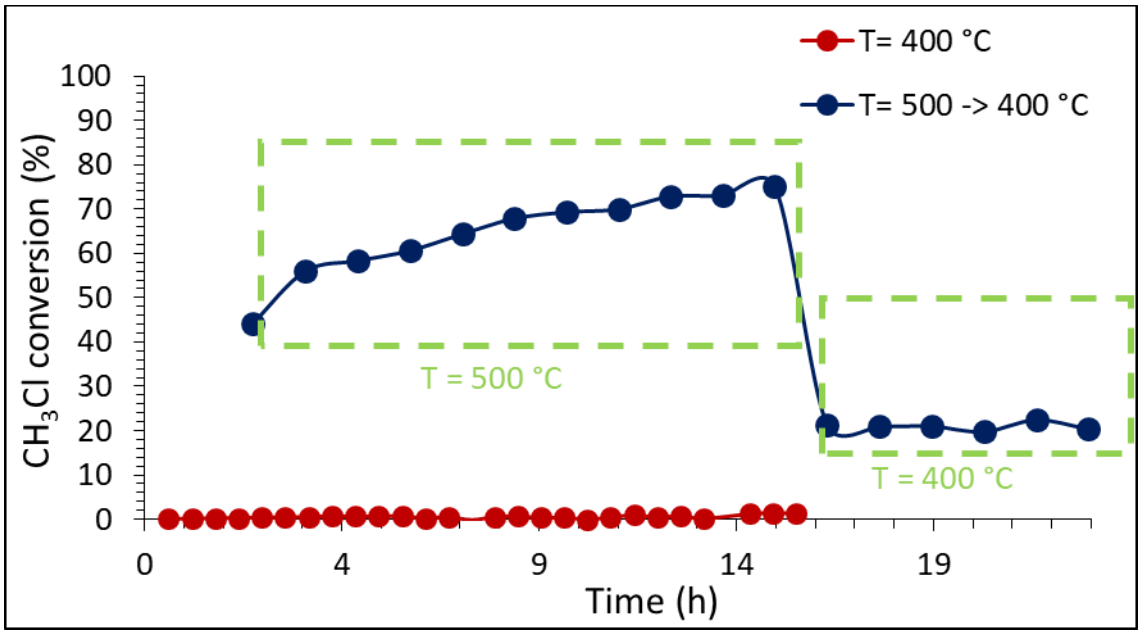


Figure 2: Conversion of CH_3Cl for thermal cracking at 400 °C and started at 500 °C and ended at 400 °C.

Catalytic cracking of CH_3Cl on metallic supported phases

It is reminded that all the cracking tests of CH_3Cl on supported phases were performed at 400 °C.

Silica support

The four phases Cu, CuCl, $CuCl_2$ and CuO, were analyzed by XRD before and after the cracking and it appears that all the copper precursors turned into CuCl when reacting with CH_3Cl, as shown in Figure 3. $CuCl_2$ and CuO have many crystallite peaks and only the more intense ones are labeled. Large CuCl crystallites were obtained with sizes ranged between 50 and 80 nm, close to the experimental half-width of the XRD instrument.

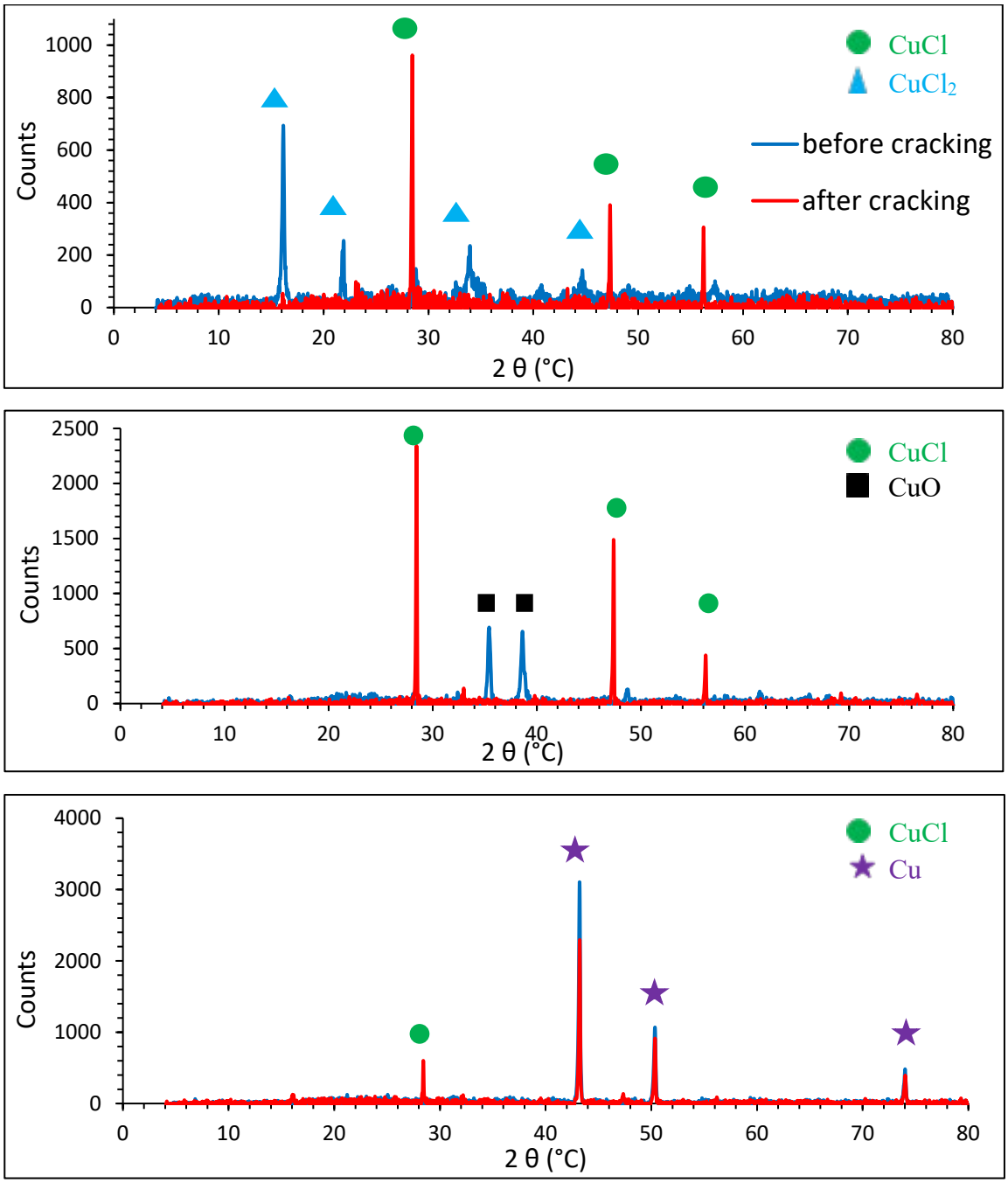


Figure 3: XRD diffractograms of copper phases supported on SiO_2, before and after the CH_3Cl cracking.

Formation of CuCl was expected since Cu and CuO are already known to undergo chlorination with CH_3Cl to form CuCl and then Cu_3Si, the active phase for the MCS synthesis [17]. Several reactions for the formation of CuCl from the copper precursors

are suggested in Table 3 but they all are hypothetical and not based on experimental data. For each reaction, C is formed with CuCl.

Table 3: Hypothetical reactions of formation of CuCl from $CuCl_2$, CuO and Cu.

Copper precursor	Reaction to CuCl	$\Delta_r G°$ (T=400 °C) (kJ/mol)
$CuCl_2$	$CH_3Cl + 2\ CuCl_2 \rightarrow 2\ CuCl + C + 3\ HCl$	-228.9
CuO	$CH_3Cl + CuO \rightarrow CuCl + C + H_2O + ½\ H_2$	-201.7
Cu	$CH_3Cl + Cu \rightarrow CuCl + ¼\ C + ¾\ CH_4$	-78.9
	$2\ CH_3Cl + Cu \rightarrow CuCl + 2\ C + HCl + {}^5/_2\ H_2$	-259.0
	$CH_3Cl + Cu \rightarrow CuCl + ½\ C + ½\ CH_4 + ½\ H_2$	-81.8

At the steady state, the conversion of CH_3Cl for the four phases is low, around 5 %, suggesting that crystalline CuCl has a low activity for the catalytic cracking of CH_3Cl. The copper precursors have neither influence on the consumption rate of CH_3Cl, calculated at the steady step and reported in Table 4, nor on the selectivities to CH_4 and solid carbon, both around 50. Such selectivity values were already obtained for the thermal cracking which leads to the conclusion that the thermal cracking is similar to the cracking on CuCl supported on SiO_2 (Eq.5). The main difference with the thermal cracking is the selectivity to H_2, lower than 3 %, suggesting that there is no chlorination reaction of the solid carbon. This difference may be explained by a temperature of carbon chlorination higher than 450 °C.

Black carbon support

The four phases Cu, CuCl, $CuCl_2$ and Cu_2O supported on black carbon were analyzed by XRD before and after the CH_3Cl cracking at 400 °C. While crystalline copper phases were observed before cracking, no diffraction peaks were observed after cracking. However, ICP did confirm the presence of copper on the support, with a weight content ranging between 2.2 and 3.9 wt.%. Copper was not seen by XRD probably because it was too dispersed to be detected, as it was confirmed in Transmission Electron Microscopy (TEM) where clusters smaller than 2 nm were observed.

To identify the copper phases on the black carbon support after cracking (either reduced, chlorinated or oxidized), CuCl, $CuCl_2$ and Cu_2O were extracted by HCl solution and the concentration of copper was determined by ICP. A low amount copper was extracted, between 5 and 30 % of the total copper, suggesting that the main part of copper was reduced (metallic Cu) after CH_3Cl cracking. Black carbon may be a reducer for CuCl and (Eq.7) suggested mechanisms of reduction.

$$\text{C-H} + CuCl \rightarrow Cu + HCl$$
$$\text{and/or C-C} + 2\ CuCl \rightarrow 2\ Cu + 2\ \text{C-Cl} \quad (7)$$

The conversion obtained at the steady step for the four supported phases is around 40-50% which confirms that metallic copper catalyzes the CH_3Cl cracking. The consumption rate of CH_3Cl cracking, reported in Table 4, seems to depend on the copper precursors as a higher rate was obtained for CuCl. This may be explained by a higher dispersion of the copper phase since the melting point of CuCl is close to the working temperature. The consumption rate is by far higher for the copper supported on carbon than in silica. This difference may be either explained by the higher dispersion of copper on carbon or if the metallic copper is a better catalyst for the CH_3Cl cracking than CuCl on silica. Based on these results, it is not possible to compare the catalyst activity of CuCl and Cu for the CH_3Cl cracking.

The copper precursors did not influence the product distribution as similar selectivity to CH_4, around 50%, and H_2, lower than 2%, were obtained. These values were already observed for the catalytic cracking on CuCl and the thermal cracking expect for the selectivity to H_2, attributed to the reaction between HCl and the thermal cracking. Therefore, it is suggested that mechanisms of catalytic cracking of CH_3Cl on CuCl and Cu is the same as the thermal cracking (Eq.5).

Table 4: Rate of CH_3Cl consumption at the steady step on copper supported on silica and black carbon at 400°C.

Supported phases	**Rate of CH_3Cl consumption x 10^{-7} (mol $_{CH_3Cl}$/s/g$_{Cu}$)**	
	SiO_2- support	C support
Cu	7.8	40
CuCl	8.3	55
CuO_x	6.8	33
$CuCl_2$	9.7	39

Conclusions

The purpose of this work was to study the CH_3Cl cracking either caused by high temperatures or catalyzed by copper phases. Copper phases investigated were CuCl, CuO_x and $CuCl_2$ supported on black carbon or on silica. The cracking mechanism, established from the selectivity set, is similar for each test (Eq.5)

$$CH_3Cl\ (g) \rightarrow \tfrac{1}{2}\ CH_4\ (g) + \tfrac{1}{2}\ C(s) + HCl\ (g) \qquad (5)$$

The thermal cracking of CH_3Cl on SiO_2 starts between 400 and 450 °C and the thermal carbon formed acts as a catalyst for the CH_3Cl cracking. As black carbon is not active for the CH_3Cl cracking, it was suggested that Cl acidifies the thermal carbon and turned it into acidic catalyst.

The four copper precursors supported on silica react with CH_3Cl at 400 °C and turned into CuCl, forming C at the same time. On the opposite, the same copper precursors supported on black carbon turned into Cu which catalyzes the CH_3Cl cracking at 400 °C. These results suggest that, during the DS, copper precursors turn into CuCl which reacts with Si to form Cu_3Si, the active phase. However, if carbon is present in the reaction bed mass, it may reduce the copper phases into Cu which catalyzes the CH_3Cl cracking.

References

1. B. Kanner, K. Lewis, *Catalyzed direct reactions of silicon,* Elsevier, 1993
2. R.J.H Voorhoeve, *Organosilanes: Precursor to silicones,* Elsevier, 1967, p 120-143
3. D.H. Sun, B.E. Bent, *Chemistry of the Direct synthesis of the methylchlorosilanes from methyl + chlorine monolayers on a Cu_3Si surface.* Catalysis Letters, **46**, 1997, p127-132
4. R. Voorhoeve, *Organosilanes: Precursor to silicones,* Elsevier, 1967
5. T. Wessel, D. Rethwisch, *Activation of CuSi and CuZnSnSi contact masses for the direct synthesis of* methylchlorosilanes, Reaction Kinetics and Catalysis Letters, **58,** 1996, p7-12
6. L. Gasper-Galvin, D. Sevenich, H. Friedrich, D. Rethwisch, *Role of metallic promoters in the direct synthesis of methylchlorosilanes.* Journal of Catalysis, **128,** 1991, p467-478
7. J. Bablin, A. Crawford, D. DeMoulpied, L. Lewis, *Effect of Low Aluminum Silicon on the Direct Process*, Industrial & Engineering Chemistry Research*,* **42**, 2003, p3555-3565
8. Olakangil, *Ph.D thesis: Effet of phosphorus and silicon purity on coke formation and reaction kinetics in the Direct Synthesis of Methylchlorosilanes,* 2002
9. J. Jokilk, V. Bazant, *Composés organiques du Si: influence de la composition du Si sur le synthèse directe des MCS,* Collection of Czechoslovak Chemical Communications, **26**, 1961, p417-426
10. M. Weissman, S. Benson, *Pyrolysis of Methyl Chloride, a Pathway in the Chlorine-Catalyzed Polymerization of Methane*, International Journal of Chemical Kinetics, **16**, 1984, p307-333
11. Y-S. Won, *Thermal Stability and Reaction Mechanism of Chloromethanes in Excess Hydrogen Atmosphere*, Journal of Industrial and Engineering Chemistry, **3**, 2007, p400-405
12. P-H. Taylor, B. Dellinger, *Thermal degradation characterisation of chloromethane mixtures*, Environmental Science and Technology, **22**, 1988, p438-447
13. A.E. Shilov, R.D. Sabirova, *The mechanism of the primary act of the thermal decomposition of methane derivates,* Russian Journal of Physical Chemistry A, **34**, 1959, p408-411
14. T.J. Wessel, D.G. Rethwisch, *Desactivation of CuSi and CuZnSnSi due to the Coke Formation during the Direct Synthesis of Methylcholorsilanes*, **161**, 1996, p861-866
15. R. C. Weast, *Handbook of Chemistry and Physics*, 65th ed., CRC, Ed., 1984-1985.
16. A. Perez-Cadenas, F. Maldonado-Hodar, C. Moreno-Castilla, *On the nature of surface acid sites of chlorinated activated carbons*, Carbon, **41**, 2003, p473-478

17. V. Bazant, *Direct Synthesis of Organo-Halogenosilanes*, Pure and Applied Chemistry, **13**, 1966, p313-326

Silicon for the Chemical and Solar Industry XV
Trondheim, Norway, June 15 – 18, 2020

Experimental investigations of monosilane pyrolysis: The importance of cyclic silanes

Guro M. Wyller[1)], Thomas J. Preston[1)], Marte O. Skare[1)], Hallgeir Klette[1)], Anjitha S.G[1)], Erik S. Marstein[1)]
1) Institutt for energiteknikk (IFE), Box 4, 2027 Kjeller, Norway

Abstract

Silicon purification technologies based on monosilane pyrolysis hold the potential to significantly reduce the energy consumption and cost related to production of solar grade silicon for the photovoltaic industry. These technologies do, however, encounter challenges related to dust formation, causing reduced material quality and reduced production yield. Further improvement of these technologies relies on an increased understanding of the underlying chemistry of the monosilane pyrolysis process.

Numerous theoretical and modelling studies of monosilane pyrolysis have been carried out throughout the last decades. Several of these works have hypothesised that *cyclic silanes* play a special role in the monosilane pyrolysis process. Because of the complexity of the process itself, the flammability and explosivity of the reactants and products and the lack of reliable measurement techniques, experimental evidence for this hypothesis has remained lacking. In this contribution, we describe how we – by using an advanced GC-MS technique in combination with horizontal tubular free space reactors – find an experimental confirmation for this long-standing hypothesis.

Experimental investigations of monosilane pyrolysis is ongoing work at IFE. Results thereof have already been published in journal articles and conference proceedings. This contribution aims to extract the key findings of this extensive body of work, both published and unpublished, and present them in a more condensed form.

Introduction

Silicon production based on monosilane pyrolysis

The preparation and purification of silicon feedstock consume up to 40 % of the energy needed in the production of a photovoltaic (PV) panel based on multicrystalline silicon [1]. It has been estimated [2] that reducing the energy consumption for solar grade silicon production by 15–17 kWh/kg-Si is, in a CO_2 emission perspective, equivalent to

a 1 % increase in the baseline efficiency for monocrystalline and multicrystalline silicon PV modules. Reducing the energy consumption of the silicon production and purification steps is therefore highly important for minimizing the carbon footprint, the cost and the energy payback time of a PV panel.

Around 80 % [3] of the silicon consumed by the PV industry is produced by the so-called Siemens process in which trichlorosilane ($SiHCl_3$) decomposes thermally onto heated silicon rods. This process is well understood and can give ultrapure (9N-11N) silicon. The energy requirement of the process is, however, rather high and the one-pass conversion is low, meaning that recycling of byproducts is necessary. One way of reducing the overall energy consumption during solar cell production is to replace the Siemens process by monosilane (SiH_4) pyrolysis. Note that the term *monosilane pyrolysis* here refers to formation of larger silicon species or to growth of silicon particles from chemical vapor deposition by application of heat. We do not refer to burning monosilane in air or oxygen.

Production of solar grade silicon by pyrolysis of monosilane is most frequently carried out in a fluidized bed reactor (FBR), which has a significantly lower energy consumption [2,4,5] than the Siemens reactor. The FBR process allows for a higher chemical yield than the Siemens process and it offers the possibility of continuous reactor operation rather than batch-wise operation as in the Siemens process. It is thus a an economically favorable process.

Formation of silicon dust (often referred to as *fines*) during the pyrolysis process is, however, creating challenges for monosilane based silicon production technologies. Fines formation constitutes a competing chemical pathway to the desired solid silicon production and therefore causes reduced overall yield. Moreover, fines formation leads to challenges with reactor clogging and reduced material quality. Further optimization of monosilane based silicon production technologies relies on the understanding of how fines arise during the pyrolysis process and how the fines production can be suppressed. Such understanding requires detailed knowledge of the underlying chemistry that converts monosilane into solid silicon.

Highly simplified, the conversion from monosilane to solid silicon can be written as

$$SiH_4(g) \rightarrow Si(s) + 2\ H_2(g) \qquad (1)$$

In reality, the conversion proceeds through a complicated reaction network including hundreds of sub- and parallel reactions and hundreds of chemical species (see e.g. [6–8] and others). The subtleties of this complicated reaction network are yet to be understood.

Cyclic silanes in the monosilane pyrolysis process

Several authors have, mainly based on modelling and theoretical considerations, stated that cyclic silanes play a special role in the reaction network that converts monosilane into solid silicon. Vepřek and co-workers [9] were among the first authors to suggest this theory. The idea was brought further when Swihart and Girshick in 1998 published a

detailed kinetic model of monosilane pyrolysis [8], containing reversible reactions among species with up to ten silicon atoms and irreversible reactions forming silicon hydrides with 11–20 silicon atoms. Cyclic species were considered in this model along with silanes, silenes and silylenes.

The authors [8,9] suggest that cluster formation proceeds first through the formation of silanes with an increasing number of silicon atoms (mainly by reversible silylene insertion reactions) until a relatively stable cyclic polysilane with five or more silicon atoms is produced. From this cyclic species, the elimination of silylene is unlikely, because it requires breaking of two silicon-silicon bonds. Hydrogen, on the other hand, can relatively easily be eliminated from a cyclic silane. The hydrogen elimination leaves a reactive site which can easily react with silylene, causing a fast growth of the molecule into larger three-dimensional clusters. Other authors (e.g. [10,11]) have expressed the same theory.

The high stability of the cyclic silanes relative to the non-cyclic ones has also been pointed to by several authors [8,10,12]. Because of this high stability, higher silanes will, once formed, be unlikely to decompose. Their concentration is therefore likely to increase. More specifically, Wong et al. [10] built further upon the kinetic model by Swihart and Girshick [8] and used automated mechanism generation to develop an even more complex mechanism. Based on this mechanism, they predicted that cyclic silanes, especially cyclopentasilane (*cyclo*-Si_5H_{10}), will be produced at high concentrations relative to other species during monosilane pyrolysis. As we shall see later, this modelled result is in good agreement with our experimental results.

Other modelling works (e.g. [6,13–15]) combine gas phase and surface phase chemical reactions with computational fluid dynamics, particle transport, convection, diffusion thermophoresis, and models of nucleation and coagulation to predict particle formation during monosilane pyrolysis. There is, in other words, a very high degree of detail in the modelled and theoretical works related to monosilane pyrolysis. A common theme amongst most of these modelling works, however, is that they lack experimental data describing the concentration development of higher order silanes for model verification.

We have identified three main challenges causing the lack of detailed experimental data in this field.

- There has been a lack of reliable measurement techniques to detect and identify higher order silanes and their isomers.
- The high reactivity of the silanes with oxygen makes them challenging and potentially dangerous to handle. This has limited the number of experiments reported in the scientific literature.
- The chemical process itself makes it challenging to detect the intermediate reaction products (i.e. the higher order silanes). Among the chemical steps in the pyrolysis process, the very first step, production of silylene and hydrogen from monosilane, has one of the highest activation energies [16]. The onset of the reaction is therefore very

abrupt: As soon as the initial step is overcome, the reaction proceeds quickly to larger and larger species, until eventually, silicon particles are produced.

IFE's work on experimental investigation of monosilane pyrolysis strives to overcome these three challenges. First, our gas chromatography - mass spectrometry (GC-MS) setup (see experimental section) provides us with the ability to measure higher order silanes with up to eight silicon atoms and differentiate between isomers of silanes with up to five silicon atoms. Second, our monosilane pyrolysis reactors enables us to map relative concentrations of higher order silanes as a function of various reactor parameters in an efficient and safe manner. Third, by controlling the pyrolysis process carefully such that it avoids proceeding all the way to silicon particles, we are able to lead higher order silanes, which are process intermediates, out of the reactor and to our GC-MS in which we detect and identify these species.

With this suite of tools, we obtain detailed experimental data on the formation of various higher order silane species as function of reactor parameters during monosilane pyrolysis. Thereby, as we shall see in the following sections, we find experimental evidence for the special role of cyclic silanes in the monosilane pyrolysis process.

Experimental

Monosilane pyrolysis reactors

Our pyrolysis experiments are conducted in two different horizontal, tubular free space reactors (FSRs) of different sizes.

The smallest reactor (see Figure 1) has already been described in our previous contributions [17] and [18]. The reactor consists of a 124 cm long 1/4'' (6.3 mm) stainless steel pipe with an inner diameter of 3.85 mm and with Swagelok fittings in both ends. The total reactor volume is only 14.4 cm^3, giving a low fire and explosion risk.

The reactor body is heated by resistive heaters and insulated by glass fibre, textile glass braiding and silicone foam tape. The temperature of the 80 cm long heated zone can be set to values from room temperature to 600 °C. In the experiments described here, we use temperatures from 450 °C to 530 °C.

During an experiment, the process gas, i.e. monosilane and hydrogen at various mixing ratios, flows through the reactor, controlled by mass flow controllers (MFCs). In the experiments presented here, we use a constant total flow of 100 standard millilitres per minute (mSLM), giving a residence time of about 2 s. We vary the monosilane inlet

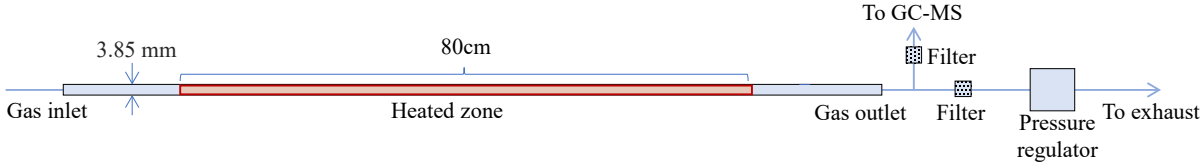


Figure 1: Sketch of our smallest horizontal tubular free-space-reactor. Reprinted from [18].

concentration (in volume percent) in the range from 2.5 % to 100 %. The reactor pressure is controlled by a back-pressure regulator. In the presented experiments, we keep the pressure constant at 1.2 bar(g).

Depending on the combination of monosilane inlet concentration, reactor temperature and residence time, particles might be produced in the reactor during experimentation. The reactor is therefore equipped with filters hindering particles from entering the pressure regulator and the GC-MS system (see next subsection). Particles and other large species will tend to clog the reactor itself as well as the particle filters. Therefore, we generally want to avoid reactor settings that cause extensive particle production.

The larger reactor (see Figure 2), already described in ref. [19], has a larger tolerance for particles than the smaller one. This reactor consists of a 3 m long, 50 mm diameter stainless steel (316L) pipe with KF flanges welded to the ends. The reactor has a 54 cm long preheating zone and a 30 cm long reaction zone, heated by resistive heating coils and insulated by glass wool and silicone foam tape.

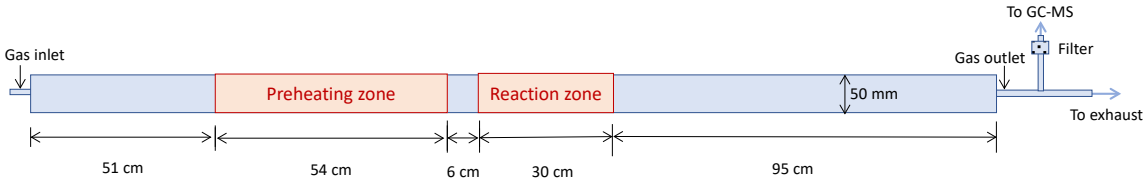


Figure 2: Sketch of the largest horizontal tubular free-space-reactor. Adapted from [20].

For the experiments reported here we use a constant gas flow of 4.0 standard liters per minute (SLM), controlled by MFCs. This flow gives a residence time between 0.6 and 1.8 seconds (see [19]). The monosilane inlet concentration is kept constant at 10.0 vol%. Hydrogen is used as dilution gas and the reactor pressure is kept constant at 1 atm. The temperature in the reaction zone is varied in the range between 450 ºC and 590 ºC, whereas the temperature in the preheating zone is kept constant at 300 ºC.

Gas Chromatography-Mass Spectrometry

Side streams of the reactor exhaust from both reactors are led to an advanced gas chromatography-mass spectrometry (GC-MS) setup in which the reaction products are analysed. The GC-MS technique allows for absolute quantification of mono-, di- and trisilane, as well as relative quantification of higher order silanes with up to eight silicon atoms. We can further differentiate between higher order silane isomers with up to five silicon atoms and identify one cyclic silane with six silicon atoms.

As of now we have no means for *absolute* quantification of the signals for species with more than three silicon atoms. We can only compare *relative* concentrations of these species. We assume that the response factor of every species in the GC-MS is constant as a function of concentration. This assumption implies that the measured signal of a species scales linearly with the concentration of that species. The scaling factors are, however, unknown. When we plot the signals of the higher order silanes semi-logarithmically (as for example in Figure 3b), the slope of each plot will be independent of the unknown

scaling factors. This way, we can compare the growth rate of the species even if their scaling factors are unknown. Readers are referred to our previous contribution [21] for further details on the GC-MS system. Some improvements to the system are also described in [17].

The combination of the two reactors for controlled experimentation with the pyrolysis reactions and the GC-MS setup for monitoring of the reaction products constitutes a unique combination which helps us understand the underlying chemistry of the monosilane pyrolysis process.

Results and Discussion

Influence of temperature on higher order silane formation

Figure 3 shows outlet concentrations of monosilane and various higher order silane species as a function of reactor temperature at a fixed monosilane inlet concentration of 10 vol% in the small FSR (Figure 1). Part (a) shows absolute outlet concentrations of monosilane, disilane and trisilane, plotted with a linear axis. Part (b) shows uncalibrated signals for various higher order silane isomers plotted with a logarithmic axis. Trisilane is included in both parts for clarity and comparison.

Figure 3a shows that the monosilane concentration *decreases* with temperature. This decrease indicates that the monosilane conversion *increases* with temperature, i.e. that at higher temperatures, more monosilane is converted into other species. The outlet concentrations of all the other species that we measure increase with temperature, until they level out at a temperature of approximately 500 °C.

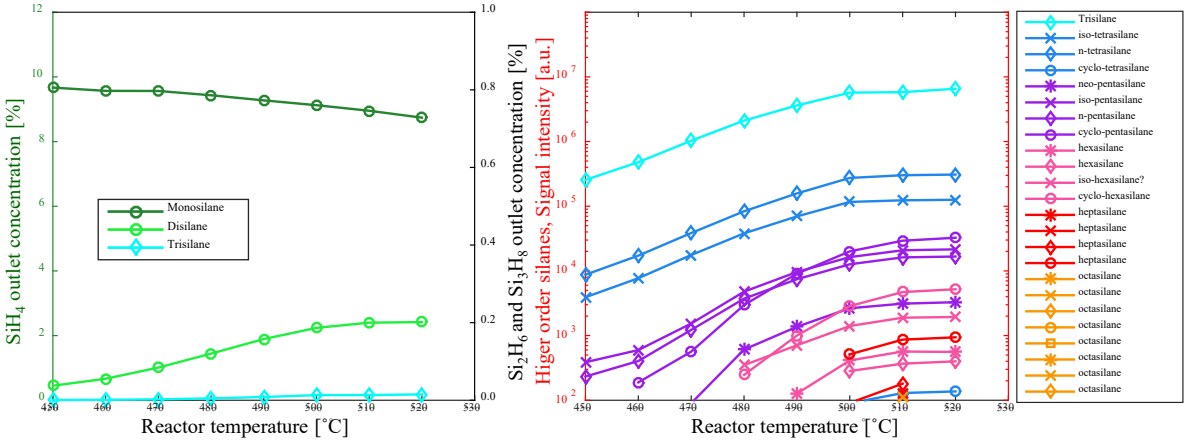


Figure 3: Outlet concentrations of various silanes as functions of temperature during pyrolysis of 10 vol% monosilane diluted in hydrogen, in the reactor sketched in Figure 1. **a)** Calibrated output concentrations of mono-, di- and trisilane. **b)** Uncalibrated signals for trisilane and higher order silane isomers. Reprinted from [18].

The signals of the non-cyclic higher order silanes grow at similar rates as function of temperature, causing parallel lines in the semilogarithmic plot (see experimental section). The concentrations of the cyclic silanes (cyclopentasilane and cyclohexasilane) however,

grow faster with temperature than the concentration of the non-cyclic species. These signals are therefore crossing several other lines in the graph. In our previous contribution [18], we show the same trend in data taken with 20 vol% monosilane inlet concentration. This observation, which we relate to the high stability of cyclic silanes compared to the non-cyclic ones [8,10,12], will be further addressed in the next section.

Figure 4 shows outlet concentrations of monosilane and various higher order silane species as function of reactor temperature at a fixed monosilane inlet concentration of 10 vol% in the large FSR (Figure 2). Part (a) shows absolute outlet concentrations of monosilane, disilane and trisilane, plotted with a linear axis. Part (b) shows uncalibrated signals for various higher order silane isomers plotted with a logarithmic axis. Trisilane is included in both parts for clarity and comparison. Note that Figure 3 and Figure 4 include data from slightly different temperature ranges.

There are both similarities and differences between the data from the small reactor (Figure 3) and that from the larger reactor (Figure 4). We expect differences caused by the different reactor geometry which give rise to differences in heat distribution, flow pattern and residence time. Still, the main trends in the data are the same. Also, in the case of the larger reactor (Figure 4) we observe that monosilane conversion increases with increasing temperature. We further observe that the outlet concentrations of all the other species increase with temperature up to approximately 520 ˚C.
At higher temperatures, they flatten out, reach a maximum, and eventually start to decrease with temperature. The decrease in concentration at higher temperatures indicates that the species that we observe have developed further into even larger species (i.e. species that we cannot measure) or even into particles.

Interestingly, the development of the cyclic silanes compared to the non-cyclic ones is very similar in the large reactor (Figure 4) as in the small reactor (Figure 3). In both reactors, we observe that the concentrations of the cyclic species grow faster than the concentration of their non-cyclic counterparts with temperature.

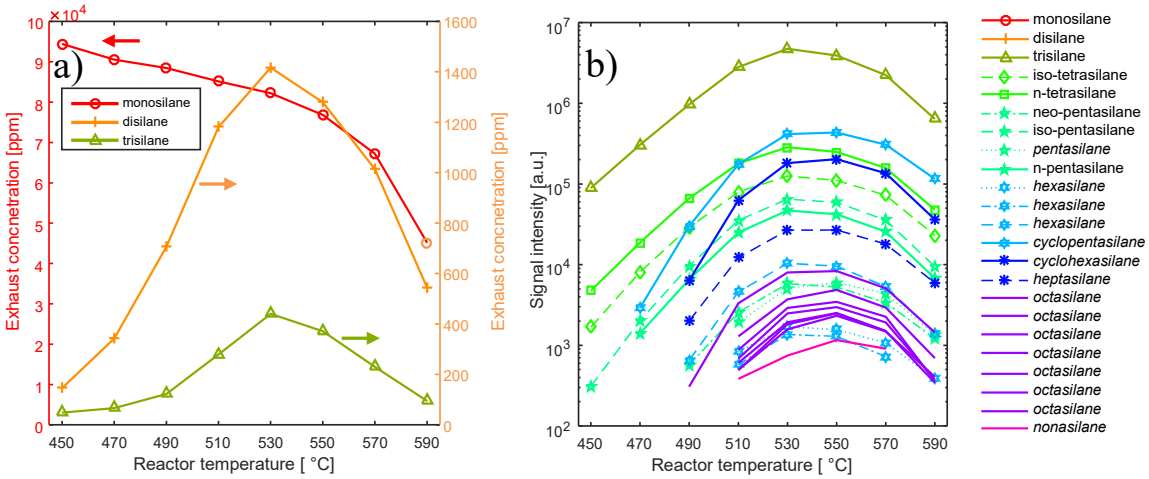


Figure 4: Outlet concentration of silanes as function of temperature during pyrolysis of 10 vol% monosilane diluted in hydrogen in the reactor sketched in Figure 2. **a)** Calibrated outlet concentrations for mono-, di- and trisilane. **b)** Uncalibrated signals for trisilane and higher order silane isomers. Reprinted from [20]. Similar plots appear in our earlier contribution in ref. [19]. In this version of the plots, the assignments of the GC-MS signals to silane isomers are updated according to our most recent knowledge [17,21]. This update includes the assignment of the cyplopentasilane and cyclohexasilane signals.

Influence of monosilane inlet concentration on higher order silane formation

Figure 5 shows uncalibrated signals for outlet concentrations of higher order silanes as function of monosilane inlet concentration at 450 °C (a) and 460 °C (b) in the small FSR (Figure 1). At 450 ˚C the lines corresponding to the different species are mostly parallel, meaning that the concentrations develop at similar rates as function of inlet concentration. At 460 ˚C most lines are still parallel, but the cyclopentasilane and cyclohexasilane signals are growing faster with monosilane inlet concentration than the signals of most of the other species. The fast increase in the concentration of cyclic silanes as function of temperature (Figure 3 and Figure 4) and monosilane inlet concentration (Figure 5) can be explained by the stability of cyclic silanes compared to their non-cyclic counterparts [8,10,12] and by the mechanism that has been suggested for the pyrolysis process. Several authors [8–11] have suggested that cluster formation goes via the formation of higher and higher order silanes until a relatively stable, cyclic polysilane is produced. From this cyclic species the elimination of silylene is unlikely since it requires the simultaneous breaking of two silicon-silicon bonds. Once a cyclic silane is formed, it will therefore be relatively unlikely that it decomposes to two separate silicon-containing species. The concentration of cyclic species can therefore build up. Our results correspond well to this explanation model and can be regarded as experimental evidence for the theory.

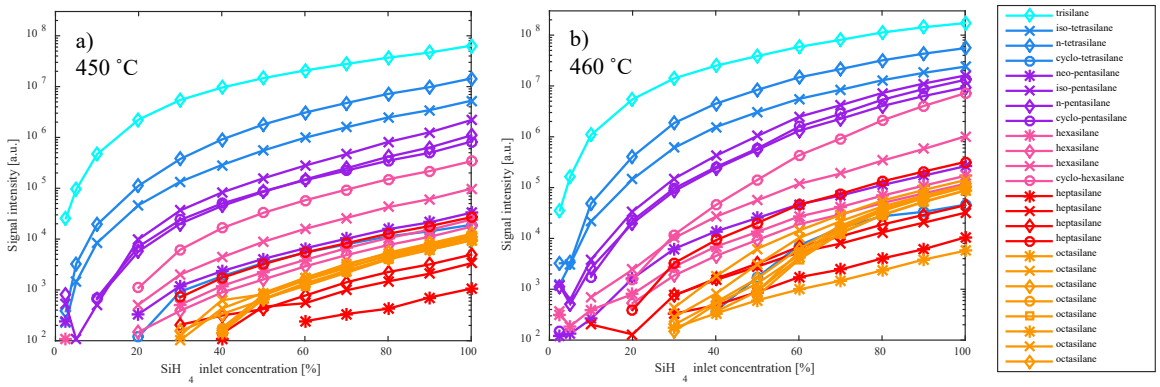


Figure 5: Development in outlet concentration of various higher order silane species (uncalibrated values in arbitrary units) as function of monosilane inlet concentration (vol%), at reactor temperatures of **a)** 450 °C and **b)** 460 °C, with hydrogen as diluent gas in the small FSR (Figure 1). The same two plots are shown as parts of Fig. 2 in reference [18]. They are here shown in more detail for clarity.

At 460 ˚C (Figure 5b) we observe that the outlet concentration of several octasilanes exhibit an inflection point at a monosilane inlet concentration of about 50 vol%. At monosilane inlet concentrations higher than 50 vol%, the development of the octasilanes with monosilane inlet concentration is similar to that of the cyclic penta- and hexasilanes. According to Swihart and Girshick [8], the dominant clusters containing eight silicon atoms are three-dimensional structures made up by five-membered rings. It is tempting to speculate that the inflection point in the octasilane concentration is related to the growth of these cyclic species. When the concentrations of the cyclic structures reach a certain level, a new reaction pathway in which polycyclic octasilanes are produced might be turned on, causing the concentration of octasilanes to develop faster.

Combined influence of temperature and monosilane inlet concentration on higher order silane formation

The results presented in the previous sections indicate that the formation of higher order silanes during monosilane pyrolysis are complicated functions of several reactor parameters. In addition to temperature and monosilane inlet concentration, other important parameters include the reactor geometry, flow rates, choice of diluent gas, and the presence of silicon particles. These parameters span a multidimensional parameter space. In one of our earlier contributions [19], we studied how *temperature* and *residence time* together influence the formation of higher order silanes during monosilane pyrolysis. In the present contribution we focus primarily on how *temperature* and *monosilane inlet concentration* together influence the process.

Figure 6 shows the two-dimensional landscapes for outlet concentrations of n-pentasilane (left pane) and cyclopentasilane (right pane) as functions of temperature and monosilane inlet concentration. The grey area indicates conditions at which no

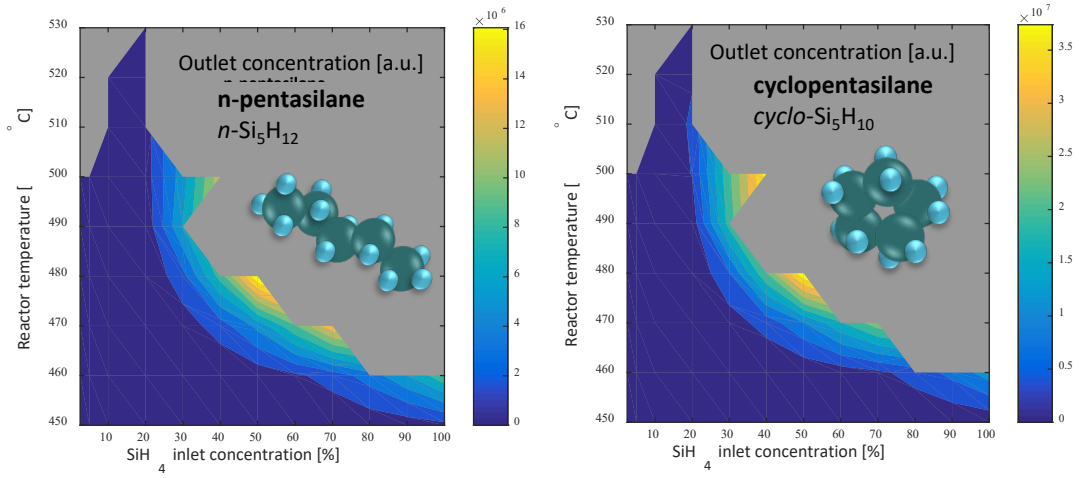


Figure 6: Maps of outlet concentrations of n-pentasilane (left pane) and cyclopentasilane (right pane) as function of temperature and monosilane inlet concentration during monosilane pyrolysis. The concentrations are given in arbitrary units. Note that the two panes are differently scaled. The grey regions indicate conditions at which no measurement was made either because clogging was anticipated or because of limitations in available laboratory capacity. Reprinted from [20] . The data visualized in this figure is also included in Fig.5 of ref [18].

measurement was made either because clogging was anticipated or because of limitations in available laboratory capacity. In ref. [18] we show similar maps for disilane, trisilane and selected tetrasilanes, pentasilanes and hexasilanes. Readers are referred to the same article [18] for details on how the data in Figure 6 is collected.

The data presented in Figure 6 suggest that cyclic and non-cyclic pentasilane have their highest outlet concentrations at slightly different combinations of temperature and monosilane inlet concentrations. For n-pentasilane, we observe the highest inlet concentration at 480 °C and 50 vol% monosilane inlet concentration. For cyclopentasilane, on the other hand, we find the highest outlet concentration at 500 °C and 40 vol% monosilane inlet concentration. Note that these are the highest concentrations *that we can measure*. These species might reach higher concentrations at reactor parameters were particles plays a major role in pyrolysis. We have been hindered from measuring these parameter combinations due to reactor clogging. Nevertheless, the cyclic pentasilane seem to reach its highest outlet concentration at a *higher temperature* and a *lower monosilane* inlet concentration than its non-cyclic counterpart. In ref. [18] we show that the same trend holds true also for other cyclic and non-cyclic silanes.

Implications for reactor operation

The operation of an FBR, which is the most used reactor for silicon production based on monosilane pyrolysis, is for several reasons different from that of an FSR, which we use here. For example, the fluidization gas in an FBR causes fast mixing and large movements of gas within the reactor, and the seed particles provide surfaces onto which

gas species can deposit. These effects are not present in the FSRs. Nevertheless, the results that we present are related to several of the processes taking place in an FBR.

As explained in the introduction, cyclic species are expected to play a special role in the formation of particles during monosilane pyrolysis. We therefore hypothesize that if it is desired to avoid particle formation during FBR operation, one should avoid parameter combinations that cause extensive production of cyclic silanes. We realize that the formation and disappearance rates of all the various higher order silane isomers are functions of a large, multidimensional parameter space of which we have only explored two dimensions in this work. Nevertheless, our results indicate that at relatively low temperatures (< 470 °C) and high monosilane inlet concentrations (70–100 vol%; the balance is hydrogen) monosilane pyrolysis takes place without extensive formation of cyclic higher order silanes. Consequently, we suggest that low temperatures combined with high monosilane inlet concentration is favorable for avoiding particle formation during monosilane pyrolysis.

Conclusion

In this contribution, which gives a summary of already published and ongoing work on monosilane pyrolysis at IFE, we describe an advanced GC-MS setup combined with two different monosilane pyrolysis reactors. Using this unique combination of tools, we give experimental evidence for the special role of cyclic silanes during monosilane pyrolysis. This role was proposed more than 25 years ago, based on theoretical considerations, but experimental evidence has remained lacking.

Our detailed maps of outlet concentrations of various higher order silanes as function of reactor temperature and monosilane inlet concentrations can give guidelines as to which reactor parameters to choose to avoid particle formation during monosilane pyrolysis in industrial silicon production reactors.

References

1. F. Cucchiella, I. D'Adamo, *Estimation of the energetic and environmental impacts of a roof-mounted building-integrated photovoltaic systems*, Renew. Sustain. Energy Rev. **16**, 2012, p.5245–5259.
2. D. Ravikumar, B. Wender, T.P. Seager, M.P. Fraser, M. Tao, *A climate rationale for research and development on photovoltaics manufacture*, Appl. Energy. **189**, 2017, p.245–256.
3. G. Cellere, T. Falcon, M. Zwegers, J. Bernreuter, J. Haase, G. Coletti, *International Technology Roadmap for Photovoltaic*, **8**, 2017, p.1–57.
4. G. Bye, B. Ceccaroli, *Solar grade silicon: Technology status and industrial trends*, Sol. Energy Mater. Sol. Cells. **130**, 2014, p.634–646.
5. A. Ramos, W.O. Filtvedt, D. Lindholm, P.A. Ramachandran, A. Rodríguez, C. del Cañizo, *Deposition reactors for solar grade silicon: A comparative thermal analysis of a Siemens reactor and a fluidized bed reactor*, J. Cryst. Growth. **431**, 2015, p.1–9.

6. H.Y. Dang, M.T. Swihart, *Computational Modeling of Silicon Nanoparticle Synthesis: II. A Two-Dimensional Bivariate Model for Silicon Nanoparticle Synthesis in a Laser-Driven Reactor Including Finite-Rate Coalescence*, Aerosol Sci. Technol. **43**, 2009, p.554–569.

7. S. Nijhawan, P.H. McMurry, M.T. Swihart, S.-M. Suh, S.L. Girshick, S.A. Campbell, J.E. Brockmann, *An experimental and numerical study of particle nucleation and growth during low-pressure thermal decomposition of silane*, J. Aerosol Sci. **34**, 2003, p.691–711.

8. M.T. Swihart, S.L. Girshick, *Thermochemistry and Kinetics of Silicon Hydride Cluster Formation during Thermal Decomposition of Silane*, J. Phys. Chem. B. **103**, 1999, p.64–76.

9. S. Vepřek, K. Schopper, O. Ambacher, W. Rieger, M.G.J. Vepřek-Heijman, *Mechanism of Cluster Formation in a Clean Silane Discharge*, J. Electrochem. Soc. **140**, 1993, p.1935–1942.

10. H. Wong, X. Li, M.T. Swihart, L.J. Broadbelt, *Detailed Kinetic Modeling of Silicon Nanoparticle Formation Chemistry via Automated Mechanism Generation*, J. Phys. Chem. A. **108**, 2004, p.10122–10132.

11. K. Tonokura, T. Murasaki, M. Koshi, *Formation Mechanism of Hydrogenated Silicon Clusters during Thermal Decomposition of Disilane*, J. Phys. Chem. B. **106**, 2002, p.555–563.

12. A.J. Adamczyk, M.F. Reyniers, G.B. Marin, L.J. Broadbelt, *Hydrogenated amorphous silicon nanostructures: Novel structure-reactivity relationships for cyclization and ring opening in the gas phase*, Theor. Chem. Acc. **128**, 2011, p.91–113.

13. H.Y. Dang, M.T. Swihart, *Computational Modeling of Silicon Nanoparticle Synthesis: I. A General Two-Dimensional Model*, Aerosol Sci. Technol. **43**, 2009, p.250–263.

14. S.S. Talukdar, M.T. Swihart, *Aerosol dynamics modeling of silicon nanoparticle formation during silane pyrolysis: A comparison of three solution methods*, J. Aerosol Sci. **35**, 2004, p.889–908.

15. P. Zhang, *Effect of operation parameters on fines formation during thermal decomposition of silane*, Sol. Energy. **155**, 2017, p.75–81.

16. A.J. Adamczyk, M.-F. Reyniers, G.B. Marin, L.J. Broadbelt, *Kinetic correlations for H2 addition and elimination reaction mechanisms during silicon hydride pyrolysis.*, Phys. Chem. Chem. Phys. **12**, 2010, p.12676–96.

17. G.M. Wyller, T.J. Preston, M.O. Skare, H. Klette, S.G. Anjitha, E.S. Marstein, Exploring thermal pyrolysis of monosilane through gas chromatography-mass spectrometry measurements of higher order silanes, in: Silicon Chem. Sol. Ind., Svolvær, 2018: pp. 267–275.

18. G.M. Wyller, T.J. Preston, S.G. Anjitha, M.O. Skare, E.S. Marstein, *Combination of a millimeter scale reactor and gas chromatography-mass spectrometry for mapping higher order silane formation during monosilane pyrolysis*, J. Cryst. Growth. **530**, 2020, p.125305.

19. G.M. Wyller, T.J. Preston, T.T. Mongstad, D. Lindholm, H. Klette, Ø. Nordseth, W.O. Filtvedt, E.S. Marstein, *Influence of temperature and residence time on thermal decomposition of monosilane*, Energy Procedia. **124**, 2017, p.814–822.

20. G.M. Wyller, Experimental investigations of monosilane pyrolysis, University of Oslo, Department of Physics, 2019.

21. G.M. Wyller, T.J. Preston, H. Klette, T.T. Mongstad, E.S. Marstein, *Identification of higher order silanes during monosilane pyrolysis using gas chromatography-mass spectrometry*, J. Cryst. Growth. **498**, 2018, p.315–327.

Silicon for the Chemical and Solar Industry XV
Trondheim, Norway, June 15 – 18, 2020

Thermodynamics of B in Si–Cu based alloys for optimizing B removal from SOG-Si

Tomohiro Mizutani, Wataru Fukada, and Kazuki Morita
Department of Materials Engineering, The University of Tokyo, Japan.

Abstract

To reasonably produce solar-grade silicon, a metallurgical refining process has been proposed. Notably, boron (B) is one of the elements that significantly influences the efficiency of solar cells and is difficult to remove from silicon. The oxidation of B via molten flux (flux treatment) is one of the promising methods of removing boron and has been intensively examined. In a previous study, it was revealed that the activity coefficient of B increased upon alloying silicon with tin, which indicates enhanced B removal from Si–Sn alloy via flux treatment. In this study, we examined the possibility of efficient B removal using the $CaO–Na_2O–SiO_2$ flux and Si–Cu based alloy. The borate capacity of the $CaO–Na_2O–SiO_2$ flux and the activity coefficient of boron in the Si–Cu-based alloy were measured, and their high values were confirmed. In addition, the distribution ratio of B was measured via actual flux treatment using the Si–Cu based alloy and $CaO–Na_2O–SiO_2$ flux, and it was observed to be 7.92 at the maximum.

Introduction

Solar-cell production is rapidly increasing in response to global warming. Solar-grade silicon (SOG-Si, 7N) is the main ingredient in solar cells and is made via a chemical refining process, which was developed for producing semiconductor-grade silicon (SEG-Si, 11N). However, the process consumes a huge amount of energy and has low productivity. Therefore, metallurgical refining processes with relatively low energy consumption and high productivity have been intensively examined as a reasonable processes for directly producing SOG-Si using metallurgical-grade silicon (MG-Si, 98%)[1), 2)]. Because most impurities in Si have small segregation coefficients, they can be easily removed using the solidification refining method. However, some elements such as boron (B) and phosphorous (P), which have exceptionally large segregation coefficients, cannot be effectively removed using this method. It was proposed that vacuum refining[3)] and oxidation refining are effective for removing P and B, respectively.

Flux treatment is one of the representative oxidation refining methods that can remove B from molten Si into molten flux in the form of BO_3^{3-}. The optimization of the flux composition has been examined, and it was confirmed that flux with high basicity is effective for B removal. However because the oxygen potential at the interface between molten Si and flux is relatively low, the distribution ratio of B (L_B) is at most 5.5, even upon using the $CaO–SiO_2$ flux with high basicity[4].

Yoshikawa et al.[5] proposed low-temperature solidification refining using Si–Al alloy and confirmed that the segregation coefficient of B was significantly reduced as the liquidus temperature decreased. To improve the removal efficiency, other elements have been examined. Ma et al.[6] used the Si–Sn alloy as a solvent; however, it was concluded that the alloy was not appropriate for removing B because the activity coefficient of B in the molten Si–Sn alloy was large, indicating that B was thermodynamically unstable in the liquid phase. They utilized this property of B to perform flux treatment in the molten Si–Sn alloy. They confirmed that B in the molten Si–Sn alloy, in which B was more unstable than in molten Si, was considerably easier to remove into flux, and consequently a significantly high distribution ratio of B, i.e., 200 at the maximum[7].

By adding Na_2O to the $CaO–SiO_2$ flux, the distribution ratio of B might improve because of the high basicity and wide liquid-phase region. In addition, it might enable reasonable B removal at temperatures lower than the melting point of Si. In this study, we evaluated the borate capacity of the $CaO–Na_2O–SiO_2$ flux at 1473 K from the thermodynamic perspective. Furthermore, the thermodynamic property of B in the molten Si–Cu based alloy, which is considered more appropriate for refining at low temperatures than the Si–Sn alloy, was evaluated. In addition, the possibility of B removal using this method was investigated via actual flux treatment using a Si–Cu–based alloy and $CaO–Na_2O–SiO_2$ flux.

Experimental

2.1 Measuring the borate capacity of the $CaO–Na_2O–SiO_2$ flux

Irrespective of the thermodynamic properties of the alloy, we consider the borate capacity ($C_{BO_3^{3-}}$) represented using eq. 2, which is based on the reaction expressed in eq. 1. The borate capacity is a thermodynamic index that indicates the B-absorption ability of the flux. In this study, the measurement of $C_{BO_3^{3-}}$ of the $CaO–Na_2O–SiO_2$ flux was attempted by equilibrating the molten $CaO–Na_2O–SiO_2$ flux using boron nitride (BN). First, $CaCO_3$ was placed in a tabletop small electric furnace at 1273 K for 12 h or more and calcined to produce CaO. Subsequently, Na_2CO_3, SiO_2, Na_2SiO_3, Na_4SiO_4, and calcined CaO were weighed, mixed, charged into a Pt crucible, and preliminarily melted in an ultra-high-speed heating melting furnace. In addition, 10 g of the pre-melted flux and 0.6 g of BN pieces were charged into a graphite crucible with a lid (outer diameter: 30 mm; inner

diameter: 22 mm; depth: 35 mm) and were maintained at 1473 K using an electric resistance furnace, as depicted in Fig. 1. An alumina tube (SSA-S) was used as the furnace tube, whose inside was filled using N_2 and CO gases. The mixture of N_2 and CO gases was de-carbonated and de-hydrated using soda lime, silica gel, and magnesium perchlorate. After the sample was held at 1473 K for a certain period, the alumina rod that held the crucible was cooled by removing it from the furnace. The BN pieces and flux were separated from the sample, and the concentration of B in the flux was analyzed via ICP-OES. One has the following:

$$\underline{\mathrm{B}}(l) + \frac{3}{4}\mathrm{O}_2(g) + \frac{3}{2}(\mathrm{O}^{2-}) = (\mathrm{BO}_3^{3-}) \quad (1)$$

$$C_{\mathrm{BO}_3^{3-}} = \frac{(\mathrm{mass\%BO}_3^{3-})}{a_{\mathrm{B}(l)} \cdot P_{\mathrm{O}_2}^{3/4}} = \frac{K_{\mathrm{B}} \cdot a_{\mathrm{O}^{2-}}^{3/4}}{f_{\mathrm{BO}_3^{3-}}} \quad (2)$$

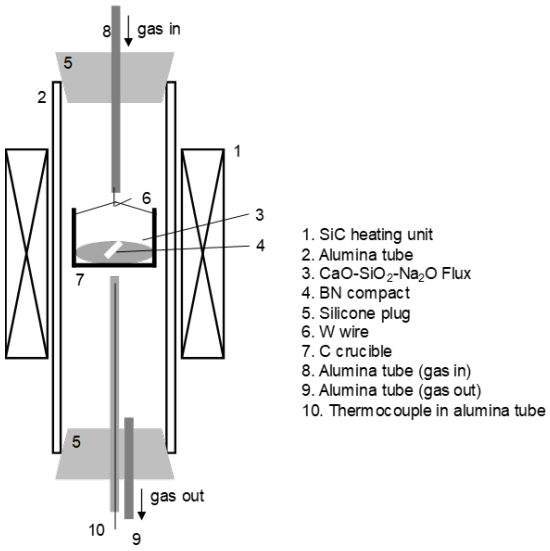


Figure 1: Apparatus for equilibration experiments.

2.2 Measuring the activity coefficient of B in the molten Si–Cu–Sn alloy

The activity coefficient of B (γ_{B}) is an index that indicates the thermodynamic instability of B in an alloy. In this study, to evaluate the thermodynamic properties of B in molten Si–Cu based alloys, the measurement of γ_{B} was attempted by equilibrating a molten Si–Cu based alloy using BN and silicon nitride (Si_3N_4). First, the grains of Si, Cu, and Sn were weighed and charged in a graphite crucible and were melted in a high-frequency induction furnace in an argon-gas atmosphere. After cooling, 0.5 g of bulk BN and 0.3 g of compacted Si_3N_4 were charged in the crucible and were maintained at a predetermined temperature ranging from 1473 K to 1673 K using an electric resistance furnace. A mullite tube (HB) was used as the furnace tube, whose inside was filled using Ar gas. During the

experiment, the Ar gas was kept flowing at 200 mL/min. The Ar gas was de-carbonated and de-hydrated using soda lime, silica gel, and magnesium perchlorate. After holding the sample at a predetermined temperature for a certain period, the crucible was quickly removed from the furnace and quenched using water. The BN pieces and Si_3N_4 were separated from the sample, and the concentrations of B, Cu, and Sn in the alloy were analyzed via ICP-OES.

2.3 B removal from the Si–Cu alloy

To verify the efficiency of B removal in the actual flux treatment, the molten Si–Cu based alloy and molten CaO–Na_2O–SiO_2 flux were equilibrated, and the distribution ratio of B (L_B), as represented in eq. 3, was measured. The compositions of the alloy and flux before the experiment are listed in Table 1. One has the following:

$$L_B = \frac{(\text{mass\%B in flux})}{[\text{mass\%B in metal}]} \quad (3)$$

Table 1: Compositions of the alloy and flux before the experiment for measuring the distribution ratio of B.

ID	Time / h	Metal			Flux		
		Si (mass%)	Cu (mass%)	B (ppmw)	CaO (mass%)	Na_2O (mass%)	SiO_2 (mass%)
LB-204040-1	1.0	34.3	65.7	777	20	40	40
LB-204040-2	2.0	34.3	65.7	777	20	40	40
LB-204040-3	3.0	30.7	69.2	683	20	40	40
LB-204040-4	4.0	30.7	69.2	683	20	40	40
LB-204040-5	6.0	30.7	69.2	683	20	40	40
LB-105040-1	0.50	34.3	65.7	777	10	50	40
LB-105040-2	1.0	34.3	65.7	777	10	50	40
LB-105040-3	2.0	34.3	65.7	777	10	50	40
LB-105040-4	4.0	30.7	69.2	683	10	50	40
LB-105040-5	6.0	30.7	69.2	683	10	50	40
LB-105040-6	7.0	30.7	69.2	683	10	50	40
LB-106030-1	0.50	34.3	65.7	777	10	60	30
LB-106030-2	1.0	34.3	65.7	777	10	60	30
LB-106030-3	2.0	30.7	69.2	683	10	60	30
LB-106030-4	4.0	30.7	69.2	683	10	60	30

First, $CaCO_3$ was held in a tabletop small electric furnace at 1273 K for 12 h or more and calcined to produce CaO. Subsequently, Na_2CO_3, SiO_2, Na_2SiO_3, Na_4SiO_4, and calcined CaO were weighed, mixed, charged in a Pt crucible, and preliminarily melted in an ultra-high-speed heating melting furnace. Subsequently, the grains of Cu and Si, and powder of B were weighed and charged in a graphite crucible with a lid (outer diameter: 30 mm; inner diameter: 22 mm; depth: 35 mm) and were then preliminarily melted in a high-frequency induction furnace. In addition, 4 g of the pre-melted Cu–Si–B alloy and 8 g of the flux were charged in a graphite crucible and kept at 1473 K using an electric resistance furnace. An alumina tube (SSA-S) was used as the furnace tube, whose inside was filled using Ar gas. The Ar gas was de-carbonated and de-hydrated using soda lime, silica gel, and magnesium perchlorate, and was further deoxidized in a magnesium deoxidizing furnace. After holding the sample at 1473 K for a certain period, the crucible was quickly removed from the furnace and quenched using water. The alloy and flux were separated from the sample, and the concentrations of B in the alloy and flux were analyzed via ICP-OES.

Results and Discussion

3.1 Measuring the borate capacity of the CaO–Na_2O–SiO_2 flux

The equilibration experiments were conducted at 1473 K in an N_2 + CO mixed gas atmosphere, and the oxygen partial pressure and B activity were controlled using eqs. 4 and 5, respectively. We measured the BO_3^{3-} concentration in the flux after the experiment to determine $C_{BO_3^{3-}}$. The compositions of the flux after the experiment are listed in Table 2. One has the following:

$$\begin{aligned} &\mathrm{C}\,(graphite) + \tfrac{1}{2}\mathrm{O_2}(g) = \mathrm{CO}\,(g) \\ &\Delta G^\circ = -115{,}000 - 85.7\,T\ (\mathrm{J/mol}) \\ &K = \frac{P_{CO(g)}}{a_{C(gr)} \cdot P_{\mathrm{O_2}}^{1/2}} = \exp(-\Delta G^\circ / RT) \end{aligned} \tag{4}$$

$$\begin{aligned} &\mathrm{B}\,(l) + \tfrac{1}{2}\mathrm{N_2}(g) = \mathrm{BN}\,(s) \\ &\Delta G^\circ = -298{,}000 + 108\,T\ (\mathrm{J/mol}) \\ &K = \frac{a_{\mathrm{BN}(s)}}{a_{\mathrm{B}(l)} \cdot P_{\mathrm{N_2}}^{1/2}} = \exp(-\Delta G^\circ / RT) \end{aligned} \tag{5}$$

The relationship between the reaction time at 1473 K and the concentration of BO_3^{3-} in the flux is depicted in Fig. 2. The concentration of BO_3^{3-} in the flux increased with time and then decreased. The initial increase in the concentration of BO_3^{3-} might be because the reaction did not reach equilibrium, and the subsequent decrease was attributed to the decrease in the basicity of the flux because of the decomposition of Na_2O in the flux. The time at which the concentration of BO_3^{3-} in the flux became the maximum was defined as the equilibrium time, and the experimental results conducted for a longer time were

treated as $C_{BO_3}^{3-}$ for the flux composition after the experiment. The theoretical optical basicity Λ_{th}, expressed in eq. 6, is introduced. The term X_i denotes the molar fraction and Λ_i the optical basicity of component i. The values of Λ_i for each component[8] are listed in Table 3. In Fig. 3, we depict the relationship between the theoretical optical basicity calculated using the flux composition after the experiment and $C_{BO_3}^{3-}$, together with the reported value of $C_{BO_3}^{3-}$ for the CaO–SiO_2–CaF_2 based flux by Teixeira et al.[9]. The value of $C_{BO_3}^{3-}$ of the CaO–Na_2O–SiO_2 flux is generally greater than that of the CaO–SiO_2–CaF_2 flux, which has the same optical basicity as that of the former, and more effective B removal can be expected in the case of the former.

Table 2: Compositions of the flux after the experiment for measuring borate capacity.

ID	Time / h	CaO (mass%)	Na_2O (mass%)	SiO_2 (mass%)	BO_3^{3-} (mass%)
BN-204040-1	1.0	20.8	36.9	42.1	0.178
BN-204040-2	5.0	21.7	32.1	46.0	0.210
BN-204040-3	10	23.3	30.6	45.9	0.237
BN-204040-4	10	20.3	31.1	48.5	0.222
BN-204040-5	15	22.8	30.5	46.4	0.526
BN-204040-6	20	23.3	24.3	51.9	0.463
BN-204040-7	20	24.0	27.5	48.2	0.469
BN-204040-8	30	24.9	25.1	49.7	0.431
BN-204040-9	40	24.1	23.5	52.1	0.415
BN-105040-1	1.0	9.77	45.5	44.4	0.404
BN-105040-2	3.0	10.5	43.8	45.4	0.634
BN-105040-3	5.0	11.4	43.0	45.2	0.703
BN-105040-4	10	11.0	41.0	47.6	0.654
BN-105040-5	20	11.8	36.9	50.9	0.670
BN-105040-6	30	12.1	35.8	51.8	0.667
BN-105040-7	40	11.0	40.7	47.9	0.704
BN-105040-8	60	12.9	31.2	55.6	0.551
BN-106030-1	1.0	8.85	50.0	40.8	0.643
BN-106030-2	3.0	9.25	45.8	44.1	1.39
BN-106030-3	5.0	11.0	44.4	44.0	0.944
BN-106030-4	7.0	10.8	44.0	44.5	1.08

In addition, as the optical basicity increases, the value of $C_{BO_3}^{3-}$ exponentially increases, as expressed in eq. 7. One has the following:

$$\Lambda_{\mathrm{th}} = \Lambda_i X_i \tag{6}$$

$$\ln C_{\mathrm{BO_3^{3-}}} = 11.7\Lambda_{\mathrm{th}} + 33.4 \tag{7}$$

Table 3: Optical basicity of each component[8)]

I	Optical basicity, Λ_i
CaO	1.00
SiO_2	0.48
Na_2O	1.10

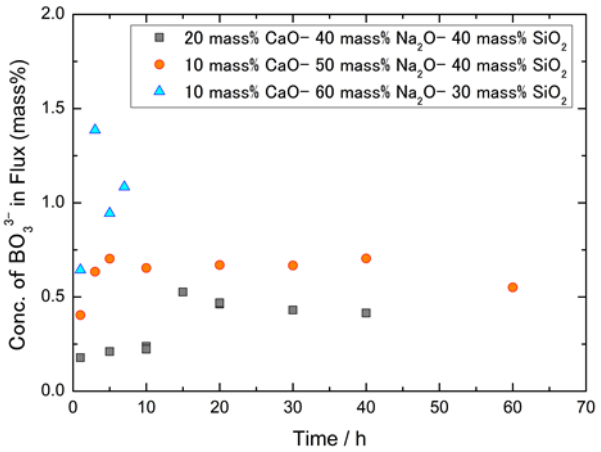


Figure 2: Relationship between experimental time and concentration of BO_3^{3-} in the flux.

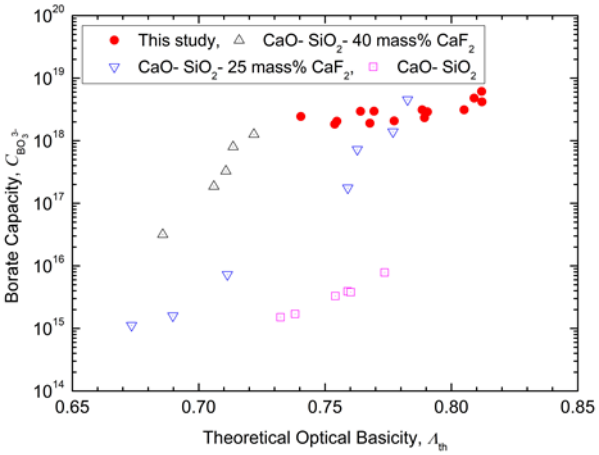


Figure 3: Relationship between theoretical optical basicity and borate capacity for the $CaO–Na_2O–SiO_2$ and $CaO–SiO_2–CaF_2$ flux systems.

To verify the validity of the theoretical optical basicity and relational expression of $C_{BO_3}^{3-}$, a comparison with the sulfide capacity (C_S^{2-}) of the Na_2O–SiO_2 based flux at 1473 K, as reported by Chan et al. [10], was conducted. Notably, C_S^{2-} is an index value for sulfur (S) removal in the slag refining of steel and is expressed using Eq. 9, which is based on the reaction shown in eq. 8. Within a similar range of optical basicity of the flux used in this experiment, C_S^{2-} can be represented as eq. 10 by using the theoretical optical basicity. One has the following:

$$\mathrm{S\ (in\ Fe)} + (\mathrm{O}^{2-}) = (\mathrm{S}^{2-}) + \tfrac{1}{2}\mathrm{O}_2(g) \quad (8)$$

$$C_{\mathrm{S}^{2-}} = \frac{(\mathrm{mass\%S}^{2-})\cdot P_{\mathrm{O}_2}^{3/4}}{P_{\mathrm{S}_2}^{1/2}} = \frac{K_{\mathrm{S}}\cdot a_{\mathrm{O}^{2-}}}{f_{\mathrm{S}^{2-}}} \quad (9)$$

$$\ln C_{\mathrm{S}^{2-}} = 6.00\Lambda_{\mathrm{th}} - 14.0 \quad (10)$$

Furthermore, eq. 11 can be derived from the definitional equations of capacity (eqs. 2 and 9) by cancelling the term $a_{O^{2-}}$ assuming that both composition dependences of activity coefficients, $f_{BO_3^{3-}}$ and $f_{S^{2-}}$, are negligible. On the other hand, eq. 12 can be derived from the experimental results represented by eqs. 7 and 10. One has the following:

$$\ln C_{\mathrm{BO}_3^{3-}} = 1.5 \ln C_{\mathrm{S}^{2-}} + A_1 \quad (11)$$

$$\ln C_{\mathrm{BO}_3^{3-}} = 1.95 \ln C_{\mathrm{S}^{2-}} + A_2 \quad (12)$$

Notably, eq. 11 is generally coincident with eq. 10. Therefore, the validity of the relational expression shown in eq. 6 between the theoretical optical basicity and $C_{BO_3}^{3-}$ of the CaO–Na_2O–SiO_2 flux was confirmed.

3.2 Measuring the activity coefficient of B in the molten Si–Cu–Sn alloy

In this experiment, on the basis of the reaction represented in Eq. 13, the chemical potentials of N and B are controlled by coexisting pure BN and Si_3N_4, whose activity is 1 on a solid basis. On the basis of the Si activity determined using the alloy composition and Eq. 14, the B activity in the Si–Cu-based alloy was uniquely determined. Using the concentration of B in the alloy after the experiment, a liquid-based activity coefficient of B in the alloy was calculated. Because there is no literature value of the activity of Si in the Si–Cu–Sn ternary alloy ($\gamma_{\mathrm{Si(SiCuSn)}}$), it was calculated using a regular solution model, as shown in eq. 15, on the basis of the literature value of the binary systems of Si-Cu[11], Si-Sn[11], and Cu-Sn[12]. The terms $\gamma_{\mathrm{Si(SiCu')}}$ and $\gamma_{\mathrm{Si(SiSn')}}$ represent the activity coefficients of Si in the Si–Cu alloy and Si–Sn alloy, respectively. In addition, $\mathrm{SiCu'}$, $\mathrm{SiSn'}$, and $\mathrm{Cu''Sn''}$ denote the compositions depicted in Fig. 4. The term $\Delta G_{mix}^{xs}(\mathrm{Cu''Sn''})$ represents the excess

Gibbs energy of the mixture of Cu and Sn. It was calculated using eqs. 16, 17, 18, and 19[12]. One has the following:

$$\mathrm{B}(l)_{\text{in alloy}} + 1/4\,\mathrm{Si_3N_4}(s) = \mathrm{BN}(s) + 3/4\,\mathrm{Si}(l) \quad (13)$$

$$\Delta G^\circ = -RT\ln\frac{a_{\mathrm{BN}(s)}\cdot {a_{\mathrm{Si}(l)\text{ in alloy}}}^{3/4}}{a_{\mathrm{B}(l)\text{ in alloy}}\cdot {a_{\mathrm{Si_3N_4}(s)}}^{1/4}} = -RT\ln\frac{{a_{\mathrm{Si}(l)\text{ in alloy}}}^{3/4}}{a_{\mathrm{B}(l)\text{ in alloy}}} \quad (14)$$

$$\Delta G^\circ = -82{,}800 + 5.82T \ \ (\mathrm{J/mol})$$

$$\log\gamma_{\mathrm{Si(SiCuSn)}} = \frac{x_{\mathrm{Cu}}}{x_{\mathrm{Cu}}+x_{\mathrm{Sn}}}\log\gamma_{\mathrm{Si(SiCu')}} + \frac{x_{\mathrm{Sn}}}{x_{\mathrm{Cu}}+x_{\mathrm{Sn}}}\log\gamma_{\mathrm{Si(SiSn')}} - (1-x_{\mathrm{Si}})^2\frac{\Delta G^{xs}_{mix}(\mathrm{Cu''Sn''})}{4\cdot 575T} \quad (15)$$

$$\Delta G^{xs}_{mix} = X_{\mathrm{Cu}}X_{\mathrm{Sn}}\{\,{}^0L + {}^1L(X_{\mathrm{Cu}} - X_{\mathrm{Sn}}) + {}^2L(X_{\mathrm{Cu}} - X_{\mathrm{Sn}})^2\} \quad (16)$$

$${}^0L = -8266.6 - 6.9973T \quad (17)$$

$${}^1L = -21662.0 + 8.4655T \quad (18)$$

$${}^2L = -26957.2 + 12.8887T \quad (19)$$

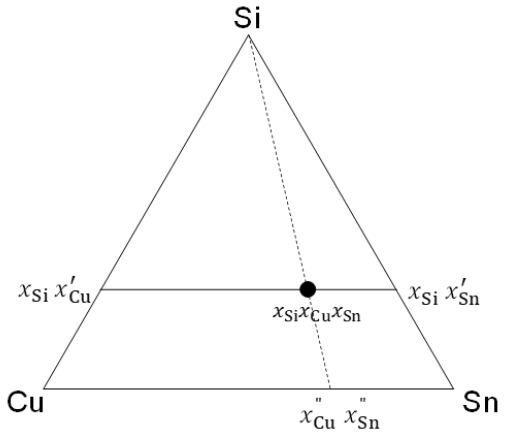


Figure 4: Composition of the Si–Cu–Sn ternary alloy referred to in eq. 15.

The experiments were performed at various reaction times using a Si-10 mass% Cu-60 mass% Sn alloy. The concentration of B in the alloy became constant after approximately 24 h. Therefore, the reaction time was determined to be 24 h or more in this experiment. The relationship between the composition of the Si–Cu–Sn alloy and obtained γ_{B} is depicted in Fig. 5. Particularly, especially high γ_{B} was obtained in the alloy with high concentration of Cu and 0–10 mass% Sn. This value is greater than that in the Si–Sn alloy when compared with the same mass concentration of Si, and it is considered a more appropriate solvent for flux treatment. Furthermore, the liquidus temperature of 24 mass% Si–65 mass% Cu–11 mass% Sn, in which the highest γ_{B} was obtained, was calculated to be approximately 1373 K using FactSage. Therefore, a solvent purification process at lower temperatures can be realized.

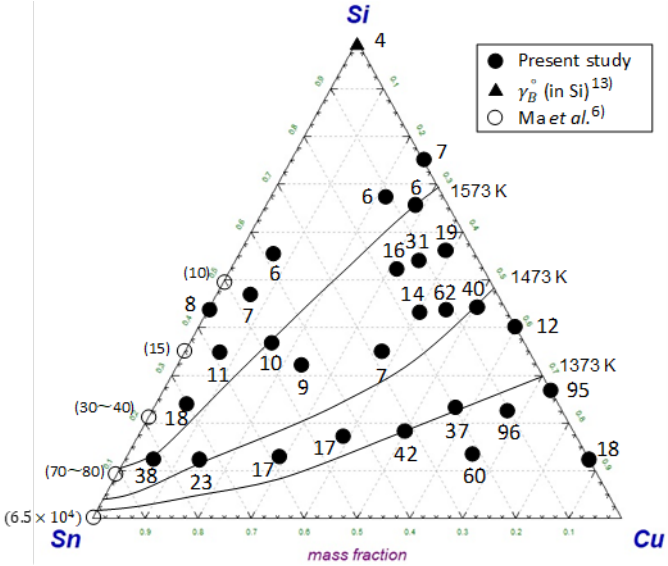


Figure 5: Relationship between the Si–Cu–Sn alloy composition and γ_B.

The temperature dependence of γ_B in two alloy compositions, i.e., 24 mass% Si–65 mass% Cu–11 mass% Sn and 27 mass% Si–73 mass% Cu, is depicted in Fig. 6. In addition, eq. 20 was obtained for the former composition. In both the compositions, it was confirmed that γ_B increased with decrease in the temperature. Therefore, both lowering the temperature of the process and increasing the efficiency of B removal might be achieved. One has the following:

(24 mass%Si–65 mass%Cu–11 mass%Sn)

$$\ln \gamma_{B(l)} = \frac{5.4(\pm 2.5)\times 10^3}{T} + 1.3(\pm 1.6) \quad (1473\ \mathrm{K} - 1673\ \mathrm{K}) \qquad (20)$$

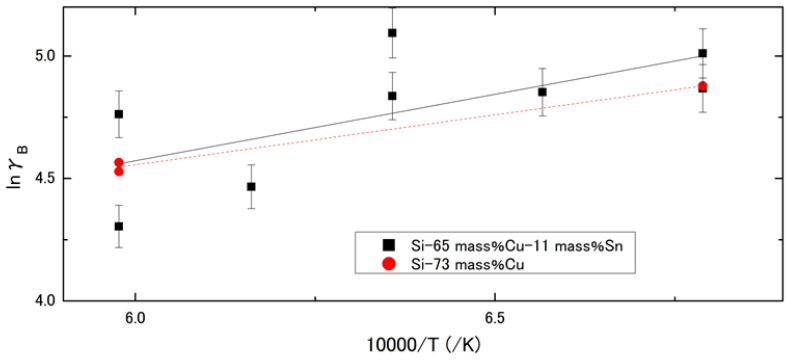


Figure 6: Temperature dependence of γ_B in the Si–Cu–Sn alloy.

3.3 B removal from the Si–Cu alloy

The compositions of the alloy and flux after the experiment are listed in Table 4. The relationship between the reaction time at 1473 K, and the concentration of B in the alloy and that of BO_3^{3-} in the flux is depicted in Fig. 7. Similar to the measurement of the borate capacity, experiments were performed for a longer time than that of the experiment in which the concentration of BO_3^{3-} in the flux reached maximum was treated as an equilibrium value, and L_B was calculated. Consequently, when the 10 mass% CaO–60 mass% Na_2O–30 mass% SiO_2 flux (initial composition) was equilibrated for 4 h, the highest L_B, i.e., 7.92, was obtained.

Table 4: Compositions of the alloy and flux after the experiment for measuring the B partition ratio .

ID	Time / h	Metal			Flux			
		Si (mass%)	Cu (mass%)	B (ppmw)	CaO (mass%)	Na_2O (mass%)	SiO_2 (mass%)	BO_3^{3-} (mass%)
LB-204040-1	1.0	36.8	63.2	34.3	19.0	26.4	54.5	0.0282
LB-204040-2	2.0	33.9	66.1	32.3	20.9	27.8	51.2	0.0317
LB-204040-3	3.0	32.8	67.2	24.2	21.3	27.9	50.8	0.0514
LB-204040-4	4.0	33.2	66.7	32.8	21.0	27.2	51.8	0.0623
LB-204040-5	6.0	31.7	68.3	28.6	23.3	23.2	53.4	0.0555
LB-105040-1	0.50	34.6	65.4	20.4	10.1	36.7	53.2	0.0672
LB-105040-2	1.0	32.7	67.3	20.1	9.30	36.3	54.4	0.0686
LB-105040-3	2.0	33.1	66.9	20.6	10.6	35.1	54.2	0.0758
LB-105040-4	4.0	34.4	65.6	25.3	10.3	32.1	57.6	0.0939
LB-105040-5	6.0	30.4	69.6	16.5	11.7	30.0	58.2	0.0588
LB-105040-6	7.0	34.3	65.7	18.1	10.7	29.3	60.0	0.0335
LB-106030-1	0.50	30.7	69.3	17.5	9.61	37.5	52.9	0.0396
LB-106030-2	1.0	30.4	69.6	17.0	10.3	34.2	55.5	0.0597
LB-106030-3	2.0	27.9	72.1	25.0	10.9	35.1	53.9	0.0992
LB-106030-4	4.0	27.9	72.1	14.7	10.1	33.1	56.7	0.0632

Fang et al.[14] reported that by conducting solidification refining using Si–Cu alloys, approximately 45% of B could be removed. Therefore, by adding Cu to MG-Si with the initial B concentration of 30 ppmw to form molten Si–Cu alloy, subjecting it to the 10 mass% CaO–60 mass% Na_2O–30 mass% SiO_2 flux, and conducting solidification refining, the concentration of B might be lowered to less than 1 ppmw. However, the

allowable concentration of B in SOG-Si is 0.3 ppmw, and the expected B removal effect could not be confirmed.

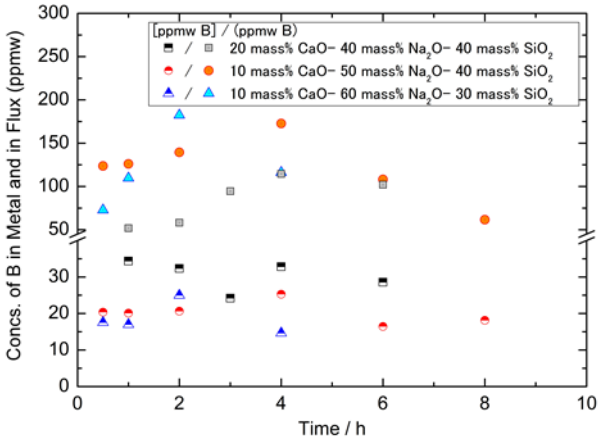


Figure 7: Relationship between experimental time, and concentrations of B in the alloy and B in flux.

Conclusions

(1) The borate capacity of the CaO–Na_2O–SiO_2 flux was measured to evaluate the B-absorption ability of the flux from a thermodynamic point of view. Consequently, for the same theoretical optical basicities, the CaO–Na_2O–SiO_2 flux had higher borate capacity than that of the CaO–SiO_2–CaF_2 flux.

(2) To evaluate the thermodynamic instability of B in the Si–Cu–Sn alloy, the relationship between the activity coefficient of B and alloy composition was investigated. Consequently, at a composition with high Cu concentration and 0–10 mass% Sn, the activity coefficient of B was dramatically increased and high B removal efficiency was expected. Furthermore, because the activity coefficient of B had a negative temperature dependency, the B-removal efficiency might be further improved by lowering the temperature of the flux treatment.

(3) To confirm the effect of B removal using the CaO–Na_2O–SiO_2 flux, the equilibrium with Si–Cu alloy and measurement of the distribution ratio of B were performed. The obtained distribution ratio was 7.92 at the maximum, and although the Si–Cu alloy was not more effective for B removal than the Si–Sn alloy, it was indicated that a reasonable flux treatment at low temperature could be realized.

References

1) K. Morita *et al.*: *Intermetallics*, **11** (2003), 1111.
2) K. Morita *et al.*: *Trans. Nonferrous Met. Soc. China*, **21** (2011), 685.
3) D. Jiang *et al.*: *J. Electron Mater.*, **43** (2014), 314.
4) L. A. V. Teixeira *et al.*: *ISIJ int*., **49** (2009), 777.
5) T. Yoshikawa *et al.*: *ISIJ Int*., **45** (2005), 967.
6) X. D. Ma *et al.*: *J. Alloy Compd*., **529** (2012), 12.
7) X. D. Ma *et al.*: *Metall. Mater. Trans. B*, **44** (2013), 528.
8) J. A. Duffy: *Phys. Chem. Glasses B*, **49** (2008), 202.
9) L. A. V. Teixeira *et al.*: *ISIJ Int*., **49** (2009), 783.
10) A. H. Chan *et al.*: *Metall. Trans. B*, **17** (1986), 491.
11) J. Safarian *et al*.: *J. Mater. Sci.*, **47** (2012), 5561.
12) M. Li *et al*.: *J. Alloy. Compd.*, **477** (2009), 104.
13) T. Yoshikawa *et al*.: *Mater. Trans.*, **46** (2005), 1335.
14) M. Fang *et al.*: *Mater. Sci. Technol.*, **29** (2013), 861.

Silicon for the Chemical and Solar Industry XV
Trondheim, Norway, June 15 – 18, 2020

Phosphorus and Boron removal from Si by vacuum and gas refining processes

Arman Hoseinpur, Gabriella Tranell, Jafar Safarian
Department of Materials Science and Engineering, Norwegian University of Science and Technology (NTNU), 7034 Trondheim, Norway.
Norwegian Center for Sustainable Solar Cell Technology (www.susoltech.no), Norway.

Abstract

Solar energy production by crystalline Si-based PV panels is increasing and hence, sustainable production of Solar grade Silicon (SoG-Si) is required for green growth of the PV sector. Metallurgical methods for Si refining have been under research and development in the recent decades due to their lower energy consumption and pollution compared to the chemical processes. This research introduces the combination of Vacuum and Gas (VG) refining processes as a new procedure for production of SoG-Si from MG-Si. In this research a Si melt with an initial phosphorus and boron concentrations about 10 ppmw has been refined by vacuum and gas refining process to the below 1 ppmw. Vacuum refining was carried out at 1750 °C, while the gas refining was performed at 1500 °C by blowing humidified hydrogen gas over the melt surface. During the refining process, several samples were taken from the melt to investigate the concentration change of the impurities over the refining time. Immediately after the refining step, the melt was unidirectionally solidified to remove all the remaining impurities from the solidification front. The results show that the VG process can produce SoG-Si at the molten state of Si.

1. Introduction

Silicon (Si) production for photovoltaic applications is of high demand due to the energy production by solar panels [1]. The Si used in solar panels must have a purity of 99.9999 (6N), which is for short called solar grade silicon (SoG-Si) [2]. However, the major part of solar Si panels is still being produced from the electronic grade silicon (EG-Si) with higher purity, i.e. 8-12N purity, this material is also called polysilicon. It could be

produced by chemical routes like the Siemens® and FBR® technologies. Metallurgical methods for production of SoG-Si were introduced in early 2000 and currently at least three of them are in industrial level or tested in large scale [3–5]. These methods are more energy efficient and environmentally friendly for SoG-Si production. A summary for the clean Si production could be found in the Fig (1) where the timeline for various methods leading to production of SoG-Si and EG-Si are shown. The research millstones in the field are mentioned above the timeline and the technological millstones are all mentioned below the timeline. As shown in Fig (1) Si was refined by the zone melting method for the first time in 1955 at the Bell's lab [6] for semiconductor applications. Then the Siemens® technology started the production of EG-Si, and FBR® added to the market in early 2000. Elkem solar® started the first metallurgical plant for refining the MG-Si to SoG-Si in 2007 by a process containing slag refining and leaching processes. Silicor Materials started pilot production of SoG-Si in 2009 by solvent refining of Si by Al addition-solidification, and a subsequent leaching process. The last metallurgical method added to the market is the Ferroglobe® (silcio ferro solar) technology which produces the solar silicon by slag and vacuum refining. The Japanese technology started by Kawasaki steel® in the early 1990s, known as the NEDO process in the literature, stopped in the pilot scale and never led to industrial productions due to its high energy consumption. All of the metallurgical methods are consisted of two steps of refining before the last ingot production.

The research on vacuum – gas refining of silicon initiated in NTNU since 2008 [7–10]. Until now many investigations on the vacuum refining for P removal and gas refining for B removal [11–14] from the Si have been done. Throughout investigations in these separate vacuum and gas refining experiments several parameters are studied for improving the kinetics of the both processes. In the vacuum refining experiments, many parameters are studied, such as; effect of temperature, pressure, and Al addition to the melt [15]. The results of vacuum refining of Si-Al melts for removing of P is published in [15,16], where we showed Al has a positive kinetic effect on P evaporation from Si. Moreover, some parameters for gas refining of Si for B removal purposes have been studied in literature such as temperature, crucible material, gas composition, humidity content of gas [13,17]. In our recent studies, we investigated each process separately to get an insight into the effect of key process parameters. Like the effect of temperature where we have investigated the P evaporation from Si over the temperature range of 1500 – 1900 °C, to discuss the kinetics of P evaporation from Si. In this type of experiments the Si material was subjected to the vacuum refining or the gas refining process separately. This research reports the first combined Vacuum and Gas refining processes in lab scale.

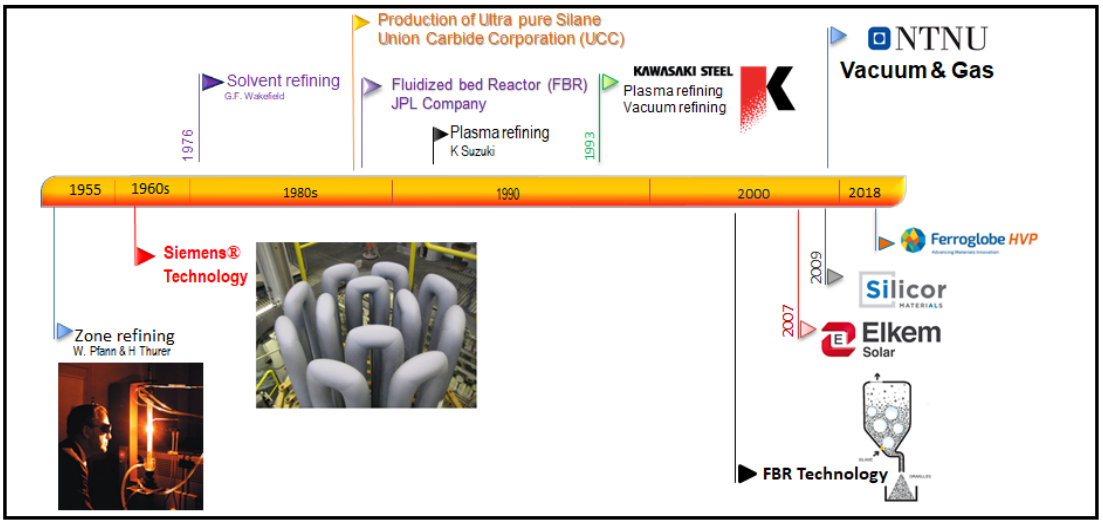


Figure 1. The timeline of the evolution for clean Si production; research millstones are presented above the line and the commercial routes are shown at the bottom of the timeline.

2. Experimental procedure

In this research we used a mixture of a commercial grade silicon (HQ-Silgrain®) with the purity of 99.76% and FBR® silicon as the initial materials. An induction furnace able to work in vacuum and Ar atmosphere was applied to do the refining experiments. For the vacuum refining of Si, two types of experiments are done in this research. The schematic representation of the furnace and the experiment setup for all the steps in the VG process are shown in the Fig (2). The inner graphite crucible shown in Fig (2) has an outer diameter of 60 mm and it is charged by the silicon mixture. The inner crucible is in a bigger crucible with the outer diameter of 85 mm and a thermocouple (type C) is between the inner crucible and the outer one. The thermocouple is in an alumina tube to be protected of carburation during the experiment. The whole setup was wrapped by graphite felt and mica sheet for safety issues and then it was put in the copper coil. Before starting the experiment, the chamber was flushed by He (5.5 N) three times. Each time the chamber was vacuumed completely and subsequently it was filled with He up to 1000 mbar. Subsequently, the heating process was started in He atmosphere while flushing it by He continually during the experiment and keeping the pressure in the range of 1040-1050 mbar. Subsequently, the power was switched on and the temperature was increased. After melting the Si the temperature was set on 1750 °C and the chamber was vacuumed to start the vacuum refining process. The vacuum pump was on during the vacuum refining process for vacuuming the chamber continuously. During the refining process some samples were taken from the melt to trace the P concentration change by time. After vacuum refining, the gas refining process was started by blowing H_2-3% H_2O gas over the melt surface. For this purpose, Hydrogen (H_2, 5.5N) was humified with 3% H_2O and was blown over the melt with 3 standard liter per minute (SLM).

The vacuum refining at 1750 °C (Fig 3a) was done for 300 minutes, followed by the B removal process carried out with the H_2-3% H_2O gas (Fig 3b). The previous researchers investigated various mixtures of the gases, and among all the gas mixtures, it is shown that the H_2 humidified with 3% H_2O had the greatest extent of boron removal. After 100 min of the gas refining experiment, the gas blowing was stopped and then the directional solidification, as shown schematically in Fig. (3c) was started. For this purpose, the temperature of the crucible was decreased down to 1450 °C, and then Ar was blown to the bottom of the graphite crucible from a 2 mm nuzzle with 1 SLM flowing rate. At the end of the gas refining process, the melt was unidirectionally solidified by the help of blowing Ar to the bottom of the crucible and after solidification, the sample was cooled down rapidly to room temperature. The samples taken from the melt were digested and then characterized by Induction coupled plasma mass spectroscopy (ICP-MS, Agilent - 8800 ICP-MS Triple Quad).

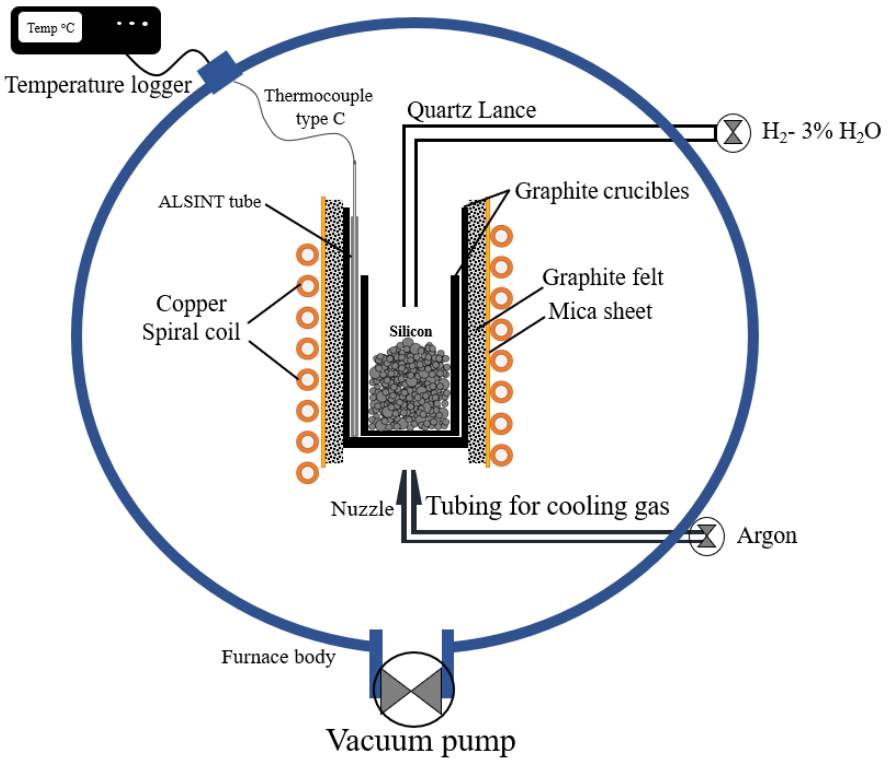


Figure 2. A schematic representation of the setup assembly used for the combined vacuum-gas-directional solidification experiment (for before starting the process). It shows all the devises on the furnace required to do the refining and their positions.

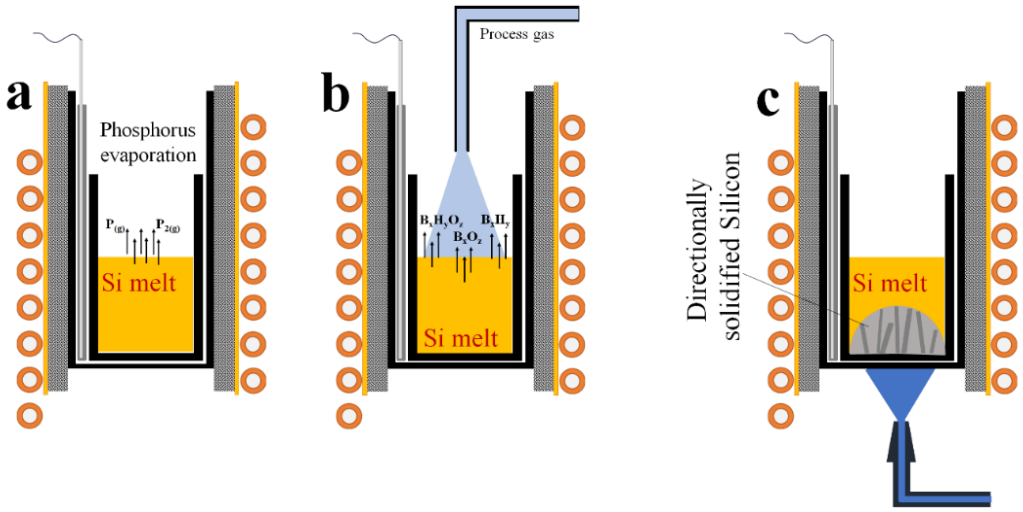


Figure 3. A schematic of the VG refining process applied in this research. (a): P removal by vacuum refining, (b): B removal from Si by Gas refining, (c): directional solidification to produce the Si ingot.

3. Results and discussions

Here, we firstly presented the experimental results from the VG process in section 3.1., then we continue to discuss the kinetics of the process in section 3.2 and at the end, the VG process will be compared from the energy consumption and process flexibilities with the other metallurgical routes in the section 3.3.

3.1. Experimental results

During the VG process, the crucible was pictured from above, and the images are all given in Fig (4). The image of the crucible during the melting is presented in Fig (4a) where the solid particles of Si could still be seen in the Si melt. Fig (4b) shows the crucible's image in the vacuum refining at 1750 °C. Fig (4c) represents the crucible image during the gas refining indicating the formation of silica fume around the crucible. Fig (4d) represents the crucible after the gas refining process and at the beginning of the solidification step. By comparing Fig (4c) with Fig (4d) it can be seen that the precipitated dust is grown over time of gas refining. Figure (4f) shows the crucible image after the solidification step. A comparison of the Figs (4e and 4f) reveals that the solidification took place successfully, and the melt has been solidified from the bottom to the surface, leaving the tail on the solidified Si surface center at the end of solidification. Figure (5) depicts the lance applied during the gas refining, and the dust precipitated on it. This dust is silica and is already investigated in [18] by SEM characterizations. This fine powder is called silica fume and has industrial applications in cement industries [19,20]. This compound is the result of oxidation of Si melt to $SiO_{(g)}$ and the subsequent oxidation $SiO_{(g)}$ to $SiO_{2(s)}$ in the gas phase. The following reactions could be suggested for the formation of this compound:

$$Si_{(l)} + H_2O_{(g)} = 2\underline{H} + SiO_{(g)} \quad (1)$$
$$SiO_{(g)} + H_2O_{(g)} = SiO_{2(g)} + H_{2(g)} \quad (2)$$

Where $\underline{H}$ is dissolved hydrogen in the Si melt [13,17]. The thermodynamics of the system was studied previously [12,13,17]. The samples were taken from the melt during the refining processes were characterized by ICP-MS and the results are shown in Table (1). According to the Table 1, boron is reduced from 11.76 to 0.9 ppmw after 100 minutes of the gas refining in the conditions of the current study. Inserting the data of the B concertation in melt to the 1st order reaction model, one can obtain the rate constant of boron removal to be $k_B = 17.33$ μm·s^{-1}. The P concertation change by the time of vacuum refining is also presented in Table 1. If we insert the data of the P concertation in the 1st order reaction model the P removal rate constant of $k_p = 7$ μm·s^{-1} is obtained. However, considering the previous researches it was supposed to get the k_p about 20 – 25 μm·s^{-1} at 1750 °C. The main reason for this discrepancy is the lack of melt stirring by the induction force in the setup used in this experiment as the mass transport in the melt may become important at the applied experimental temperature. When there are two crucibles in the coil, the electromagnetic field is mainly absorbed by the crucibles and it is weak for stirring the melt effectively in the inner crucible. Thus, the diffusion of P through a melt boundary layer could become the controlling step of the vacuum refining process. Fig (6) represents the image of the crucible and the Si ingot cut in half after the final directional solidification. The crystals of the Si are directionally solidified from the bottom to the top, indicating the success of the process.

Table 1. The P and B concentrations in Si melt characterized by ICP-MS.

Refining time [minute]	**0**	**30**	**65**	**100**	**110**	**200**
B [ppmM] in the gas refining	11.76	6.65	2.10	0.90	-	-
P [ppmM] in the vacuum refining	8.97	-	3.78	-	2.46	0.81

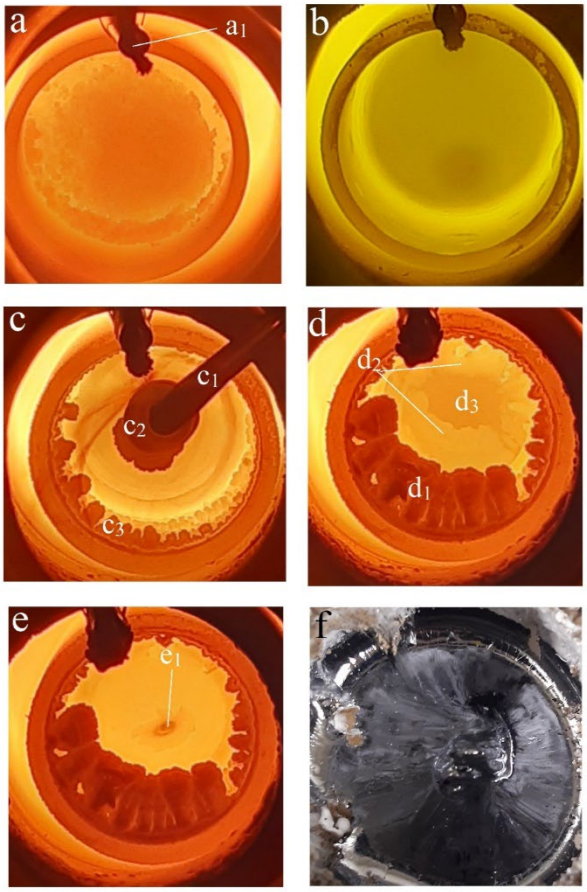


Fig (4). The pictures from the crucible during the experiment. (a): melting step, (b)vacuum refining. (c) after 30 min of gas refining, (d): during the solidification, (e): the end of the solidification, (f): solidified ingot from above. The notes; a_1: thermocouple, c_1: quartz lance, c_2: precipitated dust on the lance, c_3: dust precipitating around the crucible edge, d_1: the dust precipitated on the crucible top by the end of gas refining process (around 8 cm above the melt surface, see Fig 6), d_2: Si crystals growing from the bottom and around the crucible toward the surface of melt, d_3: the remained Si to be solidified, e_1: the last part of the melt just before the end of solidification.

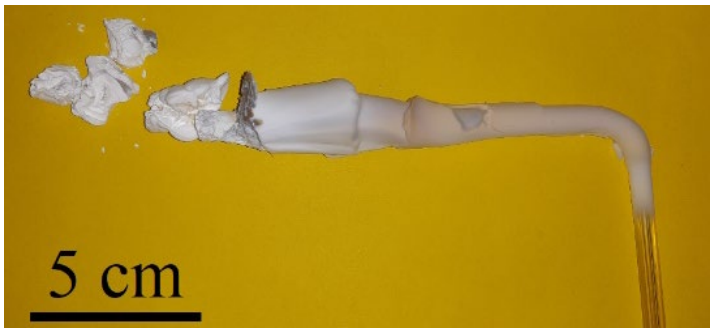


Figure 5. The quartz lance applied for blowing the H2-3%H_2O gas over the melt during the gas refining.



Figure 6. The image of the directionally solidified silicon from bottom to the top after vacuum-gas refining.

3.2. Kinetics of VG refining process

In all industrial processes for metal production and refining, the kinetics of the process plays an important role and has a great impact on the economic efficiency of the process. Here we will discuss the kinetics and the energy consumption of the VG process for refining of the silicon with regard to the results we obtained from the vacuum refining and gas refining in separate processes.

Temperature is an important parameter having a great impact on the rate of phosphorus removal and hence the required time for doing the vacuum refining. The effect of temperature is already discussed in [8,9,21,22]. Safarian et al. [8,23] have already discussed the kinetics of P removal in the same furnace and crucible type that we applied for the combined experiment presented in this paper.

The B removal from Si by humidified gas refining has been investigated in literature, and various parameters like various mixtures of the gases, Ar-H_2O, H_2-H_2O,He-H_2O [11–13,24,25], and temperatures, in addition to studying the gas flow rate, lance nuzzle diameter, and lance distance from the melt surface. The highest rate constant for B removal is reported for the H_2-3% H_2O [12,13] gas. Here, we employ the rate constant for the B removal to do the energy consumption calculations. The rate of boron removal could be obtained by various combinations of the parameters in gas the refining process.

The studies on empirical kinetics of P removal from Si by evaporation [8,9,21,22] and B removal from Si by gas refining [12,17] show that for both of the processes the 1st order kinetic model could precisely fit to the P removal from Si, presented as follows;

$$\ln(\frac{C_{\underline{i},0}}{C_{\underline{i},t}}) = k_i \,.\left(\frac{A}{V}.t\right) \qquad (3)$$

Where $C_{\underline{i},0}$ and $C_{\underline{i},t}$ show the initial and instant concentrations of element i (B or P) in the melt, A and V are the melt surface area and volume, respectively. By inserting the experimental data obtained from the refining experiments, presented in Table 1, into the equation (3), the rate constants for the P removal (k_P) and B removal (k_B) processes could be calculated as $k_P = 7$ μm·s^{-1} and $k_B = 17.3$ μm·s^{-1}.

Having the k_B and k_P, one can obtain the required time for doing the vacuum and gas refining processes to obtain the SoG-Si by vacuum and gas refining processes;

$$t_{VR}\ [h] = \frac{1}{k_P \,.\, \frac{A}{V} .\ 3600} \,.\ \ln(\frac{C_{\underline{P},0}}{C_{\underline{P},t}}) \qquad (4)$$

$$t_{GR}\ [h] = \frac{1}{k_B \,.\, \frac{A}{V} .\ 3600} \,.\ \ln(\frac{C_{\underline{B},0}}{C_{\underline{B},t}}) \qquad (5)$$

Where t_{VR} and t_{GR} are the required time of doing the vacuum or gas refining in hours. By considering the limit of 0.2 ppmw in SoG-Si for B and P and inserting the $C_{\underline{i},t} = 0.2$ into equation (4), the required time to get SoG-Si from different initial concentrations of B and P could be calculated as it is presented in Fig (7). This figure shows that by increasing the rate constant the required time of the process decreases intensively. The result from the vacuum and gas refining experiment done in this research is also marked on the Fig (7). It is worth to mention that, one can obtain the total time of the VG process to reach SoG-Si thorough the following equation:

$$t_{SoG-Si} = t_{VR} + t_{GR} \qquad (6)$$

Where t_{SoG-Si} denotes the total required time to carry out the VG process to reach to the solar grade silicon grade.

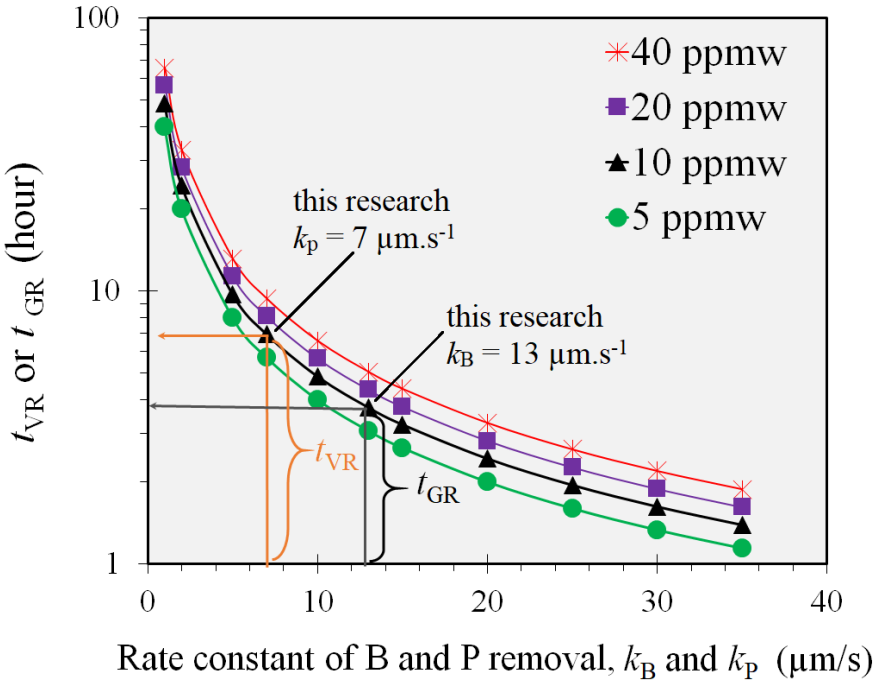


Figure 7. (a): Required time for the VG process over various k_P and k_B and calculated for different initial concentrations of P and B in melt, calculations are done by the assumption of A/V =24.68m^{-1}.

Conclusions

This research introduced the first lab-scale combined vacuum-gas refining process as a method for the production of solar- grade silicon, and the main points of the research are as follows;

- Vacuum refining of Si was performed at 1750 °C, and phosphorus concentration in the melt reduced from 8.97 to 0.91 in 200 minutes.
- Gas refining was performed with H_2 - 3% H_2O gas at 1500 °C, leading to a reduction of boron from 11.57 to 0.90 in 110 minutes.
- After the vacuum and gas refining, the Si was solidified directionally in the crucible.
- The required time to do the vacuum and gas refining to reach SoG-Si were discussed.

References

[1] D.S. Philips, W. Warmuth, Photovoltaics report, Fraunhofer ISE. (2016) 1–43. doi:10.1016/j.compedu.2008.05.004.

[2] H. Chen, K. Morita, X. Ma, Z. Chen, Y. Wang, Boron removal for solar-grade silicon production by metallurgical route:A review, Sol. Energy Mater. Sol. Cells. 203 (2019) 110169. doi:10.1016/j.solmat.2019.110169.

[3] www.silicormaterials.com, (n.d.). https://www.silicormaterials.com/.

[4] A. Murgau, J. Safarian, solar silicon production through metallurgical route and REC solar advancements, in: Silicon Chem. Sol. Ind., Avolvær, 2018: pp. 18–192.

[5] Forniés, Ceccaroli, Méndez, Souto, Pérez Vázquez, Vlasenko, Dieguez, Mass Production

Test of Solar Cells and Modules Made of 100% UMG Silicon. 20.76% Record Efficiency, Energies. 12 (2019) 1495. doi:10.3390/en12081495.
[6] M.D. Johnston, L.T. Khajavi, M. Li, S. Sokhanvaran, M. Barati, High-Temperature Refining of Metallurgical-Grade Silicon: A Review, JOM. 64 (2012) 935–945. doi:10.1007/s11837-012-0384-3.
[7] B.S. Xakalashe, Removal of Phosphorus from Silicon Melts by Vacuum, Norwegian University of Science and technology (NTNU), 2011.
[8] J. Safarian, M. Tangstad, Kinetics and Mechanism of Phosphorus Removal from Silicon in Vacuum Induction Refining, High Temp. Mater. Process. 31 (2012) 73–81. doi:10.1515/htmp.2011.143.
[9] J. Safarian, M. Tangstad, Vacuum Refining of Molten Silicon, Metall. Mater. Trans. B. 43 (2012) 1427–1445. doi:10.1007/s11663-012-9728-1.
[10] J. Safarian, K. Tang, K. Hildal, Vacuum treatment of ferrosilicon, in: 2015 Sustain. Ind. Process. SUMMIT, 2015: pp. 261–268.
[11] Ø.S. Sortland, M. Tangstad, Boron Removal from Silicon Melts by H2O / H2 Gas Blowing : Mass Transfer in Gas and Melt, Metall. Mater. Trans. E. 1 (2014) 211–225. doi:10.1007/s40553-014-0021-x.
[12] J. Safarian, C. Sanna, G. Tranell, Boron removal from silicon by moisturized gases Jafar, in: 33rd Eur. Photovolt. Sol. Energy Conf. Exhib. boron, 2016: pp. 476–479.
[13] J. Safarian, K. Tang, K. Hildal, G. Tranell, Boron Removal from Silicon by Humidified Gases, Metall. Mater. Trans. E. 1 (2014) 41–47. doi:10.1007/s40553-014-0007-8.
[14] D.G. Eskin, Ultrasonic degassing of liquids, Elsevier Ltd., 2014. doi:10.1016/B978-1-78242-028-6.00020-X.
[15] A. Hoseinpur, K. Tang, J. Safarian, Kinetic study of vacuum evaporation of elements from ternary melts; case of dilute solution of P in Si-Al melts, Sep. Purif. Technol. 235 (2020) 116284. doi:10.1016/j.seppur.2019.116284.
[16] A. Hoseinpur, J. Safarian, Phosphorus removal from Al-doped silicon by vacuum refining, in: 35th Eur. Photovolt. Sol. Energy Conf. Exhib. Phosphorus, Bruxel, 2018: pp. 469–472. doi:10.4229/35thEUPVSEC20182018.
[17] J. Safarian, K. Tang, J.E. Olsen, S. Andersson, G. Tranell, K. Hildal, Mechanisms and Kinetics of Boron Removal from Silicon by Humidified Hydrogen, Metall. Mater. Trans. B. 47 (2016) 1063–1079. doi:10.1007/s11663-015-0566-9.
[18] O.S. Sortland, Boron removal from silicon by steam and hydrogen, NTNU, 2015.
[19] M.K. Næss, G. Tranell, J.E. Olsen, N.E. Kamfjord, K. Tang, Mechanisms and Kinetics of Liquid Silicon Oxidation During Industrial Refining, Oxid. Met. 78 (2012) 239–251. doi:10.1007/s11085-012-9303-9.
[20] H. Vikan, H. Justnes, Rheology of cementitious paste with silica fume or limestone, Cem. Concr. Res. 37 (2007) 1512–1517. doi:10.1016/j.cemconres.2007.08.012.
[21] S.S. Zheng, W.H. Chen, J. Cai, J.T. Li, C. Chen, X.T. Luo, Mass transfer of phosphorus in silicon melts under vacuum induction refining, Metall. Mater. Trans. B Process Metall. Mater. Process. Sci. 41 (2010) 1268–1273. doi:10.1007/s11663-010-9422-0.
[22] S. Shi, P. Li, J. Meng, D. Jiang, Y. Tan, H.M.N. ul H.K. Asghar, Kinetics of volatile impurity removal from silicon by electron beam melting for photovoltaic applications, Phys. Chem. Chem. Phys. 19 (2017) 28424–28433. doi:10.1039/C7CP05080A.

[23]J. Safarian, L. Kolbeinsen, M. Tangstad, Thermodynamic activities in silicon binary melts, J. Mater. Sci. 47 (2012) 5561–5580. doi:10.1007/s10853-012-6449-4.
[24]E.F. Nordstrand, M. Tangstad, Removal of boron from silicon by moist hydrogen gas, Metall. Mater. Trans. B Process Metall. Mater. Process. Sci. 43 (2012) 814–822. doi:10.1007/s11663-012-9671-1.
[25]N. Nakamura, H. Baba, Y. Sakaguchi, S. Hiwasa, Y. Kato, Boron Removal in Molten Silicon with Steam Added Plasma Melting Method Naomichi, J. Japan Inst. Met. 67 (2003) 583–589.

Silicon for the Chemical and Solar Industry XV
Trondheim, Norway, June 15 – 18, 2020

The effect of Ti and Y addition on the microstructure and leaching purification of Ca-alloyed metallurgical silicon

Mengyi Zhu[1)], Kai Tang[2)], Jafar Safarian[1)]

1) *Department of Materials Science and Engineering, Norwegian University of Science and Technology (NTNU), No-7491 Trondheim, Norway*
2) *SINTEF Materials and Chemistry, No-7491 Trondheim, Norway*

Abstract

Metallurgical-grade silicon (MG-Si) purification through metal alloying combined with acid leaching is a feasible technique with low-cost and low energy consumption features. To improve the impurities removal efficiency, especially for the removal of B and P, the present work was carried out to study the effects of Ti and Y addition on the impurities removal in acid leaching of Ca-doped silicon. Commercial MG-Si was mixed with 4 wt% reagent grade Ca and specific amounts of Ti or Y. The mixture was then melted, and then was slowly solidified and cooled down. Obtained alloys were further crushed to specific particle size (0.1-0.6 mm). Acid leaching trials were performed with 10%HCl at 60 °C under ultrasonic mixing. The concentrations of the impurities of the obtained ternary Si alloys and the leaching products were characterized by inductively coupled plasma mass spectrometry (ICP-MS). Electron microscopy examination indicates that the main precipitates in Si-Ca-Y alloys are silicides such as $CaSi_2$, YSi_2, $CaAl_2Si_2$, and Al-Fe-Y-Si phase, and they are distributed between the primary silicon grains. In the Si-Ca-Ti alloys, however, the main silicide precipitates are $CaSi_2$, $TiSi_2$, $CaAl_2Si_2$, and $FeTiSi_2$. In both cases, the main impurities, such as P and Fe, are concentrated in specific silicides. After leaching, it was found that Ti and Y exhibit relatively equivalent P removal ability with both around 75% removal, but the Si-Ca-Y alloys show 20% B removal, which is higher than that of the Si-Ca-Ti alloy with 10% B removal.

Introduction

There have been significant efforts devoted to the reduction of energy consumption and the carbon footprint of the solar-grade silicon (SoG-Si) production in the photovoltaic

industry. In recent years, transformational technology for the alternate Siemens SoG-Si production has been developed in Norway, known as the ELKEM Solar process, which has been operated by REC Solar Norway in recent years, that can significantly improve process sustainability. According to the investigation from Murgau and Safarian [1], the energy consumption of the ELKEM process is significantly reduced from ~170kWh/kg Si to 30-60 kWh/kg Si with 10.8 kg CO_2/kg SoG-Si carbon footprint compared to the traditional Siemens process. In the ELKEM Solar process [1], [2], the metallurgical-grade silicon (MG-Si) produced from submerge arc furnace is further refined through a combination of a series metallurgical refining techniques; slag refining, acid leaching, and directional solidification. As one of the most crucial purification targets, phosphorus impurity is largely removed in the acid leaching procedure in order to fit the strict requirements of SoG-Si. The main principle of the leaching technique is based on the digestion of segregated impurities along Si grain boundaries and thus to obtain the pure primary Si grains. The optimum leaching conditions and leaching efficiency of direct Si leaching have been studied by many researchers [3]–[7], and it has been found out that predominant metallic impurities can be removed by this approach, but the efficiency of B and P removal is still limited, in particular B removal.

To date, considerable work had been done on the improvement of the acid leaching technique by alloying Si with other metal refiners to modify the impurity segregation behaviour. As one successful strategy, solvent refining is known to achieve high P removal degree and also a certain amount of B removal by alloying Si with a large amount of metal refiner, such as Al[8]–[12], Fe[13], Sn[14]–[16], and Cu[17], [18]. It has to be emphasized that solvent refining is a high-temperature process, which is different from the alloying-leaching process. However, the addition of a small amount of refiner metal with high impurity affinity exhibits more benefits for the industry for the alloying-leaching process. In this way, alkaline earth elements (Ca[19]–[22] and Mg[23]–[25]) are of the most often studied metal refiners due to their high P affinity and good leaching kinetics. Schei et al.[20] reported Ca addition can significantly enhance the precipitation of impurities in the leachable $CaSi_2$ phase upon solidification and reach high purification efficiency, a great number of attention has been paid to the Si-Ca related alloying systems. Shimpo et al.[21] also studied the P removal of Ca-alloyed Si by acid leaching, and measured the interaction coefficient $\varepsilon^{P}_{Ca\ in\ Si}$ to be 14.6±1.7 at 1723K, which indicates a great P activity reduction after Ca alloying into the Si melt. Meteleva-Fisher et al.[26] also confirmed the decisive role of Ca on impurity gathering and studied the effect of cooling rate on microstructure of Ca-alloyed Si. Apart from the alkaline earth elements, the Group IV elements (Ti[22], Zr[27], Hf[28]) and rare earth elements (REE)[29], [30] also attract great attention for researchers recently due to their high affinity to B and P. According to Johnston et al. [22], as much as ~50% B can be removed with 5wt% Ti addition into MG-Si, and ~80% P removal with 1wt% rare earth elements addition [29].

In the present work, novel ternary alloying refining systems of Si-Ca-Ti and Si-Ca-Y were designed to explore their purification efficiency. Since there is not much information about these alloying systems, the effect of Ti and Y addition on the microstructure of Ca-alloyed MG-Si was also studied.

Materials and methods

Commercial MG-Si was used in the present study for the alloying-leaching purification. The MG-Si was first mixed with reagent grade Ca and Ti (Y) in an alumina crucible. Materials were then heated up to 1500 °C to form a Si-Ca-Ti (Y) melt in an induction furnace. After the mixture was fully melted, the melt was slowly cooled down to the room temperature inside the furnace chamber. The obtained alloys were then crushed and milled in a ring mill, and finally sieved to the particle size range 0.1-0.6 mm for the acid leaching. The average compositions of two analysed samples for each material are listed in Table 1.

Table 1: Composition (in ppmw) of MG-Si and obtained Si-Ca-Ti and Si-Ca-Y alloys.

Impurity	Si-Ca-Ti	Si-Ca-Y
B	42±4	41.5±0.8
P	12.1±0.2	12.8±0.2
Ca	26975±499	30387±1555
Mg	16.7±0.1	20±3
Al	5782±276	8065±560
Fe	2749±8	2436±105
Ti	20822±188	218±3
Y	0.7±0.1	15694±1122

Alloy samples were leached by hydrochloric acid (HCl) with a concentration of 10% at a temperature of 60°C for 2 hours. All the leaching trials were performed in an ultrasonic bath. The samples after leaching were washed by distilled water and ethanol, and were then dried at 80°C for 1h.

The microstructure and impurity distribution of the obtained alloys were analysed by Electron Probe Micro-Analyzer (EPMA). In addition, the samples before and after leaching were analyzed by the high-resolution Inductively Coupled Plasma-Mass Spectroscopy (ICP-MS) technique for the impurities determination.

Results and discussion

Effect of Ti and Y-doping on Si microstructure

The microstructure of the obtained Si-Ca-Ti and Si-Ca-Y alloys can be seen in Figure 1. To further study the impurity segregation behaviour affected by the Ti and Y addition, EPMA analysis was performed, as typical results are shown in Figure 2. It is worth noting that the concentration of B, P, and Mg is much lower than the EPMA detection sensitivity. Thus, the mapping results of B, P, and Mg should be not reliable, while they are good for comparing the phases qualitatively. Subsequently, only the main impurity phases were discussed. The detailed compositions of detected impurity phases measured by WDS in EPMA are presented in Table 2 and Table 3 for Si-Ca-Ti and Si-Ca-Y alloys, respectively.

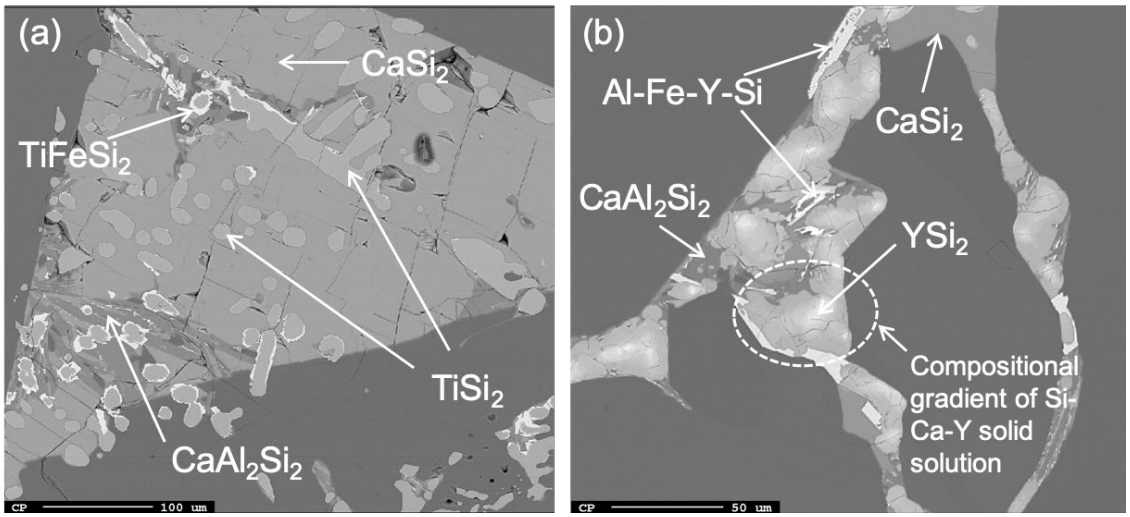
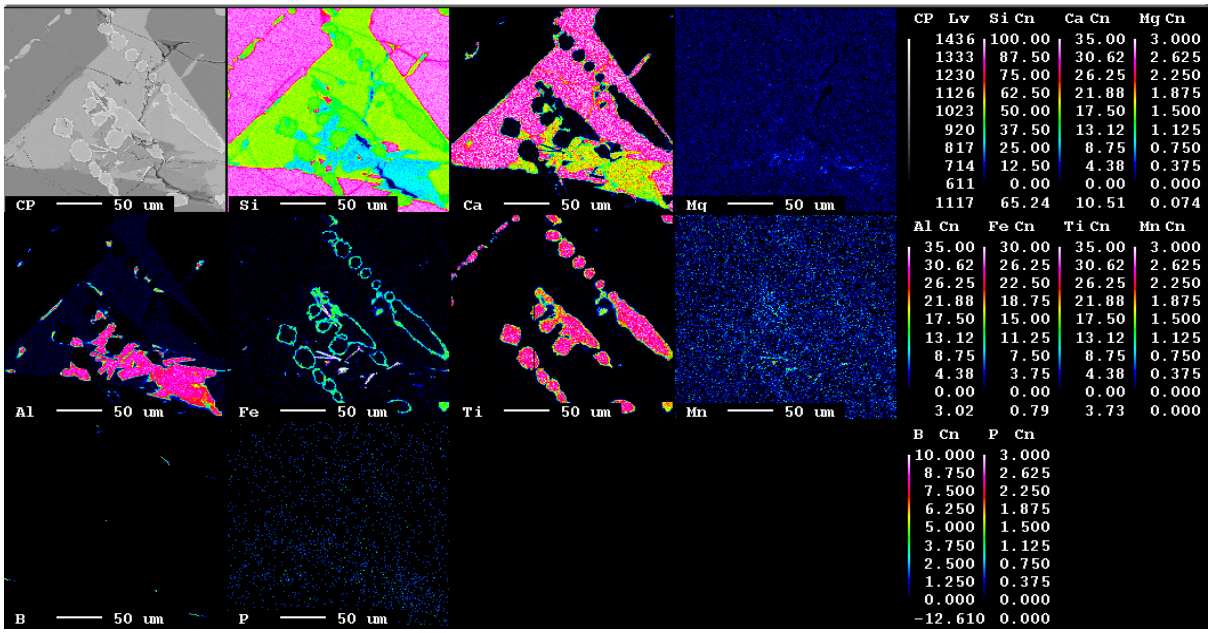


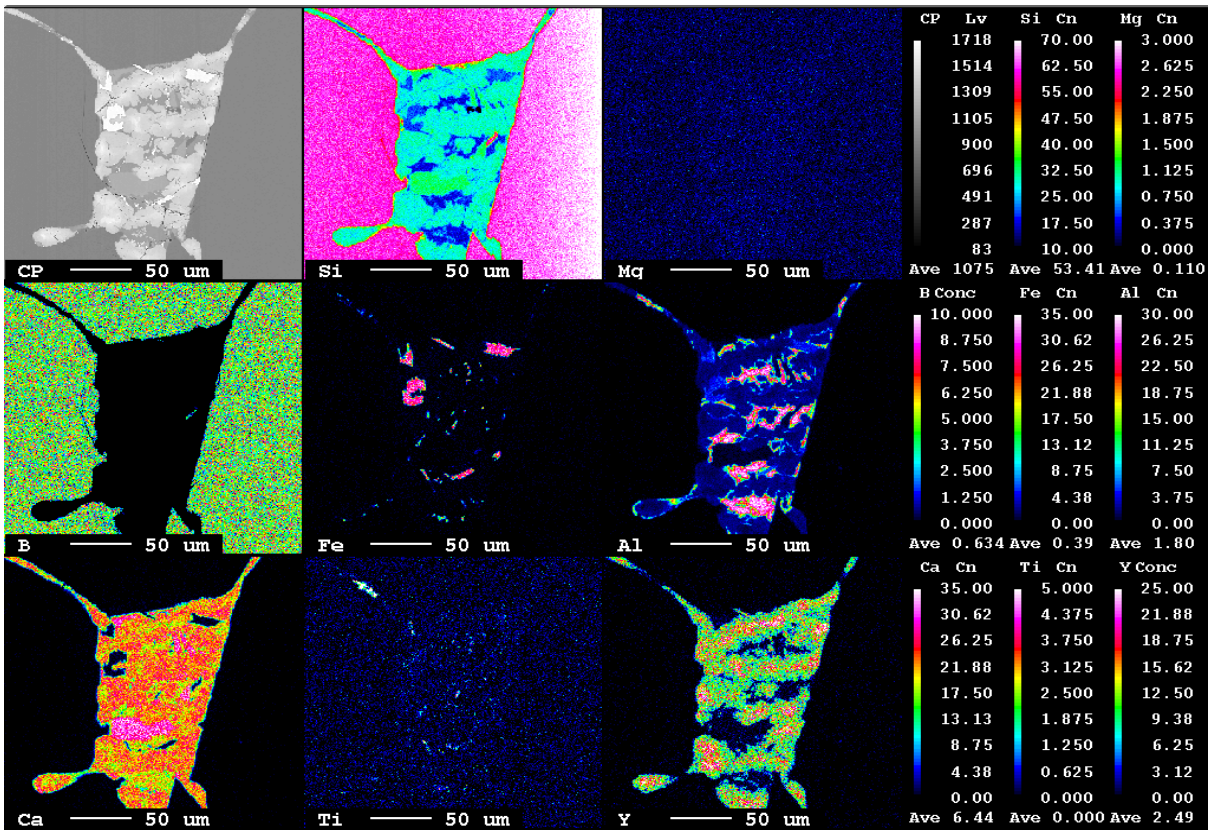
Figure 1: Microstructure of obtained alloys (a) Si-Ca-Ti, (b)Si-Ca-Y, and the characterized secondary precipitates between primary silicon grains.

It can be seen that the main abundant precipitated secondary phase in the Si-Ca-Ti alloy is $CaSi_2$. No ternary Ca-Ti-Si intermetallic phase is observed, and a number of $TiSi_2$ islands (more globular) were found embedded inside and out of the $CaSi_2$ precipitates. Compared to the morphology of the $TiSi_2$ phase observed in the binary Ti-Si system obtained by Johnston et al.[22], the $TiSi_2$ phase is more spherical rather than the irregular shape reported [22]. Additionally, the Ti-Fe-Si phase was found to surround the $TiSi_2$ phase to form either $TiFeSi_2$ compound or a $(Ti,Fe)Si_2$ solid solution. This also indicates a strong affinity between Ti and Fe in the Si melt. It is worth noting that a large amount of $CaAl_2Si_2$ phase with needle shape was found to be distributed in the $CaSi_2$ phase, which is attributed to small corrosion of the alumina crucible surface, in addition to small Al in the original MG-Si. This is found by comparing the compositions of materials in Table 1.

To the best knowledge of the authors, there have been no studies about the microstructure of the Si-Ca-Y alloy system. In the present work, it can be seen that the distribution of Ca and Y in the secondary precipitated phases has a conjugated composition gradient. The center part of the Si-Ca-Y phase is more bright, indicating more Y, and YSi_2 phase enriched with around 5at% Ca, and this area is surrounded by a $(Ca,Y)Si_2$ solid solution with less Y, i.e., 5-10at% Y. The reason for this unique microstructure may be the known Hume-Rothery rules that Ca and Y form interstitial solid solution since they sit near each other in the periodic table, and consequently, show similar atomic radius and electronegativity. The slow cooling may also have a positive effect on this phenomenon. The $CaAl_2Si_2$ phase was observed in between the Si-Ca-Y precipitates, indicating the deposition of these phases most likely upon eutectic reaction. The segregation behaviour of Fe impurity is significantly affected by the Y addition, and an Al-Fe-Y-Si intermetallic phase was observed, while neither $FeSi_{2.4}$ nor the $FeTiSi_2$ phase was formed, which usually exist along the grain boundaries of the MG-Si.



(a) Mapping results of Si-Ca-Ti alloy



(b) Mapping results of Si-Ca-Y alloy

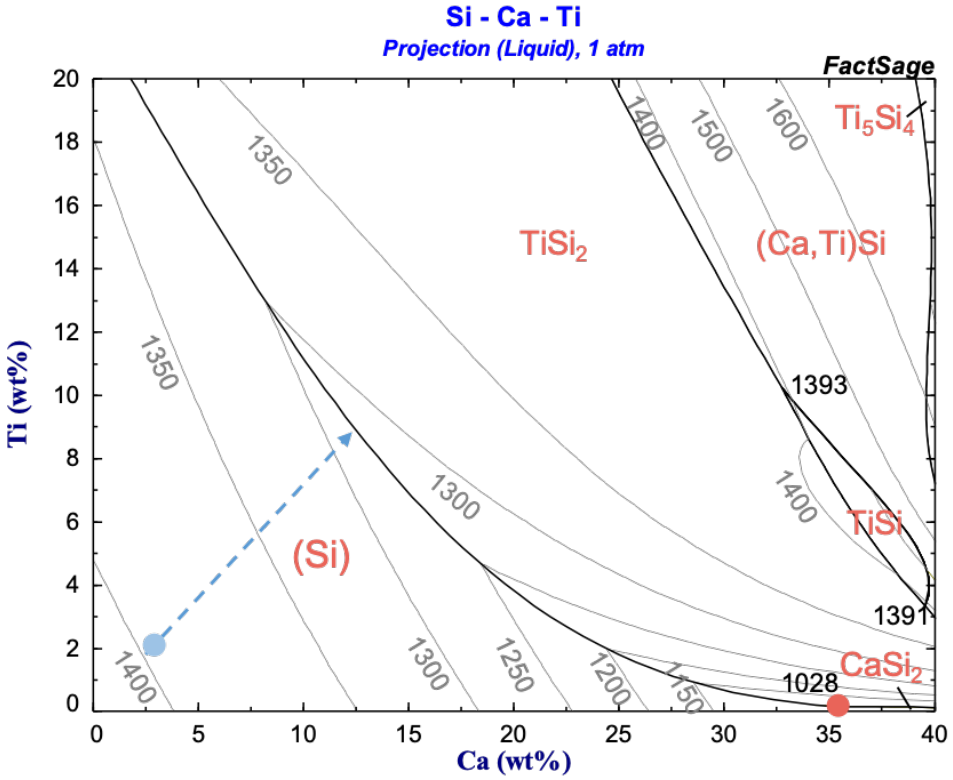
Figure 2: X-Ray elemental mapping of the obtained Si-Ca-Ti and Si-Ca-Y alloying system measured by EPMA.

Table 1: Measured composition of major impurity in Si-Ca-Ti alloy by WDS.

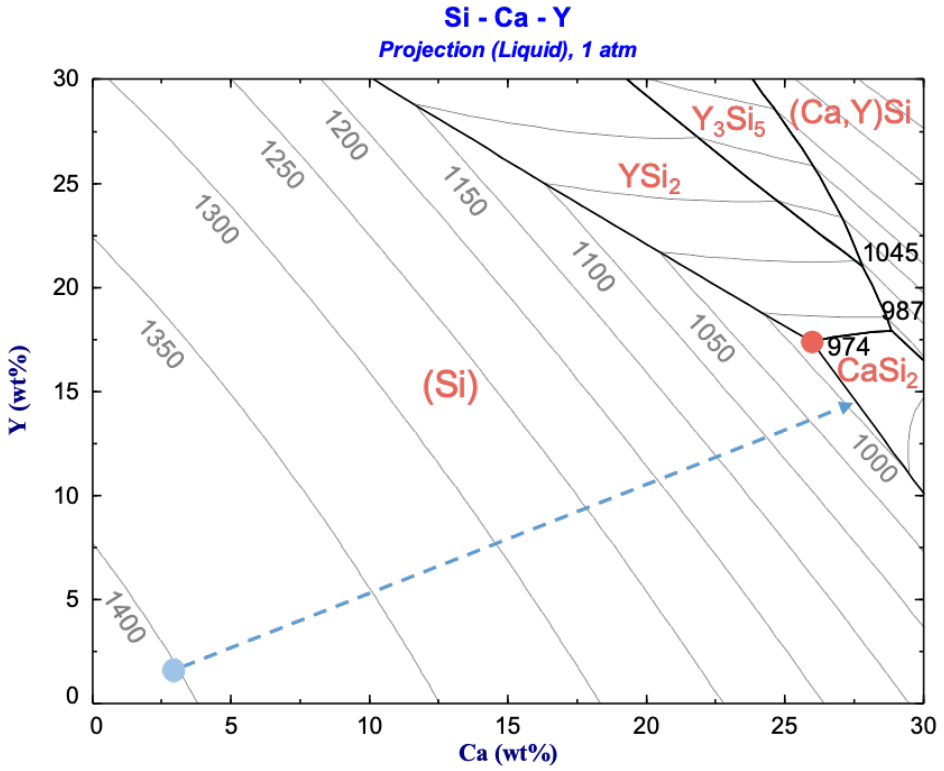
Phase	Composition (at%)				
	Si	**Ca**	**Al**	**Fe**	**Ti**
$CaSi_2$	66.2±0.1	32.9±0.1	0.8±0.1	0	0.1±0.1
$CaAl_2Si_2$	40.8±0.3	19.2±0.1	39.6±0.3	0.1±0.1	0.1±0.1
$TiSi_2$	66.0±0.2	0.3±0.1	0.2±0.1	0.1±0.1	33.3±0.2
$TiFeSi_2$	48.8±0.4	0.6±0.1	2.1±0.2	24.9±0.2	25±2
$(Ti,Fe)Si_2$	63.2±0.3	0.5±0.1	0.5±0.3	8.2±0.2	27.3±0.7

Table 3: Measured composition of major impurity in Si-Ca-Y alloy by WDS.

Phase	Composition (at%)					
	Si	**Ca**	**Al**	**Fe**	**Ti**	**Y**
$CaSi_2$	65.7±0.1	33.2±0.1	0.8±0.1	0	0	0.3±0.1
$CaAl_2Si_2$	40.5±0.1	19.1±0.1	39.0±0.1	0	0	0.3±0.1
YSi_2	64.9±0.4	5.4±0.8	0.5±0.1	0.1±0.1	0	29±1
$(Ca,Y)Si_2$	63±1	27±2	2.3±0.6	0.1±0.1	0	7±2
Al-Fe-Y-Si	59.1±0.3	0.7±0.1	8.8±0.1	24.0±0.1	0.1±0.1	7.3±0.2



(a) Calculated liquidus surface and solidification path of Si-Ca-Ti alloy



(b) Calculated liquidus surface and solidification path Si-Ca-Y alloy

Figure 3: Calculated liquidus surface and solidification path of (a) Si-Ca-Ti and (b) Si-Ca-Y alloy system where the blue circle indicates the starting alloy composition and the red circle indicates the ternary eutectic point. Isothermal lines are presented in degrees Celsius.

The phase diagram of the Si-Ca-Ti and Si-Ca-Y system was determined by thermodynamic software Factsage, and the results are shown in Figure 3. It can be seen that Si is the primary precipitate for both alloys, and no ternary intermetallic compounds were found as well. For the Si-Ca-Ti system shown in Figure 3(a), the secondary precipitating phase suggested as $TiSi_2$, which coincides with the study of Morita and Miki [31] and the finding of the separated $TiSi_2$ islands outside of the $CaSi_2$ phase. However, for the Si-Ca-Y system shown in Figure 3(b), the secondary precipitate becomes $CaSi_2$ rather than YSi_2. Compared with the microstructure presented in Figure 1 and Figure 2, it would be better for the leaching process to have the $CaSi_2$ phase as the secondary phase because other impurity phases can be well-embedded inside the leachable $CaSi_2$ phase.

In order to study further for the reason of different microstructure and impurity distribution, the values of the heat of mixing between atomic pairs ΔH_{AB}^{mix} were obtained from Miedema's model for the binary system with equal-atomic composition [32], as shown in Figure 4. It can be seen that silicides show all negative values, which suggests the possibility to form the binary silicides with Ca, Ti, Fe, and Y, for instance, $CaSi_2$, $TiSi_2$, $FeSi_{2.4}$, and YSi_2. Furthermore, in the Ca column, all values are positive. This could explain the reason why no Si-Ca-Ti and Si-Ca-Y ternary intermetallics were found in microanalysis. Additionally, the mixing enthalpy values reveal why the $TiSi_2$ islands

solely distributed in the $CaSi_2$ phase in the Ti-doped sample, since the Ca-Ti pair exhibits the most positive value. Meanwhile, the less positive Ca-Y pair value indicates only a weaker repulsive interaction between Ca and Y, and therefore it may explain the compositional gradients in Ca-Y-Si precipitates in the Si-Ca-Y alloy.

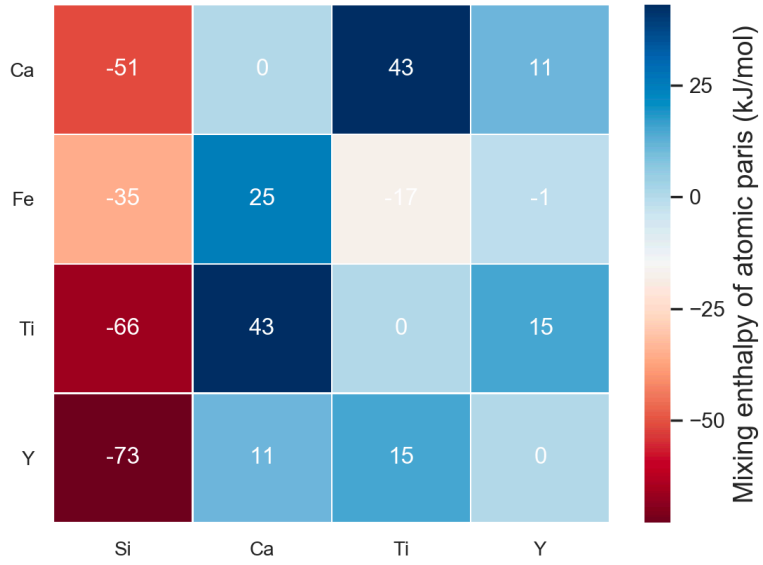


Figure 4: The values of $\boldsymbol{\Delta H_{AB}^{mix}}$ (kJ/mol) obtained by Miedema's model for atomic pairs in a Si-Ca-Ti-Y system.

Leaching performance

To further study the segregation behaviour affected by the Ti and Y addition in Ca-alloyed MG-Si, acid leaching experiments were performed, and the removal of impurities was measured by chemical composition changes. The impurity removal degree is calculated as:

$$Removal\ degree = \frac{C_i - C_f}{C_i} \times 100\% \quad (1)$$

where the C_i and C_f are initial impurity concentration (before leaching) and final concentration (after leaching) in weight percent, respectively.
The results of the leaching refining on elements removal are presented in Figure 5.

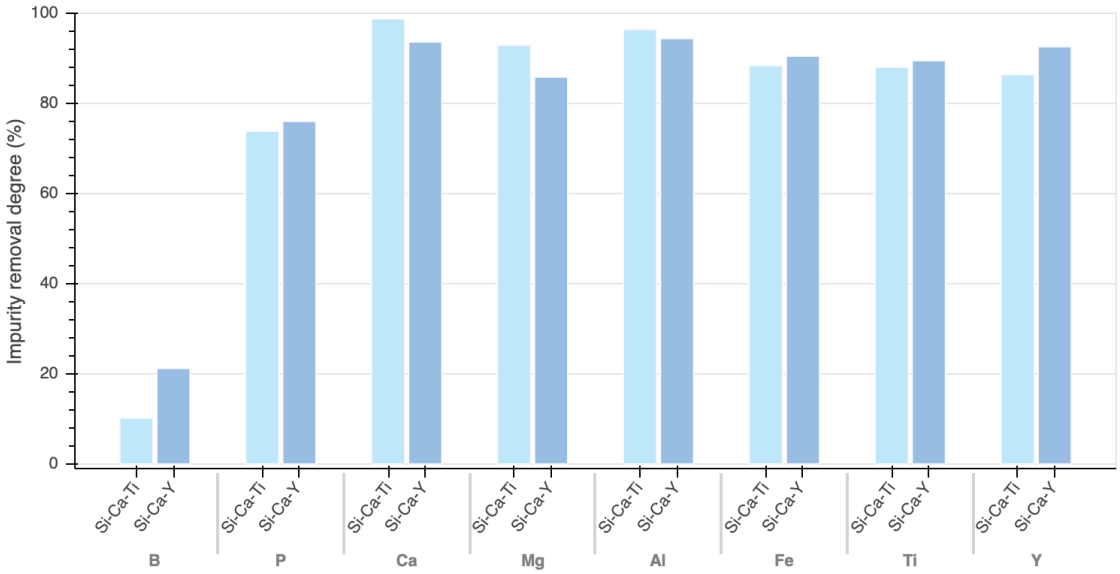


Figure 5: Comparison of impurities removal degree of the Si-Ca-Ti, and Si-Ca-Y alloying systems.

It can be seen that both of the alloys showed high purification efficiency for the metallic impurities. The $TiSi_2$ phase is known with a low leachability in HCl aqueous solution [33], but high Ti removal was achieved in the Si-Ca-Ti sample. The reason may be owing to the high reactivity of $CaSi_2$ and its cracking effect that makes the insoluble $TiSi_2$ phase easier to be carried away physically. A nearly equivalent ability for the P removal was found for the studied Si-Ca-Ti and Si-Ca-Y alloys. The ~75% P removal is also close to the performance of the well-studied binary Si-Ca alloy[22], [29]. It may draw a conclusion that Ti and Y could have similar P affinity as Ca does. However, another factor should also be considered that the adoption of alumina crucible may also affect the P impurity segregation, which seems to be a negative effect compared to the main doping metals. It is also seen that ~10% B removal is achieved by the Si-Ca-Ti sample, and ~20% B removal by the Si-Ca-Y sample. This result suggests that B segregation behaviour could be more affected by Y than Ti in the Si-Ca system. This result also indicates that the doping of rare earth elements may have the potential for the co-removal of conventionally problematic impurities B and P.

Compared to conventional alkaline earth elements doping, the major challenge of the rare earth elements doping is from the economic concern. However, the low vapor pressure of the rare earth elements makes it possible to directly dope $ReCl_3$ into Si, where the $ReCl_3$ can be directly recycled from the leaching solution. In addition, the generated $SiCl_4$ vapor can be also easily recycled by reacting with water to obtain the HCl aqueous solution. In this way, a closed-loop material flow may significantly reduce the cost. Thus, the door for the design of a potential novel Si purification process is kept open.

Conclusions

In this work, the effect of doping Ti and Y on the impurity segregation and the leaching purification performance of Ca-alloyed MG-Si has been investigated. The main results are summarized as follows:

- It was found that the doping of Si-Ca by Ti and Y significantly affects the microstructure of the precipitated phases.
- In Si-Ca-Ti alloy, the main silicide precipitates are $CaSi_2$, $TiSi_2$, $CaAl_2Si_2$, $FeTiSi_2$, and solid solution $(Ti,Fe)Si_2$.
- In the Si-Ca-Y alloy, the main precipitates are $CaSi_2$, YSi_2, $CaAl_2Si_2$, and Al-Fe-Y-Si phase. A compositional gradient in a Si-Ca-Y solid solution phase was found due to the weak repulsive interaction between Ca and Y.
- In the leaching experiments, Ti and Y exhibited relatively equivalent ability for the removal of all elements except phosphorus.
- Higher B removal (~20%) was found in the Si-Ca-Y system than Si-Ca-Ti, which shows the co-removal of B and P by rare earth elements doping.

Acknowledgement

This work was performed at NTNU within the Research Centre for Sustainable Solar Cell Technology (FME SuSolTech, project number 257639), co-sponsored by the Norwegian Research Council and industry partners.

References

1. A. Murgau and J. Safarian, *Solar silicon production through metallurgical route and REC solar advancements*, Silicon for the Chemical and Solar Industry XIV, 2018, pp. 183–192.
2. J. Safarian, G. Tranell, and M. Tangstad, *Processes for upgrading metallurgical grade silicon to solar grade silicon*, Energy Procedia. vol. 20, pp. 88–97, 2012.
3. N. P. Tucker, *Preparation of high purity silicon*, J. Iron Steel Ind., vol. 15, pp. 412–414, 1927.
4. J. Dietl, Hydrometallurgical purification of metallurgical-grade silicon, Sol. Cells, vol. 10, no. 2, pp. 145–154, 1983.
5. J. M. Juneja and T. K. Mukherjee, *A study of the purification of metallurgical grade silicon*, Hydrometallurgy, vol. 16, no. 1, pp. 69–75, 1986.
6. I. C. Santos, A. P. Goncalves, C. S. Santos, M. Almeida, M. H. Afonso, and M. J. Cruz, *Purification of Metallurgical Grade Silicon by Acid Leaching*, Hydrometallurgy, vol. 23, pp. 237–246, 1990.
7. T. L. Chu, *Partial Purification of Metallurgical Silicon by Acid Extraction*, J. Electrochem. Soc., vol. 130, no. 2, p. 455, 1983.
8. T. Yoshikawa and K. Morita, *Removal of phosphorus by the solidification refining with Si-Al melts*, Sci. Technol. Adv. Mater., vol. 4, no. 6, pp. 531–537, 2003.

9. T. Yoshikawa and K. Morita, *Refining of silicon during its solidification from a Si–Al melt, J. Cryst. Growth*, vol. 311, no. 3, pp. 776–779, Jan. 2009.
10. T. Yoshikawa and K. Morita, *An Evolving Method for Solar-Grade Silicon Production: Solvent Refining*, JOM, vol. 64, no. 8, pp. 946–951, Aug. 2012.
11. Y. Li et al., *Effect of Cooling Rate on Phosphorus Removal During Al-Si Solvent Refining*, Metall. Mater. Trans. B, vol. 46, no. 2, pp. 542–544, Apr. 2015.
12. B. Ban, X. Bai, J. Li, Y. Li, J. Chen, and S. Dai, *The Mechanism of P Removal by Solvent Refining in Al-Si-P System*, Metall. Mater. Trans. B Process Metall. Mater. Process. Sci., vol. 46, no. 6, pp. 2430–2437, Sep. 2015.
13. L. T. Khajavi, K. Morita, T. Yoshikawa, and M. Barati, *Removal of Boron from Silicon by Solvent Refining Using Ferrosilicon Alloys*, Metall. Mater. Trans. B, vol. 46, no. 2, pp. 615–620, Apr. 2015.
14. X. Ma, Y. Lei, T. Yoshikawa, B. Zhao, and K. Morita, *Effect of solidification conditions on the silicon growth and refining using Si–Sn melt*, J. Cryst. Growth, vol. 430, pp. 98–102, Nov. 2015.
15. L. Hu, Z. Wang, X. Gong, Z. Guo, and H. Zhang, *Purification of metallurgical-grade silicon by Sn – Si refining system with calcium addition*, Sep. Purif. Technol., vol. 118, pp. 699–703, 2013.
16. J. Li et al., *Effect of tin addition on primary silicon recovery in Si–Al melt during solidification refining of silicon*, J. Cryst. Growth, vol. 371, pp. 1–6, May 2013.
17. L. Huang et al., *Enhancement in extraction of boron and phosphorus from metallurgical grade silicon by copper alloying and aqua regia leaching*, Hydrometallurgy, vol. 161, pp. 14–21, 2016.
18. L. Huang et al., *Solvent extraction of phosphorus from Si-Cu refining system with calcium addition*, Sep. Purif. Technol., vol. 204, pp. 205–212, Oct. 2018.
19. Y. V. Meteleva-Fischer, Y. Yang, R. Boom, B. Kraaijveld, and H. Kuntzel, *Microstructure of metallurgical grade silicon during alloying refining with calcium*, Intermetallics, vol. 25, pp. 9–17, 2012.
20. A. Schei, *High Purity Silicon Production*, in International seminar on refining and alloying of liquid aluminium and Ferro-alloys, 1985.
21. T. Shimpo, T. Yoshikawa, and K. Morita, *Thermodynamic study of the effect of calcium on removal of phosphorus from silicon by acid leaching treatment*, Metall. Mater. Trans. B, vol. 35, no. April, pp. 277–284, 2004.
22. M. D. Johnston and M. Barati, *Calcium and titanium as impurity getter metals in purification of silicon*, Sep. Purif. Technol., vol. 107, pp. 129–134, 2013.
23. M. Zhu, A. Murgau, and J. Safarian, *Effects of Magnesium-Doping on Silicon Leaching for Solar Grade Feedstock Production*, in 35 Eur. Photovolt. Sol. Energy Conf. Exhib., 2018, pp. 465–468.
24. M. Zhu, A. Azarov, E. Monakhov, K. Tang, and J. Safarian, *Phosphorus separation from metallurgical-grade silicon by magnesium alloying and acid leaching*, Sep. Purif. Technol., vol. 240, no. January, p. 116614, 2020.

25. S. Espelien, G. Tranell, and J. Safarian, *Effect of magnesium addition on removal of impurities from silicon by hydrometallurgical treatment*, in Energy Technology 2017, Springer, 2017, pp. 355–366.
26. Y. V. Meteleva-Fischer, Y. Yang, R. Boom, B. Kraaijveld, and H. Kuntzel, *Microstructure of metallurgical grade silicon during alloying refining with calcium*, Intermetallics, vol. 25, pp. 9–17, 2012.
27. Y. Lei, W. Ma, G. Lv, K. Wei, S. Li, and K. Morita, *Purification of metallurgical-grade silicon using zirconium as an impurity getter*, Sep. Purif. Technol., vol. 173, pp. 364–371, 2017.
28. Y. Lei et al., *Leaching behaviors of impurities in metallurgical-grade silicon with hafnium addition*, Hydrometallurgy, vol. 169, pp. 433–439, 2017.
29. Y. Meteleva-Fischer, Y. Yang, R. Boom, B. Kraaijveld, and H. Kuntzel, *Alloying Refining of Metallurgical Grade Silicon with Rare Earth Elements*, in EPD Congress 2013, Hoboken, NJ, USA: John Wiley & Sons, Inc., 2013, pp. 201–209.
30. K. Tang, O. M. Løvvik, J. Safarian, X. Ma, and M. Tangstad, *Removal of Phosphorus in Metallurgical Silicon by Rare Earth Elements*, Metall. Mater. Trans. E, vol. 1, no. 3, pp. 257–262, Sep. 2014.
31. K. Morita and T. Miki, *Thermodynamics of solar-grade-silicon refining*, Intermetallics, vol. 11, pp. 1111-1117, 2003.
32. A. Takeuchi and A. Inoue, *Metallic Glasses By Atomic Size Difference, Heat of Mixing and Period of Constituent Elements and Its Application To Characterization of the Main Alloying Element*, Mater. Trans., vol. 46, no. 12, pp. 2817–2829, 2005.
33. E.G. Rochow. *The Chemistry of Silicon: Pergamon International Library of Science, Technology, Engineering and Social Studies*. vol. 9. Elsevier, 2013.

Silicon and ferrosilicon latent heat thermal batteries

Alejandro Datas[1)]
1) Instituto de Energía Solar, Universidad Politécnica de Madrid

Abstract

Electric thermal energy storage (E-TES) or power-to-heat-to-power storage (PHPS) are a kind of electricity storage device relying on the direct conversion of electricity into heat, followed by on-demand conversion of heat into electricity. The very low cost per energy capacity of these systems make them very appealing for tackling intra-day fluctuations of variable renewable energy sources (10 – 100 hours of storage periods) that are characterized by low costs of electricity input. As recently concluded by the EU-project AMADEUS, silicon and ferrosilicon alloys could be ideal candidates for thermal storage in this kind of systems. Having a volumetric latent heat higher than 1000 kWh/m^3, they enable more than twice the energy density of Li-ion batteries. Besides, they are characterized by high melting temperatures (>1000ºC), high solid-phase thermal conductivities (20-30 W/m-K near the melting point, 100-times higher than conventional salt-based PCMs) and very low costs per energy storage capacity (< 10 €/kWh), all being essential characteristics for highly efficient and cost-effective latent heat energy storage applications. In this article, I discuss on the techno-economics and the possible embodiments of these kinds system.

Electric thermal energy storage

The overall power flow diagram of an electric-thermal energy storage (E-TES) or power-to-heat-to-power storage (PHPS) system is illustrated in Figure 1. It comprises three main elements: (1) a power-to-heat converter, (2) a heat storage unit, and (3) a heat-to-power converter that transforms heat back into electricity on demand. When there is a surplus of renewable power generation, such excess of electricity (P_s) is converted into heat and stored. When needed, this heat can be either directly used (Q_{g2}) or transferred to a heat-to-power converter, which transforms part of this heat into electricity (P_{d2}). The efficiency of the heat-to-power conversion process is given by the ratio of output electric power (P_{d2}) to the input heat (Q_{g1}), which ultimately determines

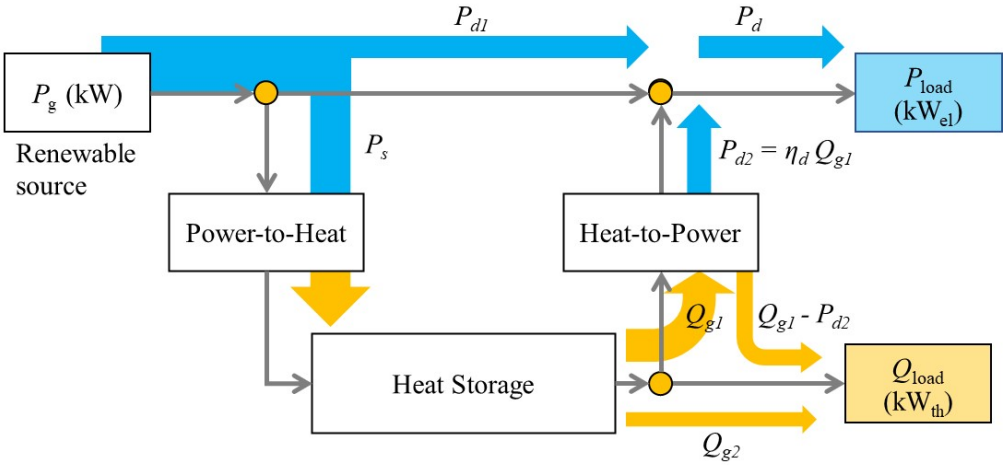


Figure 1: Overall power flow diagram of an Electric Thermal Energy storage (E-TES) or Power-to-Heat-to-Power storage (PHPS) system.

also the overall electric-to-electric round-trip efficiency of the system ($\eta_{rt} = P_{d2} / P_s$). The heat that is not converted into electricity during the heat-to-power conversion process (Q_{g1} - P_{d2}) can be also delivered as an output, and thus, enhance the overall efficiency of the system.

The key indicator for the economic feasibility of an ETES system like the one shown in Figure 1 is the levelized cost of discharged energy (LCOE). LCOE provides the average cost of the energy that is released by the system all through its lifetime (in €/kWh-cycle), including the variable cost of the input electricity (p_e in €/kWh-cycle), the capital expenditures for both energy (c_e in €/kWh$_{th}$) and power (c_p in €/kW) capacities, the maintenance costs, taxes, and lifetime of the installation (n, in years). The LCOE may consider only electricity output or both heat and electricity outputs, depending on the specific application. A simplified expression for the LCOE that assumes a constant price for the electricity input and an uniform periodic cycling can be derived (1–4)

$$LCOE = \frac{p_e}{\eta_d} + \left(\frac{c_{p,a}}{t_d} + \frac{c_{e,a}}{\eta_d}\right)\frac{1}{N}$$

being $N = 4380 / t_d$ the number of cycles in one year, t_d the discharge time (in hours), and $c_{p,a}$ ($c_{e,a}$) the annualized cost per power (energy) capacity in €/kW (€/kWh$_{th}$) that is obtained from the initial capital expenditures c_p and c_e by

$$c_{x,a} = c_x \frac{r(1+r)^n}{(1+r)^n - 1}$$

being r the discount rate and n the lifetime of the installation (in years). LCOE is necessarily higher than the input price of electricity (p_e) due to the non-negligible cost per energy storage (c_e) and power (c_p) capacities.

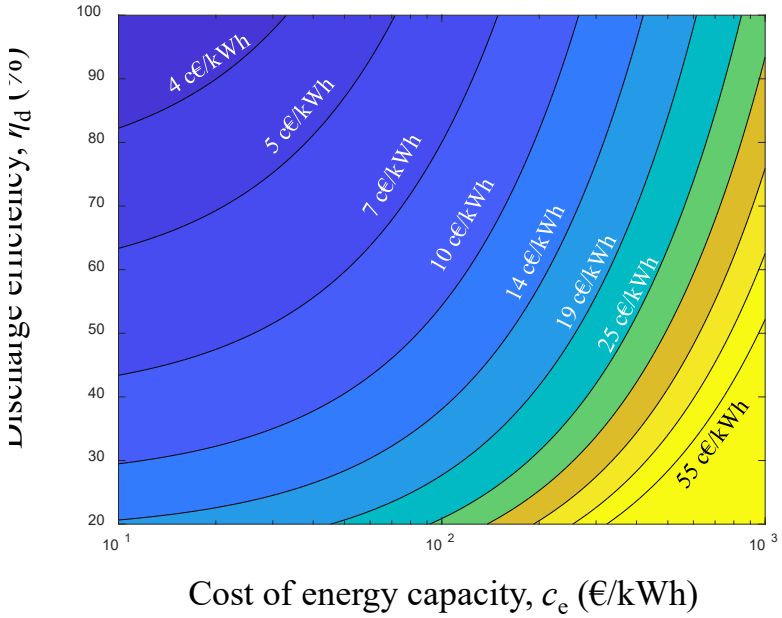


Figure 2: LCOE as a function of the energy capacity cost (c_e, in €/kWh) and discharge efficiency (η_d). The price of electricity input is set to p_e = 2.5 c€/kWh-cycle. The cost per power capacity is set to c_e = 300 €/kW. The discharge time is set to t_d = 12 hours.

Figure 2 shows the LCOE as a function of the cost per energy capacity and discharge efficiency for a generic energy storage system, according to Figure 1, with a constant price of electricity input of 2.5 c€/kWh-cycle and cost of power capacity of 300 €/kW, which are reasonable assumptions for the price of renewable power during low demand periods and the cost of DC/AC converter for electrochemical batteries. An important observation is that a highly efficient and expensive system (e.g. η_d = 90% and c_e = 200 €/kWh) provides similar LCOE than a less efficient but much cheaper system (e.g. η_d = 35% and c_e = 30 €/kWh). This basic observation represents the key requirement for any E-TES system: to reach very low cost per energy storage capacity combined with the highest possible conversion efficiency, provided that the cost per power capacity (heaters and heat engine) is low enough.

Figure 3 compares the LCOE for two specific technologies (E-TES and Li-ion batteries) as a function of the storage time (panel a) and the price of the electricity input (panel b). Panel *a* assumes minimum cycling periods of 24 hours. E-TES is characterized by a low electric-to-electric round-trip efficiency (40%), very low 'cost per energy capacity' (20 €/kWh) and high 'cost per power capacity' (1000 €/kW_{el}). On the contrary, Li-ion batteries are characterized by high electric-to-electric round-trip efficiency (90%), high 'cost per energy capacity' (200 €/kWh) and low 'cost per power capacity' (300 €/kW_{el}). Panel *a* assumes a constant price of energy input of 2.5 c€/kWh-cycle and panel *b*

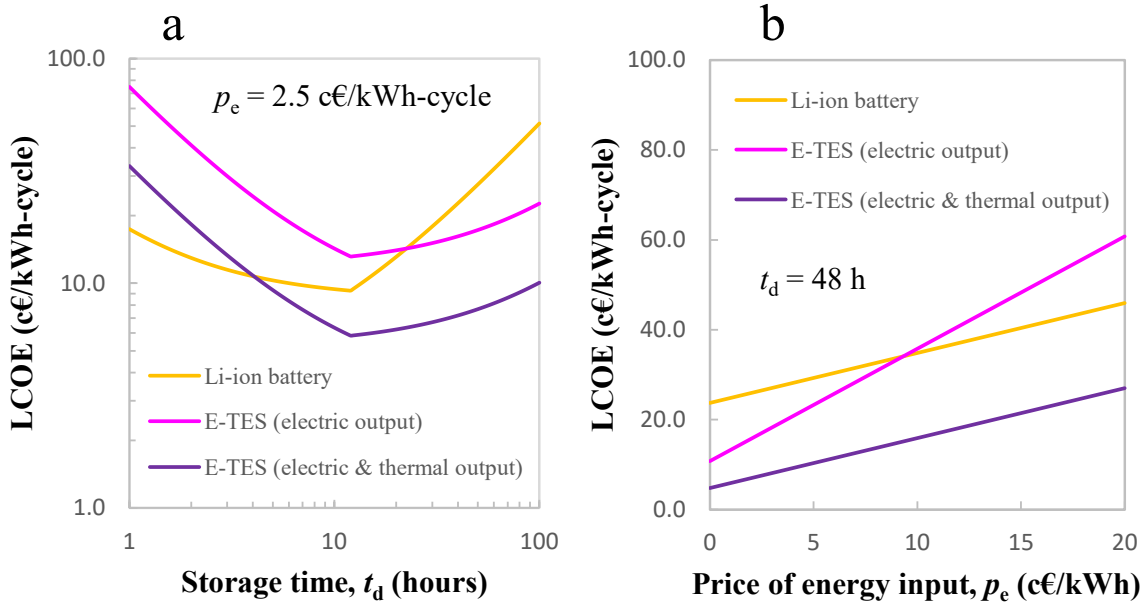


Figure 3: Levelized Cost of Energy (LCOE) of E-TES and Li-ion batteries as a function of storage time (a) and price of energy input (b). Two cases of E-TES systems are shown whether only electricity or both heat and electricity are considered as energy outcome. Plots inspired in the results shown in (1,2).

assumes a constant storage time of 48 hours. The main conclusion is that E-TES outperforms Li-ion batteries if energy storage periods are long and the price of energy input is low. In other words, if the system is going to be charged/discharged unfrequently (i.e. long discharge times) or by using very cheap electricity input, it is worth using a system with very low 'cost per energy capacity', even if the overall electric-to-electric round-trip efficiency is low. In this case, it is the priority to minimize the cost per energy capacity rather than maximizing its efficiency, and consequently, the use of E-TES systems becomes preferable. Besides, the higher 'cost per power capacity' of E-TES is not an issue for large energy-to-power capacity ratios (i.e. long discharge times), where the heat engine is small if compared to the total amount of energy that is stored. Therefore, E-TES systems where only electricity is delivered as an output aim at energy storage but not power capacity. On the other hand, if also thermal energy is demanded, E-TES outperforms Li-ion in a much broader range of applications (Figure 3), i.e. shorter storage periods and more expensive energy inputs.

It is already happening that variable renewable energy sources (VRES) such as solar and wind are delivered at very low prices (< 5 c€/kWh) and with strong intra-day (>12 hours) fluctuation. Results in Figure 3 indicate that E-TES systems will be preferable than Li-ion batteries to tackle such low-frequency variability of those renewable energy sources, especially when they represent a high share in the power generation mix. This profitability would be further guaranteed if there exist also a heat demand. Thus, E-TES

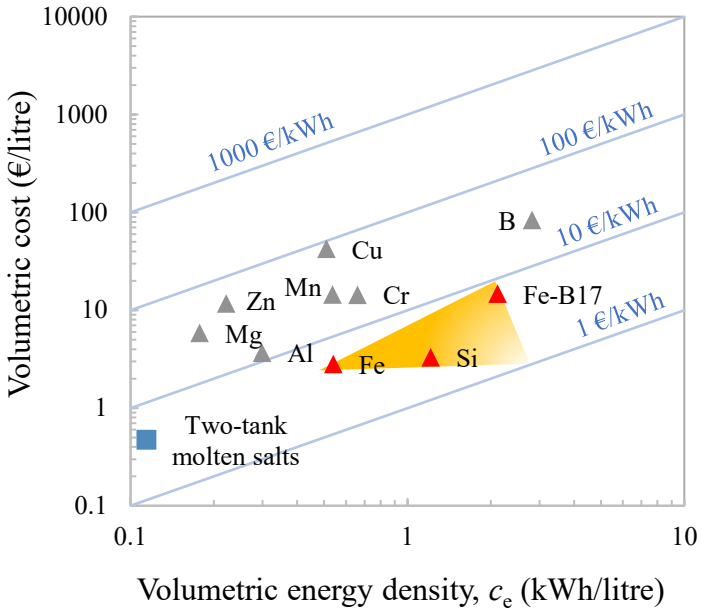


Figure 3: Volumetric cost (€/litre), volumetric energy density (kWh/litre) and the cost per energy capacity (in €/kWh) for several metallic phase change materials (PCMs) and that of the two-tank molten salt system as a reference. Iron, silicon and Iron-boron eutectic alloy (Fe-B17) are highlighted to illustrate their potential to reach costs per energy capacity lower than 10 €/kWh and energy densities greater than 1 kWh/litre.

is especially appealing for both storage and combined heat and power generation (CHP) in heat demanding sectors such as buildings, industry or district heating (5).

Silicon and ferrosilicon latent heat thermal batteries

The general concept of an E-TES system illustrated in Figure 1 can be implemented with many different technological options. An overview of currently ongoing industrial projects on E-TES can be found in (2). The most typical choice consists of resistive heating for the heat-to-power conversion, sensible heat in molten salts at ~ 590ºC (maximum) for heat storage, and Rankine engines for heat-to-power conversion. This specific choice is attributed to the high technological readiness level of all these components, which have been already validated in many different industrial sectors, especially at the CSP (Concentrated Solar Power). However, these systems are limited in terms of thermal-to-electric conversion efficiency (< 40 %) and energy storage density (~ 100 kWh/m^3). The later implies high costs per energy capacity (in €/kWh), not only because of the cost of the storage media (e.g. molten salt) but especially because of the cost of the container. Therefore, increasing energy density is important to reduce the size of the container and thus, minimize the cost per energy capacity.

Among all kinds of E-TES systems, the so-called latent heat thermal batteries are the ones with the highest energy density potential. In these systems energy is stored in the form of latent heat during the phase transformation of a material. Figure 4 shows the cost of several phase change materials (PCM) as a function of the volumetric energy density (latent heat, in kWh/m^3). Molten salt sensible heat storage (6) is also shown for reference, and the straight lines represent different costs per energy capacity. This figure shows that silicon and ferrosilicon PCMs have the greatest energy densities (> 1000 kWh/m^3) at the minimum costs per PCM energy capacity (< 10 €/kWh). Such high energy densities enable much smaller container sizes (10-fold smaller), which combined with the very low cost per PCM energy capacity could enable very low costs per stored energy capacity (< 50 €/kWh). This is well below Li-ion batteries (200 - 500 €/kWh) or other established electric energy storage technologies such as pumped hydroelectric (60-150 €/kWh).

Another advantage of latent heat thermal energy storage is the nearly isothermal energy release that ultimately results in higher round-trip conversion efficiencies, provided that heat is transferred at a temperature close to that of the solid-liquid interface. The latter is an historical challenge for latent heat storage based on salts, which are characterized by very small thermal conductivities. Thus, a complex encapsulation and heat exchanger design are needed to release the heat isothermally, which end up decreasing the energy density and increasing the cost. On the other hand, silicon and ferrosilicon alloys have thermal conductivities 100-fold higher than conventional salt-based PCMs (7,8), and thus, enable systems with higher PCM-to-container volume ratios and less complex heat exchanger designs, ultimately resulting in higher energy densities and potentially, lower costs.

The main challenge related to the use of silicon and ferrosilicon alloys as PCMs is their very high melting temperature (1414 ºC for silicon and 1538 ºC for iron). This is also an advantage from the energy conversion point of view, as it theoretically enables higher conversion efficiencies. However, very high temperatures also bring other technological challenges related to thermo-chemical compatibility with the container, as well as higher heat losses through the thermal insulation system (9). These issues have been addressed in the recently finished EU-project AMADEUS (10), where a new PCMs based on Fe-Si-B system have been developed having very high latent heat and less challenging melting temperature of ~ 1200ºC (11). The incorporation of boron in silicon-iron alloys is a very promising approach due to the extraordinarily high latent heat of boron of 2.82 kWh/l, more than twice than that of pure silicon. Despite pure boron has a prohibitive cost > 1000 €/kg, iron-boron alloys (e.g. Fe-B17 eutectic) could be produced at much lower costs. Thus, the production of low-cost Fe-Si-B alloys

appears to be an important field of research to find new materials that enable extremely low costs E-TES systems.

Another challenge concerns the ultra-high temperature energy conversion process. Most deployed Rankine engines are limited to maximum temperatures of ~ 600ºC. Temperatures higher than 1000ºC could be attained by Brayton engines that use Ni-alloys and ceramic thermal barrier coatings in the blades (12). The most advance gas turbines existing today are open-cycle Brayton engines that can operate at maximum turbine inlet temperatures of ~ 1600ºC (e.g. M501J series of Mitsubishi Hitachi Power Systems). However, reaching such high temperatures is challenging in close-cycle systems, which are the ones needed for E-TES applications. Close Brayton cycles use a heat exchanger instead of an internal combustor to heat the working fluid. Thus, such high-temperature and high-cost materials are not just needed in the blades, but also in other parts of the system (e.g. heat exchanger, valves and pipes). Less developed than open-cycle systems, close-Brayton have been mostly considered for future solar, space and fusion power systems, and the typically reported temperatures do not exceed ~ 850ºC (13,14). Currently, there exist two main options to tackle the challenges of very high temperature energy conversion: (1) increase the flow of the heat transfer fluid through the heat exchanger to reduce its temperature down to the operative limits of the heat engine, or (2) use solid state energy converters such as thermionics (TEC) or thermophotovoltaics (TPV) that enable ultra-high temperature operation. The later has been the goal of the recently finished AMADEUS project (10), where a new kind of hybrid thermionic-photovoltaic generator has been demonstrated (15,16). The use of TPV is being also targeted for E-TES applications by MIT (4) and Antora Energy.

Figure 4 shows a possible embodiment of a latent heat thermophotovoltaic (LHTPV) battery (17), indicating the different parts of the system, and showing how this system could be scaled-up for higher energy capacities. As explained elsewhere (17), this specific configuration intends to minimize the temperature gradient within the PCM and thus, ensure a minimal temperature gradient and minimal exergy loss. In this design, the PCM fills the gap between the two concentric cylinders that forms the crucible (or container). Electricity is introduced in the system through a series of heating elements that surround the crucible. During this process, the PCM changes from solid to liquid state, and thus, stores energy in the form of latent heat. When electricity is needed, the TPV generator is introduced within the (incandescent) cylindrical cavity formed by the crucible walls. The TPV generator comprises a number of infrared-sensitive photovoltaic cells (also named TPV cells) that directly produce electricity when irradiated by the thermal radiation coming from the incandescent walls of the crucible. Thus, it can produce power without establishing a direct contact with the very high temperature heat source. In order to keep the TPV cells relatively cold (< 100ºC), the

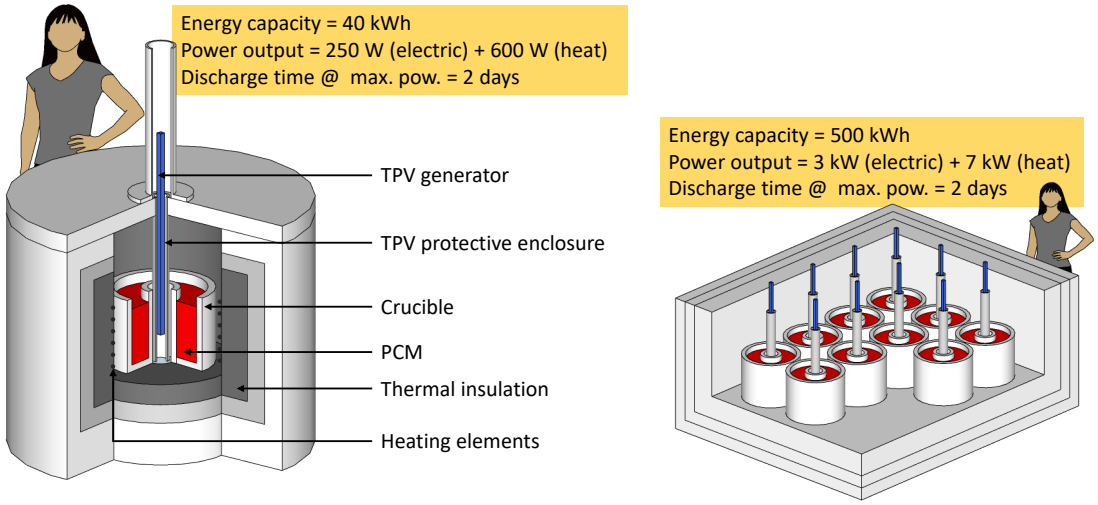


Figure 4: Example of a possible implementation of a latent heat thermophotovoltaic (LHTPV) battery comprising ultra-high temperature PCMs and TPV generators (17).

TPV generator needs to be actively refrigerated (e.g. by circulating water or other fluids). The low temperature (<100ºC) exhaust heat carried by the coolant fluid can be used for delivering other heating demands (e.g. domestic hot water) and even cooling demands (5). Also, a high temperature heat exchanger could be introduced within the furnace cavity to directly extract high temperature air or steam in a broad range of temperatures (e.g. 100 - 1000ºC) that could be directly used in an industrial process.

The main advantage of LHTPV with respect to other solutions based on dynamic heat engines (e.g. Brayton or Rankine) is the lack of moving parts and the ultra-compact design, which enables a modular solution for decentralized E-TES (5). Besides, the possibility of operating at very high temperatures, equalling the melting point of silicon and ferrosilicon PCMs, enables reaching very high conversion efficiencies. Current state of the art TPV devices have reached efficiencies of ~ 30 % at ~ 1200ºC (18), but higher efficiencies are expectable by improving the back-surface cell reflectors that are used to turn the far-IR radiation (not absorbed in the cell) back to the heat source. With these improvements, TPV cells operating at > 1200ºC could reach very high conversion efficiencies (> 40%) at very low costs per power capacity (< 500 €/kW) (4), both being essential features for enabling profitable E-TES applications.

Conclusions

Electric thermal energy storage (E-TES) is a cost-efficient solution for tackling intra-day (10 – 100 hours) fluctuation of variable renewable energy sources. The main requirements of the system are: (1) very low cost per energy capacity and (2) high conversion efficiency. Silicon and ferrosilicon-based PCMs are ideal storage media that enable very low PCM cost per energy capacity (< 10 €/kWh) and energy densities over 1000 kWh/m^3. The later is essential to reduce the size of the container, which represents

a substantial fraction of the total cost per energy capacity. Smaller containers also enable lower surface-to-stored energy ratios that mitigate the high heat losses through the thermal insulation system taking place at those high temperatures. Besides, the high melting temperature of silicon and ferrosilicon alloys (> 1200ºC) enables high conversion efficiencies, provided that heat engines are able to operate at those extreme temperatures. TPV energy conversion could be a solution to provide high conversion efficiencies and low cost per power capacity. However, further developments are needed to increase the conversion efficiency from present values of ~ 30 % to > 40 %.

References

1. Victoria M, Zhu K, Brown T, Andresen GB, Greiner M. The role of storage technologies throughout the decarbonisation of the sector-coupled European energy system. Energy Convers Manag. 2019 Dec 1;201:111977.

2. Okazaki T. Electric thermal energy storage and advantage of rotating heater having synchronous inertia. Renew Energy. 2020 May 1;151:563–74.

3. Albertus P, Manser JS, Litzelman S. Long-Duration Electricity Storage Applications, Economics, and Technologies. Joule. 2020 Jan 15;4(1):21–32.

4. Amy C, Seyf HR, Steiner MA, Friedman DJ, Henry A. Thermal energy grid storage using multi-junction photovoltaics. Energy Environ Sci. 2018 Nov 19;334–43.

5. Datas A, Ramos A, del Cañizo C. Techno-economic analysis of solar PV power-to-heat-to-power storage and trigeneration in the residential sector. Appl Energy. 2019 Dec 15;256:113935.

6. Montané M, Cáceres G, Villena M, O'Ryan R. Techno-Economic Forecasts of Lithium Nitrates for Thermal Storage Systems. Sustainability. 2017 May;9(5):810.

7. Zalba B, Marín JM, Cabeza LF, Mehling H. Review on thermal energy storage with phase change: materials, heat transfer analysis and applications. Appl Therm Eng. 2003 Feb 1;23(3):251–83.

8. Magomedov YB, Gadjiev GG. High-temperature thermal conductivity of silicon in the solid and liquid states. High Temp. 2008 May 30;46(3):422–4.

9. Datas A. Ultra-High Temperature Thermal Energy Storage, Transfer and Conversion - 1st Edition. Elsevier;

10. Datas A, Cristobal A.B., del Cañizo C, Antolín E, Beaughon M, Nikolopoulos N, et al. AMADEUS: Next generation materials and solid state devices for ultra high temperature energy storage and conversion. In: AIP Conference Proceedings [Internet]. 2018 [cited 2019 Jan 12]. p. 170004. Available from: https://aip-scitation-org.recursos.biblioteca.upc.edu/doi/abs/10.1063/1.5067168

11. Jiao J, Grorud B, Sindland C, Safarian J, Tang K, Sellevoll K, et al. The Use of Eutectic Fe-Si-B Alloy as a Phase Change Material in Thermal Energy Storage Systems. Materials. 2019 Jan;12(14):2312.

12. Klocke F, Klink A, Veselovac D, Aspinwall DK, Soo SL, Schmidt M, et al. Turbomachinery component manufacture by application of electrochemical, electro-physical and photonic processes. CIRP Ann. 2014 Jan 1;63(2):703–26.

13. Datas A, Martí A. Thermophotovoltaic energy in space applications: Review and future potential. Sol Energy Mater Sol Cells. 2017 Mar;161:285–96.

14. No HC, Kim JH, Kim HM. A review of helium gas turbine technology for high-temperature gas-cooled reactors. Nucl Eng Technol. 2007;39(1):21–30.

15. Datas A. Hybrid thermionic-photovoltaic converter. Appl Phys Lett. 2016 Apr 4;108(14):143503.

16. Bellucci A, Mastellone M, Serpente V, Girolami M, Kaciulis S, Mezzi A, et al. Photovoltaic Anodes for Enhanced Thermionic Energy Conversion. ACS Energy Lett. 2020;1364–70.

17. Datas A, Ramos A, Marti A, del Canizo C, Luque A. Ultra high temperature latent heat energy storage and thermophotovoltaic energy conversion. Energy. 2016 Jul 15;107:542–9.

18. Omair Z, Scranton G, Pazos-Outón LM, Xiao TP, Steiner MA, Ganapati V, et al. Ultraefficient thermophotovoltaic power conversion by band-edge spectral filtering. Proc Natl Acad Sci. 2019 Jul 30;116(31):15356–61.

Silicon for the Chemical and Solar Industry XV
Trondheim, Norway, June 15 – 18, 2020

Effect of operation parameters and formulation on the submicron and nano size silicon powder properties produced by mechanical grinding

B.E. Nilssen[1),2)], B.R. Henriksen[1)], R.A. Kleiv[2)]
1) Elkem ASA, Technology, Fiskåveien 100, 4675 Kristiansand, Norway
2) Department of Geoscience and Petroleum, Norwegian University of Science and Technology, S. P. Andersens veg 15a, 7031 Trondheim

Abstract

Mechanical grinding using stirred media mills is regarded as a promising route for the industrial production of submicron and nano size powders, but it is challenging to predict and control the product properties. Grinding of a metallurgical grade silicon quality provided by Elkem ASA, Silgrain® e-Si 410 was studied through a series of laboratory-scale experiments using a stirred media mill. The aim was to report the properties for the produced silicon powders (i.e. particle size, BET specific surface area, crystallite size, amount of amorphous silicon phase, concentration of contaminant and particle shape) when varying the suspension formulation (i.e. electrostatic stabilization), the target size for the silicon powder product (i.e. submicron or nano size), and the operation parameters (i.e. stirrer tip speed and grinding size). The grinding time and the specific energy input required to produce silicon powders with a d_{50} target of 100 nm varied between 14 and 3 h, and 43 and 97 $MJkg_{Si}^{-1}$, respectively. The properties of the produced silicon powders showed little variation with the exception of the crystallite size and the concentration of Zr which varied between 60 and 35 nm, and 1.16 and 1.70 wt.%, respectively. When the stirrer tip speed and the grinding media size were kept constant while varying the target particle size (i.e. d_{50}) the BET specific surface area, the amount of amorphous phase and the concentration of Zr increased while the crystallite size decreased as the d_{50} decreased. Changing the formulation did not produce silicon powders with significantly different properties.

Introduction

Submicron and nano size silicon materials are currently finding, or being considered for, a broad range of applications [1-8]. The potential use of silicon powder as the active anode material in the next generation of lithium ion batteries is receiving a lot of attention [9-13]. Each of these applications have different requirements with respect to the silicon powder properties. For anode materials the silicon particle size is stated to be of major importance and particles in the submicron and nano size range have been extensively studied [14-18]. Other properties of the silicon material (e.g. particle shape, crystallite size, amount of amorphous phase) are also considered to be of importance for the electrochemical performance in the lithium ion batteries [13,19,20]. The ability to control the powder properties throughout the production process is essential. A top-down approach for processing of nanomaterials (i.e. starting with bulk material) using high energy mills represents an interesting low-cost and high-capacity alternative to other available production routes including other top-down processes or bottom-up (i.e. starting with atoms/molecules) approaches for producing nanomaterials [21-24]. However, it is more

challenging to predict and control the product properties during mechanical grinding [22]. Elkem ASA is one of the world's leading suppliers of metallurgical silicon and is currently investigating the possibility to deliver silicon powders in the submicron and nano size range produced by ultrafine grinding with the aim to increase the company's portfolio of silicon materials.

Stirred media mills is one type of high energy mill and can be employed for lab scale experiments as well as for industrial scale production of submicron and nano size powders by wet mechanical grinding. The formulation (i.e. suspension stability) is important for the production of submicron particles in particular. This is due to the possibility of the formation of agglomerates which could affect the end product properties [25,26]. Kwade and Schwedes [27] have studied various aspects of the operation of stirred media mills, and a stress model has been developed in order to describe the energy transfer from the grinding media to the material to be ground. It correlates the operation parameters of the stirred media mill to the energy transfer which in terms will affect the product properties. According to the stress model [28], the stress energy, *SE*, in the stirred media mill during operation is dependent on the size (i.e. diameter) of the grinding media, d_{GM}, the stirrer tip speed, v_t, the density of the grinding media, ρ_{GM}, and can be estimated according to Eq. (1).

$$SE \propto d_{GM}^3 \cdot v_t^2 \cdot \rho_{GM} \tag{1}$$

The specific energy input will also affect the product properties. The specific energy input to the mill, E_m, can be estimated according to Eq. (2) which includes the power draw of the mill during operation, P, the no-load power, P_0 , the mass of the material to be ground, m, and the grinding time, t.

$$E_m = \frac{\int_0^t \left(P(t) - P_0 \right) dt}{m} \tag{2}$$

Mechanical grinding of silicon has been reported in previous studies using various mill types for various purposes (i.e. as a tool for preparing powders for further studies or for the purpose of studying the grinding process itself and the resulting silicon powder properties) [13, 29-35]. Only a limited number of studies have included the use of the industrial scalable stirred media mill [36-42]. The work described in this paper aims at reporting the silicon powder properties (i.e. particle size, BET specific surface area, crystallite size, amount of amorphous silicon phase, concentration of contaminates and particle shape) produced by ultrafine grinding of an Elkem ASA metallurgical grade silicon quality using a lab scale stirred media mill. The product properties will be reported as a function of the suspension formulation, the target product size as well as stirrer tip speed and grinding media size. I addition to reporting the properties of the silicon powders produced some practical aspects relevant for the industrial production of such powders will be presented.

Materials and methods

Silicon feed and grinding liquid

Silgrain® e-Si 410 (Elkem ASA) was the feed material in the grinding experiments. This is a silicon material produced in a hydro-metallurgical leaching process with a silicon content reported to be equal to 99.7 wt.%. It is characterized with a d_{10} of 0.750 µm, a d_{50} of 3.353 µm, a d_{90} of 6.610 µm and a specific surface area of 3.34 m^2g^{-1}. The grinding liquid consisted of absolute ethanol (99.99 %, Merck KGaA). A solution (0.5-1 M) of sodium hydroxide (NaOH,

99.98 %, Merck KGaA) and ethanol was used to achieve electrostatic stabilization of the suspension.

The grinding experiments

The grinding experiments were conducted at Institute for Particle Technology (Technical University of Braunschweig) using a PML2 stirred media mill (Bühler Holding AG) operated in circuit mode, as shown in Fig. 1.

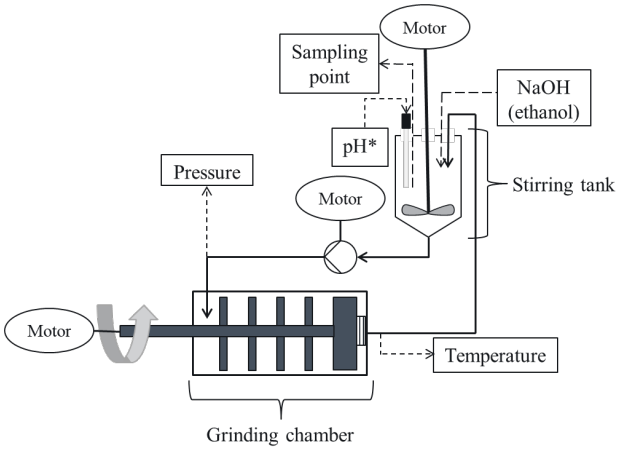


Figure 1: The grinding circuit.

The mill was equipped with a grinding chamber (0.71 L) having a smooth lining and a disc type stirrer, both in silicon carbide. The stirring vessel was open to air during the grinding process. The mill was operated with a constant filling ratio of the grinding chamber, (80 %), total suspension volume (1 L), pump speed (30 Lh^{-1}), solid concentration, (20 wt.%), and temperature (< 30°C), using grinding media made of yttrium stabilized zirconium oxide (ZrO_2 (Y_2O_3), Sigmund Linder GmbH) with a density of 6050 kgm^{-3}. To study the effect of operation parameters, the stirrer tip speed was varied between 6 and 12 ms^{-1} and three different grinding media sizes were used, 245, 315 or 430 µm. The power draw was recorded during the grinding experiment and the no-load power was registered directly after the end of each grinding experiment. Experiments were conducted both with and without the addition of the ethanol based NaOH solution. When aiming to stabilize the suspension electrostatically the solution was added until a pH* (i.e. the pH for a non-aqueous solution measured using a standard pH electrode for aqueous solutions) in the range of 7.5 to 8.5 was obtained in the stirring tank. This procedure is described by Nöske et al. [36]. The pH* was measured in the suspension during the grinding process.

At the end of each experiment, samples of the suspension were collected for determination of particle size, zeta potential, viscosity and for visual inspection using scanning electron microscopy (SEM). A sample of the suspension was dried using a rotary evaporator (Laborota 4001 efficient, Heidolph Instruments GmbH & CO) to produce dry powder for the determination of BET specific surface area, crystallite size and amount of amorphous silicon phase. All the dry samples were stored and handled in argon gas or under vacuum.

Characterization of the powder properties

The particle size and the zeta potential of the suspension were analysed by using a combined acoustic and electroacoustic spectrometer (DT1200, Dispersion Technology Inc.), whereas its viscosity was determined as a function of the shear rate using a rotational viscometer (Bohlin

Gemini 2, Malvern Instruments Ltd.). A qualitative assessment of the particle shape was obtained from scanning electron microscopy studies using a Merlin Compact (Carl Zeiss AG) operated at 3.0 kV and 3.5 mm working distance using either the InLensDuo or the secondary electron detector.

The specific surface area (SSA) for the ground products was measured with a NOVA Touch LX^4 gas adsorption analyzer (Quantachrome Instruments) using the Brunauer-Emmett-Teller theory (BET). The samples were degassed overnight under vacuum at 250°C before the BET specific surface area, SSA_{BET}, was determined using a 5-points method with nitrogen as the adsorption gas. Both the crystallite size and the amount of amorphous silicon phase were quantified using X-ray diffraction analysis (XRD). The samples were prepared by adding ~10 wt.% corundum spiking material (alumina powder, SRM 676a, NIST). The XRD instrument (D8 Advance, Bruker Corporation) was operated with Cu Kα-radiation (λ = 0.15406 nm). The step size was set equal to 0.02° in the 2θ range of 20-80° with a counting time of 1 s per step. The crystallite size was quantified by the Scherrer equation using the integral breadth which was determined by the Rietveld refinement in the Bruker software TOPAS. The Lorentzian crystallite size was identified to contribute to the peak broadening with Lorentzian microstrain detected in all the samples. The amount of amorphous silicon phase was quantified using the internal standard method based on the crystallographic open database using the Rietveld refinement.

Results and discussion

Effect of electrostatic stabilization on the silicon powder properties

Ultrafine grinding of silicon in alcohols is found to be beneficial both in terms of reduced hydrogen gas formation and oxidation compared to the use of water, and as well in terms of improved particle dispersion and stability without use of any additives [43-46]. The initial grinding experiments using ethanol as grinding liquid without use of ethanol based NaOH solution were characterized with a decreasing pH* and a zeta potential in the range of -10 mV (Fig. 2). The decreasing pH* suggests the reaction between the newly formed silicon surface and the ethanol molecule forming ethoxy groups on the particle surface followed by an increased concentration of H^+-ions in the suspension. The low absolute value of the zeta potential is an indication of a correspondingly low surface charge which probably is too low to provide electrostatic stabilization. By visual inspections of the suspension in the stirring tank it was evident that a change in the suspension behavior occurred during the grinding process which is assumed to be due to the formation of particle agglomerates. The amount of agglomeration was observed to vary between the formation of a “slightly viscous” suspension and the formation of a “gel/pudding” for the same formulation (i.e. ethanol). These observations were confirmed by viscosity studies. At low shear rates (i.e. $<5\ s^{-1}$) the suspension was characterized with a viscosity between 3.5 Pas for the “slightly viscous” suspension and 25 Pas for the “gel/pudding”. At high shear rates (i.e. $>175\ s^{-1}$) the viscosity decreased to a level below 0.1 Pas indicating shear thinning behavior. For comparison, the addition of ethanol based NaOH solution for controlling the pH* in the suspension provided a zeta potential lower than -20 mV and a viscosity below 0.01 Pas for all the shear rates studied which indicates limited agglomeration due to electrostatic stabilization of the particles (i.e. “stable” behavior for the suspension).

The differences in suspension behavior (i.e. “slightly viscous” or “stable”) due to agglomeration did not affect the development of the particle size produced within the stirred media mill nor the specific energy input (estimated according to Eq. (2)) required to produce a powder with a d_{50} of

100 nm (Fig. 2). This could be explained by the low viscosity within the grinding chamber during operation due to the high shear forces exerted by the mill. The grinding experiment for the suspension characterized as a "gel/pudding" was stopped at a d_{50} equal to 0.137 µm due to practical reasons which were not due to the suspension behavior. The characterized particle size (i.e. d_{10}, d_{50} and d_{90}) for the suspension characterized as "gel/pudding" presented as a function of the specific energy input correlates well with the development in the particle size (i.e d_{10}, d_{50} and d_{90}) for the "slightly viscous" and "stable" suspensions. Uncertainties in the grinding process for the electrostatic stabilized suspension and the uncertainty in the analysis seems to cause more variation in the product properties than the observed particle agglomeration (Table 1).

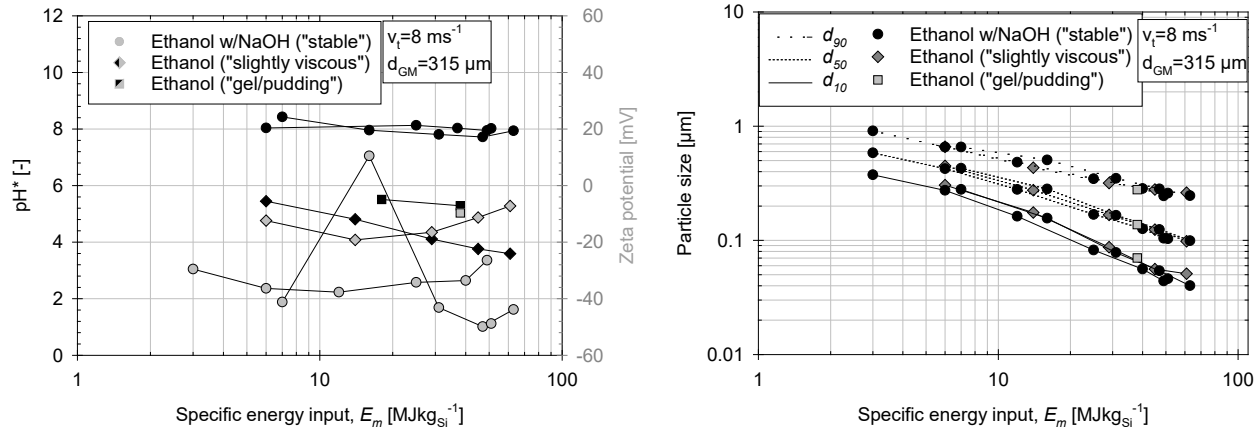


Figure 2: Measured pH* and zeta potential (left), and particle size (right) as a function of the specific energy input for suspensions produced with or without ethanol based NaOH solution at constant stirrer tip speed (8 ms^{-1}) and grinding media size (315 µm).

The properties of the silicon powders in the initial experiments were not significantly different, as evident from Table 1. The particle shape as investigated with SEM analysis was observed to be the same for the "slightly viscous" and "stable" suspensions and was characterized as irregularly shaped flaky particles (Fig. 3). For the same reason as stated in the previous section (i.e. not comparable particle size of d_{50}), the product properties in the suspension behaving as a "gel/pudding" were not evaluated.

Table 1: Properties of silicon powder produced with or without the addition of ethanol based NaOH solution at constant stirrer tip speed (8 ms^{-1}) and grinding media size (315 µm).

Formulation (suspension behavior)	Ethanol ("slightly viscous")	Ethanol w/NaOH ("stable")†
Grinding time, t [h]	8	8 ± 0
Specific energy input, E_m [$MJkg_{Si}^{-1}$]	61	54 ± 16
Particle size, d_{10} [µm]	0.051	0.043 ± 0.006
Particle size, d_{50} [µm]	0.098	0.102 ± 0.005
Particle size, d_{90} [µm]	0.262	0.250 ± 0.016
Specific surface area, SSA_{BET} [m^2g^{-1}]	97.6	88.3 ± 10.6
Crystallite size [nm]	42	51 ± 10
Amount of amorphous phase, wt.%	60	55 ± 6
Concentration of Zr, wt.%	1.16	1.16 ± 0.11

†Grinding time, specific energy input and product properties are reported as average values based on three identical grinding experiments. The error is given as 2 standard deviations.

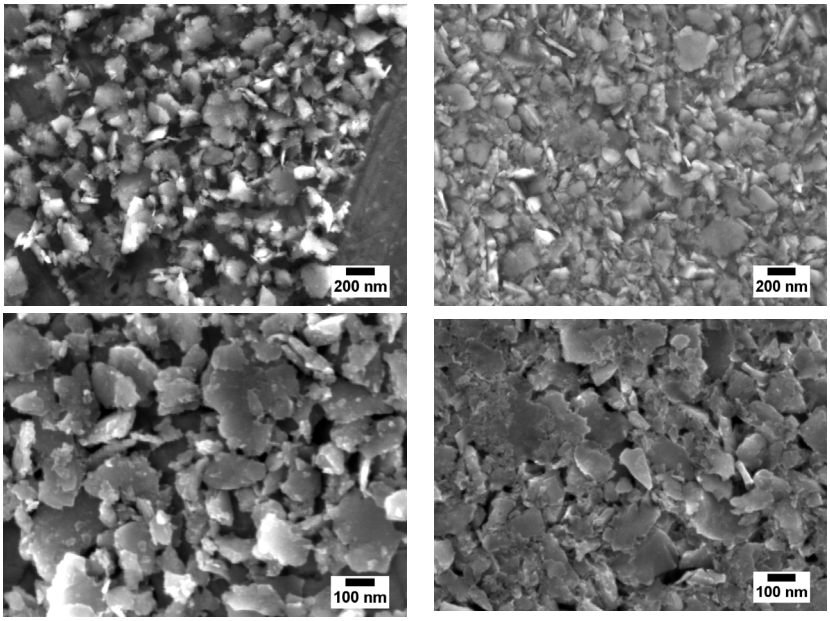


Figure 3: SEM images of silicon powder particles ground in ethanol (i.e. "slightly viscous") (left) and in ethanol with ethanol based NaOH solution (i.e. "stable") (right) at a constant stirrer tip speed (8 ms^{-1}) and grinding media size (315 μm).

The observed increase in viscosity at low shear rates for the suspensions where no ethanol based NaOH solution was added is assumed to be due to particle agglomeration. The factors causing the difference in the degree of agglomeration (i.e. "slightly viscous" vs. "gel/pudding") is however not understood and needs to be investigated further. Several mechanisms can be considered: (i) excessive evaporation of ethanol leading to an increased solid concentration, (ii) uptake of water or oxygen from air via the stirring tank, (iii) contaminants in the stirred media mill, or (iv) chemical variation in the silicon feed material. Even though the agglomeration causing a "slightly viscous" suspension did not have any significant effects on neither the specific energy input nor the other product properties compared to the electrostatic stabilized suspension (i.e. "stable" suspension), the formation of "gel/pudding" is undesirable for large scale production of silicon suspension due to the following challenges: (i) insufficient mixing in the stirring tank, and (ii) clogging of the grinding circuit and pipes used for the post-grinding handling. The suspension in all the grinding experiments presented in the following sections were stabilized electrostatically in order to avoid the possibility for uncontrolled formation of "gel/pudding" to occur.

Effect of reducing the target particle size on the silicon powder properties

During the grinding process the pH* of the suspension was kept between 7.5 and 8.5 by adding the required amount of the ethanol based NaOH solution. The suspension was characterized with a zeta potential in the range of -35 to -45 mV and a viscosity lower than 0.01 Pas for all shear rates studied, which indicates successful electrostatic stabilization of the particles. Silicon powders characterized with a d_{50} equal to 500, 300 and 100 nm were produced and the development in particle size as a function of specific energy input is provided in Fig. 4. The particle sizes (i.e. d_{10}, d_{50} and d_{90}) decreases exponentially as a function of an increased specific energy input as well as an increased grinding time. The specific energy input increased by more than a factor of 10, from 5.0 to 54 $MJkg_{Si}^{-1}$ when the d_{50} for the silicon powder product was reduced from 500 to 100 nm. The grinding time increased from 0.72 to 8 h (i.e. a factor of 11) for the same size reduction (Table 2).

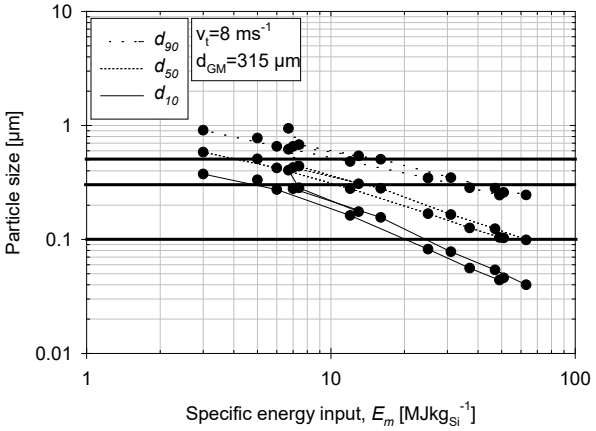


Figure 4: Particle size as a function of the specific energy input for suspensions produced with various d_{50} target size (indicated by bold horizontal lines) at a constant stirrer tip speed (8 ms^{-1}) and grinding media size (315 µm).

The product properties are provided in Table 2. As expected, the BET specific surface area increases with the decreasing particle size (i.e. d_{50}) and reached a value of 88.3 m^{2}g^{-1} for the silicon powder with a d_{50} of 100 nm. Formation of such a high BET specific surface area can be explained by the relatively small particle size combined with the observed particle shape. The silicon powders with a d_{50} of 500, 300 and 100 nm were all consisting of the same type of particle shape characterized as irregularly and flaky particles (Fig. 6). The crystallite size decreased with the decreasing particle size (i.e. d_{50}) and reached a value of 51 nm for the powder with a d_{50} of 100 nm. Both the amount of amorphous silicon phase and the contamination of Zr from the grinding media were observed to increase as a function of the decreasing particle size (i.e. d_{50}). The concentration of Zr increased from 0.29 to 1.16 wt.% as the d_{50} for the product went from 500 to 100 nm. The amount of amorphous silicon phase was quantified to reach a level as high as 55 wt.% for the silicon powder with a d_{50} of 100 nm.

Table 2: Properties of silicon powder produced with various d_{50} target size at a constant stirrer tip speed (8 ms^{-1}) and grinding media size (315 µm).

Target size for d_{50} [nm]	500	300	100[†]
Grinding time, t [h]	0.72	1.83	8
Specific energy input, E_m [MJkg$_{Si}^{-1}$]	5	13	54
Particle size, d_{10} [µm]	0.334	0.175	0.043
Particle size, d_{50} [µm]	0.509	0.308	0.102
Particle size, d_{90} [µm]	0.775	0.542	0.250
Specific surface area, SSA_{BET} [m^{2}g^{-1}]	15.8	47.0	88.3
Crystallite size [µm]	222	152	51
Amount of amorphous phase, wt.%	11	26	55
Concentration of Zr, wt.%	0.29	0.75	1.16

[†]Grinding time, specific energy input and product properties are reported as average values based on three identical grinding experiments.

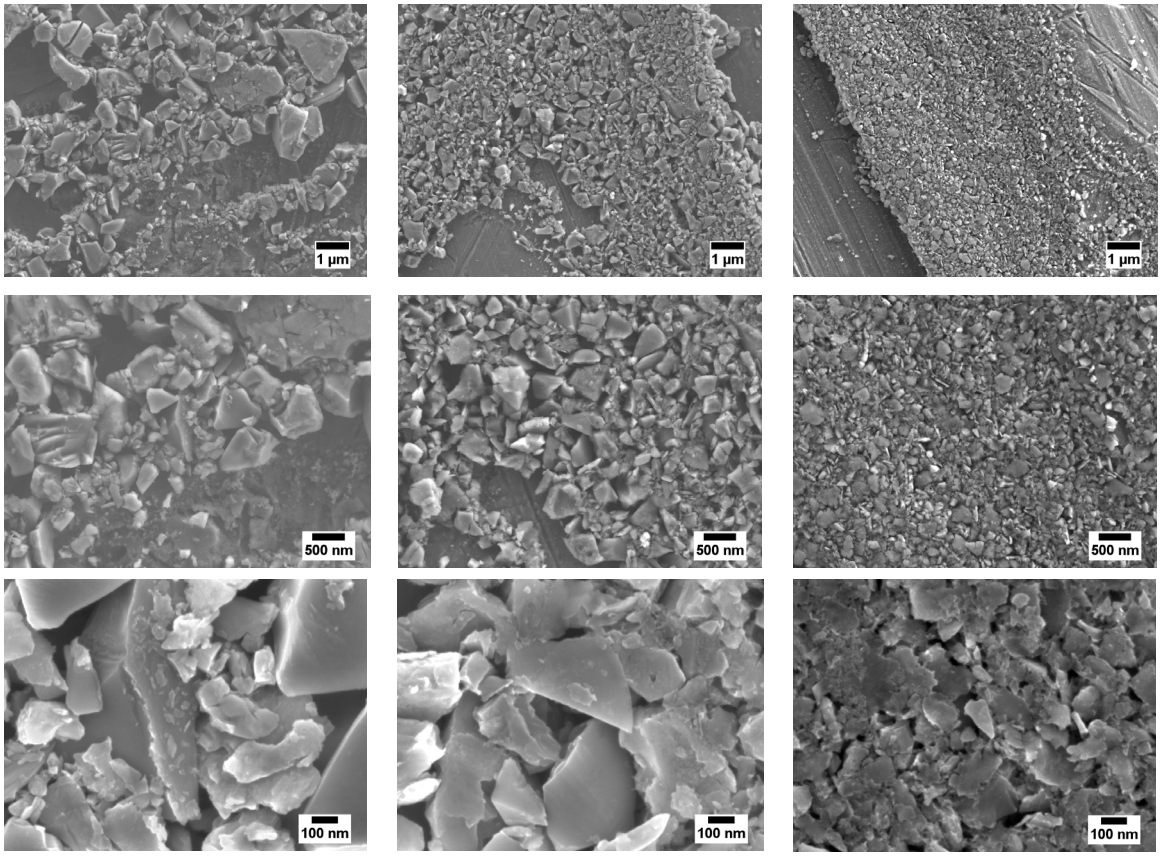


Figure 5: SEM images of silicon powder particles characterized with various d_{50} target size 500 nm (left), 300 nm (middle) and 100 nm (right) and produced at a constant stirrer tip speed (8 ms^{-1}) and grinding media size (315 µm).

Effect of various combination of stirrer tip speed and grinding media size on the silicon powder properties

During the grinding process the pH* of the suspension was kept between 7.5 and 8.5 by adding the required amount of the ethanol based NaOH solution. The suspension was characterized with a zeta potential in the range of -35 to -45 mV and a viscosity lower than 0.02 Pas for all shear rates studied, which indicates successful electrostatic stabilization of the particles. Silicon powders with a d_{50} target size of 100 nm were produced by various combinations of stirrer tip speeds and grinding media sizes. The correlation between the particle sizes (i.e. d_{10}, d_{50} and d_{90}) and the specific energy input is provided in Fig. 6. The continuously decreasing slope for all the curves provided in Fig. 6 indicate sufficient stress energy for efficient size reduction of the silicon feed material for all the studied combinations of stirrer tip speed and grinding media size.

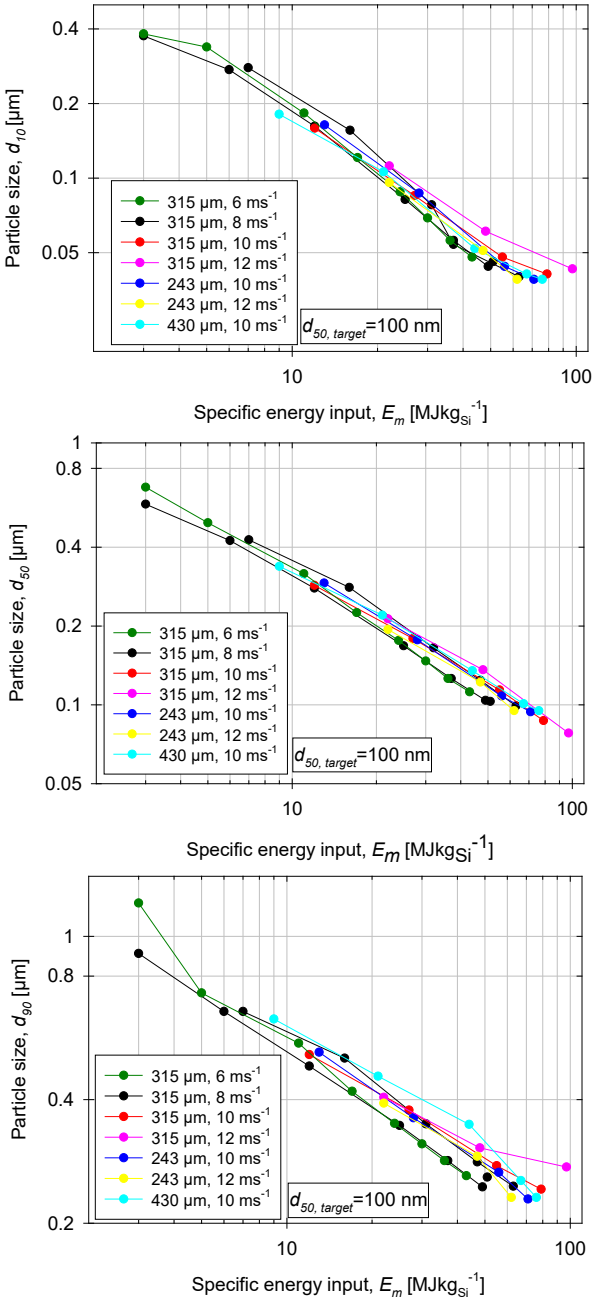


Figure 6: Particle size, d_{10} (upper), d_{50} (middle), d_{90} (lower), as a function of the specific energy input produced using various combinations of stirrer tip speed and grinding media size with a constant d_{50} target of 100 nm.

The specific energy input for the production of the silicon powders with a d_{50} target size of 100 nm varied from 43 to 97 MJkg$_{Si}^{-1}$ (i.e. a factor of more than 2). Presenting the specific energy input as a function of the stress energy (i.e. corresponding to various combinations of stirrer tip speed and grinding media size and estimated according Eq. (1)) would be expected to be described by one fitted U-shaped curve. The minimum at this curve would correspond to the optimum stress energy at which the d_{50} target size of 100 nm can be produced with a minimum specific energy input [28]. However, the span in stress energy (i.e. a factor of 7) for the grinding experiments included in this work seems to be too small to identify such an energy optimum.

One observes the tendency for a decreasing specific energy input when the stress energy is decreased. Meaning that the grinding experiment operated with a combination of stirrer tip speed and grinding media size providing the smallest stress energy studied (i.e. experiment. nr 1 indicated in Fig. 7) should be closer to the point of energy optimum than any of the other grinding experiments included in this work.

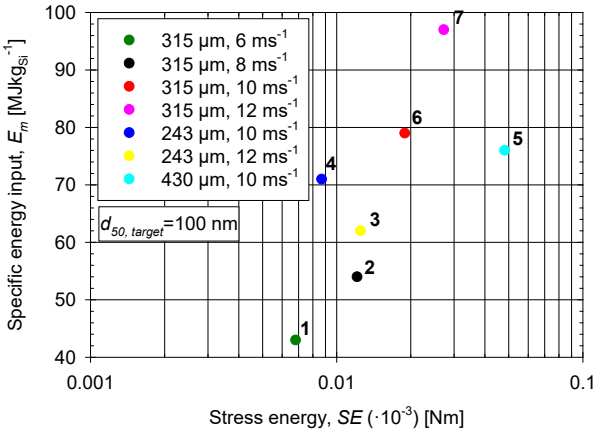


Figure 7: Specific energy input as a function of stress energy for grinding experiments operated with various combination of stirrer tips speed and grinding media size. Each number corresponds to a grinding experiment.

The grinding time for the production of the silicon powders characterized with a d_{50} in the range of 100 nm varied between 3 and 14 h (i.e. a factor of almost 5). The characterized properties of the produced silicon powders along with the operation parameters, the grinding time and the specific energy input are provided in Table 3. Images collected during the SEM analysis are provided in Fig. 8, representing silicon powder produced with a range of specific energy inputs, grinding times, and stress energies.

Table 3: Properties of silicon powder produced using various combinations of stirrer tip speed and grinding media size with a constant d_{50} target of 100 nm.

Grinding experiment	1	2†	3	4	5	6	7
Stirrer tip speed, v_t [ms^{-1}]	6	8	12	10	10	10	12
Grinding media size, d_{GM} [µm]	315	315	243	243	430	315	315
Stress energy, SE ($\cdot 10^{-3}$) [Nm]	0.007	0.012	0.013	0.009	0.048	0.019	0.027
Grinding time, t [h]	14	8	3	5	6.64	6	4
Specific energy input, E_m [MJkg$_{Si}^{-1}$]	43	54	62	71	76	79	97
Particle size, d_{10} [µm]	0.048	0.043	0.039	0.039	0.039	0.041	0.043
Particle size, d_{50} [µm]	0.112	0.102	0.095	0.094	0.095	0.087	0.078
Particle size, d_{90} [µm]	0.261	0.250	0.231	0.229	0.231	0.242	0.274
Specific surface area, SSA_{BET} [m^{2}g^{-1}]	89.5	88.3	94.6	99.0	101.0	104.8	100.4
Crystallite size [nm]	60	51	43	49	45	35	35
Amount of amorphous silicon, wt.%	48	55	51	45	42	50	65
Concentration of Zr, wt.%	1.18	1.16	1.52	1.63	1.53	1.54	1.70

†Grinding time, specific energy input and product properties are reported as average values based on three identical grinding experiments.

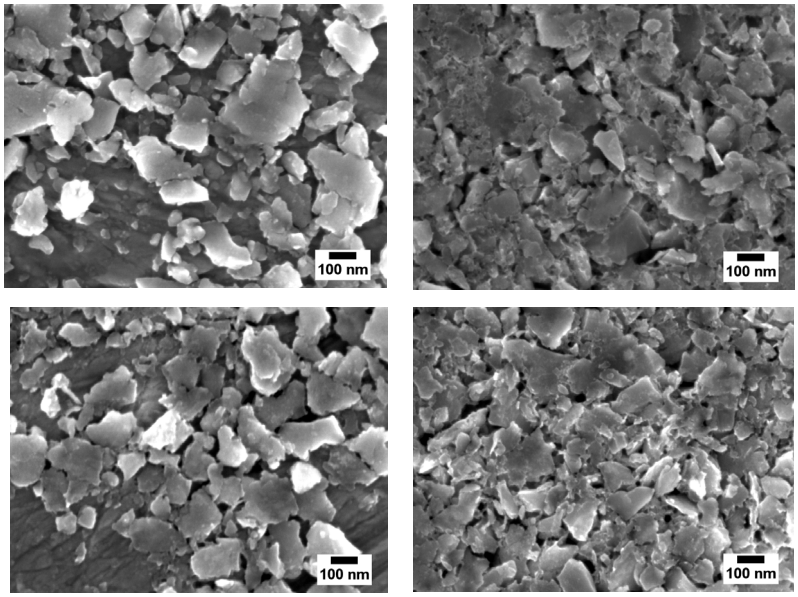


Figure 8: SEM images of silicon powder particles produced using various combinations of stirrer tip speed and grinding media diameter and a constant d_{50} target of 100 nm corresponding to grinding experiment nr. 1 (upper left), grinding experiment nr. 2 (upper right), grinding experiment nr. 3 (lower left), grinding experiment nr. 5 (lower right).

The silicon powders were characterized with a d_{50} target size of 100 nm. The small particle size in combination with the observed irregularly shaped flakey particles can describe the high BET specific surface areas reported in Table 3. Interestingly is the observed stable value for the quantified amount of amorphous silicon phase for all the powders produced with a d_{50} target of 100 nm. The reported values for the crystallite size and the concentration of Zr show a negative and positive correlation with the increased specific energy input, respectively. The crystallite size varied between 60 and 35 nm, and the concentration of Zr was reported to be in the range of 1.18 and 1.70 wt.%. From a production point of view, if the reported variation in crystallite size and concentration of Zr are acceptable for the end application this means that the grinding process could be operated in terms of the lower specific energy input or the lower grinding time (i.e. higher production capacity).

Conclusions

The product properties (i.e. BET specific surface area, crystallite size, amount of amorphous silicon and concentration of Zr) are changing with the d_{50} target size for the produced silicon powder when the suspension was stabilized electrostatically, and stirrer tip speed and the grinding media size were kept constant. The silicon powder with a d_{50} equal to 0.509 µm was characterized with the lowest SSA_{BET} (15.3 m^2g^{-1}), the smallest amount of amorphous silicon (11 wt.%), the lowest concentration of Zr (0.29 wt.%) and the largest crystallite size (222 nm). The silicon powder with a d_{50} equal to 0.102 µm was characterized with the highest SSA_{BET} (88.3 m^2g^{-1}), the largest amount of amorphous silicon (55 wt.%), the largest concentration of Zr (1.16 wt.%) and the smallest crystallite size (51 nm). Various combinations of the stirrer tip speed and grinding media size were used in order to produce silicon powders with a particle size (i.e. d_{50}) targeted 100 nm for a stabilized suspension. The grinding time and the specific energy input varied between 14 and 3 h, and 43 and 97 $MJkg_{Si}^{-1}$, respectively. The crystallite size varied between 60 and 35 nm and shows a negative correlation with the increasing specific energy input. The concentration of Zr varied between 1.16 wt.% and 1.70 wt.% and shows a positive

correlation with the specific energy input. The crystallite size showed a negative correlation with specific energy input. The other silicon powder properties (i.e. BET specific surface area, the amount of amorphous silicon phase and the particle shape) showed little variation. Hence, provided that the reported crystallite size and the concentration of Zr are within the acceptable range from an application point of view the grinding process can be operated with lower specific energy input or lower grinding times (i.e. higher capacity). An increased viscosity was observed for the non-stabilized suspension compared to their stabilized counterparts. However, it did not significantly affect the product properties nor the specific energy input to produce a silicon powder with a d_{50} target of 100 nm.

Acknowledgement

This work has been financially supported by Elkem ASA and the Norwegian Research Council through the Industrial Ph.D. Scheme (project number: 264144). The authors acknowledge Astrid Storesund (Elkem ASA) for conducting the ICP-OES analysis. Authors are also very grateful to the people in the Powder and Slurry Processes group at the Institute for Particle Technology at the Technical University of Braunschweig for providing the necessary grinding equipment, their enlightening discussions and feedback. To be mentioned in particular M.Sc. Markus Nöske, Dr.-Ing. Sandra Breitung-Faes, and Prof. Dr.-Ing. Arno Kwade.

References

1. E.M. DeLiso, A. Bleier, *Nonaqueous Processing of Silicon for Reaction-Bonded Silicon Nitride*, Journal of the American Ceramic Society, **76**, 1993, p81
2. S. Mizuta, W.R. Cannon, A. Bleier, H.S. Haggerty, *Wetting and Dispersion of Silicon Powder Without Deflocculants*, Ceramic Bulletin, **61**, 1982, p41
3. A. Reindl, A. Voronov, P.K. Gorle, M. Rauscher, A. Roosen, W. Peukert, *Dispersing and stabilizing silicon nanoparticles in a low-epsilon medium*, Colloids and Surfaces A: Physicochemical and Engineering Aspects, **320**, 2008, p183
4. A.S. Heintz, M.J. Fink, B.S. Mitchell, *Mechanochemical Synthesis of Blue Luminescent Alkyl/Alkenyl-Passivated Silicon Nanoparticles*, Advanced Materials, **19**, 2007, p3984
5. F. Erogbogbo, T. Lin, P.M. Tucciarone, K.M. Lajoie, L. Lai, G.D. Patki, P.N. Prasad, M.T. Swihart, *On-demand hydrogen generation using nanosilicon: splitting water without light, heat, or electricity*, Nano letters, **13**, 2013, p451
6. L. Xu, S. Ashraf, J. Hu, P.P. Edwards, M.O. Jones, E. Hadzifejzovic, J.S. Foord, *Ball-milled Si powder for the production of H2 from water for fuel cell applications*, International Journal of Hydrogen Energy, **41**, 2016, p12730
7. J.W. Aptekar, M.C. Cassidy, A.C. Johnson, R.A. Barton, M. Lee, A.C. Ogier, C. Vo, M.N. Anahtar, R. Yin, S. Bhatia, C. Ramanathan, D.G. Cory, A.L. Hill, R.W. Mair, M.S. Rosen, R.L. Walsworth, C.M. Marcus, *Silicon Nanoparticles as Hyperpolarized Magnetic Resonance Imaging Agents*, ACS Nano, **3**, 2009, p4003
8. E. Tolstik, L.A. Osminkina, C. Matthäus, M. Burkhardt, K.E. Tsurikov, U.A. Natashina, V.Y. Timoshenko, R. Heintzmann, J. Popp, V. Sivakov, *Studies of silicon nanoparticles uptake and biodegradation in cancer cells by Raman spectroscopy*, Nanomedicine: Nanotechnology, Biology, and Medicine, **12**, 2016, p1931
9. M. Ashuri, Q. He, L.L. Shaw, *Silicon as a potential anode material for Li-ion batteries: where size, geometry and structure matter*, Nanoscale, **8**, 2016, p74
10. Y. Jin, B. Zhu, Z. Lu, N. Liu, J. Zhu, *Challenges and Recent Progress in the Development of Si Anodes for Lithium-Ion Battery*, Advanced Energy Materials, **7**, 2017, p1

11. Y. Sun, K. Lui, Y. Zhu, *Recent Progress in Synthesis and Application of Low-Dimensional Silicon Based Anode Material for Lithium Ion Battery*, Journal of Nanomaterials, **2017,** 2017, p1
12. E. Hanelt, S. Haufe, *Electrode material and use thereof in lithium ion batteries*, 2014, patent
13. M. Gauthier, D. Mazouzi, D. Reyter, B. Lestriez, P. Moreau, D. Guyomard, L. Roué, *A low-cost and high performance ball-milled Si-based negative electrode for high-energy Li-ion batteries*, Energy & Environmental Science, **6**, 2013, p2145
14. S. Haufe, *Silicon particle-containing anode materials for lithium ion batteries*, 2018, patent
15. Z. Xu, J. Yang, Y. Nuli, J. Wang, S.-I. Hirano, *Silicon Microparticle Anodes with Self-Healing Multiple Network Binder*, Joule, **2**, 2018, p950
16. Y. Jin, B. Zhu, Z. Lu, N. Liu, J. Zhu, *Challenges and Recent Progress in the Development of Si Anodes for Lithium-Ion Battery*, Advanced Energy Materials, **7**, 2017, p1
17. M. Ashuri, Q. He, L.L. Shaw, *Silicon as a potential anode material for Li-ion batteries: where size, geometry and structure matter*, Nanoscale, **8**, 2016, p74
18. Y. Sun, K. Lui, Y. Zhu, *Recent Progress in Synthesis and Application of Low-Dimensional Silicon Based Anode Material for Lithium Ion Battery*, Journal of Nanomaterials, **2017,** 2017, p1
19. J. Lyubina, B. Fringes, A. Höfler, R. Ströger, S. Bade, *Industrial-scale synthesis of high performance Si-based nanopowders for energy storage applications*, Silicon for the Chemical and Solar Industry XIV, 2002, p21
20. G. Zhu, Y. Wang, S. Yang, Q. Qu, H. Zheng, *Correlation between the physical parameters and the electrochemical performance of a silicon anode in lithium-ion batteries*, Journal of Materiomics, **5**, 2019, p.164
21. T.P. Yadav, R.M. Yadav, D.P Singh, *Mechanical Milling: a Top Down Approach for the Synthesis of Nanomaterials and Nanocomposites, Nanoscience and Nanotechnology*, **2**, 2012, p27
22. M.H. Enayati, F.A. Mohamed, *Application of mechanical alloying/milling for synthesis of nanocrystalline and amorphous materials*, International Materials Reviews, **59**, 2014, p394
23. P. Balaz, *Mechanochemistry in Nanoscience and Minerals Engineering*, Springer-Verlag Berlin Heidelberg, **1**, 2008
24. B.A. Wills, J.A. Finch, *Chapter 7 - Grinding Mills* In: Wills BA, Finch JA (eds) Wills' Mineral Processing Technology, Butterworth-Heinemann, **8**, 2016, p147
25. S. Mende, F. Stenger, W. Peukert, J. Schwedes, *Mechanical production and stabilization of submicron particles in stirred media mills*, Powder Technology, **132**, 2003, p64
26. F. Stenger, W. Peukert, *The Role of Particle Interactions on Suspension Rheology – Application to Submicron Grinding in Stirred Ball Mills*, Chemical Engineering & Technology, **26**, 2002, p177
27. A. Kwade, J. Schwedes, *Chapter 6 Wet Grinding in Stirred Media Mills* in: Salman AD, Ghadiri M, Hounslow MJ (eds) Handbook of Powder Technology, Elsevier Science B.V., **12**, 2007, p251
28. A. Kwade, *A Stressing Model for the Description and Optimization of Grinding Processes*, Chemical Engineering & Technology, **26**, 2003, p199
29. E.A. Odo, D.T. Britton, G.G. Gonfa, M. Harting, *Structure and characterization of silicon nanoparticles produced using a vibratory disc mill*, The African Review of Physics, **7**, 2012, p45

30. L. Russo, F. Colangelo, R. Cioffi, I. Rea, L.D. Stefano, *A Mechanochemical Approach to Porous Silicon Nanoparticles Fabrication*, Materials, **4**, 2011, p1023
31. B.-C. Kim, H. Uono, T. Fuse, T. Ishihara, M. Senna, *Fabrication of nano-sized Si powders with a narrow size distribution by two-step milling*, Journal of Materials Research, **18**, 2003, p1368
32. B.E. Nilssen, R.A. Kleiv, *Silicon Powder Properties Produced in a Planetary Ball Mill as a Function of Grinding Time, Grinding Bead Size and Rotational Speed*, Silicon, 2020, p1
33. N. Števulová, M. Bálintová, K. Tkáčová, *Material and Energy Interactions between Milling Bodies, Milled Particles, and Milling Environment*, Journal of Materials Synthesis and Processing, **8**, 2000, p265
34. J.Y. Huang, H. Yasuda, H. Mori, *Deformation-induced amorphization in ball-milled silicon*, Philosophical Magazine Letters, **79**, 1999, p305
35. A.S. Heintz, M.J. Fink, B.S. Mitchell, *Silicon nanoparticles with chemically tailored surfaces, Applied Organometallic Chemistry*, **2010**, 2009, p236
36. M. Nöske, S. Breitung-Faes, A. Kwade, *Electrostatic Stabilization and Characterization of Fine Ground Silicon Particles in Ethanol*, Silicon, **11**, 2019, p3001
37. E. Hanelt, *Method for size-reduction of silicon and use of the size-reduced silicon in a lithium-ion battery*, 2016, patent
38. T.P. Herbell, T.K. Glasgow, N.W. Orth, *Demonstration of a Silicon Nitride Attrition Mill for Production of Fine Si and Si3N4 Powders*, Ceramic Bulletin, **63**, 1984, p1176
39. K. Zaghib, A. Guerfi, D. Leblanc, *Particulate Anode Materials and Methods for Their Preparation*, 2016, patent
40. A. Reindl, S. Aldabergenova, A. Alti, G. Frank, W. Peukert, *Dispersing silicon nanoparticles in a stirred media mill – investigating the evolution of morphologym structure and oxide formation*, Physica Status Solidi a, **204**, 2007, p2329
41. P. Ulmann, S.P. Benito, S. Xürcher, P. Lanz, M. Spahr, *Compositions and uses thereof*, 2018, patent
42. D. Leblanc, P. Hovington, C. Kim, A. Guerfi, D. Bélanger, K. Zaghib, *Silicon as anode for high-energy lithium ion batteries: From molten ingot to nanoparticles*, Journal of Power Sources, 2**99**, 2015, p529
43. D.D.M. Wayner, R.A. Wolkow, *Organic modification of hydrogen terminated silicon surfaces*, Journal of the Chemical Society, Perkin Transactions, **2**, 2002, p23
44. R.G. Stephen, F.L. Riley, *Oxidation of Silicon by Water, Journal of the European Ceramic Society*, **2**, 1989, p219
45. A. Reindl, W. Peukert, *Intrinsically stable dispersions of silicon nanoparticles*, Journal of Colloid and Interface Science, **325**, 2008, p173
46. A. Bleier, *Fundamentals of Preparing Suspensions of Silicon and Related Ceramic Powders*, Communications of the American Ceramic Society, 1982, p79

The PV market situation in China 2019 and the future

Songsheng Zheng*, Zhaolin Wang, Jin Chen, Xiaohui Hu, Zhibin Lin
College of Energy Xiamen University, Xiamen, China, 361005
songsheng@xmu.edu.cn

Abstract

Energy security and environment problems are two outstanding issues in front of China. In order to alleviate the problem of energy security, the government focuses on promoting the replacement of oil and gas resources and supports the development of alternative energy. Under the continuous motivation of the china government's incentives, the proportion of the cumulative installed capacity in China has occupied 34.31% to that of the global in 2018. Unfortunately, the rapid growth of PV installation made the power grid jam. The construction of power grid cannot catch up the speed of PV installed, like that of the wind power, so that there are many abandoned solar and wind power generation. In order to get rid of the current two dilemmas, it is urgent to explore more effective ways of energy storage, transportation and utilization. Ammonia (NH_3) packs in more hydrogen than hydrogen (H_2), making it the ideal hydrogen carrier. Ammonia can be utilized in almost all types of combustion engines. This is a very attractive advantage compared to other alternative fuels. Based on the electricity cost from solar power in the west-north of China, the profit and the business opportunities have emerged. The incentive policies from the government would be necessary, and ammonia will bring a breakthrough in Chinese sustainable energy storage to alleviate the problem of energy security.

Keywords： Energy security, CO_2 emission, Policy, Ammonia

1. Introduction

Energy security is always a hot topic in china. The GDP grew nine times in the past decade, and the annual energy consumption increased correspondingly 3times, which makes the Chinese petrol external dependency becomes higher and higher, even reaching 72% in 2019 [1].

Chinese government has set up two-stage development goals [2]: (1) In the first stage from 2020 to 2035, we will build on the foundation created by the moderately prosperous society with a further 15 years of hard work to see that socialist modernization is basically realized. (2) In the second stage from 2035 to the middle of the 21st century, we will, building on having basically achieved modernization, work hard for a further 15

years and develop China into a great modern socialist country that is prosperous, strong, democratic, culturally advanced, harmonious, and beautiful.

On the other hand, we have to face with the environmental issues and achieve another target: 2009, the Copenhagen Climate Change Conference, China pledged that on the basis of 2005, China will reduce its carbon emissions per million GDP by 40% to 45% by 2020 [3]. China aimed to reduce its carbon dioxide emissions per unit of GDP by 60-65% by 2030, from 2005 levels, increase the share of non-fossil energy to 20% of total energy consumption in 2030, and to peak carbon dioxide emission before 2030 [4, 5].

So there are a conflict between our economy development goals and the environmental issues based on fossil fuels. Solar energy is one of the green ways to solve the problems on energy consumption and CO_2 emissions. This paper will systematically summarize the relevant photovoltaic policies in the past and analyze its impact on China's photovoltaic development before 2019. As well as the PV market future will be discussed.

2. The photovoltaic in China before 2019

In 1983, Gansu Institute of Natural Energy built 10kW civilian photovoltaic power station in Yuzhong area, about 40km away from Lanzhou city. This oldest photovoltaic power station in China is now preserved in the research institute base for more than 30 years and can still be maintained at about 7KW (Fig.1) [6].



Fig.1 the first photovoltaic power station in China built in 1983

Since 1998, according to the change of market supply and demand, the Chinese government has continuously issued a number of photovoltaic policies, as is summarized in table 1.

Table 1 the main policies and important events of photovoltaic market in China

Time	Main Policies	Important events
1998	Chinese government began investing in solar power generation, and made plans to build the first 3MW.	Baoding Yingli new energy Co., Ltd has been set up and took the project from government.
2001	The "Guang'ming engineering project" aimed to solve the problem of electricity use in mountainous areas through PV power generation.	1. Around 2002, Suntech, Yingli and other component factories were put into production successively, 2. In August 2004, a 1 MWP grid connected photovoltaic power station in Shenzhen has been succeeded. It was the first large-scale megawatt grid connected photovoltaic power station in Asia at that time.
2005	The Renewable Resources Law was introduced to encourage the development and use of renewable resources	1. In 2005, LDK Solar Energy Technology Co., Ltd has been set for silicon wafer, 2. Suntech listed on NYSE in 2005.
2007	The NDRC (National Development and Reform Commission) issued the Medium and Long-Term Development Plan for Renewable Energy, which emphasized the importance of solar energy for the development of renewable resources.	1. Yingli listed on the New York Stock Exchange (NYSE), raising 319 million US dollars, 2. In June 2007, LDK was listed on the NYSE, raising 469 million US dollars.
2009	1. On March, The government provides subsidies for BIPV projects. This subsidy amounts to CNY20 (USD2.93) per Wp. 2. On July, China is launching what it calls the "Golden Sun" demonstration project to install at least 500 megawatts of solar farms across the country in the next two to three years.	1. Polysilicon prices began to plummet in 2009, falling from the peak of $400 / kg to $40 / kg in less than a year. 2. Hanergy Mobile Energy Holding Group Limited started on thin solar cell. 3. In 2011, the United States took the lead in launching a "double anti" investigation on China's photovoltaic enterprises. 4. GCL group has grown into a global leader in polysilicon materials and silicon wafers.
2012	1. On July, the government issued the 12th Five Year Plan for the development of solar power generation, which further	Longji Co., Ltd., a leading monocrystalline silicon enterprise, listed on the main board of Shanghai Stock Exchange.

	increased the installed target to 21gw and 50gw in 2015 and 2020. 2. On October, the State Grid issued the opinions on grid connected services of distributed photovoltaic power generation to open the grid connected time and fully support distributed energy generation.	
2013	1. On July, Several Opinions on Promoting the Healthy Development of Photovoltaic Industry. China approves subsidy for distributed solar power pilot projects, Subsidy is 0.42CNY (USD0.07) per kWh (including tax). 2. On August, The government set out the following ground power station subsidies for the three types of resource area, such as, CNY0.9 per kWh for class I, CNY0.95 per kWh for class II and CNY1 per kWh for class III, respectively.	1. On March 2013, Suntech announces bankruptcy of its main subsidiary in China.
2014	The State Council issued the Strategic Action Plan for Energy Development (2014-2020), stated that the new energy benchmarking on-grid tariffs would be gradually reduced in order to rationally guide new energy investment.	1. China photovoltaic industry association was established in Beijing. 2. On September, Evergrande Group officially signed a strategic cooperation agreement with Zhangjiakou City, which will invest about 90 billion yuan in the local area and build a 9.2 MW solar photovoltaic power generation project, becoming the largest photovoltaic power generation project in the mainland China. 3. Longji began to accelerate the promotion of diamond wire slicing technology.

2015	China Top Runner Program was to increase the use of high-efficiency PV products, thus maximizing (and eventually increasing) energy yield, initiating PV industry transformation. The Chinese Government enforced a standard subsidy for projects under this program.	Jingke Energy announced that it will start mass production of new technology efficient polycrystalline solar cell with an average efficiency of 20.13% by the end of 2015
2016	The Photovoltaic Poverty Alleviation (PVPA) projects, which utilize the subsidies and income from PV power to alleviate poverty in rural areas, are part of a comprehensive energy policy innovation in China.	Climate change agreement signed in New York on April 22, 2016, which makes arrangements for global action to address climate change after 2020. Photovoltaic industry ushered in a new round of explosive growth.
2018	On May 31st, the government issued a notice on matters relating to PV power generation, which reduced the tariff levels, in order to further improve the mechanism of PV electricity generation and accelerate the decline of the PV electricity price.	On January 19, Longji Co., Ltd. issued a three-year strategic plan for single crystal silicon chip business, which mentioned that the company's single crystal silicon chip production capacity should reach 28gw by the end of 2018, 36gw by the end of 2019 and 45gw by the end of 2020 on the basis of 15gw by the end of 2017. At the same time, the quality parameters and cost level are also explained: the silicon chip quality should be able to support the conversion efficiency of the single crystal perc battery to reach more than 22.5%, the light attenuation is less than 1%, and the non-silicon cost of the new silicon chip production capacity should be reduced to less than 1 CNY.
2019	The national development and Reform Commission and the National Energy Administration issued the notice on actively promoting the work related to the grid access of wind power and photovoltaic power generation at non subsidized parity	Longji invested nearly 30 billion in 2019 to expand 87.25GW single crystal silicon solar cell capacity.

Based on the continuous stimulus policies, till 2018, the cumulative installed capacity of solar PV in China has reached 174.51GW, 34.31% of the global installation. The annual new installation of solar PV in China and its proportion to that of the annual new electric power are plotted in Fig.2.

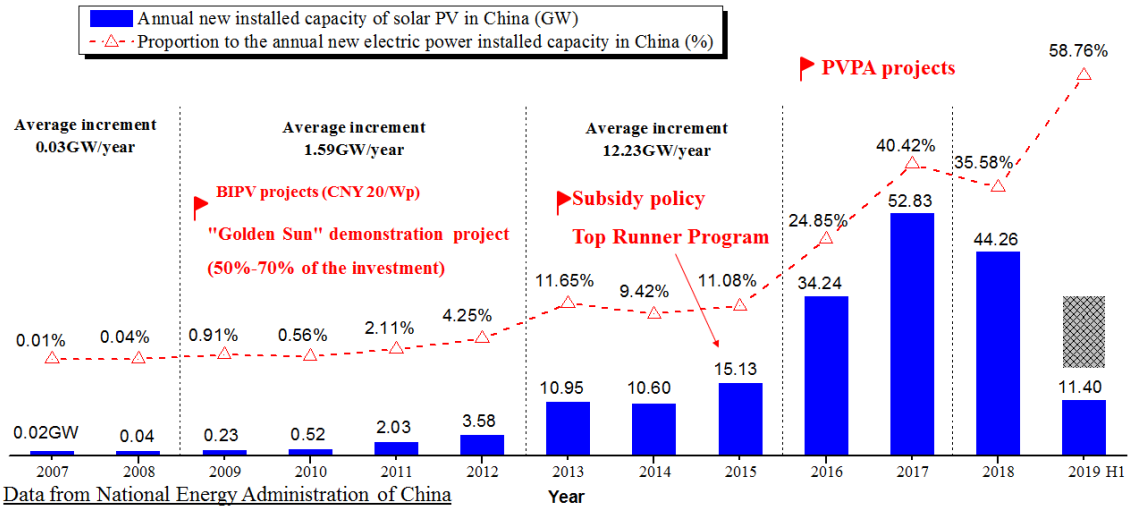


Fig.2 the annual PV installation capacity of China and the related increments

As is shown in Fig.2, the average increment of China PV installation is only 0.03GW/year before 2008. And this number increased to 1.59GW/year from 2009 to 2012, because of the two strong projects launched by Chinese government, which is BIPV projects and 'Golden Sun' demonstration project. The average increment goes sharply up to 12.23GW/year from 2013 to 2015, due to the subsidy policy and Top Runner Program. When Chinese government set up a PVPA project, the annual PV installation increased faster in 2016, and even achieved at 52.83GW/year in 2017. It seems going down slightly to 44.26GW in 2018, because of a new negative policy launched in May 31th 2018.

However, the rapid growth of PV installation made the power grid jam. The construction of power grid cannot catch up the speed of PV installed, similar to that of the wind power. The abandoned solar power generation gradually becomes a big issue due to the energy traffic on grid, which hinders the rapid development of photovoltaic industry.

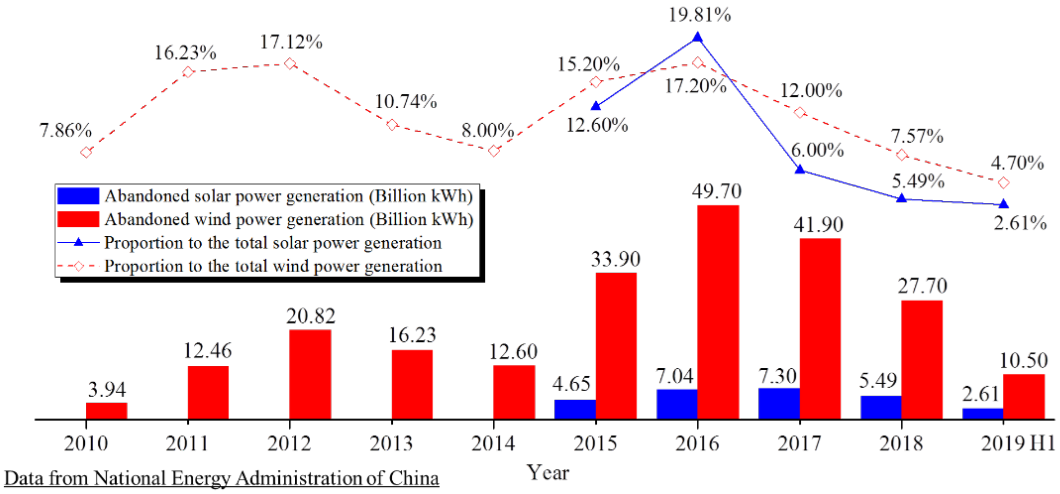


Fig.3 the abandoned solar and wind power generation and their proportion to the total

Fig.3 shows that the abandoned solar power generation accounts for 19.81% of the annual installed capacity in 2016, and even 49.70GW, 17.20% of the 2016 wind power installed capacity was abandoned.

Hydrogen has high combustion calorific value, environmental friendliness and various forms of utilization. Therefore, it is a better energy storage medium, which is gradually concerned by the industry. However, referring to the characteristics of storage and transportation, liquid hydrogen is usually stored at -253°C and its liquefaction is a high energy consumption process and its storage requires a high-level container material. [7-9]

It is interesting that, Ammonia (NH_3) actually packs in more hydrogen than hydrogen (H_2), making it the ideal hydrogen carrier. Ammonia can be utilized in almost all types of combustion engines, e.g., gas turbines and directly in fuel cells, as a sustainable fuel with only small modifications. This is a very attractive advantage compared to other alternative fuels [10-12]. Taking ammonia as a media of energy storage, PV installation will not be limited by power grid, as well as CO_2 emission will directly cut down. A green energy scenery based on ammonia as an energy storage media will be realized as in Fig.4.

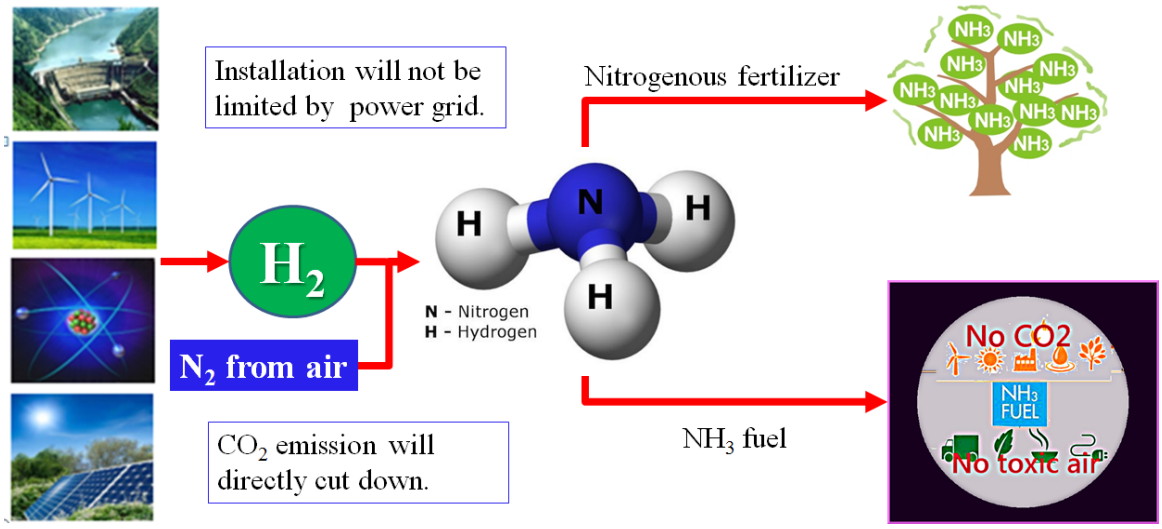


Fig.4 A green energy scenery based on ammonia as an energy storage media

3. Conclusion

Energy security is always a hot topic in china. The GDP grew nine times in the past decade, and the annual energy consumption increased correspondingly 3 times, which makes the Chinese petrol external dependency becomes higher and higher. On the other hand, we have to face with the environmental issues, and there is a conflict between our economy development goals and the environmental issues based on fossil fuels. Solar energy is one of the green ways to solve the problems on energy consumption and CO_2 emissions. Under the continuous motivation of the china government's incentives, the proportion of the cumulative installed capacity in China has occupied 34.31% to that of the global in 2018. The rapid development of photovoltaic industry in China just shows that the Chinese government is forging ahead in the use of renewable energy. Unfortunately, the rapid growth of PV installation made the power grid jam and resulted to a large number of abandoned solar power generation. Therefore, it is urgent to explore more effective ways of energy storage, transportation and utilization. Ammonia (NH_3) actually packs in more hydrogen than hydrogen (H_2), making it the ideal hydrogen carrier. Taking ammonia as a media of energy storage, PV installation will not be limited by power grid, as well as CO_2 emission will directly cut down.

Acknowledgment

The authors appreciate the supports of the National Natural Science Foundation of China (Grant No: 21875199), the National "Double First-class" Construction Special Funds Project (Grant No: 0290-X2100502), the University-Industry-Research Cooperation Project in Fujian Province (Grant No: 2018H6021), the Development fund of College of Energy, Xiamen University (Grant No: 2017NYFZ05).

Reference

[1] Data from the National Bureau of Statistics of China: http://www.stats.gov.cn (in Chinese).

[2] http://cpc.people.com.cn/n1/2017/1028/c64094-29613660.html, 2017 (in Chinese).

[3] Copenhagen Climate Change Conference - December 2009, https://unfccc.int/process-and-meetings/conferences/past-conferences/copenhagen-climate-change-conference-december-2009/copenhagen-climate-change-conference-december-2009.

[4] L. Chen, X. Li, S. Xue, L. F. Qu, and M. X. Wang, Carbon intensity and emission reduction potential in China: spatial measuring method. Journal of Economic Structures, 2019, 8: 11.

[5] Technical report, People's Republic of China, Enhanced Action on Climate Change: China's Intended Nationally Determined Contributions, (June 2015).

[6] Gansu Institute of Natural Energy，http://www.gneri.com.cn/index.php/szxw/705.html

[7] V. Chintala and K. A. Subramanian, A comprehensive review on utilization of hydrogen in a compression ignition engine under dual fuel mode, Renewable and Sustainable Energy Reviews, 2017, 70: 472-491.

[8] T. Tsujimura and Y. Suzuki, The utilization of hydrogen in hydrogen/diesel dual fuel engine. International Journal of Hydrogen Energy, International Journal of Hydrogen Energy, 2017, 11: 1-11.

[9] Y. Du, X. Yu, L. Liu, R. Li, X. Zuo, and Y. Sun, Effect of addition of hydrogen and exhaust gas recirculation on characteristics of hydrogen gasoline engine, International Journal of Hydrogen Energy, 2017, 42(12): 8288-8298.

[10] R. Liu, D. S. Ting, and M. D. Checkel, Ammonia as a fuel for SI engine, SAE Technical Paper, 2003, 2003-01-3095.

[11] E. S. Starkman, H. K. Newhall, R. Sutton, T. Maguire, and L. Farbar, Ammonia as a spark ignition engine fuel: theory and application, SAE Technical Paper, 1966, 660155, https://doi.org/10.4271/660155.

[12] S. Frigo and R. Gentili, Analysis of the behaviour of a 4-stroke Si engine fueled with ammonia and hydrogen, International Journal of Hydrogen Energy, 2013, 38: 1607-1615.

Recycling Silicon Kerf: Challenges, Solutions and Applications

Jan-Philipp Mai[1], Qian Yu*[2]

[1]*JPM Silicon® | JPM Technologies GmbH, Bueltenweg 95, 38106 Braunschweig, Germany*
[2]*JPM Silicon (HK) Ltd., 48 Des Voeux Road, Hong Kong*
**email: j.mai@jpmsilicon.com*

In this paper, we will give a comprehensive overview on technologies to recycle silicon kerf from diamond-wire sawing. Recycling silicon kerf provides numerous challenges. Silicon kerf is usually obtained by filter pressing the used sawing slurry. The remaining filter cake contains water, coolant, plastics from glue, particles from glass holder, loose diamond particles and traces of metallic elements from the nickel coated steel cutting wire. Besides the mix of impurities, the small particle size of approx. 1 µm tend to have high oxide contents. The latter one can prevent the kerf from melting in high-temperature processing and is a major challenge. During the past decade different technologies and applications for recycling diamond-wire silicon kerf have been discussed. This includes recovery of solar silicon, high-quality silicon powders or silicon droplets. While production capacities were re-located from Europe to China, also the boundary conditions for recycling technologies have to be adapted. Hence, we present a low-cost recycling technology with respect to the local market conditions.

1 Introduction

Due to the on-going technology shift from SiC-slurry based wire sawing of silicon wafers to diamond-wire, requirements for recycling silicon kerf change [1]. While before recycling focused at recovery of coolant and SiC cutting particles, diamond-wire allows to recover the silicon itself. With a silicon consumption of approx. 3.6 g/W_p and an installed capacity of 108-143 GW_p [2], the global solar silicon demand in the year 2020 is approx. 388,000-514,800 tons. Silicon kerf sums up to approx. 40% [3] or 183,200 tons of the incoming raw material. Until today, there is not economical feasible solution to recycle silicon kerf.

With a market share of 97%, crystalline silicon solar cells dominate the photovoltaics (PV) market. After crystallization, silicon wafers for solar cells are produced by wire sawing. Today, slurry-based wire sawing using silicon carbide (SiC) particles is nearly completely substituted by diamond wire sawing. This allowed a further reduction in wafer thickness, higher material efficiency and thus lower production costs. Although the silicon consumption [g/W_p] has significantly dropped over the last years and is expected to hit 3.6 g/W_p by 2020 [4], the on-going shift to renewable energy increase solar silicon demand. Figure 1 gives a forecast on the following silicon kerf loss.

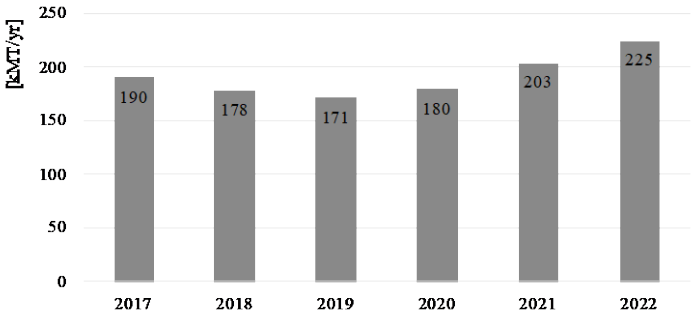


Figure 1: Silicon kerf loss from production of silicon wafers for solar cells (Data: [4], [5]).

Despite new, promising materials for solar cells like perovskite, silicon is expected to remain the predominate material of the PV industry within the next decade. Recycling silicon kerf will be important, both economical and ecological.

2 General Concepts

To close the recycling cycle in solar cell production means to recycle silicon kerf to solar silicon. This would be considered the holy grail in recycling silicon kerf as seen in Figure 2.

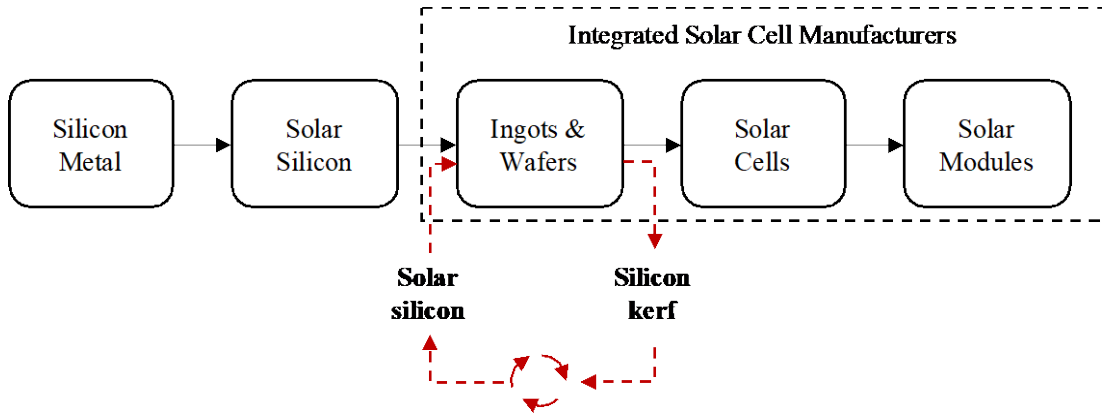


Figure 2: Basic idea of recycling silicon kerf directly into solar silicon to close the raw material cycle within the PV Industry.

While the boom in PV installations between the years 2006-2010 led to a shortage in solar silicon and increasing prices, recycling technologies for silicon kerf seemed appropriate to lower raw material costs. However, following its rapid increase, solar silicon prices quickly dropped to below US-$10/kg and are not expected to surpass US-$ 8/kg [6]. Today, recycling silicon kerf to solar silicon would require low-cost technologies and meet the increasing quality requirements. Thus, besides the development of adequate recycling technologies, companies are looking into new applications for silicon kerf.

2.1 Characteristics of Silicon Kerf

Silicon kerf is filtered from the used sawing fluid by filter press. Besides the silicon particle, the filter cake contains some percentages of cutting fluid and impurities from the nickel-coated steel wire, diamond particles, brick holder and glue.

Due to the high specific surface of the small silicon particles with a diameter < 1 µm [7], silicon particles are instantaneously passivated by a thin silicon dioxide (SiO_2) layer [3], [8]. The reaction occurs with ambient air or water from the cutting fluid. Oxidation of silicon kerf imposes a potential fire and explosion risk, since oxidation is an exothermic reaction. The released heat can lead to fire, while oxidation with water also generates hydrogen (H_2). To handle silicon kerf, precautions are necessary.

While oxidation itself is a problem, the SiO_2 layer hinders further processing and usage of silicon kerf. Melting oxidized silicon particles will generate either gaseous silicon monoxide (SiO) or lead to slag formation. Furthermore, melting silicon kerf under oxidizing condition will in most cases not result in molten silicon, but generate further SiO_2 with the silicon yield dropping to zero.

Besides the oxide related challenges, further impurities influence the later product quality. Besides metallic impurities like iron (Fe), nickel (Ni) and titanium (Ti), diamonds and organics from cutting fluid [9] will incorporate carbon (C) into molten silicon. Carbon will react with silicon to form SiC participates. If directly used in crystallization SiC particles will lead to increased wire breakage.

Although, critical impurities for solar cells like born (B) and phosphorous (P) are consider quite low 1-10 ppmw, further refining efforts have to be undertaken to remove other metallic impurities as for the carbon content. Table 1 gives a brief summary of typical impurities to be found inside silicon kerf.

Table 1: Typical composition of silicon kerf (filter cake).

Water	10-30%
Volatiles (at 1,000°C)	3-4%
Metals	100 ppmw
SiO_2	3-6%
Carbon	2-3%
B, P	1-5 ppmw

2.2 Recycling Concepts

Recycling silicon kerf can be separated into two routes: (1) Either use of silicon powders as received from the sawing process or by (2) production of briquettes and pellets for later metallurgical treatment. In both cases, recycling technologies have to compete with the primary products in their markets. While applications for high-quality silicon powders remain market niches, metallurgical silicon is a commodity with a wide range of applications. The general concept combines some basic operations as seen in Figure 3.

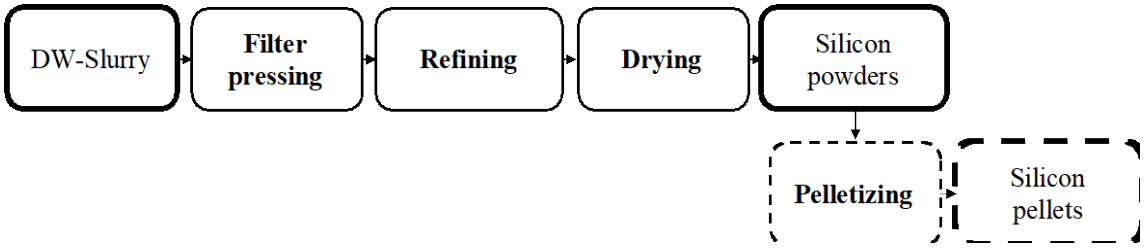


Figure 3: Basic process steps for handling the used diamond wire (DW) slurry for production of silicon wafers for solar cells to produce silicon powders or pellets for metallurgical applications.

The used slurry is usually processed on-site by filter pressing to remove the cutting fluid. Recycling the cutting fluid itself is already an important part of recycling efforts along the solar cell production chain. Next, the oily filter cake will be refined by a series of techniques to remove impurities and left cutting fluid. The cleaned silicon powders can be either used as a raw material or treated further to yield briquettes or pellets for metallurgical processing. Production of briquettes and pellets will overcome the challenge of charging powdery materials to furnaces and increase heat transfer. While there have been numerous projects on recycling silicon kerf, first of all from SiC-based slurry, only a few projects made it to a commercial scale.

3 Projects Overview

Within the SIKELOR project [8] the Italian company Garbo focussed on recovery of high-purity silicon pellets as solar silicon. The process combines three unique steps: (1) Refining the incoming silicon kerf by etching and washing; (2) Production of pellets using a methyl silicate binder; (3) Drying and sintering to increase pellets density. A simplified process diagram is given in Figure 4

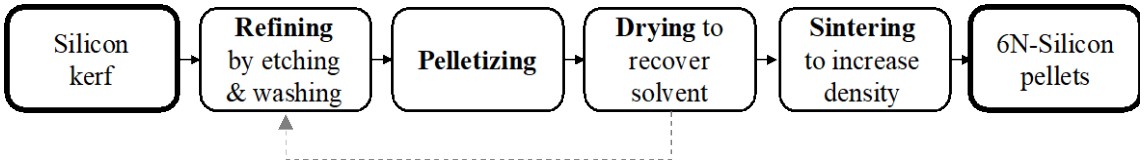


Figure 4: Process steps as implemented by Garbo inside the SIKELOR project to yield silicon pellets with a purity of 99.9999% (6N).

One of the key factors is sintering the produced pellets in order to achieve a high load factor. By sintering the density increases from 1.3 g/cm^3 towards 2.0 g/cm^3 [8]. With a target purity of 99.9999% (6N) the pellets are directly inserted into the crystallization furnace. With estimated production costs of US-

$10/kg, costs are above current market prices. The company does not advertise this particular product anymore.

The Norwegian company ReSiTec is specialised in recycling metals powders and slurry. Within the research project CABRISS the company investigated two routes to utilize silicon kerf. The first one follows the idea of Garbo to produce high-purity silicon pellets (6N), the second utilization route is silicon powder with a purity of maximum 99.9% (3N). While the first product is inserted again into the PV value chain, high-purity silicon powder can be used primary in the ceramic industry.

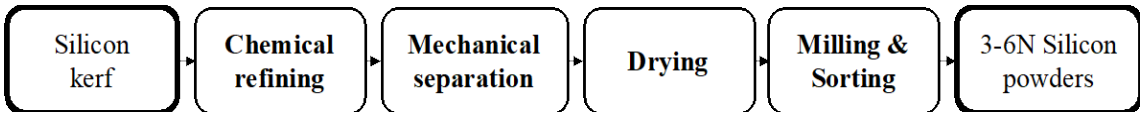


Figure 5: Process steps as implemented by ReSiTec inside the CABRISS project to yield silicon powders with a purity of 3-6N to be used as powders or further processed into pellets.

Silicon kerf is purified by acid leading and washing. The still wet kerf is further treated by mechanical processes, dried and jet milled. Depending on the purification efforts, the received silicon powders have a purity of 3-6N. By further processing them to pellets they can be added to crystallization furnaces.

The French start-up company ROSI combines a former process from the Swiss company PlusMAT [10] for refining silicon kerf and a novel metallurgical process [11]. In the process as outlines in Figure 6, impurities are removed by chemical means due to flotation. The received silicon powder is dried and inserted into a (semi-)continuous induction furnace to form silicon pellets.



Figure 6: Process steps as implemented by ROSI based on PlusMAT processes and innovative induction furnace.

ROSI focusses on production of silicon pellets or droplets by induction melting. The induction furnace as outlined in the patent applications allows a (semi-)continuous production of small silicon droplets up to 10 mm. Oxides are collected inside the induction furnace and have to be discharged frequently. Besides the term “high-purity silicon droplets” the company does not give further details on the silicon quality and production costs are unknown.

The German technology company JPM Silicon® develops a recycling process to recycle silicon kerf into metallurgical silicon. The primary market is thus the PV industry. As for the concepts before, briquettes and pellets are used to overcome slow heat transfer within the melting process as seen in Figure 7.



Figure 7: Process steps as implemented by JPM Silicon to recycle silicon kerf to metallurgical silicon.

With a purity of approx. 99% the silicon is comparable to metallurgical silicon as used in the aluminium, chemical and PV industry, while production costs are expected to be 30% lower than primary production.

4 Discussion & Conclusion

Although, new materials for solar cells like perovskite evolve, silicon is expected to remain the predominate material of the PV industry. With declined silicon prices and a strong cost pressure on the PV industry, prices for solar silicon are not expected to reach more than US-$10/kg anytime in the future. Recycling technologies have to compete with the primary production of solar silicon. Recycling silicon kerf is a two-sided development process. On the raw material side, a detailed knowledge of the incoming silicon kerf composition is necessary, while on the other hand knowledge on the intended application is needed. Matching both sides by the right recycling technologies, is the primary challenge.

Recycling silicon kerf into solar silicon addresses the same challenges as marketing upgraded metallurgical-grade (UMG) silicon. A reduced silicon quality has to result in a significant price advantage. Furthermore, the trend to mono-crystalline or mono-like solar cells raises the quality bar for raw materials. However, low-cost recycled silicon kerf as an alternative to primary MG-Silicon might enable a renaissance of metallurgical solar silicon routes. Additionally, silicon for lithium-ion batteries seems a promising market niche for products from recycled silicon kerf.

Literature

[1] J. Peguiron, R. Mueller, J. Zanetti, S. Habegger, M. Burri, and F. Monti di Sopra, 'Reducing Wire Wear by Mechanical Optimization of Equipment in Diamond-Wire Wafering'. Accessed: Jun. 10, 2020. [Online]. Available: https://www.meyerburger.com/user_upload/dashboard_news_bundle/2d114c43c6f51eaf7a5a1eefc54c8a40ab0c8d7d.pdf.

[2] S. Enkhradt, 'BNEF Lowers 2020 Global PV Outlook due to Coronavirus Concerns', Mar. 13, 2020. https://www.pv-magazine.com/2020/03/13/bnef-lowers-2020-global-pv-outlook-due-to-coronavirus-concerns/ (accessed Jun. 10, 2020).

[3] T. Halverson, 'Recycling of Silicon Kerf from PV', Freiberg, 2017.

[4] J. Bernreuter, 'Silicon Consumption to Drop to 3.6 Grams per Watt by 2020', Bernreuter Research, Würzburg, 2017.

[5] SolarPower Europe, 'Global Market Outlook 2019-2023', Dec. 2019. Accessed: Jun. 10, 2020. [Online]. Available: http://www.solarpowereurope.org/wp-content/uploads/2018/09/Global-Market-Outlook-2018-2022.pdf.

[6] E. Bellini, 'Polysilicon Prices to Rebound in September', Aug. 20, 2019. https://www.pv-magazine.com/2019/08/20/polysilicon-prices-to-rebound-in-september/ (accessed Jun. 10, 2020).

[7] I. Lombardi *et al.*, 'High Yield Recycling Process of Silicon Kerf from Diamond Wire Wafering', *La Chimica & L'Industria*, pp. 111–113, Mar. 2012.

[8] A. Cramer *et al.*, *SIKELOR - Silicon kerf loss recycling*. Bamberg, 2015.

[9] M. Vazquez-Pufleau, T. S. Chadha, G. Yablonsky, H. F. Erk, and P. Biswas, 'Elimination of Carbon Contamination from Silicon Kerf Using a Furnace Aerosol Reactor Methodology', *Ind. Eng. Chem. Res.*, vol. 54, no. 22, pp. 5914–5920, Jun. 2015, doi: 10.1021/acs.iecr.5b00577.

[10] Plus MAT AG, 'Resources from Waste: PV-Silicon Recovery from Wafer Sawing Process'. https://fr.slideshare.net/YunLuo-CH/presentation-plus-mat?nomobile=true&smtNoRedir=1 (accessed Jun. 10, 2020).

[11] G. Chichignoud, J. Altenberend, and D. Bajolet, 'Device for Producing Molten Silicon', WO 2019/234072 A1, Jun. 05, 2019.